

UIIU-ENG 92-3601

Report No. 160

AN INVESTIGATION INTO THERMOMECHANICAL FATIGUE
OF METAL MATRIX COMPOSITES

by

Metin Karayaka

A Report of the

MATERIALS ENGINEERING—MECHANICAL BEHAVIOR

College of Engineering, University of Illinois at Urbana-Champaign

January 1992

AN INVESTIGATION INTO THERMOMECHANICAL FATIGUE OF METAL MATRIX COMPOSITES

ABSTRACT

Experimental and theoretical approaches are used to characterize the thermomechanical deformation behavior of metal matrix composites. Experiments on unreinforced and SiC particulate reinforced Al 2xxx-T4 have been conducted under several mechanical strain-temperature phasing conditions. Based on stress range, substantial improvements in fatigue life have been observed. However, based on strain range, the effect of reinforcement on fatigue lives differs depending on the mechanical strain-temperature phasing, temperature, and strain rate. Several deformation mechanisms of unreinforced and reinforced Al 2xxx-T4 have been identified, including void formation, crack initiation, intergranular/ transgranular crack growth, oxide penetration at the crack tips, crack deflection due to particle interference, and mean stress effects.

Theoretical approaches include the development of a general micromechanistic constitutive equation, based on Eshelby's equivalent inclusion theory, and a life prediction methodology for metal matrix composites. Synergistic effects of particulate reinforcement on high temperature thermomechanical behavior are studied. The constitutive model provides insight into the internal stress-strain behavior, including effective and hydrostatic stresses, of both the matrix and the reinforcement developed during cyclic loading conditions. The deformation behavior of the constituents is used to develop an experimentally based micromechanistic life prediction model. The damage caused by internal stresses, oxidation, creep, and fatigue mechanisms as a function of reinforcement volume fraction is quantified for wide range of loading conditions.

ACKNOWLEDGEMENTS

This work is supported by a grant from the Ford Foundation. The cooperation of Dr. John Allison, Materials Science Department, Ford Motor Company is appreciated.

My advisor, Professor Huseyin Sehitoglu, is acknowledged for his friendship, encouragement, and insightful suggestions during the course of my graduate career. His time spent in discussions and review of this research is greatly appreciated.

I thank Yavuz Kadioglu and his family for their love and support during my college education.

I especially thank Lisa Kaye DeSelms for editing this manuscript and for her support during last two years.

My parents and family are thanked for their unselfish sacrifice and encouragement throughout my education.

TABLE OF CONTENTS

	Page
LIST OF TABLES.....	vii
LIST OF FIGURES.....	viii
NOMENCLATURE.....	xvi
1. INTRODUCTION.....	1
2. BACKGROUND.....	4
2.1 Elevated Temperature Fatigue Behavior of Al 2xxx Alloys.....	5
2.2 Fatigue Crack Initiation and Growth Behavior of SiC/Al Composites.....	6
2.3 Room Temperature Fatigue Life Behavior of SiC/Al Composites.....	7
2.4 Creep of SiC/Al Composites.....	8
2.5 Strengthening Behavior of SiC/Al Composites.....	9
3. MATERIALS AND EXPERIMENTAL PROCEDURE.....	12
3.1. Materials.....	12
3.2. Experimental Equipment.....	13
3.3. Experimental Procedure.....	14
4. EXPERIMENTS.....	16
4.1. Isothermal Fatigue Experiments.....	16
4.2. Monotonic and Cyclic Behavior.....	17
4.3. Thermomechanical Fatigue Experiments.....	18
4.4. Metallographic Examination.....	19
4.5. Crack Growth Mechanism Maps.....	21
4.6. Discussion.....	22
5. DEFORMATION MODEL FOR METAL MATRIX COMPOSITES.....	25
5.1. Background.....	25
5.2. Theory.....	28
5.2.1. Eshelby's Equivalent Inclusion Method.....	28

5.2.2. Modified Eshelby's Equivalent Inclusion Method.....	29
5.3. Constitutive Equation for the Composite	33
5.4. Constitutive Equation for Al 2xxx-T4.....	36
5.4.1. Flow Rule	38
5.4.2. Hardening Functions.....	39
5.4.3. Recovery Functions.....	40
5.5. Simulations.....	41
5.5.1. Monotonic Behavior.....	42
5.5.2. Cyclic Behavior.....	42
5.5.3. Average Stress-Strain Behavior of the Matrix	44
5.6. Discussion.....	47
6. LIFE PREDICTION MODEL FOR METAL MATRIX COMPOSITES.....	52
6.1. Background	52
6.2. Life Prediction Methodology for Al 2xxx-T4.....	54
6.2.1. Fatigue Damage.....	54
6.2.2. Oxidation Damage	55
6.2.3. Creep Damage.....	58
6.3. Life Prediction Methodology for SiCp Reinforced Al 2xxx-T4.....	60
6.4. Life Prediction Results at Elevated Temperatures.....	62
6.5. Discussion.....	64
7. CONCLUSIONS.....	67
TABLES.....	69
FIGURES.....	74
REFERENCES	160

LIST OF TABLES

	Page
Table I	Modulus and flow strength properties of 0%, 15%, and 20% SiC _p reinforced Al 2xxx-T4..... 70
Table II	Material constants for Al 2xxx-T4..... 71
Table III	Material constants used in fatigue life prediction model for Al 2xxx-T4..... 72
Table IV	Experiments used to determine constants of the life prediction equations..... 73

LIST OF FIGURES

	Page
Figure 3.1 Grain boundary cavitation, isothermal fatigue, 200 °C, $\dot{\epsilon} = 3.0 \times 10^{-3}$ 1/sec; unreinforced material longitudinal section.....	75
Figure 3.2 Grain boundary cavitation, isothermal fatigue, 200 °C, $\dot{\epsilon} = 3.0 \times 10^{-3}$ 1/sec; unreinforced material horizontal section.....	76
Figure 3.3 Grain boundary cavitation, isothermal fatigue, 200 °C, $\dot{\epsilon} = 3.0 \times 10^{-3}$ 1/sec; reinforced material longitudinal section.....	77
Figure 3.4 Schematic of mechanical strain-temperature variation in TMF In-Phase, TMF Out-of-Phase, and isothermal fatigue loading	78
Figure 4.1 Mechanical strain range-cycles to failure data for isothermal fatigue of unreinforced Al 2xxx-T4.....	79
Figure 4.2 Mechanical strain range-cycles to failure data for isothermal fatigue of 15% reinforced Al 2xxx-T4.....	80
Figure 4.3 Mechanical strain range-cycles to failure data for isothermal fatigue of 20% reinforced Al 2xxx-T4.....	81
Figure 4.4 Mechanical strain range-cycles to failure data for isothermal fatigue of unreinforced and 20% SiC _p reinforced Al 2xxx-T4 at 200 °C	82
Figure 4.5 Mechanical strain range-cycles to failure data for isothermal fatigue of unreinforced and 20% SiC _p reinforced Al 2xxx-T4 at 300 °C	83
Figure 4.6 Mechanical stress range-cycles to failure data for isothermal fatigue of unreinforced and 20% SiC _p reinforced Al 2xxx-T4 at 200 °C	84

Figure 4.7	Mechanical stress range-cycles to failure data for isothermal fatigue of unreinforced and 20% SiC _p reinforced Al 2xxx-T4 at 300 °C	85
Figure 4.8	Stress amplitude versus mechanical strain, unreinforced material 200 °C.....	86
Figure 4.9	Stress amplitude versus mechanical strain, unreinforced material 300 °C.....	87
Figure 4.10	Stress amplitude versus mechanical strain, 15% reinforced material 200 °C	88
Figure 4.11	Stress amplitude versus mechanical strain, 15% reinforced material 300 °C	89
Figure 4.12	Stress amplitude versus mechanical strain, 20% reinforced material 200 °C	90
Figure 4.13	Stress amplitude versus mechanical strain, 20% reinforced material 300 °C	91
Figure 4.14	Stress versus mechanical strain, unreinforced material, TMF IP 100- 300 °C.....	92
Figure 4.15	Stress versus mechanical strain, unreinforced material, TMF OP 100- 300 °C	93
Figure 4.16	Stress versus mechanical strain, 20% reinforced material, TMF IP 100- 300 °C	94
Figure 4.17	Stress versus mechanical strain thermomechanical fatigue, 20% reinforced material, TMF OP 100- 300 °C	95
Figure 4.18	TMF IP and TMF OP; mechanical strain range versus life of unreinforced material.....	96
Figure 4.19	TMF IP and TMF OP; Mechanical strain range versus life of 0% and 20% reinforced materials	97

Figure 4.20	Crack initiation sites, 20% reinforced material, TMF IP, 100-300 °C.....	98
Figure 4.21	Crack initiation sites, 20% reinforced material, isothermal fatigue, 300 °C, $\dot{\epsilon} = 3.0 \times 10^{-5}$ 1/sec.....	99
Figure 4.22	Crack initiation sites, 15% reinforced material, isothermal fatigue, 200 °C, $\dot{\epsilon} = 3.0 \times 10^{-3}$ 1/sec.....	100
Figure 4.23	Transgranular and intergranular (mixed) crack growth, reinforced material, isothermal fatigue, 200 °C, $\dot{\epsilon} = 3.0 \times 10^{-3}$ 1/sec.....	101
Figure 4.24	Transgranular crack growth in the unreinforced material, TMF OP, 100-200 °C.....	102
Figure 4.25	Auger electron spectroscopy analysis of crack tip, TMF OP 100-300 °C, a) SEM photograph, b) Oxygen dot map.....	103
Figure 4.26	Auger electron spectroscopy analysis of crack tip, TMF OP 100-300 °C, a) SEM photograph, b) Oxygen dot map.....	104
Figure 4.27	Auger electron spectroscopy analysis of crack tip, TMF IP 100-300 °C, a) SEM photograph, b) Oxygen dot map.....	105
Figure 4.28	Crack growth map at $\dot{\epsilon} = 3.0 \times 10^{-5}$ 1/sec, unreinforced material.....	106
Figure 4.29	Crack growth map at $\dot{\epsilon} = 3.0 \times 10^{-5}$ 1/sec, 20% reinforced material.....	107
Figure 4.30	Crack growth map of unreinforced and reinforced materials.....	108
Figure 5.1	Schematic illustration of Eshelby's model.....	109
Figure 5.2	Inelastic strain rate versus yield strength for Al 2xxx-T4.....	110
Figure 5.3	Change in elastic modulus with temperature for Al 2xxx- T4.....	111

Figure 5.4	Flow rule for Al 2xxx-T4.....	112
Figure 5.5	Monotonic stress-strain behavior of Al 2xxx-T4, experiments and simulations	113
Figure 5.6	Monotonic stress-strain behavior of Al 2xxx-T4 15%SiC _p , experiments and simulations	114
Figure 5.7	Monotonic stress-strain behavior of Al 2xxx-T4 20%SiC _p , experiments and simulations	115
Figure 5.8	Flow rule relating inelastic strain rate to effective stress for Al 2xxx-T4 and simulations for 15%, 20%, and 30% SiC _p reinforcement.....	116
Figure 5.9	Isothermal cyclic stress-strain behavior of Al 2xxx-T4, experiment and simulation, T = 200 °C, $\dot{\epsilon} = 3.0 \times 10^{-3}$ 1/sec.....	117
Figure 5.10	Isothermal cyclic stress-strain behavior of Al 2xxx-T4, experiment and simulation, T = 200 °C, $\dot{\epsilon} = 3.0 \times 10^{-5}$ 1/sec.....	118
Figure 5.11	Isothermal cyclic stress-strain behavior of Al 2xxx-T4, experiment and simulation, T = 300 °C, $\dot{\epsilon} = 3.0 \times 10^{-3}$ 1/sec.....	119
Figure 5.12	Isothermal cyclic stress-strain behavior of Al 2xxx-T4, experiment and simulation, T = 300 °C, $\dot{\epsilon} = 3.0 \times 10^{-5}$ 1/sec.....	120
Figure 5.13	Isothermal cyclic stress-strain behavior of Al 2xxx-T4 20% SiC _p , experiment and simulation, longitudinal stress- strain behavior, T = 200 °C, $\dot{\epsilon} = 3.0 \times 10^{-3}$ 1/sec.....	121
Figure 5.14	Isothermal cyclic stress-strain behavior of Al 2xxx-T4 15% SiC _p , experiment and simulation, longitudinal stress- strain behavior, T = 200 °C, $\dot{\epsilon} = 3.0 \times 10^{-5}$ 1/sec.....	122
Figure 5.15	Isothermal cyclic stress-strain behavior of Al 2xxx-T4 15% SiC _p , experiment and simulation, longitudinal stress- strain behavior, T = 300 °C, $\dot{\epsilon} = 3.0 \times 10^{-3}$ 1/sec.....	123

Figure 5.16	Isothermal cyclic stress-strain behavior of Al 2xxx-T4 15% SiC _p , experiment and simulation, longitudinal stress-strain behavior, T = 300 °C, $\dot{\epsilon} = 3.0 \times 10^{-5}$ 1/sec.....	124
Figure 5.17	Isothermal cyclic stress-strain behavior of Al 2xxx-T4 15% SiC _p , longitudinal stress-strain behavior simulations of matrix, reinforcement, and composite.....	125
Figure 5.18	Isothermal cyclic stress-strain behavior of Al 2xxx-T4 15% SiC _p , transverse stress-strain behavior simulations of matrix, reinforcement, and composite.....	126
Figure 5.19	TMF OP 100-300 °C cyclic stress-strain behavior of Al 2xxx-T4, experiment and simulation.....	127
Figure 5.20	TMF IP 100-300 °C cyclic stress-strain behavior of Al 2xxx-T4, experiment and simulation.....	128
Figure 5.21	TMF OP 100-200 °C cyclic stress-strain behavior of Al 2xxx-T4, experiment and simulation.....	129
Figure 5.22	TMF IP 100-200 °C cyclic stress-strain behavior of Al 2xxx-T4, experiment and simulation.....	130
Figure 5.23	TMF OP 100-300 °C cyclic stress-strain behavior of Al 2xxx-T4 20% SiC _p , experiment and simulation.....	131
Figure 5.24	TMF OP 100-300 °C cyclic stress-strain behavior of Al 2xxx-T4 20% SiC _p , experiment and simulation.....	132
Figure 5.25	TMF OP 100-300 °C cyclic stress-strain behavior of Al 2xxx-T4 15% SiC _p , experiment and simulation.....	133
Figure 5.26	TMF OP 100-300 °C cyclic stress-strain behavior of Al 2xxx-T4 15% SiC _p , transverse stress-strain behavior simulations of matrix, reinforcement, and composite.....	134

Figure 5.27	TMF OP 100-300 °C cyclic stress-strain behavior of Al 2xxx-T4 15% SiC _p , transverse stress-strain behavior simulations of matrix, reinforcement, and composite.....	135
Figure 5.28	Ratio of hydrostatic stress to effective stress in the matrix versus volume fraction of reinforcement, isothermal fatigue simulations, T = 300 °C	136
Figure 5.29	Ratio of matrix strain (stress) to composite strain (stress), isothermal fatigue simulations T = 20 °C, T = 300 °C.....	137
Figure 5.30	TMF IP, simulation of transverse stress-strain behavior in the matrix for different thermal expansion coefficient mismatch of matrix and reinforcement	138
Figure 5.31	TMF OP, simulation of transverse stress-strain behavior in the matrix for different thermal expansion coefficient mismatch of matrix and reinforcement	139
Figure 5.32	Ratio of hydrostatic stress to effective stress in the matrix versus volume fraction of reinforcement at 300 °C end of a TMF OP cycle, simulation.....	140
Figure 5.33	Ratio of hydrostatic stress to effective stress in the matrix versus volume fraction of reinforcement at 300 °C end of a TMF IP cycle, simulation.....	141
Figure 6.1	The variation of $(\alpha_1 \bar{\sigma}^m + \alpha_2 \sigma_H^m/K)$ during a TMF IP loading cycle.....	142
Figure 6.2	The variation of $(\alpha_1 \bar{\sigma}^m + \alpha_2 \sigma_H^m/K)$ during a TMF OP loading cycle.....	143
Figure 6.3	Room temperature strain-life behavior and predictions.....	144
Figure 6.4	Isothermal strain-life prediction, unreinforced Al 2xxx-T4, T = 200 °C, $\dot{\epsilon} = 3.0 \times 10^{-3}$ 1/sec, 3.0×10^{-5} 1/sec.....	145

Figure 6.5	Isothermal strain-life prediction, 20% reinforced Al 2xxx-T4, T = 200 °C, $\dot{\epsilon} = 3.0 \times 10^{-3}$ 1/sec, 3.0×10^{-5} 1/sec.....	146
Figure 6.6	Isothermal strain-life prediction, unreinforced Al 2xxx-T4, T = 300 °C, $\dot{\epsilon} = 3.0 \times 10^{-3}$ 1/sec, 3.0×10^{-5} 1/sec.....	147
Figure 6.7	Isothermal strain-life prediction, 20% reinforced Al 2xxx-T4, T = 300 °C, $\dot{\epsilon} = 3.0 \times 10^{-3}$ 1/sec, 3.0×10^{-5} 1/sec.....	148
Figure 6.8	Isothermal stress-life prediction, unreinforced Al 2xxx-T4, T = 200 °C, $\dot{\epsilon} = 3.0 \times 10^{-3}$ 1/sec, 3.0×10^{-5} 1/sec.....	149
Figure 6.9	Isothermal stress-life prediction, 20% reinforced Al 2xxx-T4, T = 200 °C, $\dot{\epsilon} = 3.0 \times 10^{-3}$ 1/sec, 3.0×10^{-5} 1/sec.....	150
Figure 6.10	Isothermal stress-life prediction, unreinforced Al 2xxx-T4, T = 300 °C, $\dot{\epsilon} = 3.0 \times 10^{-3}$ 1/sec, 3.0×10^{-5} 1/sec.....	151
Figure 6.11	Isothermal stress-life prediction, 20% reinforced Al 2xxx-T4, T = 300 °C, $\dot{\epsilon} = 3.0 \times 10^{-3}$ 1/sec, 3.0×10^{-5} 1/sec.....	152
Figure 6.12	TMF OP life predictions 0%, 20% reinforced Al 2xxx-T4, $\dot{\epsilon} = 3.0 \times 10^{-5}$ 1/sec	153
Figure 6.13	TMF IP life predictions, 0%, 20% reinforced Al 2xxx-T4, $\dot{\epsilon} = 3.0 \times 10^{-5}$ 1/sec.....	154
Figure 6.14	TMF OP life predictions 0%, 20%, 40% SiC _p reinforced Al 2xxx-T4, $\dot{\epsilon} = 3.0 \times 10^{-5}$ 1/sec, creep damage only.....	155
Figure 6.15	TMF IP life predictions 0%, 20% , 40% SiC _p reinforced Al 2xxx-T4, $\dot{\epsilon} = 3.0 \times 10^{-5}$ 1/sec, creep damage only.....	156
Figure 6.16	TMF OP life predictions 0%, 20% , 40% SiC _p reinforced Al 2xxx-T4, $\dot{\epsilon} = 3.0 \times 10^{-5}$ 1/sec, oxidation damage only.....	157
Figure 6.17	TMF IP life predictions 0%, 20% , 40% SiC _p reinforced Al 2xxx-T4, $\dot{\epsilon} = 3.0 \times 10^{-5}$ 1/sec, oxidation damage only	158

Figure 6.18 TMF OP or TMF IP life predictions 0%, 20% , 40% SiC_p,
fatigue damage only 159

NOMENCLATURE

a	Strain rate sensitivity exponent of oxide growth
A	Flow rule coefficient of the matrix
A_{cr}	Coefficient in creep damage equation
b	Fatigue strength exponent
B	Drag stress hardening rate coefficient of the matrix
B_{ox}	Rate of oxidation due to repeated rupture
c	Fatigue ductility exponent
C_{ijkl}^r, C_{ijkl}^m	Reinforcement and matrix stiffness tensors
\dot{C}_{ijkl}^m	Matrix stiffness tensor rate
D_o	Diffusion coefficient for oxidation
D^{creep}	Creep damage per cycle
D_{matrix}^{creep}	Creep damage per cycle in the matrix
D^{fat}	Fatigue damage per cycle
D_{matrix}^{fat}	Fatigue damage per cycle in the matrix
D^{ox}	Oxidation damage per cycle
D_{matrix}^{ox}	Oxidation damage per cycle in the matrix
D^{tot}	Total damage per cycle
E^r, E^m	Reinforcement, matrix elastic modulus
h_{cr}	Critical thickness of oxide growth rate
h_k	Back stress recovery function of the matrix
h_α	Back stress hardening function of the matrix
K	Drag stress of the matrix
\dot{K}	Drag stress rate of the matrix
K_{cr}	Critical oxide growth rate
K_o	Initial drag stress of the matrix

K_p	Parabolic oxidation growth constant
K_p^{eff}	Effective parabolic oxidation constant
K_{rec}	Drag stress recovery of the matrix
K_{sat}	Saturated drag stress of the matrix
N_f	Number of cycles to specimen failure
N_f^{creep}	Number of cycles to failure from creep damage
N_f^{fat}	Number of cycles to failure from fatigue damage
N_f^{ox}	Number of cycles to failure from oxidation damage
Q	Activation energy for parabolic oxide growth
r_α	Back stress recovery function of the matrix
r_k	Drag stress recovery function of the matrix
R	Universal gas constant
R_e	Minimum strain to maximum strain ratio
s_{ij}	Deviatoric stress tensor of the matrix
S_{ijkl}	Eshelby's tensor
t	Time
t_c	Period of a fatigue cycle
T	Temperature
\dot{T}	Temperature rate
T_{max}	Maximum temperature of a TMF cycle
T_{min}	Minimum temperature of a TMF cycle
T_{mean}	Mean temperature of a TMF cycle
T_o	Reference temperature
v_m	Matrix volume fraction
v_r	Reinforcement volume fraction
α_1, α_2	Scaling factors for creep damage in tension and compression
α_{ij}	Back stress tensor of the matrix

α'_{ij}	Deviatoric back stress tensor of the matrix
$\dot{\alpha}'_{ij}$	Deviatoric back stress rate tensor of the matrix
β	Oxidation growth exponent
δ_o	Measure of oxide ductility
δ_{ijkl}	Fourth order identity tensor
ΔC_{ijkl}	Difference of reinforcement and matrix stiffness tensors
$\Delta \epsilon_{\text{mech}}$	Mechanical strain range
$\Delta \epsilon_{ij}^m, \Delta \epsilon_{ij}^r, \Delta \epsilon_{ij}^c$	Stress range of the matrix, reinforcement, and composite
ΔH	Activation energy for creep
$\Delta \theta_{ij}$	Thermal expansion difference between matrix and
$\Delta \sigma_{ij}^m, \Delta \sigma_{ij}^r, \Delta \sigma_{ij}^c$	Stress range of the matrix, reinforcement, and composite
ΔT	Temperature range
$\epsilon_{ij}^{\text{cn}}$	Constraint strain tensor
$\epsilon_{ij}^{\text{in}}$	Matrix inelastic strain tensor
$\epsilon_{ij}^m, \epsilon_{ij}^r, \epsilon_{ij}^c$	Total matrix, reinforcement, composite strain tensors
$\epsilon_{ij}^{\text{me}}, \epsilon_{ij}^{\text{re}}, \epsilon_{ij}^{\text{ce}}$	Elastic matrix, reinforcement, composite strain tensors
ϵ_{mech}	Mechanical strain
ϵ_{net}	Net strain
ϵ_{ij}^o	Remote elastic strain field in Eshelby's theory
$\epsilon_{ij}^{\text{pm}}$	Total eigenstrain of the matrix
$\epsilon_{ij}^{\text{pr}}$	Total eigenstrain of the reinforcement
$\epsilon_{ij}^{\text{th}}$	Thermal strain due to mismatch of thermal expansion coefficients
ϵ_{ij}^*	Transformation strain tensor
$\dot{\epsilon}$	Strain rate
$\dot{\epsilon}_{ij}^{\text{in}}$	Matrix inelastic strain rate tensor
$\dot{\bar{\epsilon}}^{\text{in}}$	Effective matrix inelastic strain rate

$\dot{\epsilon}_{ij}^m, \dot{\epsilon}_{ij}^r, \dot{\epsilon}_{ij}^c$	Matrix, reinforcement, composite strain rate tensors
$\dot{\epsilon}_{ij}^{me}, \dot{\epsilon}_{ij}^{re}, \dot{\epsilon}_{ij}^{ce}$	Matrix, reinforcement, composite elastic strain rate tensors
$\dot{\epsilon}_{mech}$	Mechanical strain rate
$\dot{\epsilon}_{th}$	Thermal strain rate
$\dot{\epsilon}_{ij}^*$	Transformation strain rate tensor
ϵ_{ij}^{**}	Modified transformation strain tensor
ϵ_f'	Fatigue ductility coefficient
$\tilde{\epsilon}_{ij}^m, \tilde{\epsilon}_{ij}^r$	Matrix, reinforcement average strain disturbance tensors
ϕ^{creep}	Phasing factor for creep
ϕ^{ox}	Phasing factor for oxidation
Φ^{creep}	Phasing function for creep
Φ^{ox}	Phasing function for oxidation
θ	Coefficient of thermal expansion
$\theta_{ij}^m, \theta_{ij}^r$	Matrix, reinforcement thermal expansion tensors
Θ	Change in the matrix drag stress with temperature
$\Theta_{ijk\ell}^1, \Theta_{ijk\ell}^2, \Theta_{k\ell}^3$	Strain concentration tensors of the matrix
$\Theta_{ijk\ell}^4, \Theta_{ijk\ell}^5, \Theta_{k\ell}^6$	Strain concentration tensors of the reinforcement
$\sigma_{ij}^m, \sigma_{ij}^r, \sigma_{ij}^c$	Total matrix, reinforcement, composite stress tensors
$\dot{\sigma}_{ij}^m, \dot{\sigma}_{ij}^r, \dot{\sigma}_{ij}^c$	Matrix, reinforcement, composite stress rate tensors
$\bar{\sigma}^m, \bar{\sigma}$	Effective stress in the matrix
σ_H^m	Hydrostatic stress in the matrix
σ_f'	Fatigue strength coefficient
$\tilde{\sigma}_{ij}^m, \tilde{\sigma}_{ij}^r$	Matrix, reinforcement average stress disturbance tensors
ζ_{creep}	Phasing factor for creep
ζ_{ox}	Phasing factor for oxidation
11	Longitudinal, loading direction
$22, 33$	Transverse direction

1. INTRODUCTION

In many elevated temperature applications increased demands for dimensional stability, high temperature strength, and thermomechanical fatigue resistance are not met through use of conventional materials. Silicon carbide particulate reinforced aluminum alloys are potential materials for these applications. Recent developments in the processing technology of these materials have resulted in lower fabrication costs and improvements in microstructural uniformity. SiC/Al composites, compared to their monolithic counterparts, possess higher strength to density ratios, improvements in fatigue crack growth resistance, higher stiffness, and lower coefficients of thermal expansion. However, the behavior of these materials as a function of their constituent properties is not well established. Once this relationship is better understood, it will be possible to design them to suit specific applications and to achieve higher reliability than monolithic aluminum alloys.

An understanding of the thermomechanical cyclic deformation behavior of metal matrix composites is of significant importance. Many applications of metal matrix composites are in components which experience complicated cyclic temperature-strain loading histories. Recent studies indicate that a multitude of deformation mechanisms are operative on steel and Ni based superalloys under thermomechanical fatigue loading conditions [1-4]. Whether or not these mechanisms operate on aluminum alloys and SiC/Al composites has not yet been reported.

This study encompasses experimental and theoretical approaches for characterizing the thermomechanical fatigue behavior of metal matrix composites. The experimental study is conducted on unreinforced and SiC_p

reinforced Al 2xxx-T4. Two types of experiments are considered to investigate high-temperature fatigue behavior of unreinforced and reinforced materials: isothermal fatigue (IF) experiments and thermomechanical fatigue (TMF) experiments. The effects of reinforcement on fatigue lives and on monotonic and cyclic stress-strain behavior has been established for a wide range of loading conditions. Evidence of void formation at grain boundaries, crack deflection due to particles, and oxide penetration at the crack tips is provided using scanning electron microscopy and Auger spectroscopy analysis. Chapter 4 presents experimental results and observations on damage mechanisms of unreinforced and reinforced materials.

Theoretical studies include the development of micromechanistic models to predict the deformation behavior and fatigue lives of metal matrix composites. Current models are designed to evaluate overall effective properties, while in fatigue and fracture studies a measure of internal stresses and strains, albeit approximate, is needed. Chapter 5 presents a general micromechanistic constitutive model based on Eshelby's equivalent inclusion theory. The ability of the constitutive model to predict cyclic isothermal and cyclic thermomechanical deformation behavior is demonstrated. The model provides insight into volumetric average stresses and strains of the matrix and the reinforcement developed during cyclic loading.

A fatigue life prediction methodology for metal matrix composites, suitable for cyclic temperature-strain loading histories, is presented in Chapter 6. At elevated temperatures a multitude of damage mechanisms are synergistically combined to decrease fatigue lives. The effects of reinforcement on these damage mechanisms and fatigue lives are identified under isothermal and thermomechanical fatigue loading conditions. The model

quantifies the contribution of environmental, creep, and fatigue damage mechanisms to failure for elevated temperature fatigue loading of metal matrix composites. The effects of internal stresses and reinforcement on these deformation mechanisms are studied.

2. BACKGROUND

Studies of the mechanical properties of aluminum matrix composites reinforced with SiC whisker, nodule, or particulate reinforcement have been widely reported. These studies concentrate on understanding of the effects that matrix microstructural changes and reinforcement volume fraction, size, and spacing have on mechanical behavior and strengthening mechanisms. In general, SiC/Al composites exhibit higher elastic modulus, yield strength, ultimate strength, and better crack growth resistance with increasing reinforcement volume fraction. Experimental observations indicate that flow strength and elastic modulus of SiC/Al composites do not change significantly with reinforcement size. However, enhanced ductility, ultimate strength, and work hardening rate result from a reduction in reinforcement size, provided it is homogeneously distributed.

Although there have been a number of studies reported on the basic mechanical and physical properties of SiC/Al composites, systematic studies on elevated temperature behavior, particularly fatigue and fracture behavior, have not been reported. Most studies on elevated temperature behavior of SiC/Al composites have concentrated on monotonic properties. For 20% SiC volume fraction, the reported SiC/Al composite yield strengths are approximately 100 MPa higher than those of the unreinforced aluminum alloy at room temperature [5]. The temperature dependence of yield strength and ultimate strength of the SiC/Al composites follows closely that of the unreinforced aluminum alloy [5-7]. Both the reinforced and unreinforced materials maintain their room temperature yield strengths to 200 °C, but between 200 °C and 300 °C their strengths decrease by a factor of three. The

yield strength of SiC/Al composites decreases faster and approaches that of the unreinforced aluminum alloy at temperatures above 300 °C.

2.1 Elevated Temperature Fatigue Behavior of Al 2xxx Alloys

An understanding of isothermal and thermomechanical fatigue behavior of unreinforced aluminum alloys is necessary for characterizing the behavior of SiC/Al composites. Very few studies on high temperature fatigue of monolithic aluminum alloys have been reported. At elevated temperatures several damage mechanisms, in addition to pure fatigue damage, operate in aluminum alloys. Bhat and Laird reported cyclic hardening at room temperature and gradual cyclic softening at high temperatures in Al-Cu binary alloys with semicoherent (up to 250 °C) and fully coherent (up to 160 °C) precipitates [8,9]. Although evidence was found for transgranular crack nucleation and slip, predominantly intergranular crack growth was observed at 250 °C [10]. Isothermal fatigue studies on Al-Mg alloys at temperatures up to 300 °C have been reported by Baik and Raj [11]. In their study, 'r-type' cavitation at grain boundaries was reported for tension hold cases at temperatures exceeding 200 °C. Smith et al., reported that the fatigue crack growth rate of the Al 2219 alloy increased by a factor of ten through an increase from room temperature to 300 °C [12]. Elevated temperature isothermal fatigue of an Al-Cu-Li alloy was considered in Srivatsan's work. In the low strain range, the isothermal fatigue lives decreased about five times with an increase in temperature from room temperature to 160 °C in a vacuum environment [13].

It is well known that aluminum alloys display higher crack growth rates in air relative to vacuum [13-16]. Under high temperature fatigue loading conditions, crack initiation and growth are aided by oxidation on

surfaces exposed to environment. At 160 °C, fatigue lives in air are x2.5 lower compared to those in vacuum [13]. Based on fundamental studies of the kinetics of oxidation and the mechanism of diffusion of species in oxide films in aluminum, oxidation damage is expected to be significant as 300 °C is approached [17-19].

2.2 Fatigue Crack Initiation and Growth Behavior of SiC/Al Composites

In characterizing the fatigue and fracture behavior of SiC/Al composites it is important to identify the effects of reinforcement on crack initiation and propagation behavior. The addition of SiC to aluminum alloys has been shown to significantly influence fatigue crack growth behavior [20-29]. Reinforcement size and shape, and matrix-reinforcement interface characteristics influence the crack growth rate [20-22]. In SiC/Al composites, for a crack growing in the composite, several possibilities exist: the crack can propagate a) in the matrix, b) at the reinforcement/matrix interface, or c) by fracturing the particles ahead of it. For composites with strong interfaces, the fatigue crack path shows some tendency to avoid the SiC particles. When the bond is strong, the SiC reinforcement effectively deflects the original crack growth direction, resulting in tortuous crack paths predominantly in the matrix [23-25]. For composite systems with weak interfaces, a propagating crack results in debonding, and is associated with poor fatigue resistance [26].

Direct experimental measurements of the bond strength of SiC/Al composites have not been reported in the literature. However, observation of the fracture surfaces in numerous studies indicates that a very strong bond forms between SiC and aluminum [22-24,30-33]. The SiC area fraction on the fracture surface is found to be either lower [34] or the same as the volume fraction in the composite [35].

The size and clustering of the SiC reinforcement also plays a role in the fatigue crack growth behavior. It has been observed that a propagating crack has a tendency to break particles larger than 15 μm [36-39]. However, smaller particles deflect a propagating crack. There is no indication of fracture of SiC particles smaller than 10 μm [23, 40]. Although it was not found to be a major factor in crack growth behavior, microcracking at the particle/matrix interface has been observed at regions of clustered particles [22, 27]. Lewandoski et.al also reported a propensity for particle fracture in regions of clustered particles [36].

Crack initiation sites in SiC/Al composites have been investigated by several researchers [27, 40, 41]. It has been reported that more than half of the observable crack initiation sites are associated with large intermetallics in the matrix of SiC_p/Al₂xxx fatigue specimens [27] and on SiC_w/7090 tensile specimens [41]. Only clustered or large SiC particulates are identified as crack initiation sites. When the SiC particles are associated with fatigue crack initiation, they are fractured, not decohered. Fatigue crack initiation at the reinforcement/matrix interface has been reported by Williams and Fine [26], but this can be explained by the unusually poor bond strength of the SiC_w/Al₂124 composite considered in their study.

2.3 Room Temperature Fatigue Life Behavior of SiC/Al Composites

The effect of reinforcement on fatigue life performance of SiC/Al composites has been investigated by several researchers [27, 42-44]. All of these results concur that room temperature fatigue lives of aluminum alloys, based on stress range, improve with the addition of SiC. Bonnen et.al [27] investigated the room temperature fatigue life behavior of the 15% SiC_p reinforced alloy considered in this study. They conducted stress controlled

experiments at stress ratios of -1, 0.1, and 0.7. As in the unreinforced alloy, the $\text{SiC}_p/\text{Al 2xxx-T4}$ composite exhibited a decrease in fatigue life as mean stress increased. They also noted that, while the $\text{SiC}_p/\text{Al 2xxx-T4}$ composite exhibited longer lives than the unreinforced Al 2xxx-T4 when based on plastic strain range, the unreinforced Al 2xxx-T4 exhibited longer lives based on total strain range. Williams and Fine [26] reported that the number of cycles necessary to initiate a fatigue crack in 20% SiC whisker reinforced Al 2124 alloy is much greater than for the unreinforced Al 2124; 80% and 5% of the total lifetime, respectively.

2.4 Creep of SiC/Al Composites

The steady state creep rate of the SiC/Al composites shows more sensitivity to temperature and stress than that of the unreinforced aluminum alloy [45-50]. High stress exponents (as much as 20.5) have been reported for the SiC/Al composites, while in unreinforced aluminum alloys the stress exponent is near 4. The steady state creep deformation of SiC/Al composites has been described as simple power law creep by Nieh [46] and Pickard and Darby [47], ($\dot{\epsilon} \propto \sigma^n \exp[Q/RT]$), power law creep with threshold stress by Nardone and Strife [48] and Mishra and Mukherjee [49] ($\dot{\epsilon} \propto [\sigma - \sigma_0]^n$, where σ_0 is the threshold stress), and exponential law creep by Morimoto et. al [50] ($\dot{\epsilon} \propto \exp[C\sigma]$).

Creep characteristics of SiC/Al composite materials also vary, depending on the type of reinforcement. Webster [45] found that particulate reinforced Al 2024 has a slightly weaker creep resistance than the unreinforced Al 2024, while the whisker reinforced Al 2024 displays superior creep resistance. Nieh [46] showed that both particulate and whisker reinforcement improve the creep resistance of the Al 6061 alloy. However,

particulate reinforced Al 6061 has a creep rate as much as two orders of magnitude higher than the creep rate of whisker reinforced Al 6061. Major improvements in the creep strength of SiC/Al composites should not be expected, because the flow strength of these composites at elevated temperatures, especially over 300°C, is similar to that of the unreinforced aluminum alloys.

2.5 Strengthening Behavior of SiC/Al Composites

Experimental observations indicate that strengthening of SiC/Al composites is dependent on reinforcement volume fraction, size and spacing, and matrix microstructural changes, and interface characteristics. There are two main approaches to interpreting the strengthening behavior of SiC/Al composites. Models based on continuum micromechanics lead to a dependence of mechanical properties on reinforcement volume fraction but not on particulate size or spacing. In the continuum approaches it is assumed that the presence of reinforcement does not affect the matrix behavior, allowing the properties of the unreinforced alloy to be incorporated. A survey of continuum micromechanics approaches is given in chapter 5. The dislocation-crystal plasticity based approaches lead to the modelling of mechanical properties of composites as a function of reinforcement volume fraction, size, and spacing.

The dislocation-crystal plasticity based approaches were originally developed for conventional alloys containing precipitates, and were then applied to predict strengthening of metal matrix composites. It has been proposed that SiC/Al composites display an Orowan strengthening effect. In the Orowan strengthening model, the correlation of flow stress varies with the inverse of the particle spacing. Nardone and Prewo [51] have shown that

the Orowan stress, or stress required for a dislocation to bypass a particle, is far lower than the observed strength because the distance between the particles is too large to provide any strengthening effect (for $2\mu\text{m}$ spacing the predicted strength increase is 4 MPa). As particle size increases, the continuum models tend to correlate better with the experimental data than the dislocation-crystal plasticity based models [52,54].

Recent dislocation-crystal plasticity based approaches suggest that matrix microstructural changes, due to addition of reinforcement, contribute to strengthening [40, 55-61]. The aluminum matrix has a higher dislocation density and a different grain morphology than the wrought aluminum alloy [58, 59]. The synergistic effects of quench strengthening, grain strengthening, work hardening, and Orowan strengthening mechanisms are combined to predict overall strengthening of metal matrix composites, and correlate well with the experimental data [40,56].

Taya and Mori combined continuum and dislocation micromechanics models to predict the strengthening of metal matrix composites [60,61]. The increase in the flow strength of the composite is attributed to matrix microstructural changes and the resistance of particles to the plastic flow of the matrix. Dislocations generated due to thermal expansion coefficient differences contribute to microstructural changes in the matrix. A "punched out dislocation" model has been developed to incorporate the contribution of dislocations to overall strengthening. Strengthening of the metal matrix composites due to the resistance of particles to plastic flow is modelled by modifying Eshelby's equivalent inclusion model.

McHugh and Asaro [62] carried out a computational study, based on the crystallographic theory of plastic slip, to investigate effects of reinforcement volume fraction and morphology and matrix properties on the deformation

behavior of Al/SiC_p composites. They indicated that the build-up of hydrostatic stress due to the particle interaction contributes to composite strengthening.

3. MATERIALS AND EXPERIMENTAL PROCEDURE

3.1. Materials

In this study unreinforced, 15% reinforced, and 20% SiC_p reinforced Al 2xxx-T4 are considered. Reinforced and unreinforced materials were produced using powder metallurgy techniques. The materials were provided in the form of extruded panels. Specimens were taken from the center of plate thickness with their axes parallel to the extrusion direction. The machined specimens had a circular cross-section with a diameter of 7.6 mm and a gage length of 25.4 mm.

The Al 2xxx-T4 alloy has a nominal alloy content of 3.5% Cu, 1.5% Mg and 0.14% Zr and has ALCOA trade name of MB85. Apart from the S(CuMgAl₂) and S' precipitates typically found in Al 2124 class alloys [63], this material has Al₃Zr precipitates.

The microstructures of the reinforced and the unreinforced materials are shown in Figures 3.1-3.3. These specimens have been tested under isothermal fatigue conditions at 200 °C. The presence of 'r-type' voids on the grain boundaries, as well as a number of isolated voids within the grains, are evident. Grains of the unreinforced material are elongated in the longitudinal direction and have an average length of 11 microns and an average diameter of 2 microns. The average grain diameter and grain length of the reinforced material are 3 microns and 5 microns, respectively. The average silicon carbide particle size is 4.5 × 4.5 × 9.0 microns.

Before the experiments were initiated the thermal expansion coefficient was determined by temperature cycling of the specimens at zero load. The thermal expansion coefficients of the unreinforced, 15%, and 20%

reinforced materials were found to be $30.0 \times 10^{-6} \text{ 1/}^\circ\text{C}$, $24.0 \times 10^{-6} \text{ 1/}^\circ\text{C}$, and $22.0 \times 10^{-6} \text{ 1/}^\circ\text{C}$, respectively, over the range of $100 \text{ }^\circ\text{C}$ to $300 \text{ }^\circ\text{C}$.

3.2. Experimental Equipment

All experiments were performed on a 20 kip servohydraulic MTS fatigue machine capable of two channel control. In the thermomechanical fatigue experiments the fatigue test machine and the induction heater were controlled by a closed-loop computer system. The same specimen design was used throughout the experimental program. Axial strain was measured with a 25.4 mm MTS high temperature extensometer utilizing quartz rods. Specimens were heated using a 2.5 kW Lepel induction heater. The amount of heat generation by induction is inversely proportional to the thermal conductivity of the specimen. The high thermal conductivity of aluminum led to weak magnetic coupling of the specimen and the induction coil, so special attention was given to the coil design.

Two type K thermocouples, attached at different locations to the gage section, were used to measure temperature throughout the experiments. Spot welding of the thermocouples to the specimen was virtually impossible in the materials considered. The thermocouple beads were held in contact with the specimen by wrapping them with thermocouple wire. Thermocouples attached by this method successfully measured temperature throughout the experiments. Neither disconnection of the thermocouple beads nor nucleation of fatigue cracks at the contact region was observed.

3.3. Experimental Procedure

In thermomechanical fatigue experiments both the temperature and the net (total) strain of the specimen are changed simultaneously. Temperature at the gage section and the net strain (measured with extensometer) on the specimen are computer controlled to achieve the desired mechanical strain range-temperature phasing. The mechanical strain is the sum of elastic and inelastic strain components, while the net strain is the sum of thermal and mechanical strain components:

$$\epsilon_{\text{net}} = \epsilon_{\text{th}} + \epsilon_{\text{mech}} = \theta (T - T_0) + \epsilon_{\text{mech}} \quad (3.1)$$

where ϵ_{net} is the net or total strain, ϵ_{th} is the thermal strain, T_0 is the reference temperature (at which experiment was begun), and θ is the coefficient of thermal expansion.

Two baseline TMF experiments with proportional phasings have been conducted: out-of-phase (TMF OP) and in-phase (TMF IP). In TMF OP experiments maximum temperature coincides with minimum compressive mechanical strain and minimum temperature corresponds with maximum tensile mechanical strain. In TMF IP condition the phasing of the mechanical strain and temperature is reversed. Variations of mechanical strain with thermal strain are indicated in Figure 3.4 for TMF OP, TMF IP, and isothermal loading conditions. These two types of phasings reproduce many mechanisms which develop under complicated cyclic temperature-strain loading histories.

The frequency of thermomechanical fatigue experiments was severely restricted by the low magnetic coupling capacity of the aluminum and its low free convection cooling rate. The cycle period (total heating and cooling time)

was 100 seconds for the thermomechanical fatigue experiments, which corresponds to an average strain rate of 5.0×10^{-5} 1/sec. The TMF experiments started at the mean temperature of the cycle. The specimen heated to maximum temperature of the cycle and cooling to minimum temperature followed. The net strain on the specimen is controlled accordingly to achieve desired mechanical strain-temperature phasing.

4. EXPERIMENTS

4.1. Isothermal Fatigue Experiments

Strain controlled isothermal fatigue experiments under completely reversed loading conditions ($R_e = -1$) were conducted at 200 °C and 300 °C. The higher temperature, 300 °C, was chosen as it corresponds to strength levels significantly inferior to those at room temperature. Mechanical strain ranges from 0.0025 to 0.015 were examined. The two mechanical strain rates considered were 3.0×10^{-3} 1/sec and 3.0×10^{-5} 1/sec.

The effect of strain rate and temperature on isothermal fatigue lives of unreinforced and reinforced materials are presented as mechanical strain range versus cycles to failure in Figures 4.1 - 4.3. The runout experiments are denoted by a horizontal arrow. Substantial strain rate sensitivity at both 200°C and 300°C is noted in the unreinforced material for fatigue lives exceeding 1000 cycles. The decrease in strain rate by two orders of magnitude decreased the fatigue lives by as much as a factor of ten. However, the difference in fatigue life with changing strain rate is minimal for the 15% and 20% reinforced materials. Furthermore, the fatigue lives of the reinforced materials at 200°C and 300°C lie in a narrower band compared to unreinforced material, indicating that reinforcement also decreases the effect of temperature on fatigue lives.

To gain insight into effect of reinforcement on isothermal fatigue lives the results for unreinforced and reinforced materials at 200 °C and 300 °C are replotted in Figures 4.4 and 4.5, respectively. The isothermal fatigue life curves of the 15% reinforced material fall between fatigue life curves of the unreinforced and 20% reinforced materials. Therefore, they are not shown in

these plots. The fatigue lives of the unreinforced material are longer than those of the 20% reinforced material (as much as x8), particularly in the 3.0×10^{-3} 1/sec experiments. The 20% reinforced material displayed superior (x3 longer in life) fatigue lives only at 300 °C, 3.0×10^{-5} 1/sec strain rate experiments.

The isothermal fatigue lives of the 20% reinforced and unreinforced materials are also compared based on first cycle stress range (Figures 4.6, 4.7). Based on stress range, the isothermal fatigue life of the reinforced alloy is always superior to that of the unreinforced alloy. Furthermore, the lives at 200°C is significantly longer than at 300°C for both unreinforced and reinforced materials.

4.2. Monotonic and Cyclic Behavior

First cycle (monotonic) and half-life (cyclic) stress-strain behavior of the unreinforced, 15% reinforced and 20% reinforced materials at 200 °C and 300 °C are presented in Figures 4.8 - 4.13. Cyclic hardening occurred only at 200 °C, 3.0×10^{-3} 1/sec for both unreinforced and reinforced materials. In all other loading conditions a gradual decrease in stress amplitude with cycles was observed. The half-life stress amplitude is found to be a factor of 1.2 to 1.6 lower than the first cycle. The monotonic strength of the reinforced alloy is higher than that of the unreinforced alloy (as much as 45%), at 200 °C and 300 °C. However, the benefit of reinforcement on cyclic strength is much smaller, especially for 300 °C, 3.0×10^{-5} 1/sec loading conditions. The cyclic strength of the 20% reinforced material is 60 MPa compared to 50 MPa in unreinforced material. For the loading conditions considered, elastic modulus, 0.2% offset yield strength in first cycle, and 0.2% offset yield strength at half life are

summarized in Table I. Note that elastic modulus and 0.2% offset yield strength increased with increasing volume fraction of reinforcement. The 20% reinforced alloy displayed 45% and 55% higher elastic modulus than that of the unreinforced alloy at temperatures 200 °C and 300 °C, respectively.

4.3. Thermomechanical Fatigue Experiments

Thermomechanical fatigue experiments were conducted under $T_{\min} = 100$ °C, $T_{\max} = 300$ °C and $T_{\min} = 100$ °C, $T_{\max} = 200$ °C conditions. Typical stress versus mechanical strain curves for 100-300 °C TMF IP and 100-300 °C TMF OP cases of unreinforced and reinforced materials are given in Figures 4.14-4.17. During the heating period of the thermomechanical fatigue cycle the magnitude of stress reaches a maximum and then decreases with increasing temperature. The half life stress range is lower than the first cycle stress range in all cases. The stress ranges of the reinforced material for both TMF IP and TMF OP cases exceed those observed in the unreinforced alloy. The difference in the stress range is mainly a result of the higher strength of the reinforced material at the 100 °C end of the cycle. The stress levels corresponding to 300 °C are similar for both materials. Tensile and compressive mean stresses develop in TMF OP and TMF IP cases, respectively.

Mechanical strain range-life plots of both TMF OP and TMF IP experiments for the unreinforced material are presented in Figure 4.18. The unreinforced alloy displayed shorter fatigue lives in 100-300 °C experiments than in 100-200 °C experiments under both TMF IP and TMF OP loading conditions. The TMF OP loading condition was more damaging than the TMF IP loading condition for 100-300 °C thermomechanical fatigue

experiments. However, a crossover of TMF IP and TMF OP life curves was observed for 100-200 °C experiments.

The thermomechanical fatigue lives of the 20% reinforced and the unreinforced materials under 100-300 °C loading conditions are compared in Figure 4.19. Under TMF IP loading conditions both materials exhibited similar lives. However under TMF OP loading, reinforced material resulted in improvements in life by as much as a factor of ten compared to unreinforced material. If the results are compared based on stress range, fatigue lives of the reinforced material are superior to those of unreinforced material for all of the thermomechanical fatigue loading conditions.

4.4. Metallographic Examination

The fatigued specimens were sectioned longitudinally and transversely and then polished with diamond paste. The grain structure of the specimens was revealed by etching with dilute Keller's reagent (Figures 3.1-3.3). It is noted that the etchant chemically reacts with the interface of the copper rich precipitates of the matrix. Selection of etching time and concentration of the etchant was critical to avoid overetching or underetching problems. The polished and etched specimens were examined by scanning electron microscopy.

The fatigue crack initiation sites for the reinforced material were found to be in the matrix phase for most of the loading conditions considered (Figures 4.20-4.22). Figure 4.20 shows a small fatigue crack initiated from the matrix region for TMF IP, 100-300 °C. Note that in Figure 4.20 bifurcation (deflection) of the crack due to the silicon carbide particle is observed. Similarly, Figure 4.21 (isothermal fatigue at 300 °C) shows that crack

nucleation occurred in the matrix. There are numerous cracks on the specimen surface which conform to these figures. Isolated coarsened precipitates are also visible in Figure 4.21. It is noted that preferential void or precipitate formation around the silicon carbide particles was not observed.

Over wide range of loading conditions mixed (combination of intergranular and transgranular) crack growth was observed for both materials. Crack growth behavior of 20% reinforced material in isothermal fatigue experiments conducted at 200 °C, 3.0×10^{-3} 1/sec is shown in Figure 4.23. The crack path is intergranular over 80% of its length. However, some portions of the crack show transgranular growth, depending on the orientation of the grain boundaries with respect to the crack path. No crack growth through the silicon carbide particulates is apparent in this photograph. Metallographic examination indicates that crack initiation predominantly occurs in the matrix phase and subsequent crack growth is confined to the matrix phase.

An etched longitudinal section of an unreinforced alloy tested under TMF OP, 100-200 °C loading conditions is given in Figure 4.24. Several cracks, all transgranular, are visible in this photograph. Note that there is also evidence of grain boundary damage for the TMF OP loading condition. In the TMF OP experiments the tensile mean stresses and specimen instability effects, towards the latter part of life, result in large crack opening displacements. The magnitude of crack opening displacements can approach the grain width. Therefore, it proves difficult to identify the details of the crack path in some TMF OP cases.

Auger electron spectroscopy analyses were performed to study preferential oxidation at the crack tips. Spectroscopy analyses of longitudinally

sectioned 20% reinforced specimens tested under TMF OP, 100-300 °C conditions indicated oxygen concentration near the crack surface (Figures 4.25,4.26). Similar analyses did not reveal preferential oxidation for the TMF IP loading condition. In Figure 4.27 silicon, oxygen, and aluminum maps of a specimen tested under TMF IP, 100 °C- 300 °C condition are presented. The right hand side of the micrographs coincide with the specimen surface. The oxygen dot map indicated that no excessive oxygen concentration near the specimen surface. The oxidation is more pronounced for TMF OP than for TMF IP, which is consistent with results found on other materials [1-4].

4.5. Crack Growth Mechanism Maps

Crack growth regimes of the unreinforced and the 20% reinforced materials are given in Figures 4.28-4.30. Temperature versus thermal strain rate to mechanical strain rate ratio is plotted for a mechanical strain rate of 5.0×10^{-5} 1/sec in Figures 4.28 and 4.29. The thermal strain to mechanical strain ratio is negative for TMF OP case, zero for isothermal fatigue, and positive for TMF IP loading conditions. The maximum temperature of the thermomechanical fatigue cycle is used in these diagrams. Solid lines indicate bounds of transgranular, mixed, and intergranular crack growth regions.

For both materials, there is a wide region in which mixed (intergranular and transgranular) crack growth is observed. In the mixed regime, a data point midway between the solid lines represents approximately 50% transgranular - 50% intergranular crack growth. The tendency for transgranular crack growth in the unreinforced material is evident when T_{max} is 200 °C in TMF OP case (Figure 4.24). As the thermal strain to

mechanical strain ratio becomes positive (in-phase) the crack growth behavior favors the intergranular regime.

The effects of strain rate on the crack growth regimes for the isothermal experiments are depicted in Figure 4.30. The solid lines represent the bounds for the mixed crack growth regime for the unreinforced alloy while the dashed lines provide the bounds for the reinforced alloy. For example, at 200 °C, 3.0×10^{-5} 1/sec a mixed crack growth, 80% intergranular/20% transgranular, is observed for the reinforced material (Figure 4.23). Under same loading conditions, crack growth is also mixed, 10% intergranular/90% transgranular, for the unreinforced material.

4.6. Discussion

The fatigue life and the stress-strain behavior of unreinforced Al 2xxx-T4 changed considerably with strain rate at 200 °C and at 300 °C. By increasing the strain rate from 3.0×10^{-5} 1/sec to 3.0×10^{-3} 1/sec the fatigue life of the unreinforced material was increased by a factor of ten. The isothermal fatigue life of the reinforced material is less sensitive to strain rate at 200 °C and at 300 °C compared to the unreinforced material.

Experimental results demonstrated that, the thermomechanical lives can not be simply predicted based on isothermal data. The 100-300 °C thermomechanical fatigue lives of unreinforced and reinforced alloys are lower than the isothermal lives corresponding to maximum temperature of the cycle (300 °C isothermal fatigue experiments). However, the isothermal fatigue lives at 200 °C are lower compared to 100-200 °C thermomechanical fatigue lives.

The results reveal the shortcomings of comparing fatigue lives of reinforced and unreinforced materials based on stress range. If the results were compared based on stress range, as adopted in early studies at room temperature, the reinforced material would always exhibit longer fatigue lives. The comparison of fatigue life results based on strain range identifies the conditions under which the reinforced alloy provides advantages and disadvantages in life. Superior room temperature fatigue lives of the unreinforced material compared to 15% reinforced material, based on strain range, is also observed by Bonnen et. al [27].

Grain structures of the unreinforced and reinforced Al 2xxx-T4 have an influence on the crack growth behavior. The elongated grain structure of the unreinforced alloy promotes transgranular crack growth, and intergranular crack growth is promoted by the grain structure of the reinforced material. Comparison of crack growth mechanism maps of the unreinforced and reinforced materials reveals the tendency of reinforced material to exhibit intergranular crack growth.

The trends in the fatigue life results are extremely complex. Several damage mechanisms compete to increase or decrease the damage on the material. These mechanisms are briefly discussed below:

(a) Creep Damage (Void Growth): This mechanism adds to the fatigue damage and was observed in all experiments. It is worth noting that the cavitation on grain boundaries at 300 °C and at 200 °C is comparable. This may occur because creep damage is a function of both temperature and stress, and the stresses are significantly higher at 200 °C than at 300 °C.

(b) Oxidation Damage: This mechanism was observed to be almost equally effective in both the reinforced and unreinforced material. In the

TMF OP loading oxide fracture would occur repeatedly since, at elevated temperature end of the cycle material forms oxides which fracture in tension upon cooling.

(c) Mean Stress: The yield strength (at T_{\min} and T_{\max}) variation in the thermomechanical fatigue cycle dictates the mean stress of the cycle. The mean stress effect would be more significant in 100-300 °C case than in 100-200 °C case.

(d) Crack Deflection Mechanisms: This was observed in the experiments on the reinforced material. It is expected that this mechanism would decrease the crack growth rate of the reinforced material when compared to the unreinforced material. This effect should not be confused with the mixed intergranular/transgranular crack growth.

(e) Internal Stress-Strain Fields: Under fatigue cycling conditions the strain range in the matrix exceeds the applied (composite) strain range. Since the crack initiation/crack growth is confined to the matrix in the loading conditions considered, the damage rate based on this mechanism in the reinforced material would be faster than in unreinforced material.

5. DEFORMATION MODEL FOR METAL MATRIX COMPOSITES

5.1. Background

There is a need to develop time and temperature dependent constitutive models for metal matrix composites as these materials are candidates for high temperature applications. The current models are designed to evaluate overall effective properties, while in fatigue and fracture studies a measure of internal stresses and strains, albeit approximate, is needed. This chapter presents a unified constitutive model, based on Eshelby's equivalent inclusion theory, for metal matrix composites capable of simulating time and temperature dependent cyclic loading. The model leads to a general description of deformation of metal matrix composites under thermomechanical loading.

Many models using constituent properties and their interactions have been proposed for the evaluation of macroscopic behavior of composite materials [64-84]. Earlier micromechanistic models concentrated on predicting elastoplastic behavior of polycrystalline materials. The self consistent method, first proposed by Hershey [64,65] and developed by Kroner [66] and Budiansky and Wu [67], was a procedure for the estimation of elastic-plastic behavior of polycrystalline aggregates which utilized the single crystal properties. This method is based on a single crystal, with uniform plastic strain as its only transformation strain, embedded in a matrix with the unknown polycrystalline properties. The self consistent micromechanics of multiphase materials was established by Hill [68, 69]. Hill's procedure was based on the solution of an elastic inclusion problem by Eshelby [69,70]. In his procedure instantaneous moduli were used to model the inelastic behavior of the

polycrystalline materials. The self consistency approach has been applied to polycrystals undergoing elastic-plastic deformation [72, 73] and steady state creep deformation [74-76].

While the self consistency method has been used to predict elastic-plastic behavior of multiphase materials, the elastic behavior of the composite materials has been investigated by utilizing Eshelby's equivalent inclusion method. Direct use of Eshelby's equivalent inclusion method for predicting elastic modulus of a composite material is applicable to dilute volume fraction of reinforcement [77]. The interaction among the reinforcements is implicitly accounted for in the self consistency model by assuming that the single fiber is embedded into an equivalent medium. The self consistency method is applicable to higher volume fraction of reinforcements than the Eshelby's direct method.

The plastic deformation of the matrix with elastic inclusion has been treated within the context of Eshelby's equivalent inclusion method as follows. Tanaka and Mori [78] were the first to apply this approach to the case of an inclusion and matrix with different elastic moduli. Plastic deformation in the matrix was assumed to be uniform and restored to the reinforcement as transformation strain. This theory was used to determine the yield strength and the hardening rate of crystals with disc, needle, and spherical inhomogeneities. With this approach, Tanaka, Wakashima and Mori [79] have demonstrated the anisotropy of deformation under uniaxially applied stress for ellipsoidal reinforcement geometries.

At finite volume fraction of reinforcement, the stress and strain in the matrix are disturbed from the remotely applied loading due to interaction of the particles. Eshelby's equivalent inclusion method was improved by means

of volumetric average stress concept of Mori and Tanaka [80] to account for inclusion matrix interaction at finite volume fraction of reinforcement. In order to satisfy the equilibrium condition, the volumetric average of the perturbed stress and strain can be forced to vanish when integrated over the entire composite domain. Mori and Tanaka considered plastically deforming inclusions in an elastic domain with the same elastic modulus as the matrix. The volumetric averaging method was used by Wakashima, Otsuka, and Umekawa [81] for inclusions which have different elastic modulus than the matrix to study overall thermoelastic properties of the two phase system. The model was used to predict macroscopic thermal expansion behavior of 32% and 44% reinforced unidirectional tungsten-copper composites. They noted that a uniform temperature change in the composite results in internal stresses due to the mismatch of thermal expansion coefficients.

A more important problem, one in which the elastic reinforcement is embedded in an elastic-plastic domain has recently been addressed by Arsenault and Taya [82] and Tandon and Weng [83] who utilized Eshelby's modified equivalent inclusion method. Arsenault and Taya predicted the thermal residual stress and the yield strength of whisker reinforced composites. Their interest was on the effect of residual stress on the decreased composite yield strength; therefore cyclic deformation was not considered. Tandon and Weng accounted for the disturbance of the field variables by interaction of the inclusions, and predicted monotonic stress-strain behavior. Since their approach was not incremental, it can not be used directly to model cyclic loading with temperature dependent material properties.

5.2. Theory

5.2.1. Eshelby's Equivalent Inclusion Method

The transformation and inhomogeneity problem solved by Eshelby considers a domain ϕ , which has different elastic constants than the rest of the medium, embedded in an infinite elastic body D (Figure 5.1a). Since its deformation is constrained by the surrounding matrix, a perturbed strain field results. The problem, then, is to find how a remotely applied loading, ϵ_{ij}^0 is disturbed by the existence of the inhomogeneity. The total strain on the inhomogeneity is summation of the remotely applied strain and the constraint strain:

$$\sigma_{ij}^r = C_{ijk\ell}^r \epsilon_{k\ell}^r = C_{ijk\ell}^r (\epsilon_{k\ell}^0 + \epsilon_{k\ell}^{cn}) \quad (5.1)$$

In the "equivalent inclusion method" the domain ϕ is replaced by an equivalent inclusion which has the same elastic constants as the matrix. The equivalent inclusion is assumed to undergo a stress free transformation under a fictitious eigenstrain (transformation strain), ϵ_{ij}^* . The resulting total stress in the equivalent inclusion is:

$$\sigma_{ij}^r = C_{ijk\ell}^m (\epsilon_{k\ell}^0 + \epsilon_{k\ell}^{cn} - \epsilon_{k\ell}^*) \quad (5.2)$$

Eshelby proved that the stress field in a single ellipsoidal inhomogeneity is constant and Equations 5.1 and 5.2 are equivalent:

$$\sigma_{ij}^r = C_{ijk\ell}^r \epsilon_{k\ell}^r = C_{ijk\ell}^r (\epsilon_{k\ell}^0 + \epsilon_{k\ell}^{cn}) = C_{ijk\ell}^m (\epsilon_{k\ell}^0 + \epsilon_{k\ell}^{cn} - \epsilon_{k\ell}^*) \quad (5.3)$$

Superscripts ^r and ^m denote reinforcement (inhomogeneity) and matrix, respectively. Isotropic or anisotropic stiffness tensors may be used in Equation 5.3, depending on the constituent properties.

The relation between the eigenstrain, ϵ_{ij}^* , and the constrained strain, ϵ_{ij}^{cn} , is given by Eshelby's well known tensor, S_{ijkl} , as:

$$\epsilon_{ij}^{cn} = S_{ijkl} \epsilon_{kl}^* \quad (5.4)$$

S_{ijkl} depends only on reinforcement geometry and Poisson's ratio of the matrix. S_{ijkl} for different reinforcement geometries may be found in a book by Mura [84].

5.2.2. Modified Eshelby's Equivalent Inclusion Method

The procedure for determining stress in the inclusion is described in Figure 5.1, where the net strain, eigenstrain and stresses in the matrix and the reinforcement are given for different stages of the problem. Figure 5.1a describes the classical Eshelby problem given by Equations 5.1 through 5.3. Figure 5.1b demonstrates the case of a single elastic inclusion in an infinite elastic-plastic matrix under thermomechanical loading. In this case, the matrix is subjected to a total strain composed of elastic, ϵ_{ij}^{me} , and inelastic, ϵ_{ij}^{in} , strains and has temperature dependent material properties, while the reinforcement remains elastic. To utilize Eshelby's equivalent inclusion method the transformation strains of the reinforcement and the matrix are modified, without disturbing the stress fields. In this case the reinforcement has its own eigenstrain, $\theta_{ij}^r \Delta T$, due to thermal loading. Thermal strain in the matrix, $\theta_{ij}^m \Delta T$, and the inelastic strain in the matrix, ϵ_{ij}^{in} , are restored in the

domain ϕ as eigenstrains. After these modifications the total eigenstrain of the reinforcement, ϵ_{ij}^{pr} , is:

$$\epsilon_{ij}^{pr} = \theta_{ij}^r \Delta T - \theta_{ij}^m \Delta T - \epsilon_{ij}^{in} = \epsilon_{ij}^{th} - \epsilon_{ij}^{in} \quad (5.5)$$

The stress in the reinforcement is:

$$\sigma_{ij}^r = C_{ijk\ell}^r (\epsilon_{k\ell}^{me} + \epsilon_{k\ell}^{cn} - \epsilon_{k\ell}^{pr}) \quad (5.6)$$

After the modifications the matrix is entirely elastic (no eigenstrains) and the reinforcement is subjected to a modified eigenstrain of ϵ_{ij}^{pr} . The domain D is subjected to ϵ_{ij}^{me} which is also entirely elastic.

This equivalent model can simulate the current problem by the use of equivalent inclusion method. The inhomogeneity with eigenstrain of ϵ_{ij}^{pr} can be replaced by an equivalent inclusion with the same properties as the matrix with the addition of fictitious eigenstrain, ϵ_{ij}^* . Then the transformation strain which relates the stresses in the equivalent inclusion to the current problem is:

$$\epsilon_{ij}^{**} = \epsilon_{ij}^* + \epsilon_{ij}^{pr} = \epsilon_{ij}^* - \epsilon_{ij}^{in} + \epsilon_{ij}^{th} \quad (5.7)$$

The transformation strain is also related to constraint strain through Eshelby's tensor as:

$$\epsilon_{ij}^{cn} = S_{ijk\ell} \epsilon_{k\ell}^{**} \quad (5.8)$$

Eshelby's equivalency condition is written as:

$$\begin{aligned} \sigma_{ij}^r &= C_{ijk\ell}^r \{ \epsilon_{k\ell}^{me} + \epsilon_{k\ell}^{cn} + \epsilon_{k\ell}^{in} - \epsilon_{k\ell}^{th} \} \\ &= C_{ijk\ell}^m \{ \epsilon_{k\ell}^{me} + \epsilon_{k\ell}^{cn} + \epsilon_{k\ell}^{in} - \epsilon_{k\ell}^{th} - \epsilon_{k\ell}^* \} \end{aligned} \quad (5.9)$$

In the current problem, domain D contains a finite volume fraction of reinforcement and is subjected to isothermal and thermomechanical loading conditions (Figure 5.1c). For finite volume fraction of reinforcement the remote strain field, ϵ_{ij}^0 , is no longer equivalent to the undisturbed matrix strain field. It is replaced by the composite elastic strain field, ϵ_{ij}^{ce} . Average matrix elastic strain, ϵ_{ij}^{me} , differs from remotely applied strain by the additional term $\tilde{\epsilon}_{ij}^m$:

$$\epsilon_{ij}^{me} = \epsilon_{ij}^{ce} + \tilde{\epsilon}_{ij}^m \quad (5.10)$$

The term $\tilde{\epsilon}_{ij}^m$ represents average elastic strain disturbance of the matrix due to finite volume fraction of reinforcement. The average matrix stress is disturbed from the composite stress by $\tilde{\sigma}_{ij}^m$

$$\sigma_{ij}^m = \sigma_{ij}^c + \tilde{\sigma}_{ij}^m \quad (5.11)$$

The term $\tilde{\sigma}_{ij}^m$, which is to be determined, represents the average stress disturbances in the matrix. Similarly, the reinforcement stress and elastic strain are defined as follows (Figure 5.1c):

$$\epsilon_{ij}^{re} = \epsilon_{ij}^{ce} + \tilde{\epsilon}_{ij}^r \quad (5.12)$$

$$\sigma_{ij}^r = \sigma_{ij}^c + \tilde{\sigma}_{ij}^r \quad (5.13)$$

In the model, the particles are considered to be randomly distributed in the matrix in such a way that the composite is homogeneous at a macroscopic scale. For a homogeneous body in static equilibrium a volume integral of the disturbance of field variables should vanish over the entire body, D. In that case,

$$\int_D \tilde{\sigma}_{ij}^r dV = 0 \quad (5.14)$$

$$\int_D \tilde{\varepsilon}_{ij}^m dV = 0 \quad (5.15)$$

Then using Equations 5.12 and 5.13

$$v_r (\sigma_{ij}^r - \sigma_{ij}^c) + v_m (\sigma_{ij}^m - \sigma_{ij}^c) = 0 \quad (5.16)$$

$$v_r (\varepsilon_{ij}^{re} - \varepsilon_{ij}^{ce}) + v_m (\varepsilon_{ij}^{me} - \varepsilon_{ij}^{ce}) = 0 \quad (5.17)$$

where v_r and v_m are reinforcement and matrix volume fractions, respectively.

Following the above modifications, Eshelby's equivalence condition (Equation 5.3) is rewritten as:

$$\begin{aligned} \sigma_{ij}^r &= \sigma_{ij}^c + \tilde{\sigma}_{ij}^r = C_{ijkl}^r \{ \varepsilon_{kl}^{ce} + \tilde{\varepsilon}_{kl}^m + \varepsilon_{kl}^{cn} + \varepsilon_{kl}^{in} - \varepsilon_{kl}^{th} \} \\ &= C_{ijkl}^m \{ \varepsilon_{kl}^{ce} + \tilde{\varepsilon}_{kl}^m + \varepsilon_{kl}^{cn} + \varepsilon_{kl}^{in} - \varepsilon_{kl}^{th} - \varepsilon_{kl}^* \} \end{aligned} \quad (5.18)$$

From Equations 5.10, 5.12, 5.17, and 5.18 the matrix and the reinforcement strain disturbances are calculated as:

$$\tilde{\varepsilon}_{ij}^m = -v_r (\varepsilon_{ij}^{cn} - \varepsilon_{ij}^{th} + \varepsilon_{ij}^{in}) \quad (5.19)$$

$$\tilde{\varepsilon}_{ij}^r = v_m (\varepsilon_{ij}^{cn} - \varepsilon_{ij}^{th} + \varepsilon_{ij}^{in}) \quad (5.20)$$

Note that as the volume fraction of reinforcement goes to zero the matrix strain disturbance, $\tilde{\varepsilon}_{ij}^m$, becomes zero and reinforcement strain approaches to the one given by Eshelby's equivalent inclusion method.

5.3. Constitutive Equation for the Composite

The composite was allowed to undergo an arbitrary strain-temperature history. For a given loading history, strain increments of the matrix and the reinforcement should be written in terms of the incremental loading parameters. Using Equations 5.8, 5.19 and 5.20 the equivalency condition (Equation 5.18) reduced to the following equation which leads to solution of incremental transformation strain rate, $\dot{\epsilon}_{\bar{y}}^*$.

$$\begin{aligned} & -[C_{\bar{y}k\ell}^m + v_m \Delta C_{\bar{y}mn} S_{mnk\ell}] \dot{\epsilon}_{k\ell}^* \\ & = \Delta C_{\bar{y}k\ell} \dot{\epsilon}_{k\ell}^{ce} + v_m \Delta C_{\bar{y}mn} (S_{mnk\ell} - \delta_{mnk\ell}) (\dot{\epsilon}_{k\ell}^{th} - \dot{\epsilon}_{k\ell}^{in}) - \dot{C}_{\bar{y}k\ell}^m \epsilon_{k\ell}^K \end{aligned} \quad (5.21)$$

where, $\Delta C_{\bar{y}k\ell} = C_{\bar{y}k\ell}^r - C_{\bar{y}k\ell}^m$ and $\epsilon_{\bar{y}}^K$ is given by

$$\epsilon_{\bar{y}}^K = \{ \epsilon_{\bar{y}}^{ce} + \tilde{\epsilon}_{\bar{y}}^m + \epsilon_{\bar{y}}^{cn} + \epsilon_{\bar{y}}^{in} - \epsilon_{\bar{y}}^{th} - \epsilon_{\bar{y}}^* \}$$

Note that $\dot{\epsilon}_{\bar{y}}^{ce} = \frac{d\epsilon_{\bar{y}}^{ce}}{dt}$ where t is time.

Then $\dot{\epsilon}_{\bar{y}}^*$ is substituted into the Equations 5.10 and 5.12 to solve the matrix elastic strain rate, $\dot{\epsilon}_{\bar{y}}^{me}$, and the reinforcement elastic strain rate, $\dot{\epsilon}_{\bar{y}}^{re}$, in terms of the loading parameters $\dot{\epsilon}_{\bar{y}}^{ce}$ and \dot{T} .

The matrix elastic strain rate is

$$\dot{\epsilon}_{\bar{y}}^{me} = \Theta_{\bar{y}k\ell}^1 \dot{\epsilon}_{k\ell}^{ce} + \Theta_{\bar{y}k\ell}^2 (\dot{\epsilon}_{k\ell}^{th} - \dot{\epsilon}_{k\ell}^{in}) + \dot{C}_{\bar{y}k\ell}^m \Theta_{k\ell}^3 \quad (5.22)$$

and the reinforcement elastic strain rate is

$$\dot{\epsilon}_{\bar{y}}^{re} = \Theta_{\bar{y}k\ell}^4 \dot{\epsilon}_{k\ell}^{ce} + \Theta_{\bar{y}k\ell}^5 (\dot{\epsilon}_{k\ell}^{th} - \dot{\epsilon}_{k\ell}^{in}) + \dot{C}_{\bar{y}k\ell}^m \Theta_{k\ell}^6 \quad (5.23)$$

The inelastic strain rate of the matrix, $\dot{\epsilon}_{ij}^{in}$, is explicitly related to the composite strain through the constitutive equations of the matrix. The strain concentration tensors in Equations 5.22 and 5.23 are given as follows:

$$[C_{ijmn}^m + v_m \Delta C_{ijts} S_{tsmn}] \Theta_{mnkl}^1 = [C_{ijkl}^m + \Delta C_{ijmn} S_{mnkl}] \quad (5.24)$$

$$[C_{ijmn}^m + v_m \Delta C_{ijts} S_{tsmn}] \Theta_{mnkl}^2 = v_r C_{ijmn}^m (\delta_{mnkl} - S_{mnkl}) \quad (5.25)$$

$$[C_{ijmn}^m + v_m \Delta C_{ijts} S_{tsmn}] \Theta_{mn}^3 = -v_r S_{ijkl} \epsilon_{kl}^K \quad (5.26)$$

$$[C_{ijmn}^m + v_m \Delta C_{ijts} S_{tsmn}] \Theta_{mnkl}^4 = C_{ijkl}^m \quad (5.27)$$

$$[C_{ijmn}^m + v_m \Delta C_{ijts} S_{tsmn}] \Theta_{mnkl}^5 = v_m C_{ijmn}^m (S_{mnkl} - \delta_{mnkl}) \quad (5.28)$$

$$[C_{ijmn}^m + v_m \Delta C_{ijts} S_{tsmn}] \Theta_{mn}^6 = v_m S_{ijkl} \epsilon_{kl}^K \quad (5.29)$$

Equation 5.24 leads to the solution of Θ_{ijkl}^1 , Equation 5.25 leads to the solution of Θ_{ijkl}^2 , and so on.

The strain coefficient tensors given in Equations 5.22 and 5.23 satisfy the following identities:

$$v_m \Theta_{ijkl}^1 + v_r \Theta_{ijkl}^4 = \delta_{ijkl} \quad (5.30)$$

$$v_m \Theta_{ijkl}^2 + v_r \Theta_{ijkl}^5 = 0 \quad (5.31)$$

$$v_m \Theta_{ij}^3 + v_r \Theta_{ij}^6 = 0 \quad (5.32)$$

To determine matrix, reinforcement and composite stresses, Equations 5.22 and 5.23 should be coupled with the constitutive equations of the matrix and reinforcement.

When the matrix undergoes elastic-plastic deformation under thermal loading conditions the following equations are valid:

$$\dot{\sigma}_{ij}^m = C_{ijkl}^m (\dot{\epsilon}_{kl}^m - \dot{\epsilon}_{kl}^{in} - \theta_{kl}^m \dot{T} + g_{kl} \dot{T}) \quad (5.33)$$

where,

$$g_{ij} = \frac{dC_{ijkl}^r}{dT} (\epsilon_{kl}^m - \epsilon_{kl}^{in} - \theta_{kl}^m \Delta T)$$

For the elastic reinforcement:

$$\dot{\sigma}_{ij}^r = C_{ijkl}^r (\dot{\epsilon}_{kl}^r - \theta_{kl}^r \dot{T}) \quad (5.34)$$

By combining equations 5.16, 5.22, 5.23, 5.33, and 5.34 the composite stress increment was found in terms of composite elastic strain, matrix inelastic strain, and temperature increments:

$$\begin{aligned} \dot{\sigma}_{ij}^c = & [v_m \Theta_{ijkl}^1 C_{klmn}^m + v_r \Theta_{ijkl}^4 C_{klmn}^r] \dot{\epsilon}_{mn}^{ce} - v_r \Theta_{ijkl}^5 \Delta C_{klmn} \dot{\epsilon}_{mn}^{in} \\ & + [v_r \Theta_{ijkl}^5 \Delta C_{klmn} \Delta \theta_{mn} + v_m g_{ij}] \dot{T} \\ & + v_r \Delta C_{ijkl} \dot{C}_{klmn}^m \Theta_{mn}^6 \end{aligned} \quad (5.35)$$

Total composite strain is:

$$\dot{\epsilon}_{ij}^c = \dot{\epsilon}_{ij}^{ce} + v_m \dot{\epsilon}_{ij}^{in} \quad (5.36)$$

In order to solve this equation, the matrix inelastic strain needs to be defined in terms of the current state variables. At this point, the formulation is general. Any constitutive model which relates the inelastic strain rate to the current state variables of the matrix, can be used to solve for the

reinforcement, matrix, and composite stresses. The current model utilizes a unified constitutive equation developed for Al 2xxx-T4.

The model is used to simulate uniaxial cyclic loading conditions. Under axial loading conditions, fourth order tensors are reduced to 3×3 matrices, and second order tensors are reduced to 3×1 vectors. Three parameters need to be specified to solve for reinforcement, matrix and composite stress and strain rates. Under uniaxial loading, transverse strain increments of the composite can not be specified under elastic-plastic loading. Transverse composite stress rates are zero ($\dot{\sigma}_{22}^c = \dot{\sigma}_{33}^c = 0$), and the elastic strain rate in the loading direction, $\dot{\epsilon}_{ij}^{ce}$, is specified. Temperature is varied linearly with the longitudinal net strain of the composite during thermomechanical fatigue loading such that prespecified minimum and maximum temperatures coincide with maximum and minimum mechanical strain levels. With these boundary conditions Equation 5.35 can be solved for $\dot{\sigma}_{11}^c$, $\dot{\epsilon}_{22}^{ce}$ and $\dot{\epsilon}_{33}^{ce}$. The corresponding matrix and reinforcement strain increments can then be calculated using Equations 5.22 and 5.23. After finding plastic strain rate of the matrix, the plastic strain rate of the composite is calculated by volumetric averaging of the plastic strain rates of the constituents.

5.4. Constitutive Equation for Al 2xxx-T4

A unified constitutive model suitable for elevated temperature isothermal and thermomechanical loading has been developed for the unreinforced Al 2xxx-T4. Since the composite behavior over a broad range of temperatures and strain rates is of interest, a unified creep-plasticity model is chosen. Incremental inelastic strain given by this unified model is used in Equation 5.35 to calculate the volumetric average stresses. The proposed

constitutive equation is capable of predicting cyclic hardening or softening, strain rate and temperature sensitivity, and recovery effects for a wide range of temperature-strain histories.

In the unified theories, the plastic strains and creep strains are combined as inelastic strains [85,86]. The concept of yield surface is replaced by a stress surface. Inelastic flow may occur inside the stress surface, though this is not permitted in the yield surface models. Furthermore, stress states outside the stress surface are permissible. The flow rule, which relates the inelastic strain rate to deviatoric stress, internal stress, and effective stress normalized by drag stress, $\bar{\sigma}/K$ is:

$$\dot{\epsilon}_{ij}^{\text{in}} = 3/2 f(\bar{\sigma}/K) \left(\frac{s_{ij} - \alpha'_{ij}}{\bar{\sigma}} \right) \quad (5.37)$$

where K denotes the drag stress state variable and is related to the stress surface size, $f(\bar{\sigma}/K)$ is a scalar function and depends on power law creep, plasticity or diffusional flow mechanisms. The deviatoric internal (back) stress, α'_{ij} , represents the center of the stress surface in the deviatoric stress space. This term allows for non-linear stress hardening and the Bauschinger effect under cyclic loading. Its steady value determines the steady state creep rate. The final term of Equation 5.37 determines the direction of the inelastic strain rate.

Two state variables were used to represent combined isotropic and kinematic hardening. The drag stress state variable, K , is related to the stress surface size. The deviatoric back stress variable, α'_{ij} , represents the stress surface center in the deviatoric stress space. The internal stress state evolves throughout the deformation history in a recovery-hardening format as:

$$\dot{\alpha}'_{\dot{\gamma}} = 2/3 h_{\alpha} \dot{\epsilon}_{\dot{\gamma}}^{\text{in}} - r_{\alpha} \alpha'_{\dot{\gamma}} \quad (5.38)$$

$$\dot{K} = h_k - r_k + \Theta \dot{T} \quad (5.39)$$

where $\dot{\alpha}'_{\dot{\gamma}}$ is the deviatoric back stress rate, $\dot{\epsilon}_{\dot{\gamma}}^{\text{in}}$ is the inelastic strain rate, and \dot{K} is the drag stress rate. The back stress hardening term, h_{α} , represents the evolution of back stress during high strain rate experiments in which recovery is small. The recovery term, r_{α} , represents a decrease in back stress to itself as time or temperature increases, and dictates the steady state creep behavior. The term h_k represents the hardening of drag stress. Recovery (decrease) of strength in the material during cyclic loading or due to high temperature exposure is represented by r_k . The term Θ accounts for changes in drag stress with temperature. The functions f , h_k , h_{α} , r_{α} , r_k , and Θ are determined from experiments.

5.4.1. Flow Rule

Inelastic strain rate versus yield strength (first cycle, 0.2% offset) measurements for unreinforced Al 2xxx-T4 are shown in Figure 5.2. Experiments performed by Ding [87] on 2xxx series aluminum alloy are also included. The aluminum alloy 2xxx-T4 exhibits considerable strain rate sensitivity above 100 °C. At high strain rates and low temperatures (<100°C) the strain rate sensitivity of the yield strength is lower compared to results at low strain rates and high temperatures. The power law creep regime has a lower slope (high strain rate sensitivity of yield strength) compared to the plasticity regime (low strain rate sensitivity).

Figure 2 is used to establish the flow rule, $f(\bar{\sigma}/K)$, for the Al 2xxx-T4. The inelastic strain rate and the yield strength in Figure 5.2 are normalized as

follows. At the intersection of power law and plasticity mechanisms the yield strength is set equal to K_0 . At other temperatures the the initial drag stress level, K_0 , is determined by setting $K_0/E = \text{constant}$. The elastic modulus of the unreinforced Al 2xxx-T4 at several temperatures was determined from the monotonic stress-strain curves of the material (Figure 5.3). The constant A is used in normalizing effective inelastic strain, $\dot{\epsilon}^{in}$. The temperature dependencies of constants Λ and K_0 are given in Table II.

The normalized inelastic strain rate versus $\bar{\sigma}/K$ for Al 2xxx-T4 is given in Figure 5.4. The flow rule, which relates the inelastic strain rate to effective stress is:

$$\dot{\epsilon}_{ij}^{in} / A = \begin{cases} \exp[(\bar{\sigma}/K)^{10.1} - 1] ((s_{ij} - \alpha'_{ij})/\bar{\sigma}) & \bar{\sigma}/K \geq 1 \\ (\bar{\sigma}/K)^{4.6} ((s_{ij} - \alpha'_{ij})/\bar{\sigma}) & \bar{\sigma}/K < 1 \end{cases} \quad (5.40)$$

This relation accounts for both power law creep, $\bar{\sigma}/K < 1$, and plastic deformation, $\bar{\sigma}/K \geq 1$, mechanisms. The higher slope (10.1) in the plasticity mechanism regime represents rate-insensitive material behavior. The power law creep exponent was found to be 4.6, which is consistent with the models based on dislocation climb. These models predict a stress exponent near 4.

5.4.2. Hardening Functions

The internal stress hardening function h_α is determined as a function of temperature from high strain rate experiments at 200°C.

$$h_{\alpha} = \begin{cases} X(T) (a - b \bar{\alpha}) & \alpha_{\dot{\gamma}}^{\text{in}} \geq 0 \\ X(T) \quad a & \alpha_{\dot{\gamma}}^{\text{in}} < 0 \end{cases} \quad (5.41)$$

where the function $X(T)$ and constants a and b are given in Table II.

The drag stress hardening function (due to deformation) that could produce cyclic hardening or softening toward the stable state is:

$$h_k = B (K_{\text{sat}} - K) \dot{\epsilon}^{\text{in}} \quad (5.42)$$

where K_{sat} and B are material constants obtained from the first cycle and saturated cycle stress amplitude. The initial drag stress, K_0 is determined from material behavior in the first cycle. The saturated drag stress, K_{sat} , is determined from the saturated cyclic response of high strain rate experiments. The temperature dependence of the saturation stress is given as $K_{\text{sat}} = h_3 + h_4 T$, and the constants h_3, h_4 are given in Table II.

The drag stress rate indicates cyclic hardening or softening of the material for a given loading condition. For $\dot{K} > 0$ the material will cyclically harden. For $\dot{K} < 0$ the material will cyclically soften. For $\dot{K} = 0$ the material is cyclically stable.

5.4.3. Recovery Functions

The drag stress recovery term, r_k , accounts for structural coarsening in the material during cyclic loading. During experiments at temperatures exceeding 200°C, overaging of aluminum with time contributes significantly to softening. The decrease in drag stress is characterized as:

$$r_k = C (K - K_{\text{rec}}) \quad (5.43)$$

where C and K_{rec} are material constants. The term C indicates the rate of recovery to the stable state. The term K_{rec} is the recovery drag stress, corresponding to stress amplitude after recovery. These constants are determined from cyclic stress-strain behavior for low strain rate experiments at 300°C after recovery has occurred. Using the steady state cyclic stress-strain behavior of low strain rate experiments, the aging term is found as $K_{rec} = r_1 - r_2 T$. These constants are given in Table II.

The recovery function, $r_{\alpha'}$, is determined from steady state material response under monotonic straining at 3.0×10^{-5} 1/sec, 300°C, where $\dot{\epsilon}^{in} \simeq$ constant = 3.0×10^{-5} 1/sec, $\dot{\sigma} = 0$, and $\alpha'_y = \dot{K} = 0$. Monotonic stress-strain behavior can be used to determine $r_{\alpha'}$ for different values of back stress and temperature. It was found that the back stress recovery term for Al 2xxx-T4 is very small compared to the h_a term. Therefore, the $r_{\alpha'}$ term is taken as zero.

5.5. Simulations

The cyclic and monotonic stress-strain behavior of unreinforced and silicon carbide particulate reinforced Al 2xxx-T4 under isothermal and thermomechanical loading conditions were simulated. The silicon carbide particulates are characterized by spherical reinforcements. The reinforcement was assumed to be elastic and isotropic ($E^r = 450000$ MPa) for the loading conditions considered. The Poisson's ratio of the matrix and the reinforcement were 0.33 and 0.17, respectively, and independent of temperature. The thermal expansion coefficients of the unreinforced Al 2xxx-T4 and the silicon carbide were 30.0×10^{-6} 1/°C and 5.0×10^{-6} 1/°C, respectively.

The mechanical strain components were used in the stress-strain plots for the matrix, reinforcement and the composite. In the isothermal

experiments the net strain component is equivalent to the mechanical strain component. The stress-strain behavior of the unreinforced Al 2xxx-T4 was obtained by setting $v_r = 0$ in the deformation model of the composite.

5.5.1. Monotonic Behavior

Simulation of the monotonic stress-strain behavior of the unreinforced Al 2xxx-T4 is presented in Figure 5.5. The stress-strain behavior was simulated at room temperature, 200°C, and 300°C, at several strain rates. The strain rate and temperature sensitivity of the material behavior were successfully simulated with the constitutive equation. Simulations of the monotonic stress-strain behavior of the 15% and 20% reinforced materials are given in Figures 5.6 and 5.7, respectively. The elastic modulus and yield strength were predicted successfully. Predicted stress levels during inelastic deformation correlated well with the experiments for the strain levels considered. Flow rule predictions for several volume fraction of SiC_p is presented in Figure 5.8. This figure could be used to obtain the yield strength of the 15%, 20% and 30% SiC_p reinforced composite for a given strain rate and temperature.

5.5.2. Cyclic Behavior

Isothermal cyclic stress-strain behavior simulation of unreinforced Al 2xxx-T4 at 200 °C and 300 °C are presented in Figures 5.9-5.12. First cycle and stable cycle stress-strain behavior is very closely predicted. The change of drag stress recovery term, r_k , during cyclic loading successfully accounted for cyclic hardening and softening behavior of the material to a stable state.

Isothermal cyclic stress-strain behavior simulations of the reinforced materials are given in Figure 5.13-5.16. The simulations of composite, matrix, and reinforcement behavior in the loading direction are illustrated in Figure 5.17. It is noted that the matrix strain range is higher than the composite strain range, while the composite stress range is higher than the matrix stress range. The matrix and the reinforcement stress-strain behaviors in the transverse direction are given in Figure 5.18. The transverse stress in the matrix is approximately one fifth of the longitudinal stress component. The matrix stress and the reinforcement stress in the transverse directions are self equilibrating such that Equation 5.16 is satisfied. Note that transverse stress-strain components in 22 and 33 directions are equal. The internal stress-strain behavior of the constituents in isothermal deformation is extensively studied in section 5.5.3.

Thermomechanical cyclic stress-strain behavior simulations of the unreinforced material are presented in Figures 5.19-5.22 for TMF OP loading and TMF IP loading. In the TMF IP case the material undergoes tension upon heating. Due to a decrease in strength with increasing temperature, the stress magnitude decreases as the maximum temperature is approached. Upon cooling, deformation occurs in the reverse direction. Experimental results indicate that the inelastic strain range at zero stress in the TMF IP case exceeds the inelastic strain range in TMF OP case. This can be explained due to the higher constraint in the matrix under the TMF OP case. A good correlation between the experiments and simulations was observed.

Thermomechanical behavior simulations of the reinforced material are presented in Figures 5.23-5.25. The stress-strain behavior simulations of the matrix, reinforcement, and the composite in the transverse direction are

given in Figures 5.26 and 5.27 for TMF OP and TMF IP cases, respectively. Transverse stresses in the matrix, at T_{\max} of the TMF OP cycle, are one half the the longitudinal component in the matrix. At the low temperature end, the transverse stress to longitudinal stress ratio is much lower than one half. In the TMF IP case, at T_{\max} , transverse stresses in the matrix are compressive, while the longitudinal stress component is tensile. The magnitude of the transverse stresses are slightly higher compared to the longitudinal component. At T_{\min} of the TMF IP cycle, the transverse stresses are also of opposite sign of the longitudinal stress component. However, the magnitude of the longitudinal stress far exceeds the magnitude of the transverse component at T_{\min} .

5.5.3. Average Stress-Strain Behavior of the Matrix

This section is devoted to the investigation of the internal stress-strain behavior of the matrix. An understanding of the deformation behavior of the matrix is useful for the investigation of experimentally observed damage mechanisms of the matrix. To illustrate the multiaxiality of internal stresses, the change of hydrostatic stress to effective stress ratio of the matrix with volume fraction of reinforcement is plotted in Figure 5.28. The hydrostatic stress, σ_H^m , is defined as $(\sigma_{11}^m + \sigma_{22}^m + \sigma_{33}^m)/3$. The results are presented at the maximum strain of the cycle, whose ranges are given in the figure. When $v_f=0$, $\sigma_H^m/\bar{\sigma}^m$ ratio is 0.33 under uniaxial loading. For the strain ranges of interest in fatigue research (0.003 to 0.012), appreciable hydrostatic stresses developed in the matrix. When reinforcement volume fraction is 10%, the hydrostatic stresses are small except at large strains. For 20% volume fraction reinforcement the $\sigma_H^m/\bar{\sigma}^m$ ratio approached 1. Beyond influence on fatigue

behavior, these results have implications in explaining early matrix fracture in metal matrix composites and lowered creep strain rates at elevated temperatures.

Figure 5.29 illustrates the ratios of matrix strain range to composite strain range and the matrix stress range to composite stress range in the longitudinal direction. The change in stress and strain concentrations of the matrix at 20°C, and at 300°C for volume fraction of reinforcements up to 40% were examined. The simulations indicate clearly that the strain concentration in the matrix increases with increasing volume fraction of reinforcement. The stress ratio, $\Delta\sigma_{II}^m/\Delta\sigma_{II}^c$, decreases with increasing volume fraction of reinforcement, and the rate of decrease of this ratio is higher at elevated temperatures. Due to larger mismatch in the mechanical properties of the constituents, volume fraction of reinforcement dependency of concentrations is greater at 300°C compared to 20°C. The stress and strain concentrations of the reinforcement follows the opposite trend of the matrix behavior (e.g. strain concentration decrease and stress concentration increase with increasing volume fraction of reinforcement).

In the isothermal loading conditions the transverse stresses are generated due to only mismatch of mechanical properties of the constituents. However, in thermomechanical fatigue loading conditions the mismatch of thermal expansion coefficients of the constituents also contributes to transverse stresses. The tensile or compressive nature of the transverse stresses, especially at high temperature end of the cycle, could critically alter the damage mechanisms. Figures 5.30 and 5.31 explores the influence of mechanical property mismatch versus thermal property mismatch in the metal matrix composites under TMF IP and TMF OP conditions, respectively.

In these figures, the thermal expansion coefficient of matrix was $30.0 \times 10^{-6} \text{ 1/}^\circ\text{C}$, while three different coefficients of thermal expansion, $30.0 \times 10^{-6} \text{ 1/}^\circ\text{C}$, $15.0 \times 10^{-6} \text{ 1/}^\circ\text{C}$, and $5.0 \times 10^{-6} \text{ 1/}^\circ\text{C}$ were used for the reinforcement. The arrows indicate ranges of thermal and mechanical property mismatch for $\theta^r = 5.0 \times 10^{-6} \text{ 1/}^\circ\text{C}$ case (maximum thermal expansion coefficient mismatch). When the thermal expansion coefficients of the particulate and matrix are equal ($\theta^r = \theta^m = 30.0 \times 10^{-6} \text{ 1/}^\circ\text{C}$), the transverse stresses develop due to mechanical property mismatch only. As the thermal mismatch is increased, the transverse stresses in the TMF IP case gradually change sign, and transverse stresses of opposite sign to the longitudinal stress component develop. In the TMF OP case, the behavior of transverse stresses differed. The transverse stresses due to mechanical property mismatch and thermal property mismatch add, and this resulted in transverse stresses that have the same sign as the longitudinal stress component.

The hydrostatic stress to effective stress ratio of the matrix at the maximum temperature of a thermomechanical fatigue cycle is given in Figures 5.32, 5.33, for TMF OP and TMF IP cases, respectively. In these simulations the temperature range of the cycle kept constant. Therefore, the contribution of thermal mismatch on hydrostatic stresses is constant. The contribution of mechanical property mismatch on hydrostatic stresses increases with strain range of the simulation. The change of $\sigma_H^m/\bar{\sigma}^m$ ratio for TMF IP case reflected the competition between thermal property versus mechanical property mismatch. When thermal property mismatch is dominant, e.g. for small $\Delta\varepsilon_{11}^c$, the $\sigma_H^m/\bar{\sigma}^m$ ratio is near zero, indicating pure shear type of internal stresses. Increase in applied mechanical strain, $\Delta\varepsilon_{11}^c$, resulted in an increase in the hydrostatic stress and lead to tensile hydrostatic

stresses at 0.03 mechanical strain range. In the TMF OP case, the hydrostatic stresses are in compression and the magnitude of hydrostatic stresses increases with increasing volume fraction of reinforcement and strain range. Note that these stress ratios are higher than observed in the TMF IP case.

5.6. Discussion

A unified constitutive model capable of simulating elevated temperature cyclic behavior of metal matrix composites is developed. The capabilities of the model is demonstrated by simulating experiments conducted on unreinforced and reinforced Al 2xxx-T4 alloy. The elastic moduli, strain rate sensitivity of yield strength, cyclic stress-strain behavior, and hardening behavior of the composite were predicted very closely over a broad range of temperatures.

It is important to compare the model with the proposed models on the strengthening of metal matrix composites with reinforcement in isothermal loading. The current model predicted an increase in yield strength (0.2% offset) of 25% for the 20% volume fraction material. Finite element modelling of Levy and Papazian [88], with $E = 485$ GPa for the SiC in aluminum alloy, predicted the elastic modulus and strength consistent with the model presented in this paper (ie. 25% increase in strength for volume fraction of 20%). Duva's [89] and McMeeking's [90] models predict less strengthening than observed experimentally. In Duva's study, for a matrix material with a strain hardening exponent of 0 and 0.1 the predicted increase in yield strength is 8% and 12% , respectively (strain hardening exponent of Al 2xxx-T4 is between 0 and 0.1). The reason for this discrepancy between the proposed model and of the others is not clear. The use of rigid particles in

References 89 and 90 may result in early yielding around the particles and a lower apparent yield strength than observed experimentally, however the results converge to correct limit stresses. The elastic modulus of the composite and the stress-strain behavior at low strains is not predicted accurately when rigid particles are used.

In the current study the inelastic strain in the matrix is accounted for as negative transformation strain in the particle, and the constraint power of the matrix on the reinforcement is taken as elastic. As inelastic deformation of the matrix occurs, the constraint is weakened. Hill [68], in his treatment of polycrystal plasticity, accounted for this effect by changing the stiffness tensor of matrix as deformation proceeded. Along similar lines, Tandon and Weng [83], in their study of monotonic deformation, used a secant modulus which decreased with increasing strain. It was noted that the S_{ijkl} tensor also required modification in these cases. These modifications are expected to lower predicted stress levels. On the other hand, as shown by Tandon and Weng, the improvement is not significant at small strains of interest in fatigue research.

One important result of this study is the gained insight on volumetric average stress-strain behavior of the matrix. It is difficult to compare the predicted internal stresses due to thermal and mechanical property mismatch with experiments, since experimental results on internal stresses are not available for particle reinforced composites. Residual stresses due to cooling were evaluated in a whisker reinforced aluminum composite in Reference 82. The sign and magnitude of stresses reported in this study are in general agreement with those reported. The hydrostatic stresses levels were

comparable to those reported in finite element studies by Christman et al. [91] under monotonic loading conditions at similar strain levels.

The strain range in the matrix relative to strain range in the composite is greater by approximately a factor of 1.2 for 20% SiC_p reinforced composite. This ratio increases to 1.5 when the volume fraction of particulates increased to 40% (Figure 5.29). The stress range in the matrix is appreciably smaller than in the composite. This ratio depends on the temperature, and for 20% volume fraction reinforcement at 300°C this ratio is approximately 0.7. The elevated matrix strains explain the shorter room temperature fatigue lives of the 15% SiC_p material, based on strain range, compared to the unreinforced material.

The internal stress-strain behavior of the matrix is extensively studied with the model. For isothermal loading, the transverse stresses in the matrix increased as the strain amplitude or the volume fraction of particulates were increased (Figure 5.28). As the strain amplitude of the simulation increase, the effective stress also increase. However, the rate of increase in hydrostatic stresses is greater than that of effective stresses. An increase of $\sigma_H^m/\bar{\sigma}^m$ ratios up to 1.0 is predicted, for applied strain ranges less than 0.01, while for the monolithic materials this ratio would be 0.333.

The transverse stresses due to mechanical property mismatch for isothermal and thermomechanical loading conditions follow the same sign with the longitudinal stresses. The change of temperature during thermomechanical loading leads to the contribution of thermal property mismatch to transverse stresses. This contribution would be greater than that of mechanical property mismatch. The thermal mismatch strains can increase either by increasing the thermal expansion coefficient mismatch or increasing

the temperature range. The transverse stresses due to thermal and mechanical property mismatches are additive in the TMF OP case and subtracted in the TMF IP case (Figures 5.30-31). The additive nature of the transverse stresses results considerably greater transverse stresses in the TMF OP case than in the TMF IP case. In TMF IP case, the increase in thermal mismatch results a decrease in the magnitude of the transverse stresses,. This resulted in compressive transverse stresses at the maximum temperature end of the cycle while the longitudinal stresses were tensile.

The progressive increase in compressive hydrostatic stress in TMF OP with increasing volume fraction (Figure 5.32) is beneficial in suppressing the creep damage. Under cyclic loading conditions of monolithic alloys, the benefits of compressive stresses under unsymmetric cycling have been documented [92-93]. In the composites, it is expected that these benefits will be accentuated due to the hydrostatic nature of the stress fields acting on the voids. The improvement in fatigue lives under TMF OP for the 20% SiC_p material is consistent with the increased compressive hydrostatic stresses at the high temperature end of the cycle. Upon heating, the matrix develops a compressive hydrostatic stress which suppresses cavitation. The reinforced Al 2xxx-T4 displayed x3 longer fatigue life than the unreinforced material under TMF OP loading conditions.

The advantage of the model is its simplicity, and its capabilities for predicting the stress-strain behavior in the small strain range regime. A comparison of stress-strain simulations with experimental results indicate that the elastic moduli of the composite and yielding behavior were predicted closely for over 60 experiments. The initial slopes of the stress strain curves in the TMF experiments, which are influenced by elastic and thermal mismatch,

were also predicted closely. Different reinforcement shapes can be analyzed in the model by changing Eshelby's tensor although this has not been considered in this study.

6. LIFE PREDICTION MODEL FOR METAL MATRIX COMPOSITES

6.1. Background

At elevated temperatures creep and environmentally activated damage micromechanisms synergistically combine with fatigue damage, decreasing life. For monolithic materials a multitude of damage mechanisms have been identified under thermomechanical fatigue loading conditions. Although many applications of metal matrix composites are in components experiencing complicated cyclic temperature-strain loading histories, the elevated temperature damage mechanisms of these materials have not been reported. The experimental and theoretical investigations presented in previous chapters indicate that the thermomechanical deformation behavior of Al 2124-T4 is significantly affected by the addition of SiC reinforcement. For metal matrix composites, internal stresses and strains generated due to mismatch of mechanical and thermal properties of the constituents will alter the creep, fatigue and oxidation damage behaviors in the matrix.

To date, two main approaches have been proposed to predict thermomechanical fatigue lives of monolithic materials: oxidation-fatigue models and creep-fatigue models. The earliest life prediction model to account for oxidation damage was the frequency modified strain life equation proposed by Coffin [94]. Several other attempts have been made to predict TMF lives based on isothermal data. However, the oxidation induced damage micromechanisms occurring during a TMF cycle can be different from those of an isothermal cycle. More recent models are based on micromechanistic approaches to characterizing environmentally induced crack initiation [95,96] or crack growth [97,98] to a certain size.

A number of models have been developed to address creep-fatigue interaction at elevated temperatures. The strain range partitioning method [93,99] has been developed based on the identification of plastic and creep strains in a fatigue cycle. The time-cycle fraction rule (adopted as an ASME Code [100]) involves the linear summation of fatigue and creep damages, where the fatigue damage is expressed as a cycle ratio and the creep damage is written as a time ratio. A modified time-cycle fraction rule, for applications involving cumulative damage, has been proposed by Lemaitre and coworkers [101].

Several researchers have considered creep-fatigue interaction to be a propagation controlled problem where the damage micromechanisms and fatigue crack growth are assumed to influence each other. By considering cavity formation ahead of the crack tip, fracture mechanics parameters have been modified to handle creep-fatigue crack growth [97,102,103]. In their damage-rate equations Majumdar and Maiya [92] have included the influence of creep cavity growth ahead of a fatigue induced crack. In their model, the sintering of cavities occurs in compression, effectively reversing the creep damage occurring in tension. Damage-rate equations have recently been applied to thermomechanical fatigue loadings [104].

The micromechanistic life prediction model by Neu and Sehitoglu [1-4] combines fatigue, creep, and environmentally induced damages in a total damage term. Integration of creep and oxidation damage over the fatigue cycle enables the model to cover a wide range of loading conditions. The life prediction methodology presented in this chapter follows a similar approach. By using Eshelby's equivalent inclusion based deformation model, the applications of this thermomechanical fatigue life prediction methodology are extended to metal matrix composites.

6.2. Life Prediction Methodology for Al 2xxx-T4

Mechanical properties and fatigue lives of unreinforced Al 2xxx-T4 at elevated temperatures were found to be dependent upon the temperatures and strain rates of the experiments. In addition to fatigue damage, creep and oxidation damages were identified for Al 2xxx-T4 in isothermal and thermomechanical fatigue loading. Fatigue lives at 300 °C were found to be shorter than at room temperature by as much as x10. The decrease in fatigue lives at elevated temperatures can be attributed to oxidation and creep damage. In the proposed life prediction model, damage accumulation due to fatigue, oxidation, and creep mechanisms leads to failure of the material. The total damage per cycle (D^{tot}) is considered as the sum of fatigue (D^{fat}), creep (D^{creep}), and oxidation (D^{ox}) damage terms:

$$D^{\text{tot}} = D^{\text{fat}} + D^{\text{ox}} + D^{\text{creep}} \quad (6.1)$$

This equation can also be written in terms of failure life, N_f , assuming linear damage is equal to 1 at failure;

$$\frac{1}{N_f} = \frac{1}{N_f^{\text{fat}}} + \frac{1}{N_f^{\text{ox}}} + \frac{1}{N_f^{\text{creep}}} \quad (6.2)$$

Here, fatigue, creep, and oxidation damage are $\frac{1}{N_f^{\text{fat}}}$, $\frac{1}{N_f^{\text{creep}}}$, $\frac{1}{N_f^{\text{ox}}}$, respectively. These damage terms are calculated separately in the following sections. However, they are implicitly coupled through stress, strain, and, temperature quantities.

6.2.1. Fatigue Damage

At ambient temperatures oxidation and creep damages are small compared to fatigue damage. Therefore, pure fatigue damage mechanisms

dictate the failure. Fatigue life is governed by mechanical strain range, $\Delta\varepsilon_{\text{mech}}$. The strain-life equation [105] is used to calculate the fatigue life term, N_f^{fat} :

$$\frac{\Delta\varepsilon_{\text{mech}}}{2} = \frac{\sigma_f'}{E} (2N_f^{\text{fat}})^b + \varepsilon_f' (2N_f^{\text{fat}})^c \quad (6.3)$$

where E is Young's modulus, σ_f' is the fatigue strength coefficient, b is the fatigue strength exponent, ε_f' is the fatigue ductility coefficient, and c is the fatigue ductility exponent. The constants in the strain-life equation were determined from isothermal room temperature fatigue experiments conducted on unreinforced Al 2xxx-T4. The material constants in the strain-life equation are given in Table III.

6.2.2. Oxidation Damage

Extensive studies on aluminum have found an accelerated fatigue damage in air relative to vacuum environment [14-17]. In the proposed life prediction methodology, an oxidation induced crack initiation and growth model is used to calculate the oxidation damage. Oxidation induced crack growth is the repeated formation of an oxide layer and its rupture at the crack tip, which exposes fresh material to the environment. During fatigue loading of aluminum at elevated temperatures an oxide intrusion along the crack surface undergoes rupture, channeling crack growth into the matrix. Micrographs of a fatigue crack indicating oxidation in its wake and ahead of the crack tip are given in Figures 4.24-4.26.

Oxidation damage is initiated at the environmentally exposed surfaces of the specimen, and the early stages of oxidation contributes to crack nucleation. Oxidation of aluminum starts with the formation of an amorphous alumina layer which transforms, with further heating, into

crystalline alumina [18]. During the early stages of oxidation, amorphous and crystalline alumina grow together. Although the exact mechanism of oxidation is not clear, coexistence of these two oxide morphologies leads to a change in the kinetics of oxidation. Beck found that the oxidation of aluminum followed two different parabolic rate laws, one in the initial stage and one in the final stage [17].

There are discrepancies in the reported values of activation energy for the parabolic growth rate of oxide formation in aluminum. Beck reported 57 Kcal/mole [17], 26 Kcal/mole was reported by Maurin [106], and Gulbransen reported 22.8 Kcal/mole [107]. In the life prediction model, the parabolic oxidation growth law suggested by Maurin was used. The temperature dependency of the parabolic oxidation constant, K_p , was expressed as:

$$K_p = 8.8 \times 10^{-15} \exp\left(-\frac{26000}{R(T+273)}\right) \text{ (cm}^4\text{/sec)} \quad (6.4)$$

In the Neu-Sehitoglu model [1-4] oxidation induced crack growth was found to be a function of mechanical strain range, temperature-mechanical strain phasing, effective oxidation constant, and strain rate. The oxidation damage is given as:

$$\frac{1}{N_f^{\text{ox}}} = \left[\frac{h_{\text{cr}} \delta_o}{B_{\text{ox}} \Phi^{\text{ox}} K_p^{\text{eff}}} \right]^{-1/\beta} \frac{2(\Delta\epsilon_{\text{mech}})^{2/\beta+1}}{\dot{\epsilon}^{(1-a/\beta)}} \quad (6.5)$$

Due to lack of oxide thickness measurements in aluminum, the material constants h_{cr} (critical oxide length), δ_o (a measure of oxide ductility), and B_{ox} (a constant which indicates change in the rate of oxidation due to repeated rupture) can not be identified individually. These material constants

are combined into one material constant, K_{cr} , which has the same unit as the parabolic oxidation constant:

$$\frac{1}{N_f^{ox}} = \left[\frac{K_{cr}}{\Phi^{ox} K_p^{eff}} \right]^{-1/\beta} \frac{2(\Delta\epsilon_{mech})^{2/\beta+1}}{\dot{\epsilon}^{(1-a/\beta)}} \quad (6.6)$$

A propagating crack continuously exposes fresh metal to the environment. The oxide growth is interrupted, and the effective oxide growth at the crack tip no longer follows the parabolic law [2]. The constant β represents the increased oxidation growth rate due to the repeated rupture of the oxide layer. The constant a predicts the strain rate sensitivity of the oxidation fracture. The constants, K_{cr} , β , and a were calculated through experiments conducted at low strain ranges. The stress levels of low strain range experiments are too low to induce a significant creep damage, so the failure is dominated by oxidation.

An effective parabolic oxidation constant, K_p^{eff} , has been defined for a cycle which undergoes a varying temperature history:

$$K_p^{eff} = \frac{1}{t_c} \int_0^{t_c} D_0 \exp \left[-\frac{Q}{R T(t)} \right] dt \quad (\text{cm}^4/\text{sec}) \quad (6.7)$$

where t_c is the period of the cycle, D_0 is the diffusion coefficient, Q is the activation energy for oxidation, R is the universal gas constant, and $T(t)$ is temperature as a function of time.

In TMF experiments the degree of oxidation was found to be dependent on mechanical strain-temperature phasing [1-4]. For TMF OP loading, preferential oxidation at the crack tip was observed (Figures 4.25,4.26). Tensile loading of the oxide layer at the low temperature end of the cycle promoted oxide induced crack initiation and growth. For TMF IP loading, Auger

Spectroscopy analysis indicated insignificant oxidation damage at the crack tip. A phasing factor, Φ^{ox} , was introduced to quantify relative oxidation damage between phasings. The phasing factor is defined as follows:

$$\Phi^{\text{ox}} = \frac{1}{t_c} \int_0^{t_c} \phi^{\text{ox}} dt \quad (6.8)$$

$$\phi^{\text{ox}} = \exp \left[-\frac{1}{2} \left(\frac{\dot{\epsilon}_{\text{th}}/\dot{\epsilon}_{\text{mech}} + 1}{\zeta_{\text{ox}}} \right)^2 \right] \quad (6.9)$$

The form of ϕ^{ox} was chosen to represent the behavior of oxide cracking that has been observed for different phasing conditions [1-4]. The parameter, ζ_{ox} , is a measure of the relative amount of oxidation damage for different thermal strain to mechanical strain ratios and is calculated based on the experiments. The constants in the oxidation damage term are given in Table III.

6.2.3. Creep Damage

At temperatures exceeding 150 °C aluminum alloys undergo creep damage in the form of grain boundary cavitation [13,108,109] and intergranular crack growth [8]. Creep damage in the form of void formation at the grain boundaries has been observed in both isothermal and thermomechanical fatigue experiments. Intergranular crack growth from the specimen surface is illustrated in Figure 4.22. The dependence of creep damage on effective and hydrostatic stresses has been established through multiaxial creep experiments conducted by Leckie, Hayhurst, and co-workers [110-112]. The creep damage term is a function of temperature, effective stress,

and hydrostatic stress components. The total creep damage is obtained by integrating the creep damage in each cycle throughout the fatigue life of the material:

$$D^{\text{creep}} = \int_0^{t_c} A_{\text{cr}} \Phi^{\text{creep}} \exp\left(-\Delta H / RT(t) \left((\alpha_1 \bar{\sigma} + \alpha_2 \sigma_H) / K\right)^m\right) dt \quad (6.10)$$

ΔH is the activation energy for the rate-controlled creep mechanism, R is the gas constant, $T(t)$ is temperature as a function of time, $\bar{\sigma}$ is the effective stress, σ_H is the hydrostatic stress, and K is the drag stress. The constants α_1 and α_2 account for the degree of damage occurring under tension and compression. A and m are material constants.

The constants A and ΔH were calculated using isothermal fatigue experiments conducted at high strain ranges, where pure fatigue and creep damages dominate the failure. The power law creep exponent was found to be 4.6, which is consistent with the creep models based on dislocation climb. These models predicted a stress exponent near 4.

For Al 2xxx-T4, crack growth is mainly intergranular for TMF IP and transgranular for TMF OP loading conditions. A mixed (intergranular and transgranular) crack growth behavior has been observed for a wide region of $\dot{\epsilon}_{\text{th}}/\dot{\epsilon}_{\text{mech}}$ values. As $\dot{\epsilon}_{\text{th}}/\dot{\epsilon}_{\text{mech}}$ becomes negative (out-of-phase) transgranular crack growth behavior is favored. This indicates that creep damage occurring under in-phase loading is more extensive than under out-of-phase loading. A phasing factor, ϕ^{creep} , was introduced to account for the effect of mechanical strain-temperature phasing. The form of the creep phasing factor is the same as the oxidation phasing factor:

$$\Phi^{\text{creep}} = \frac{1}{t_c} \int_0^{t_c} \phi^{\text{creep}} dt \quad (6.11)$$

$$\phi^{\text{creep}} = \exp \left[-\frac{1}{2} \left(\frac{\dot{\epsilon}_{\text{th}} / \dot{\epsilon}_{\text{mech}} + 1}{\zeta_{\text{creep}}} \right)^2 \right] \quad (6.12)$$

Instantaneous evaluation of the stresses during fatigue loading is required to calculate the creep damage experienced by the material. The unified constitutive equation developed in chapter 5 is coupled with the creep damage equation.

6.3. Life Prediction Methodology for SiC_p Reinforced Al 2xxx-T4

The damage leading to failure of metal matrix composites during fatigue loading may occur in the matrix, in the reinforcement, or at their interface. Examination of fatigue cracks of 15% and 20% SiC_p reinforced Al 2xxx-T4 specimens have revealed that fatigue crack initiation and growth is confined predominantly to the matrix. In the life prediction model, the damage equations of the unreinforced material developed in the previous section are coupled with the unified constitutive model of the composite material.

The total damage on the composite is sum of the damage terms of the matrix:

$$D^{\text{tot}} = D_{\text{matrix}}^{\text{fat}} + D_{\text{matrix}}^{\text{ox}} + D_{\text{matrix}}^{\text{creep}} \quad (6.13)$$

It is recognized that local deformation of the matrix at the periphery of the reinforcement plays an important role in the initiation of creep and fatigue damages. However, excellent chemical wetting compatibility between SiC and Al alloys provides an adequate bond to protect the interface from cyclic failure. In these materials interface failure is very rare [22-33], proving

that damage occurs in the matrix. The grain boundary damage during creep deformation at elevated temperatures is uniformly distributed in the matrix phase and is not confined to proximity of particulates.

The fatigue damage of the reinforced Al 2xxx-T4 is calculated using equation 6.3, based on the longitudinal matrix strain range, $\Delta\varepsilon_{11}^m$, obtained from the constitutive equation of the composite. The constants in the strain-life equation are the same for both unreinforced and reinforced materials.

The predictions on elevation of strain concentration in the matrix, $\Delta\varepsilon_{11}^m/\Delta\varepsilon_{11}^c$, during cyclic loading are presented in Figure 5.29. The behavior at 20 °C, and at 300 °C were examined. Mismatch in mechanical properties of the matrix and the reinforcement changed the temperature dependence of the strain ratio slightly. Simulations clearly indicate that the strain concentration in the matrix increases with increasing volume fraction of reinforcement. This is consistent with the inferior fatigue life performance, based on strain range, of the reinforced material compared to unreinforced material. The strain ratio increases to 1.50 when the volume fraction of particulates increases to 40%. The stress ratio decreases with an increase in volume fraction of reinforcement. Also, the rate of decrease is higher at elevated temperatures. At 300 °C this ratio is approximately 0.7 for 20% volume fraction reinforcement.

Creep damage of the reinforced Al 2xxx-T4 is calculated by using the multiaxial stresses of the matrix in equation 6.10. The constants of the creep damage of the unreinforced and reinforced Al 2xxx-T4 are the same, except for phasing factor. As noted in Figures 3.1- 3.3, the reinforced material exhibited a uniaxial grain morphology, resulting in a higher tendency for intergranular growth compared to the unreinforced material which has a more directional

grain structure. The phasing factor, ζ_{creep} , would be the same for the reinforced and the unreinforced materials if the grain sizes were the same.

The multiaxial stress state in the matrix changes with an increase in volume fraction of reinforcement. The variations of $(\alpha_1\bar{\sigma} + \alpha_2\sigma_H)$ under TMF IP and TMF OP loading are presented in Figures 6.1 and 6.2, respectively. The $\alpha_1\bar{\sigma}$ term is positive during both the compressive and tensile portions of the cycle. The $\alpha_2\sigma_H$ term changes sign within the cycle. Under TMF OP loading, at T_{max} , $(\alpha_1\bar{\sigma} + \alpha_2\sigma_H)$ becomes compressive with increasing volume fraction of reinforcement (Figure 6.1). Since the creep damage is modified with a temperature term, the compressive portion of the cycle generates a healing effect on the creep damage. Note that, despite the reduction of creep damage, a net positive creep damage accumulation occurs under TMF OP loading. In the TMF IP loading, increasing volume fraction of reinforcement contributes to healing of creep damage insignificantly. TMF IP lives are not a strong function of volume fraction of reinforcement.

Oxidation damage on the reinforced material was calculated using equation 6.6, based on the mechanical strain range and mechanical strain rate of the matrix in the loading direction. The oxidation rate is a function of the matrix mechanical strain range, $\Delta\epsilon_{\text{mech}}$. Thus, and the oxidation rate in the composite is expected to be higher due to the increased $\Delta\epsilon_{\text{mech}}$. The constants in the oxidation damage equation are the same as the unreinforced material constants.

6.4. Life Prediction Results at Elevated Temperatures

The contributions of creep, fatigue, and oxidation damage mechanisms to failure were analyzed for a wide range of loading conditions. Life predictions were made at strain ranges from 0.002 to 0.02. At strain ranges

lower than 0.002, where stresses experienced by the material were too low to induce a considerable creep damage, failure was largely dominated by the oxidation induced damage mechanism. Creep damage became dominant at mid-strain ranges. Both oxidation and creep damages were found to be more detrimental in experiments conducted at strain rates of 3.0×10^{-5} 1/sec than at 3.0×10^{-3} 1/sec. Finally, at strain ranges higher than 0.01 pure fatigue damage began to contribute to failure.

Under isothermal fatigue loading, when fatigue damage is dominant (such as at 20 °C or 200 °C strain rate of 3.0×10^{-3} 1/sec), the reinforced material lives are shorter than the matrix alloy lives when compared based on strain range. Room temperature fatigue life predictions on 15% SiC_p reinforced Al 2xxx-T4 are shown in Figure 6.3. The model has correctly accounted for the decrease in fatigue lives with an increase in reinforcement. The simulations for 40% reinforcement show the trends with increasing volume fraction.

Strain range based isothermal fatigue life predictions for unreinforced and reinforced materials are given in Figures 6.4-6.7. Isothermal life predictions of the same experiments, based on stress range, are plotted in Figures 6.8-6.11. The enhancement in composite life, when stress quantities are used, is predicted accurately with the model. Creep damage has been found to be more extensive at 300 °C than at 200 °C. The oxidation mechanism was enhanced by the slower strain rates, allowing more time for oxidation at the crack tips and on the surface.

The model has been used to predict the lives of TMF OP and IP experiments conducted at 100-300 °C (Figures 6.12-6.13). The strain range dependency of the damage mechanisms has been found to be similar to that under isothermal fatigue loading conditions. Extensive creep damage has been found under TMF IP and TMF OP loading conditions at high strain

ranges. For TMF OP loading, compression at the high temperature end of the cycle could lead to suppression of void growth and intergranular cracking mechanisms. This observation is consistent with improvement of life with reinforcement under TMF OP loading. The TMF OP lives improve with SiC_p reinforcement, but the TMF IP lives are not changed.

TMF life predictions considering only the creep damage term are shown in Figures 6.14 and 6.15. It is noted that TMF OP lives improve with increasing the volume fraction of reinforcement and TMF IP lives are relatively insensitive to volume fraction of reinforcement. TMF life prediction due to oxidation only is shown in Figures 6.16 and 6.17. We note the higher oxidation damage in the TMF OP case and the insensitivity of oxidation damage to volume fraction of reinforcement. TMF life prediction due to fatigue damage only is illustrated in Figure 6.18. The results are the same for TMF OP and TMF IP loadings.

6.5. Discussion

Cycles to failure for unreinforced and reinforced Al 2xxx-T4 are satisfactorily predicted over a broad range of strain rates and temperatures and strain-temperature phasings. The evolution of mechanical strain range, effective stress, and hydrostatic stress under cyclic loading is established by using Eshelby's equivalent inclusion model. These quantities and matrix properties are utilized to develop a fatigue life prediction methodology for metal matrix composites. The contributions of oxidation, creep and fatigue damage mechanisms to failure are quantified for a wide range of loading conditions.

When the strain range is controlled on the composite, the corresponding strain range on the matrix is higher for both isothermal and

thermomechanical fatigue loading. Therefore, a composite is expected to exhibit a shorter life based on strain range; except under conditions such as TMF OP, where compressive hydrostatic stresses played a significant role. The results point out the utility of average internal stress-strain behavior, rather than localized stress-strain behavior, to quantify damage micro-mechanisms of metal matrix composites. When the matrix strain range is utilized in the predictions, as noted in Figure 6.3, the fatigue life predictions of the 15% SiC_p reinforced material are very satisfactory. If the maximum local strain range at the particle-matrix interface were used, it would underestimate the fatigue lives by orders of magnitude.

For 15%, 20%, and 30% SiC_p reinforced materials the $\Delta\epsilon_{II}^m/\Delta\epsilon_{II}^c$ ratios are 1.15, 1.2 and 1.35, respectively (Figure 5.29). Similarly, the stress-life behavior of the composite may be predicted based on $\Delta\sigma_{II}^m/\Delta\sigma_{II}^c$ vs volume fraction of reinforcement curves in Figure 5.29. The volumetric average stress range in the matrix is lower than the applied composite stress range. Therefore, the composite exhibits longer lives based on stress parameters, as predicted with the model. Note that as the strain range is increased in the isothermal case, the hydrostatic stresses are also increased. It is worth noting that the stress ranges corresponding to the half life values are used in Figures 6.8-6.11. If the results are compared based on the first cycle stress range, the stress ranges would be higher and the distance between the 0% and 20% curves would be broadened. The enhancement in composite lives based on stress range has encouraging implications when designing with metal matrix composites. For example, if notched members are tested, the local strains at the notch root would be smaller for the reinforced material as compared to the unreinforced material. If the strain-life behavior of the

composite and matrix are similar, then the composite material will always exhibit longer initiation lifetimes.

For metal matrix composites, mismatch in thermal and mechanical properties results in multiaxial stress states in the constituents. The changes of volumetric effective stress and hydrostatic stress in the matrix with volume fraction of reinforcement are established for isothermal and TMF loading. The highest hydrostatic stresses are found in the TMF OP loading at the minimum temperature end of the cycle. Creep damage occurring in the tensile portion of the cycle is subjected to healing under the compressive portion (high temperature end) of the cycle. The predictions shown in Figure 6.14 confirm the healing effect under TMF OP loading. However, the apparent improvement of fatigue lives with increasing volume fraction of reinforcement at long lives (where creep mechanism is no longer dominant) is not resolved. Under TMF IP loading, the material experiences high temperatures in the tension portion of the cycle, and it is shown that the hydrostatic stresses in this case are near zero.

7. CONCLUSIONS

1. The fatigue lives of unreinforced Al 2xxx-T4 are sensitive to strain-rate at 200 °C and 300 °C. The addition of SiC particulate reinforcement decreases temperature and strain-rate sensitivity. Based on stress range, substantial improvements in fatigue life have been observed with reinforcement under both isothermal and thermomechanical loading conditions.

2. The damage mechanisms occurring under isothermal and thermomechanical fatigue loading of unreinforced and reinforced Al 2xxx-T4 are identified. Evidence of void formation at the grain boundaries, crack deflection due to particle interference, and oxide penetration at the crack tips is demonstrated. The damage micromechanisms under TMF loading of both unreinforced and reinforced Al 2xxx-T4 are similar. The TMF OP loading was more favorable to transgranular cracking than the TMF IP loading.

3. A major contribution of the proposed deformation model to the composite micromechanics field is the representation of the time-temperature dependent deformation behavior of the matrix with a unified model, compared to the use of time independent models considered in earlier studies. The proposed model leads to a general description of deformation of metal matrix composites under thermomechanical loading. The present analysis provides insight into the internal stress fields developed due to the mismatch of elastic and inelastic properties and the thermal expansion coefficients of the constituents during cyclic loading under both isothermal and thermomechanical loading conditions.

4. The physically based life prediction methodology predicts contributions of fatigue, creep, and environmental damages to failure under

isothermal and thermomechanical fatigue loading. The model is able to simulate cyclic deformation behavior under isothermal and thermomechanical loading conditions. The proposed life prediction methodology offers the possibility of using existing knowledge about the matrix in the design and service life prediction of composite materials.

TABLES

Table I : Modulus and flow strength properties of 0%, 15%, and 20% SiC_p reinforced Al 2xxx-T4.

	T (°C)	$\dot{\epsilon}$ (1/sec)	E (Mpa)	First cycle 0.2% offset flow stress	Half life 0.2% offset flow stress
Al 2xxx-T4	200	3.0×10^{-5}	62700	220	160
0% SiC _p	200	3.0×10^{-3}	65100	320	340
	300	3.0×10^{-5}	55700	75	50
	300	3.0×10^{-3}	54900	140	105
Al 2xxx-T4	200	3.0×10^{-5}	85500	230	175
15% SiC _p	200	3.0×10^{-3}	86200	330	355
	300	3.0×10^{-5}	78600	85	60
	300	3.0×10^{-3}	79400	150	120
Al 2xxx-T4	200	3.0×10^{-5}	93200	250	215
20% SiC _p	200	3.0×10^{-3}	92400	350	385
	300	3.0×10^{-5}	86300	100	60
	300	3.0×10^{-3}	87700	205	185

Table II: Material constants for Al 2xxx-T4

Flow Rule

$$n_1=4.6$$

$$n_2=10.1$$

$$A= 9.8 \cdot 10^{11} \exp [- 18,722 / (T+273)] \text{ 1/sec}$$

Elastic Modulus

$$E = \begin{cases} 82000 - 90 T & T \geq 150 \text{ }^\circ\text{C} \\ 72500 - 50 T & T < 150 \text{ }^\circ\text{C} \end{cases} \quad (\text{MPa})$$

Drag Stress

$$K_o = \begin{cases} 256 - 0.28 T & T \geq 150 \text{ }^\circ\text{C} \\ 226 - 0.15 T & T < 150 \text{ }^\circ\text{C} \end{cases} \quad (\text{MPa})$$

Hardening Functions

$$a = 20,000 \text{ (MPa)}$$

$$b = 1,000 \text{ (MPa/}^\circ\text{C)}$$

$$X(T) = 1.013 - 8.8 \times 10^{-4} T - 2.7 \times 10^{-6} T^2$$

$$B = 5$$

$$K_{\text{sat}} = \begin{cases} 420 - 0.30 T & T \geq 150 \text{ }^\circ\text{C} \\ 620 - 1.66 T & T < 150 \text{ }^\circ\text{C} \end{cases} \quad (\text{MPa})$$

Recovery Functions

$$C(T) = 4.9 \times 10^{-10} + 4.0 \times 10^{-6} T - 3.2 \times 10^{-8} T^2 \\ + 1.2 \times 10^{-10} T^3 - 2.3 \times 10^{-13} T^4 + 1.70 \times 10^{-16} T^5$$

$$K_{\text{rec}} = \begin{cases} 20 & T \geq 150 \text{ }^\circ\text{C} \\ 260 - 0.8 T & T < 150 \text{ }^\circ\text{C} \end{cases} \quad (\text{MPa})$$

Table III. Material constants used in fatigue life prediction model for Al 2xxx-T4

Material constants used in fatigue strain life term

$$E=71500 \text{ MPa}$$

$$\sigma_f' = 750 \text{ MPa}$$

$$b=-0.08$$

$$\epsilon_f' = 0.28$$

$$c=-0.63$$

Material constants used in oxidation damage term

$$a = 1.2$$

$$b = 2.4$$

$$K_{cr} = 1.08 \cdot 10^{-12} \text{ cm}^4/\text{sec}$$

$$Q = 26 \text{ KCal/ mole}$$

$$D_o = 8.8 \cdot 10^{-15} \text{ cm}^4/\text{sec}$$

$$\zeta_{ox} = 5$$

Material constants used in creep damage term

$$A = 1.543 \cdot 10^{-2} \text{ 1/sec}$$

$$m = 4.6$$

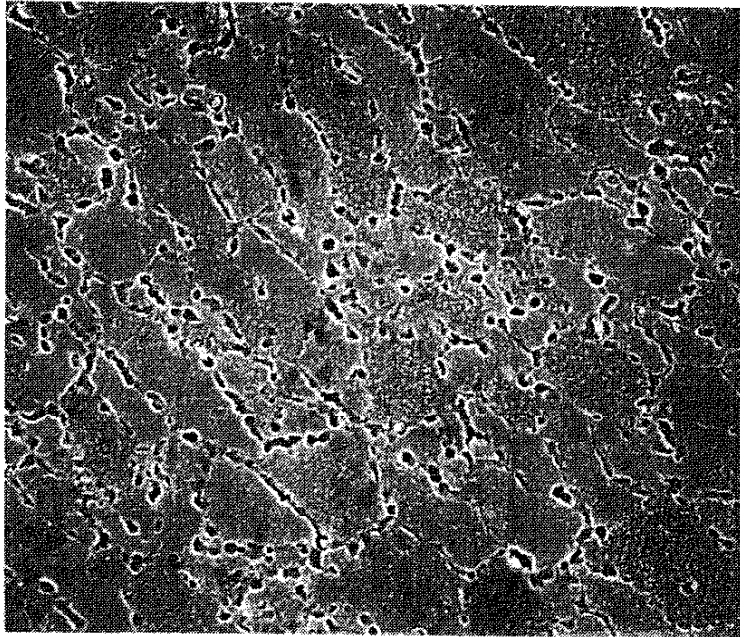
$$\Delta H = 15.6 \text{ KCal/ mole}$$

$$\zeta_{creep} = 1$$

Table IV: Experiments used to determine constants of the life prediction equations

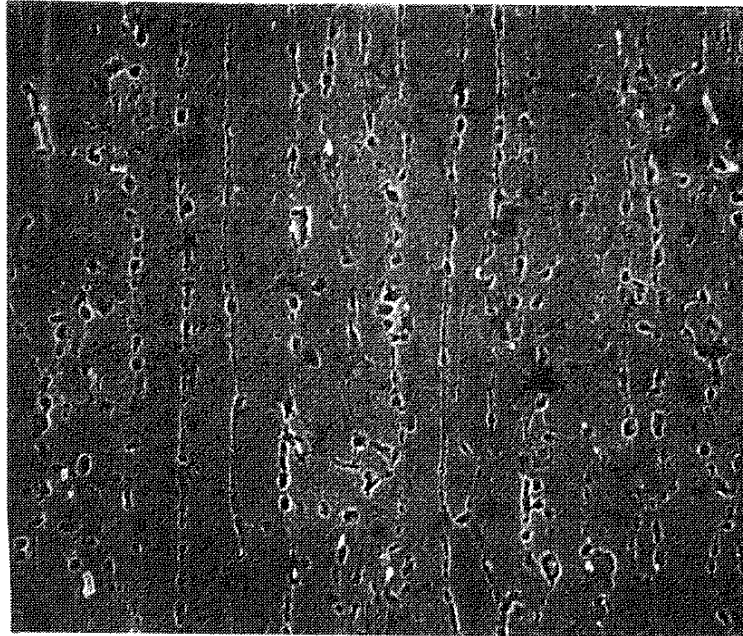
	Constants	Experiments
Fatigue	$E, \sigma_f', b, \epsilon_p', c$	IF, Room Temperature [27]
Oxidation	a,b	IF, 200°C, $\dot{\epsilon} = 3.10^{-5}$ 1/sec, $\Delta\epsilon = 0.0031$ IF, 200°C, $\dot{\epsilon} = 3.10^{-3}$ 1/sec, $\Delta\epsilon = 0.0026$
	K_{CR}	IF, 300°C, $\dot{\epsilon} = 3.10^{-5}$ 1/sec, $\Delta\epsilon = 0.0031$
	ξ_{OX}	TMF OP, 100-300°C, $\Delta\epsilon = 0.0036$
Creep	A,m	IF, 300°C, $\dot{\epsilon} = 3.10^{-5}$ 1/sec, $\Delta\epsilon = 0.0101$ IF, 300°C, $\dot{\epsilon} = 3.10^{-3}$ 1/sec, $\Delta\epsilon = 0.0098$
	ΔH	IF, 200°C, $\dot{\epsilon} = 3.10^{-3}$ 1/sec, $\Delta\epsilon = 0.0031$
	ξ_{CR} (unreinforced)	0% SiC _p , TMF IP, 100-300°C, $\Delta\epsilon = 0.0115$
	ξ_{CR} (reinforced)	20% SiC _p , TMF IP, 100-300°C, $\Delta\epsilon = 0.0101$

FIGURES



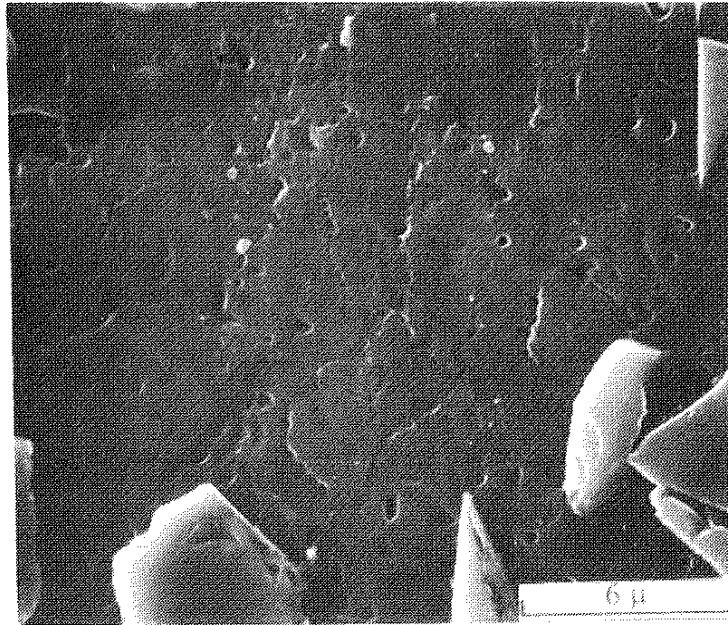
6 μ

Figure 3.1: Grain boundary cavitation, isothermal fatigue, 200 °C, $\dot{\epsilon} = 3.0 \times 10^{-3}$ 1/sec; unreinforced material longitudinal section



6 μ

Figure 3.2: Grain boundary cavitation, isothermal fatigue, 200 °C, $\dot{\epsilon} = 3.0 \times 10^{-3}$ 1/sec; unreinforced material horizontal section



6 μ

Figure 3.3: Grain boundary cavitation, isothermal fatigue, 200 °C, $\dot{\epsilon} = 3.0 \times 10^{-3}$ 1/sec; reinforced material longitudinal section

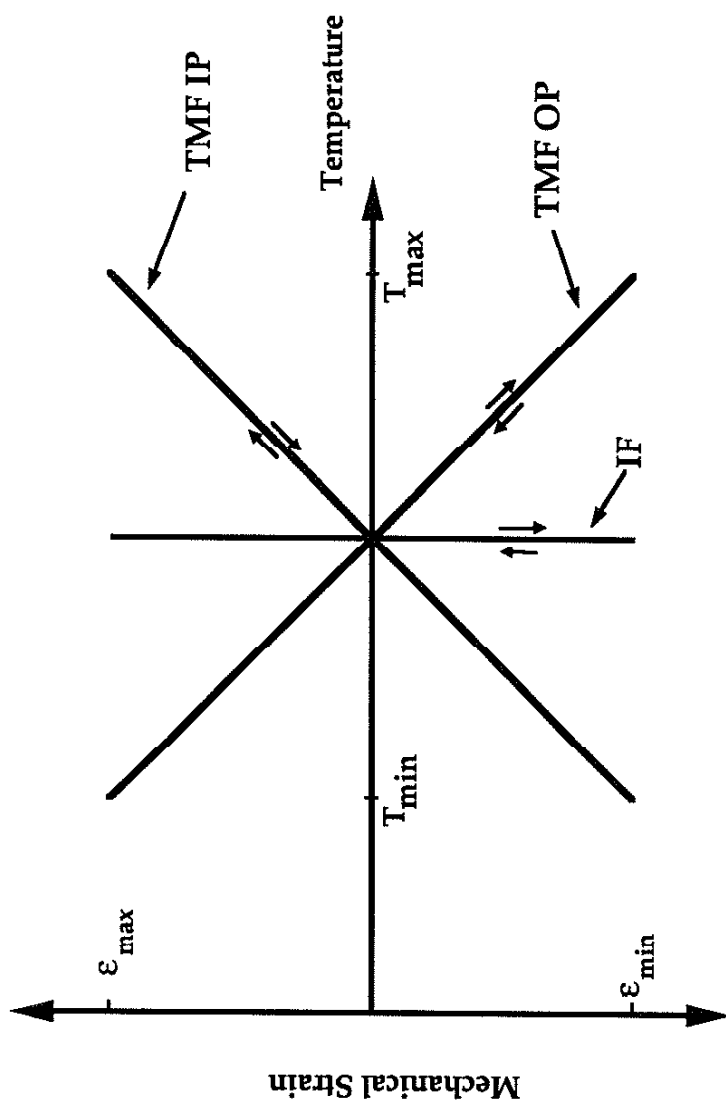


Figure 3.4: Schematic of mechanical strain-temperature variation in TMF In-Phase, TMF Out-of-Phase and isothermal fatigue loading

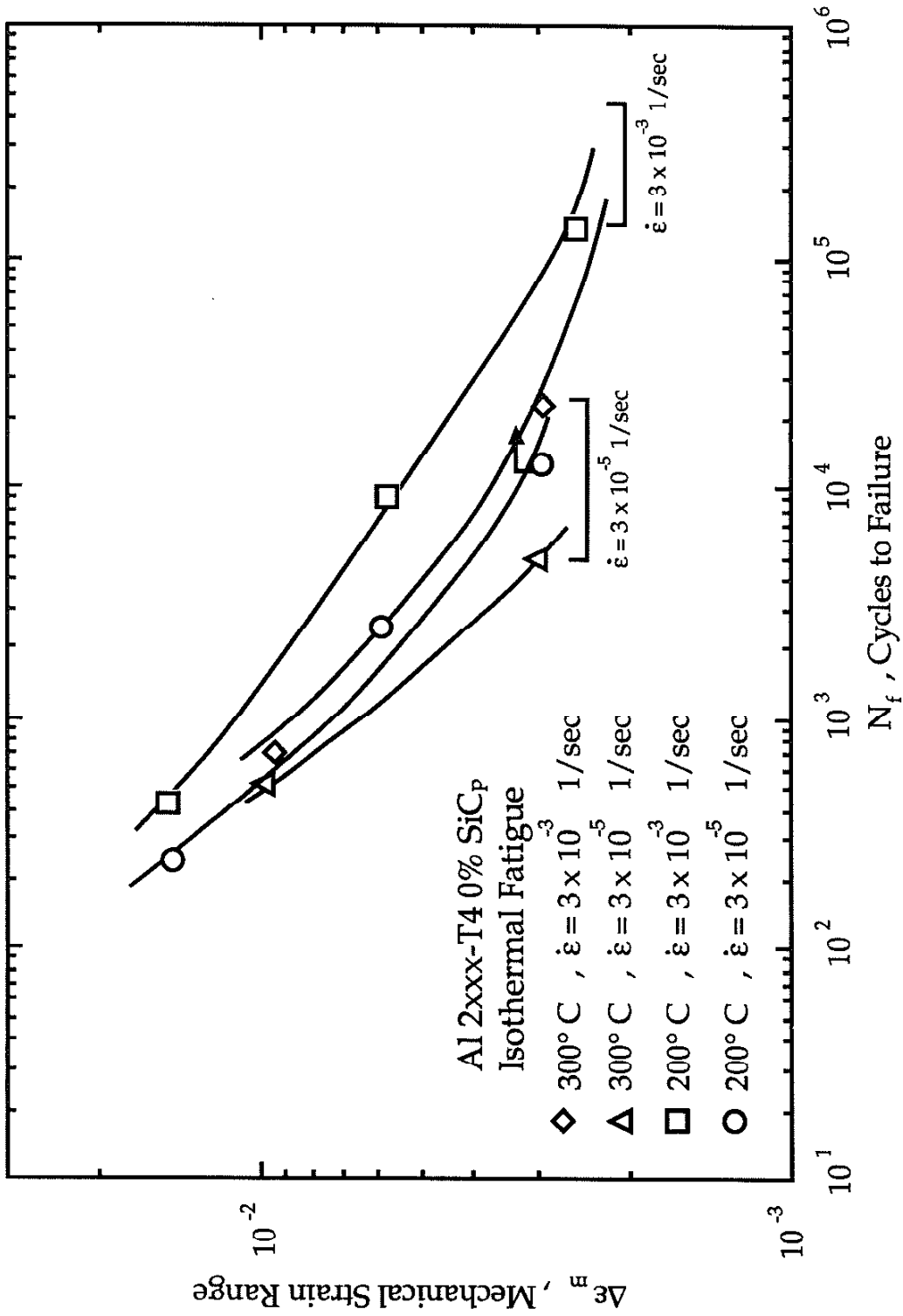


Figure 4.1: Mechanical strain range-cycles to failure data for isothermal fatigue of unreinforced Al 2xxx-T4

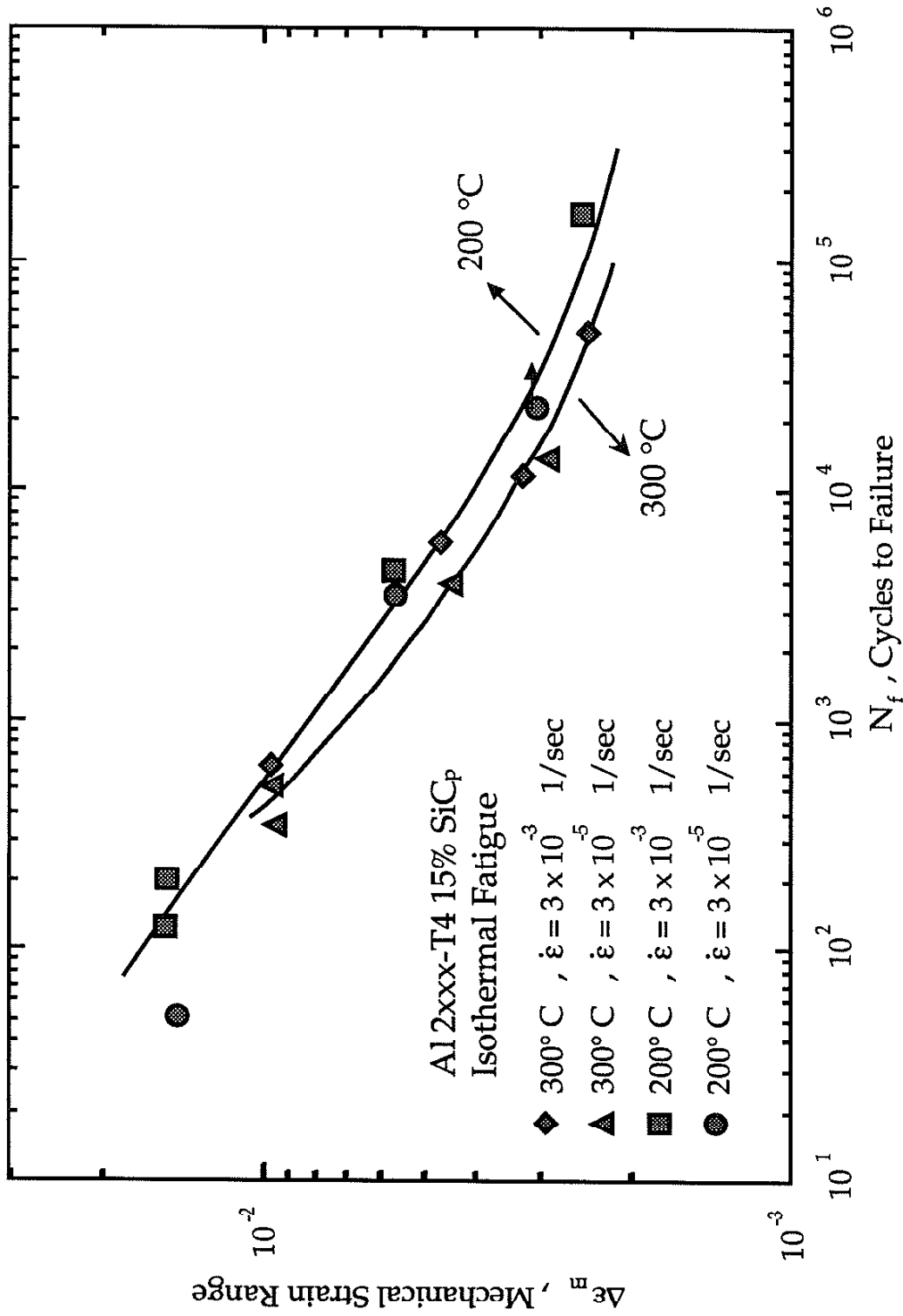


Figure 4.2: Mechanical strain range-cycles to failure data for isothermal fatigue of 15% reinforced Al 2xxx-T4

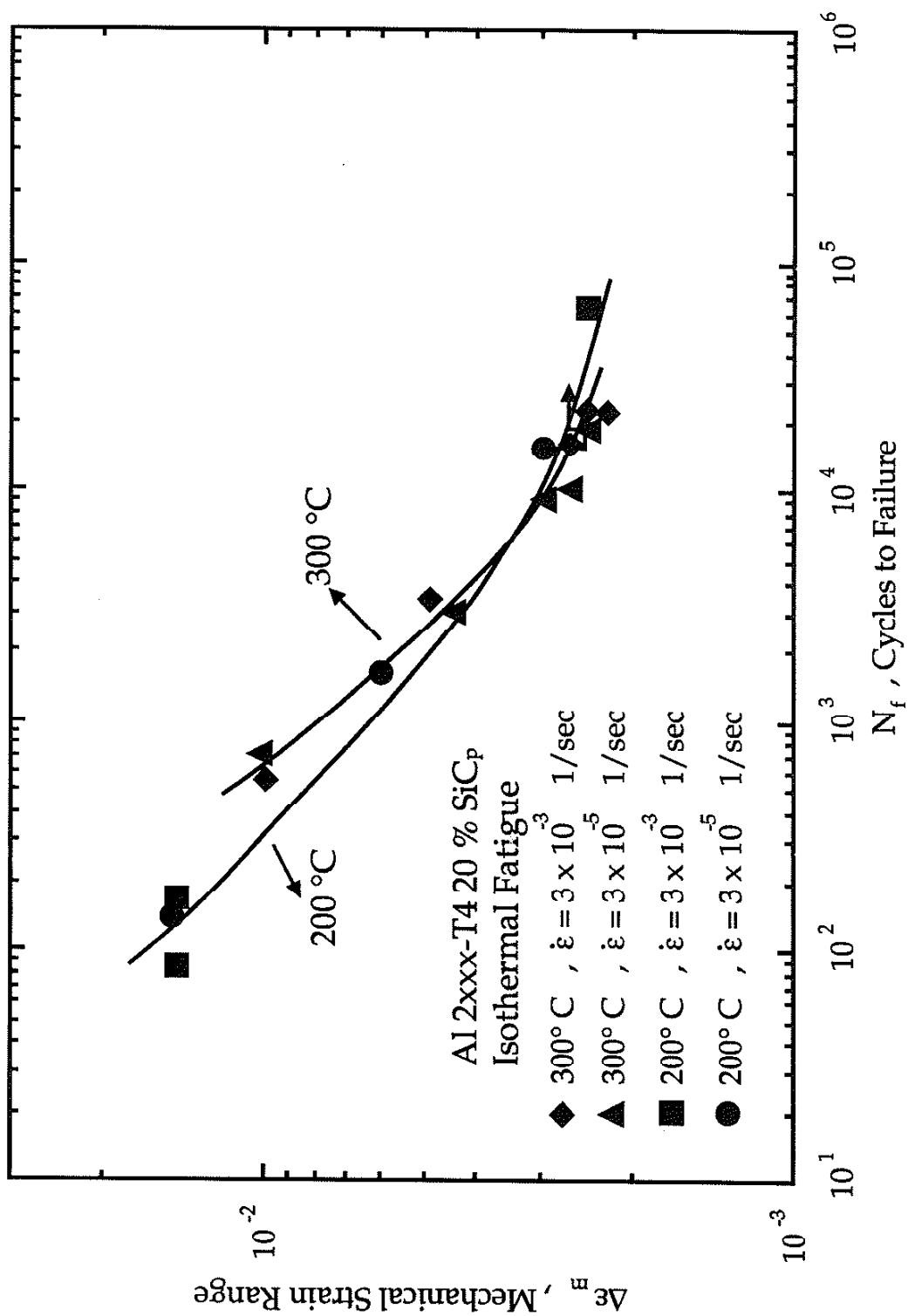


Figure 4.3: Mechanical strain range-cycles to failure data for isothermal fatigue of 20% reinforced Al 2xxx-T4

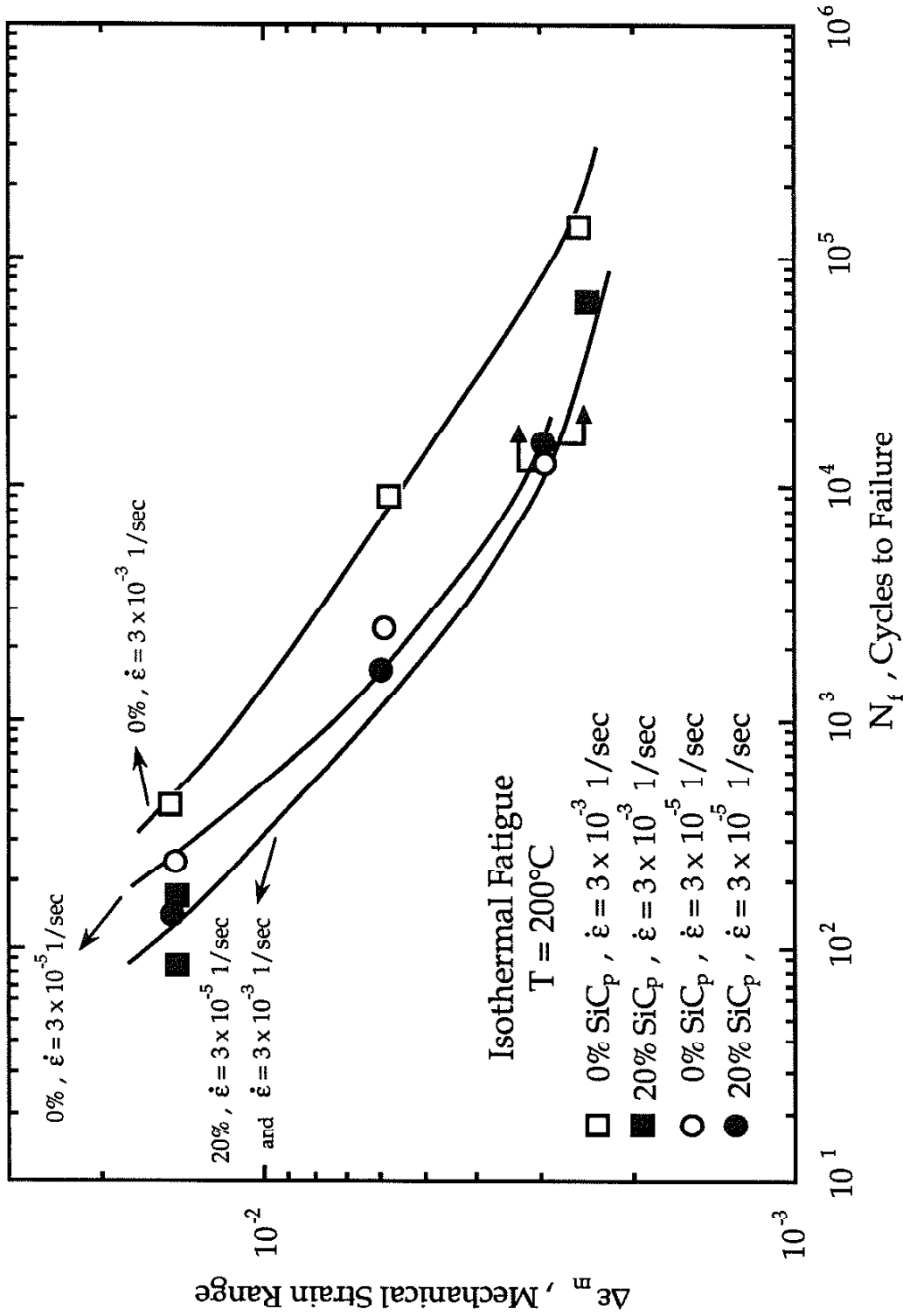


Figure 4.4: Mechanical strain range-cycles to failure data for isothermal fatigue of unreinforced and 20% SiC_p reinforced Al 2xxx-T4 at 200°C

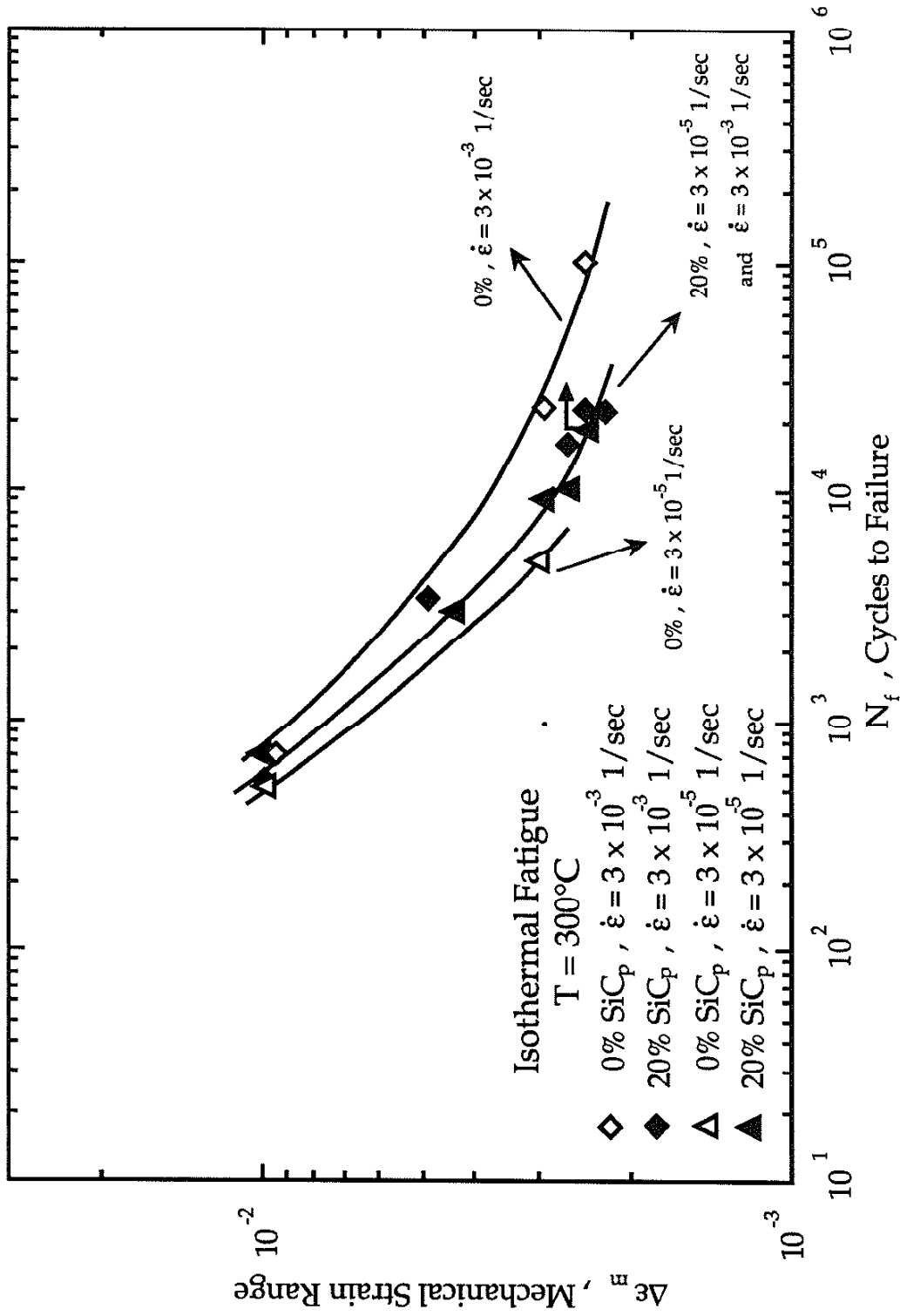


Figure 4.5: Mechanical strain range-cycles to failure data for isothermal fatigue of unreinforced and 20% SiCp reinforced Al 2xxx-T4 at 300°C

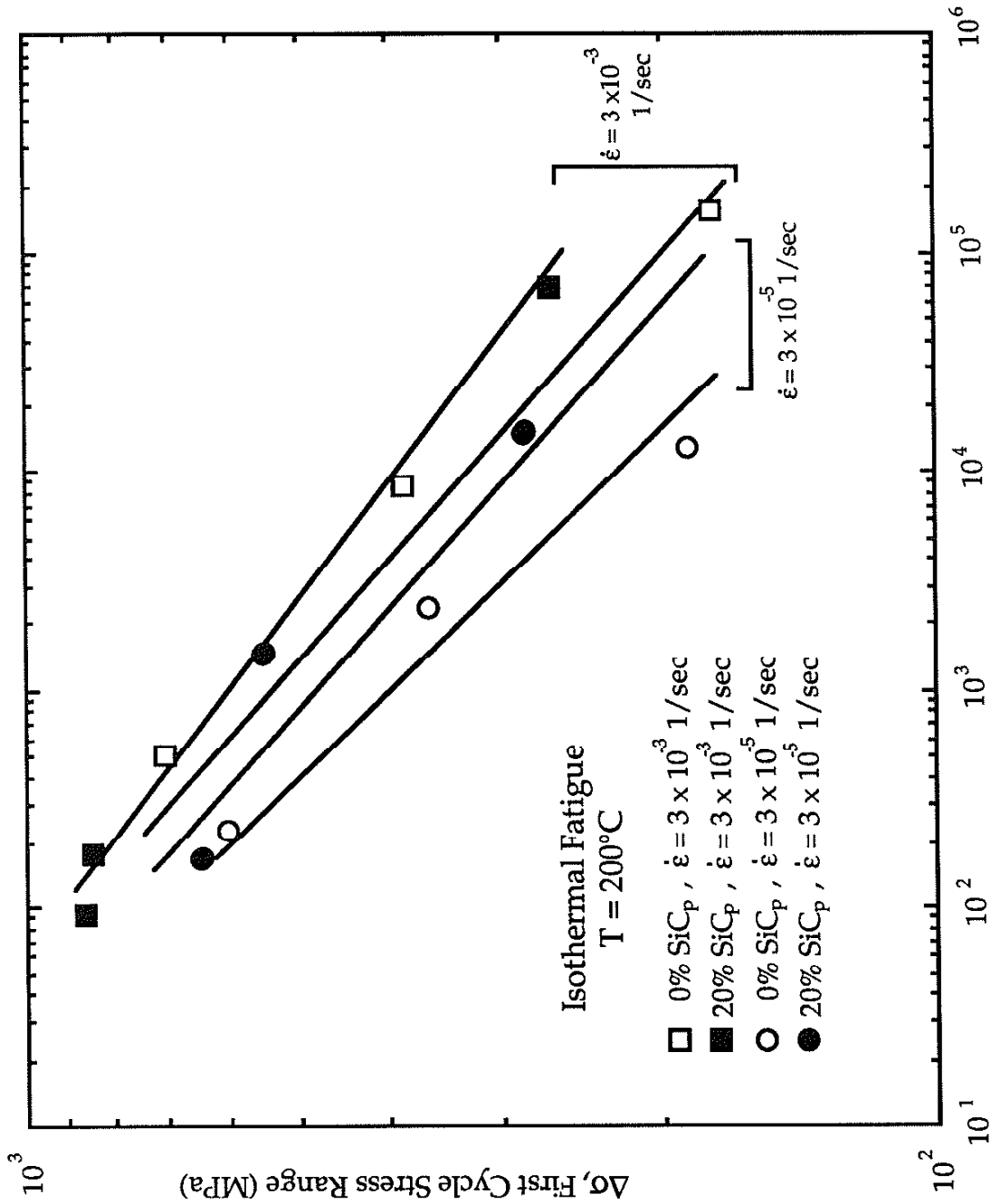


Figure 4.6: Mechanical stress range-cycles to failure data for isothermal fatigue of unreinforced and 20% SiC_p reinforced Al 2xxx-T4 at 200°C

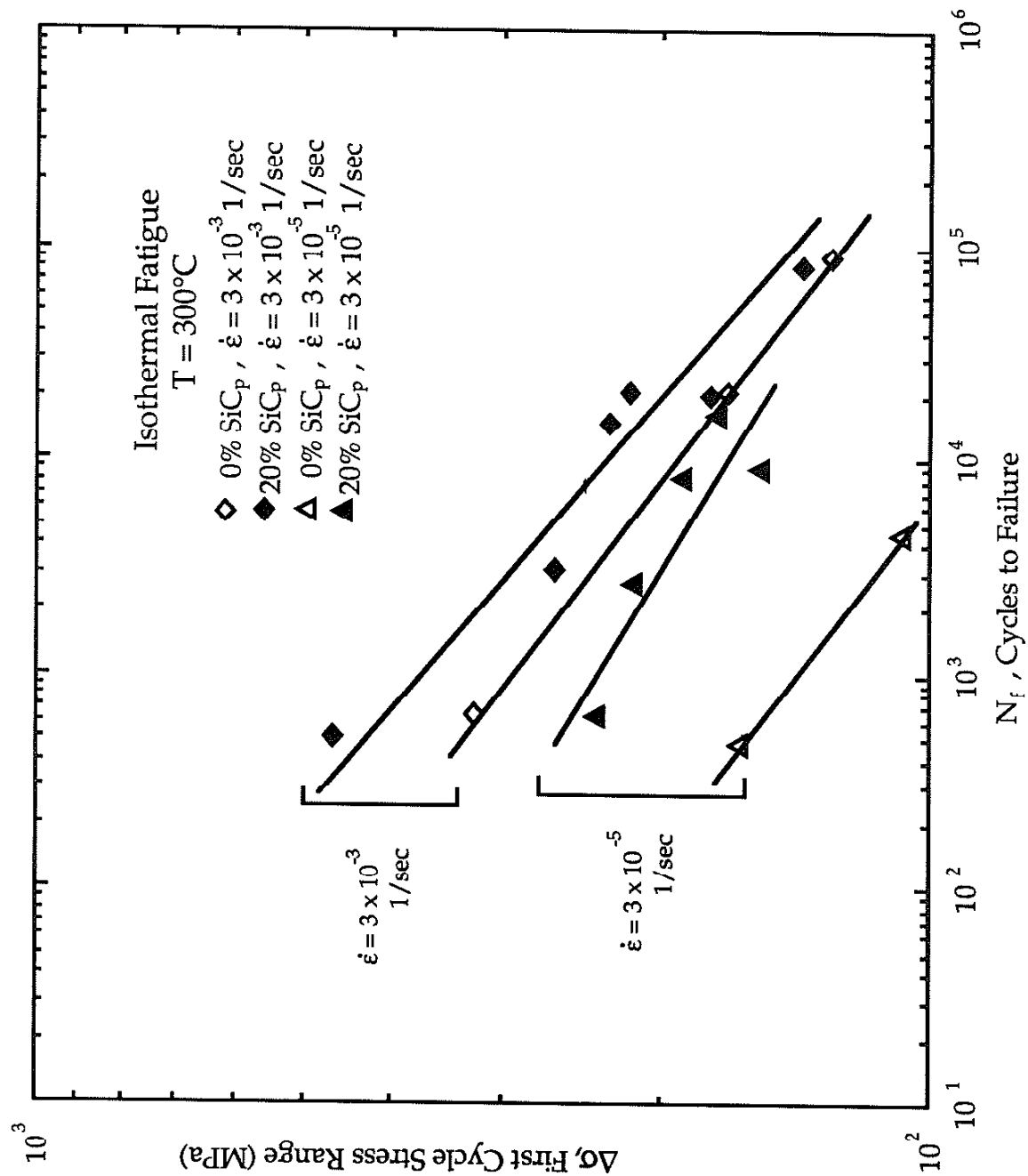


Figure 4.7: Mechanical stress range-cycles to failure data for isothermal fatigue of unreinforced and 20% SiC_p reinforced Al 2xxx-T4 at 300°C

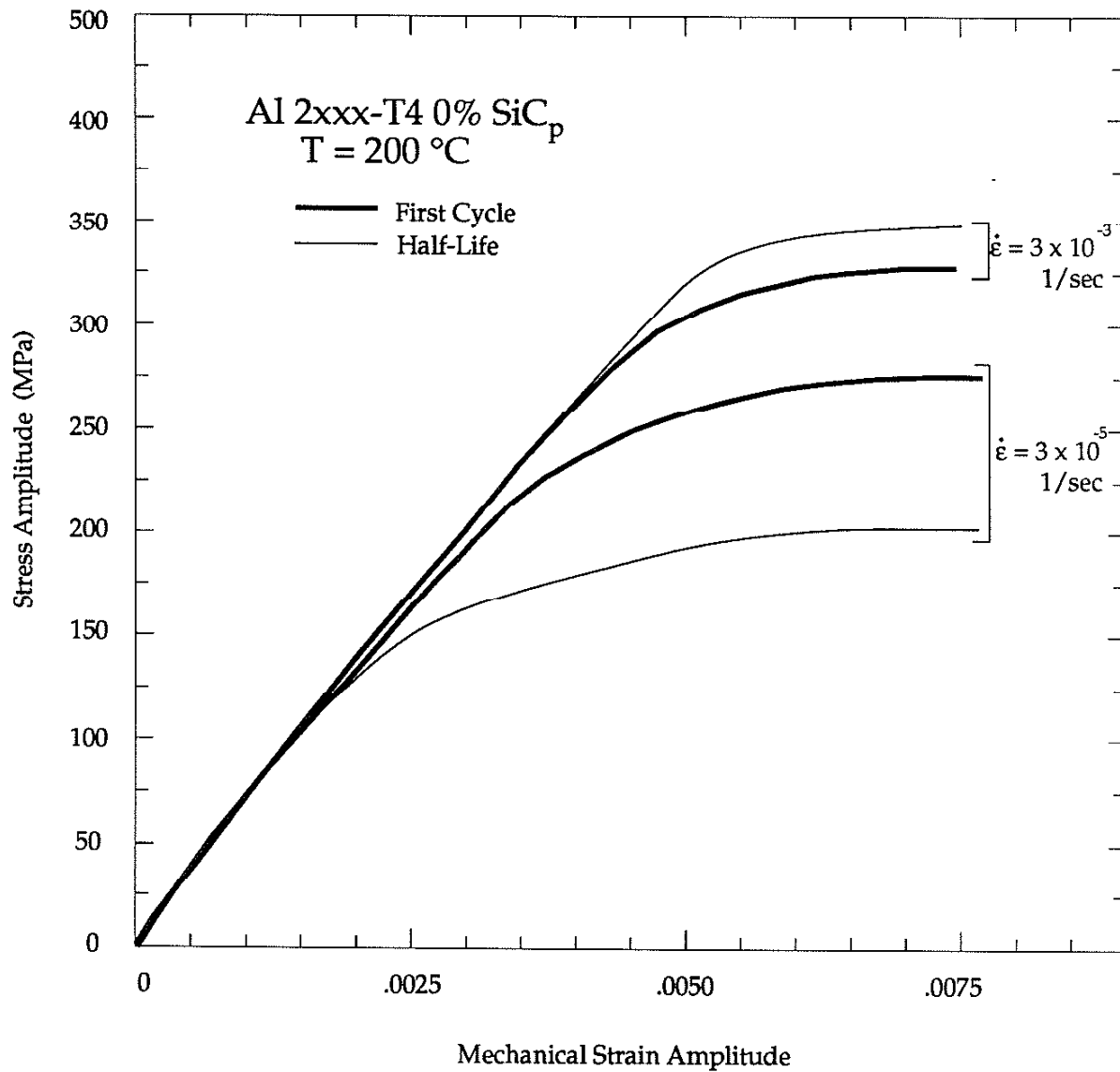


Figure 4.8: Stress amplitude versus mechanical strain; unreinforced material, 200 °C

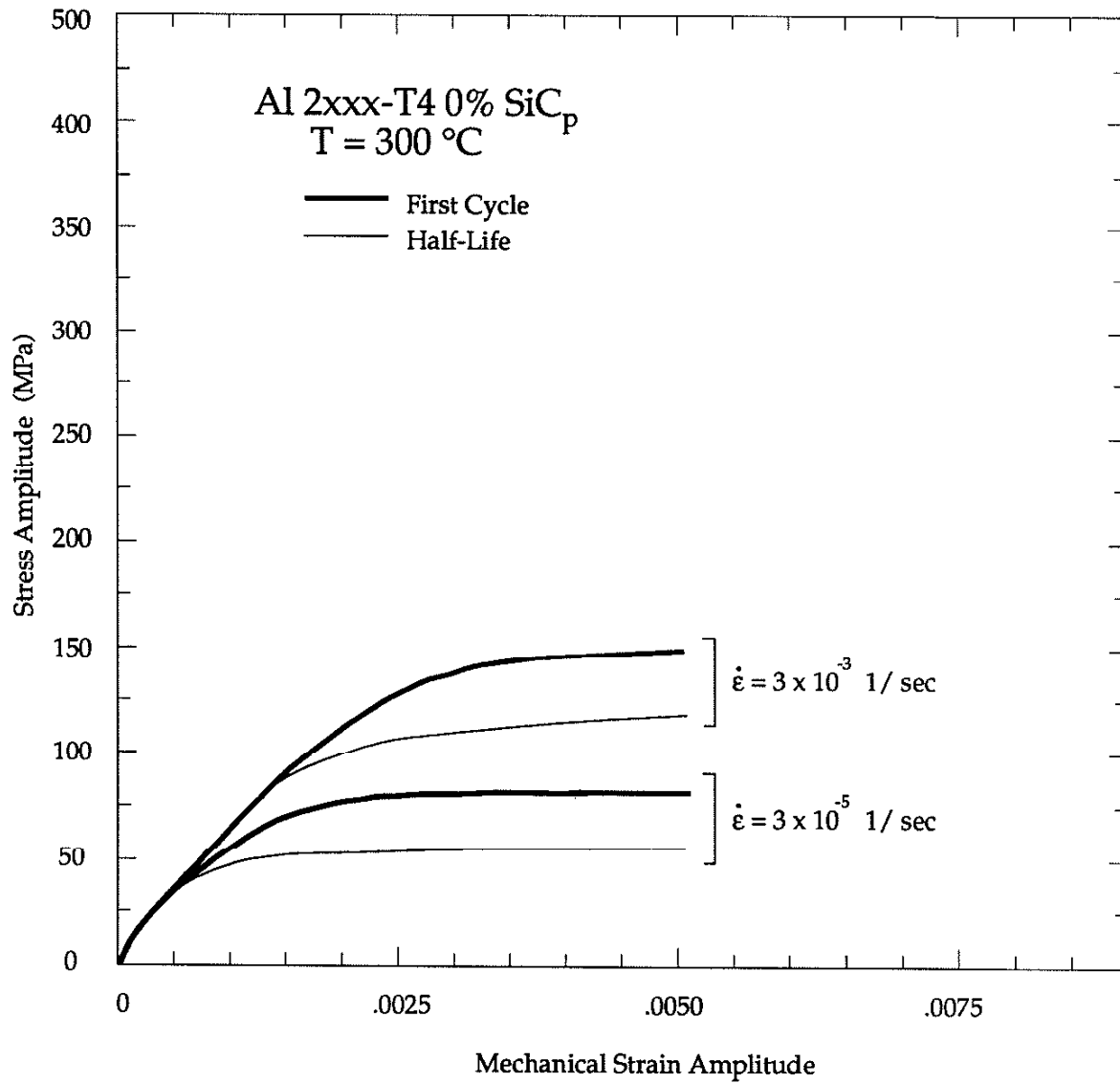


Figure 4.9: Stress amplitude versus mechanical strain; unreinforced material, 300 °C

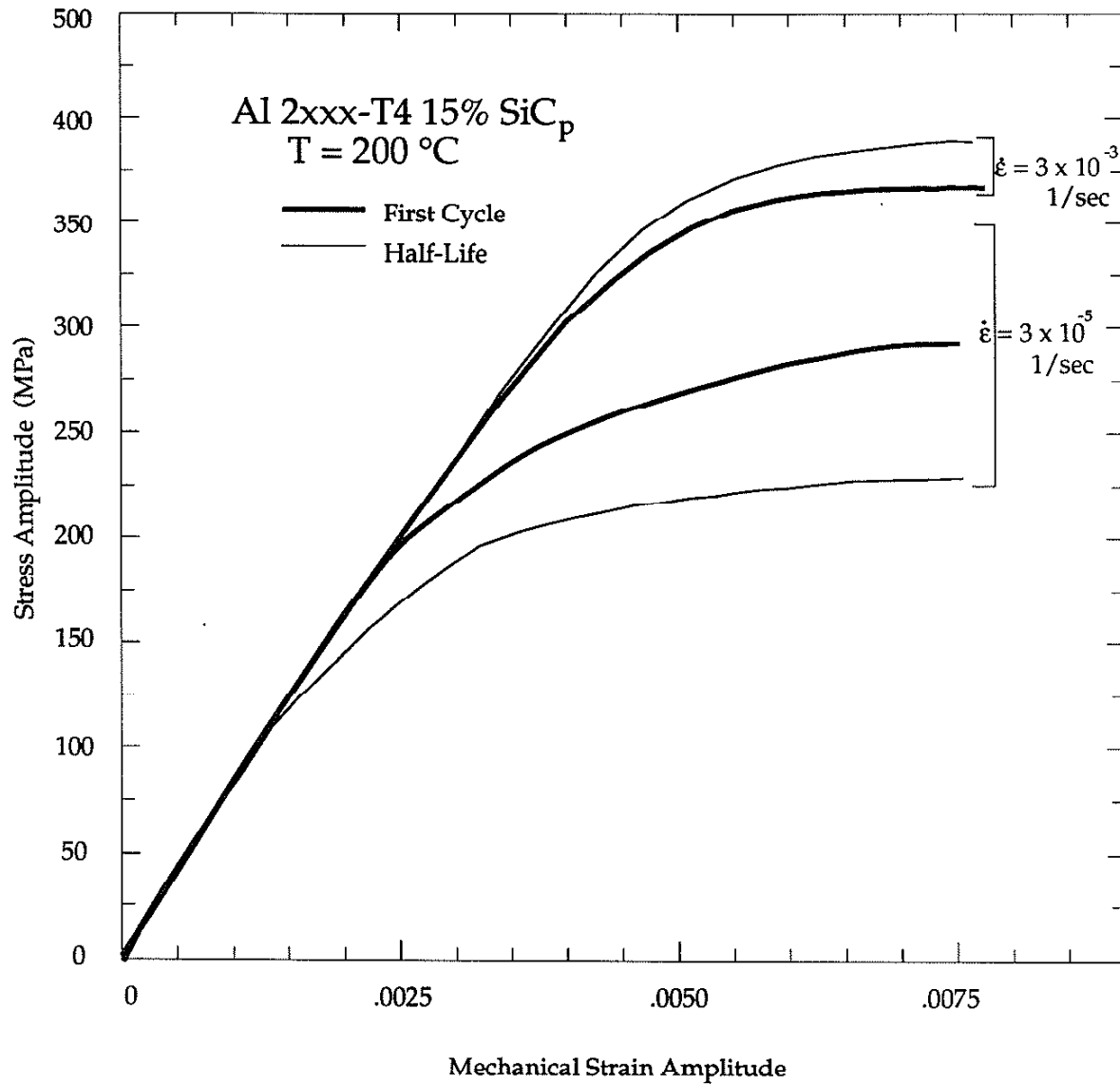


Figure 4.10: Stress amplitude versus mechanical strain; 15% reinforced material, 200 °C

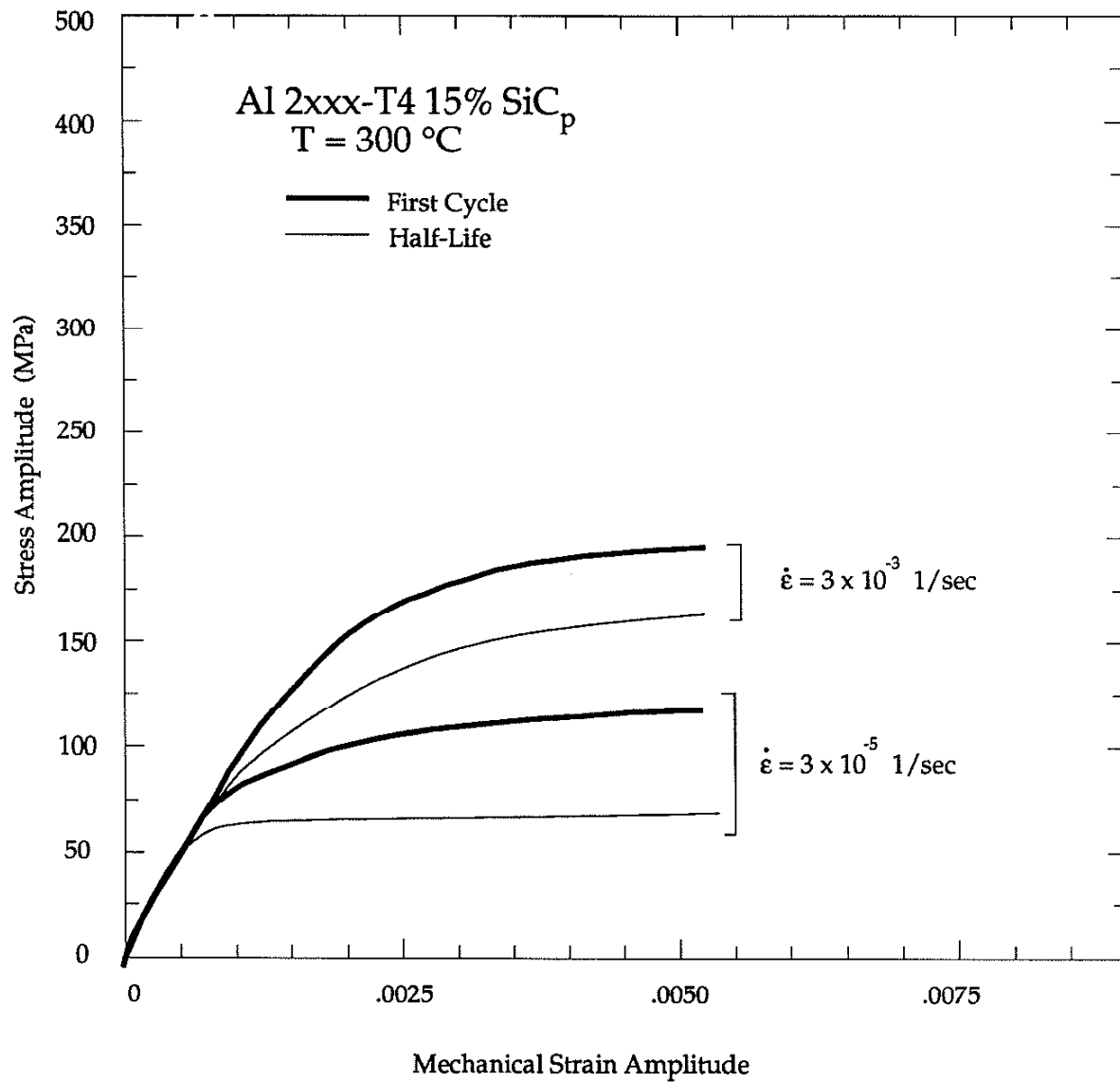


Figure 4.11: Stress amplitude versus mechanical strain; 15% reinforced material, 300 °C

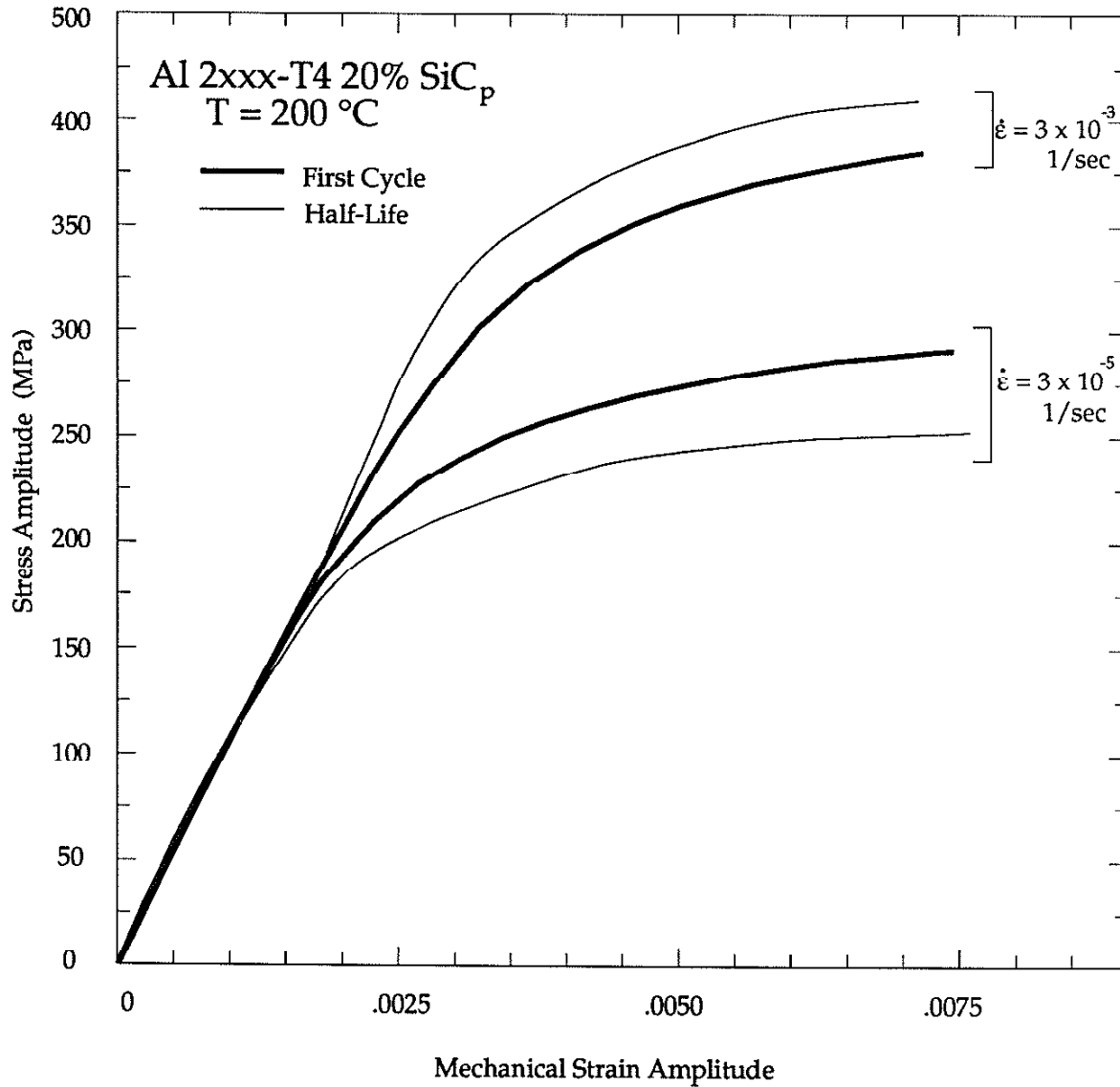


Figure 4.12: Stress amplitude versus mechanical strain; 20% reinforced material, 200 °C

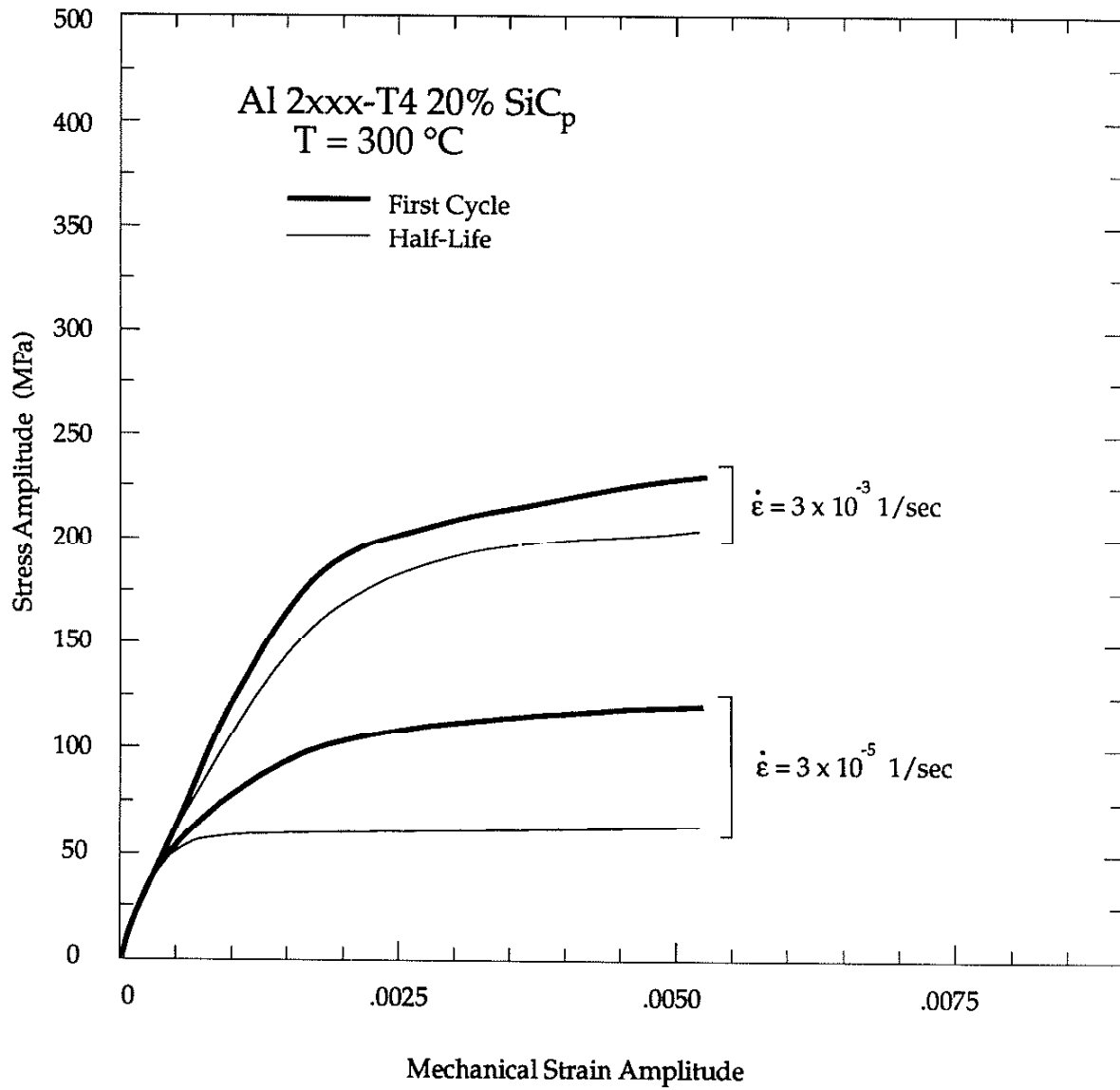


Figure 4.13: Stress amplitude versus mechanical strain; 20% reinforced material, 300 °C

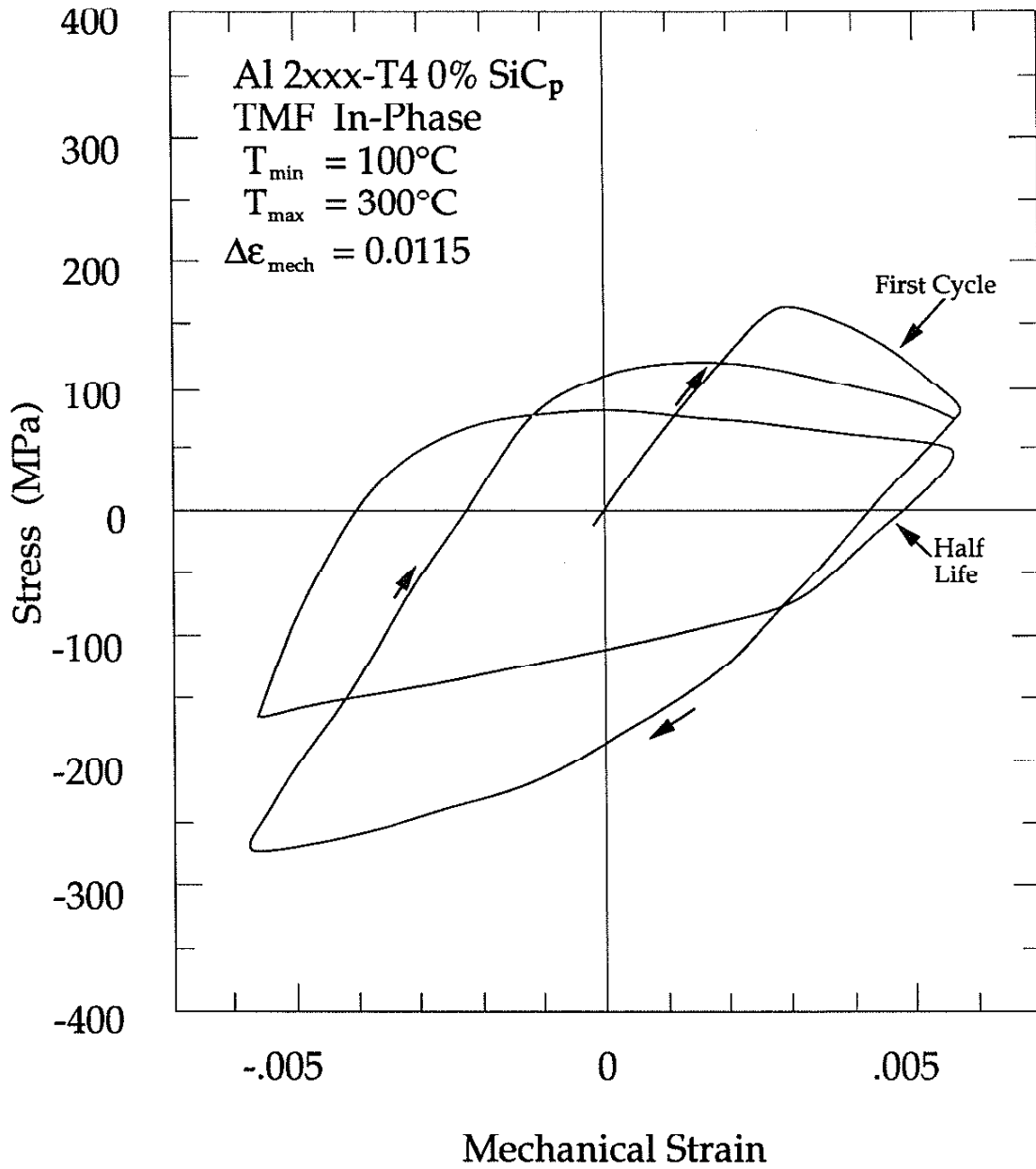


Figure 4.14: Stress versus mechanical strain; unreinforced material, TMF IP 100°C-300°C

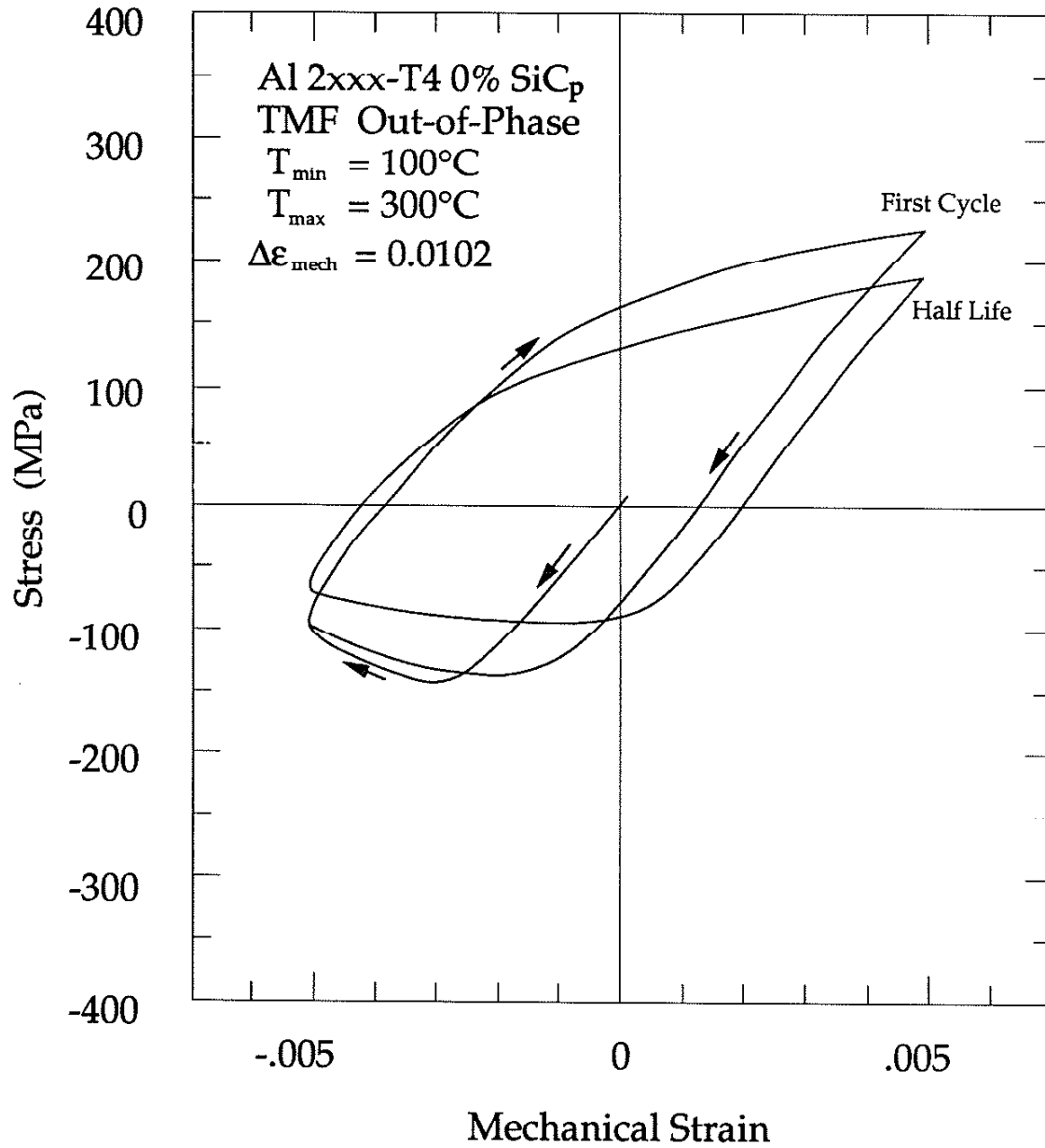


Figure 4.15: Stress versus mechanical strain; unreinforced material, TMF OP, 100°C-300°C

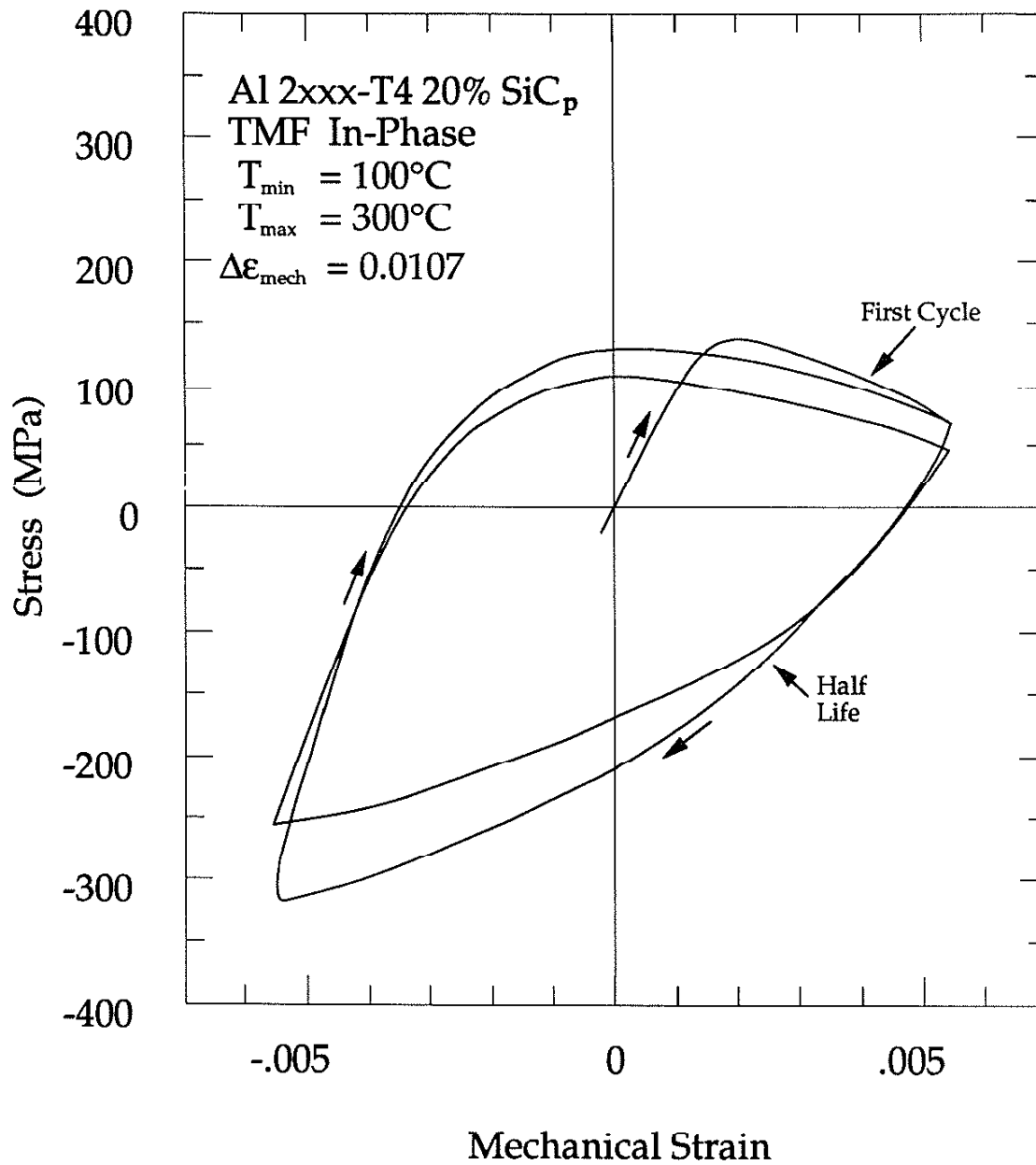


Figure 4.16: Stress versus mechanical strain; 20% reinforced material, TMF IP 100°C-300°C

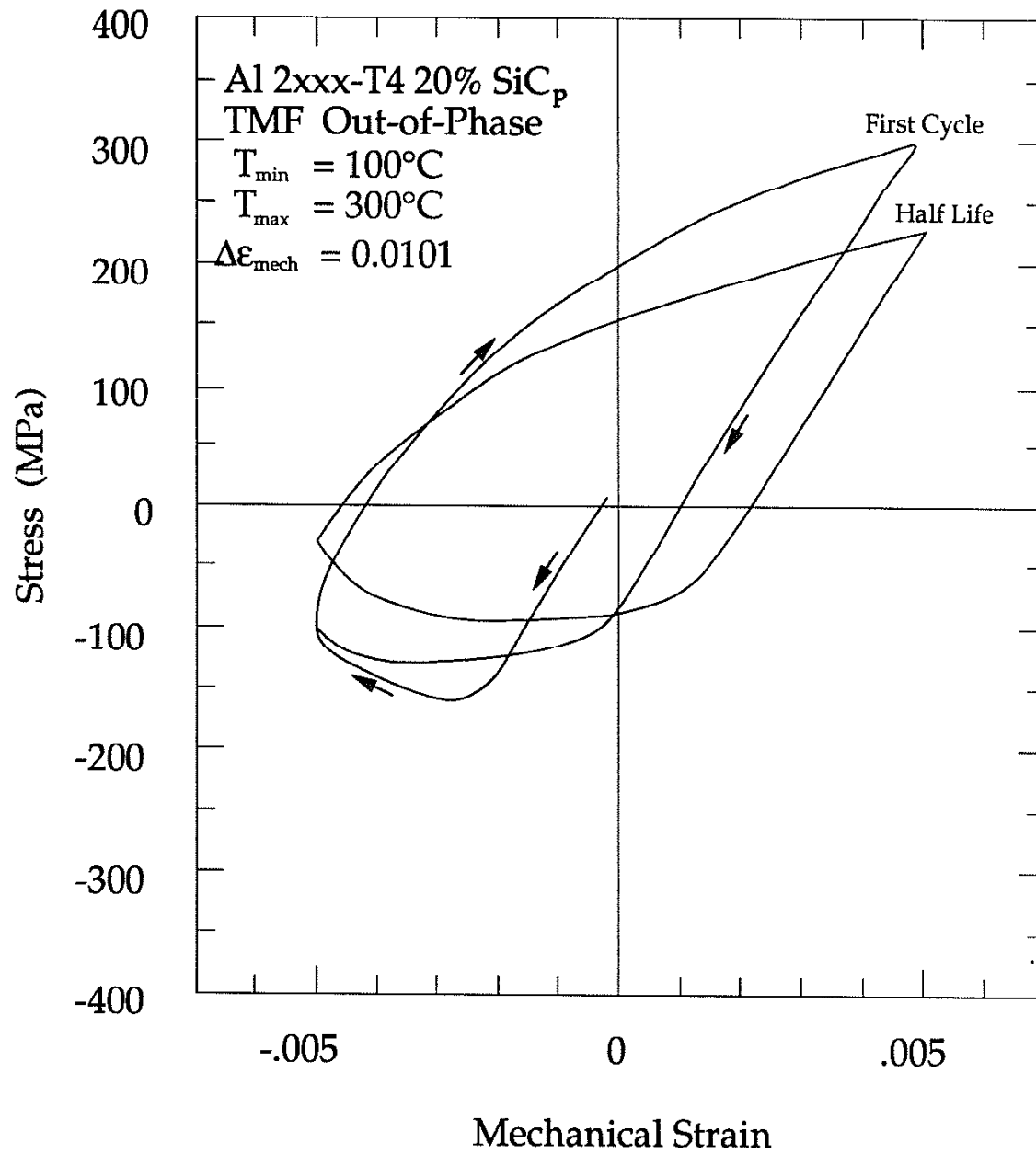


Figure 4.17: Stress versus mechanical strain; 20% reinforced material, TMF OP 100°C-300°C

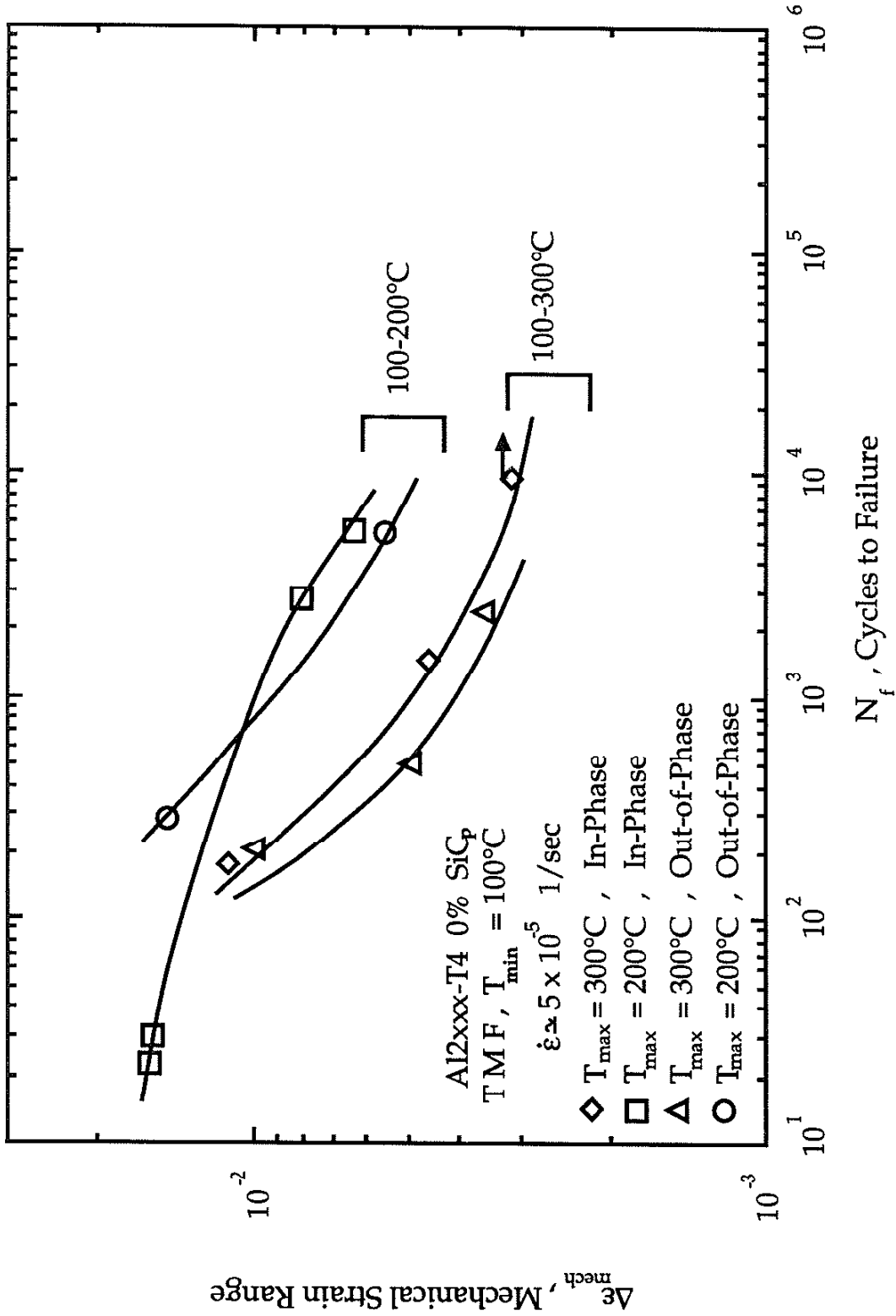
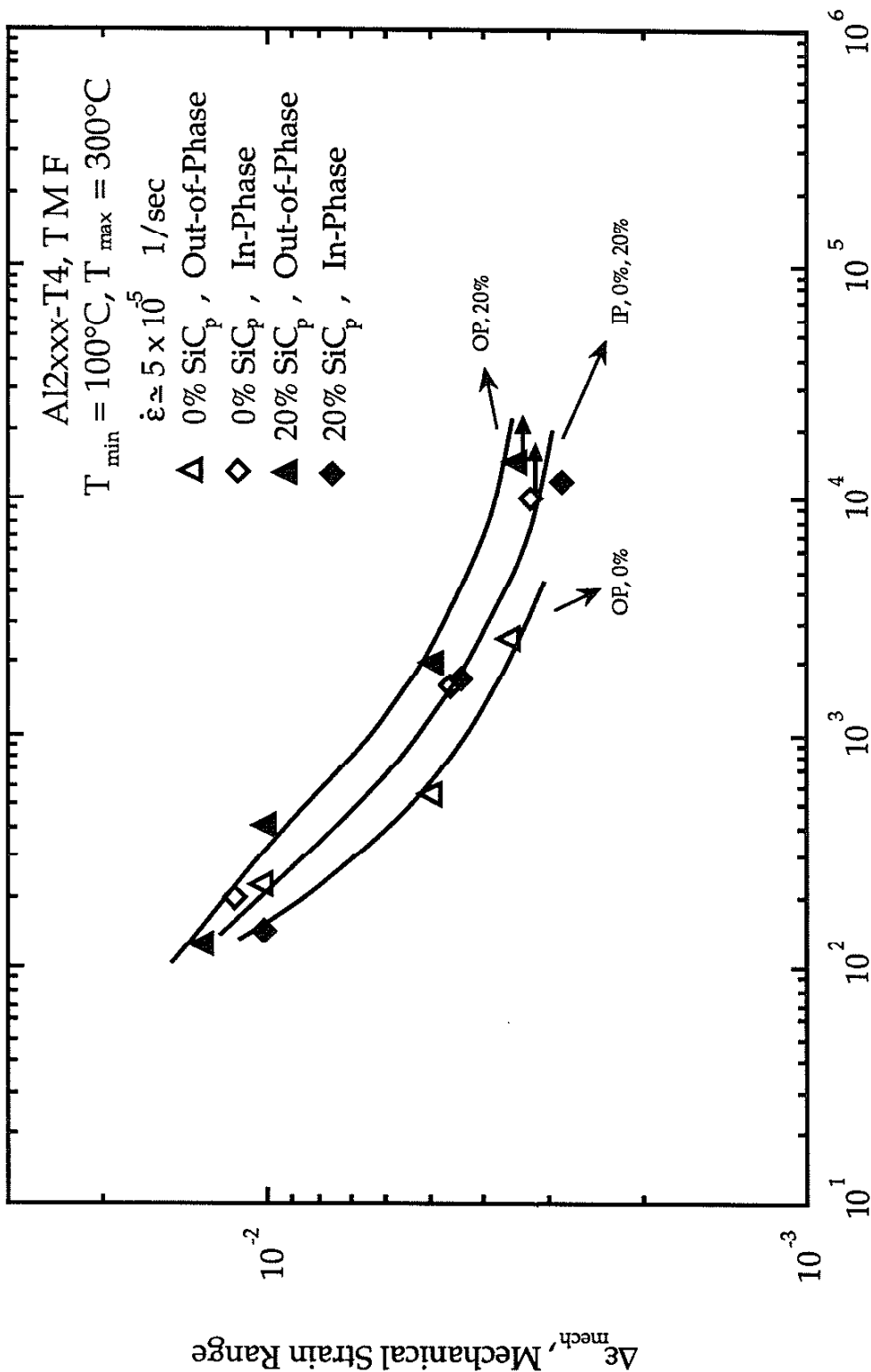


Figure 4.18: TMF IP and TMF OP; Mechanical strain range versus life of unreinforced material



N_f , Cycles to Failure

Figure 4.19: TMF IP and TMF OP; Mechanical strain range versus life of 0% and 20% reinforced materials



Figure 4.20: Crack initiation sites, 20% reinforced material, TMF IP, 100-300 °C

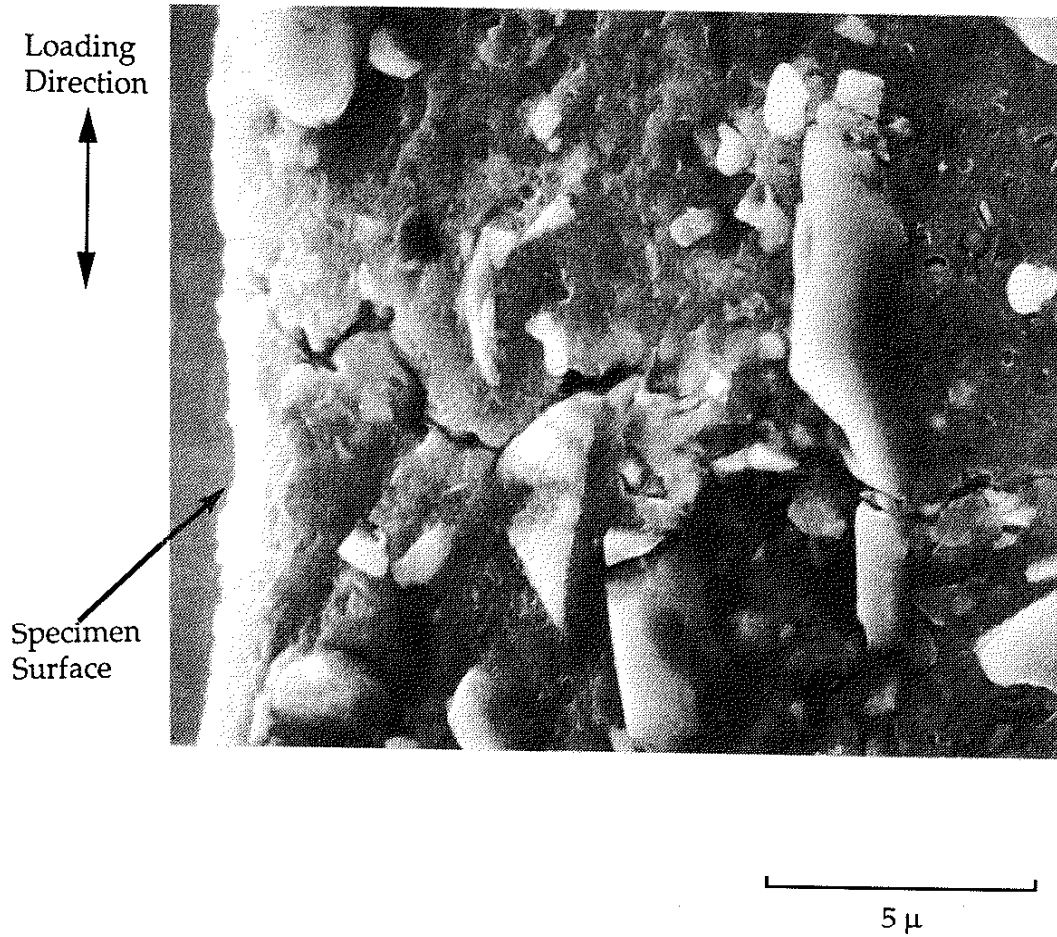


Figure 4.21: Crack initiation sites, 20% reinforced material, isothermal fatigue, 300 °C, $\dot{\epsilon} = 3.0 \times 10^{-5}$ 1/sec

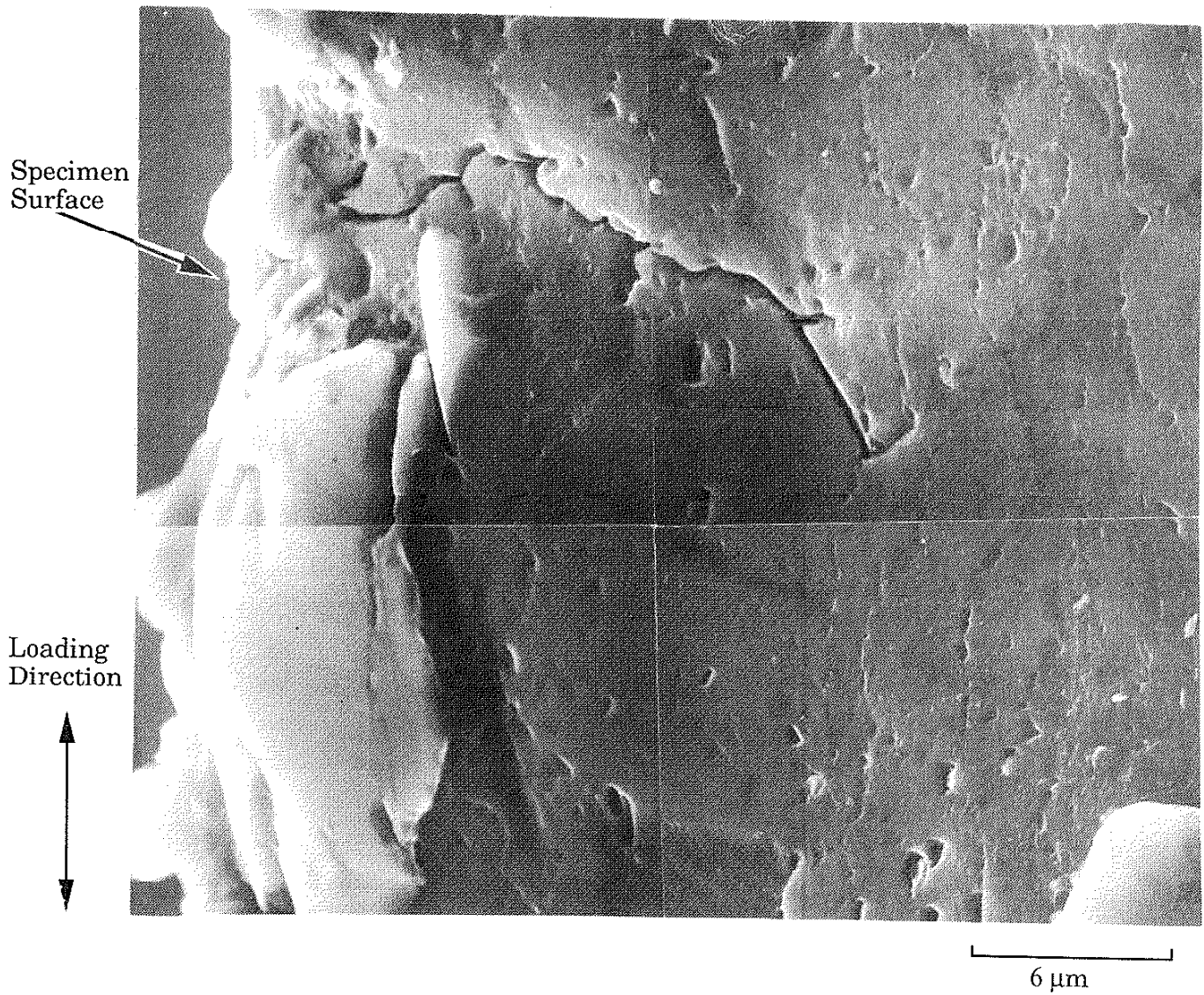


Figure 4.22: Crack initiation sites, 15% reinforced material, isothermal fatigue, 200 °C, $\dot{\epsilon} = 3.0 \times 10^{-3}$ 1/sec

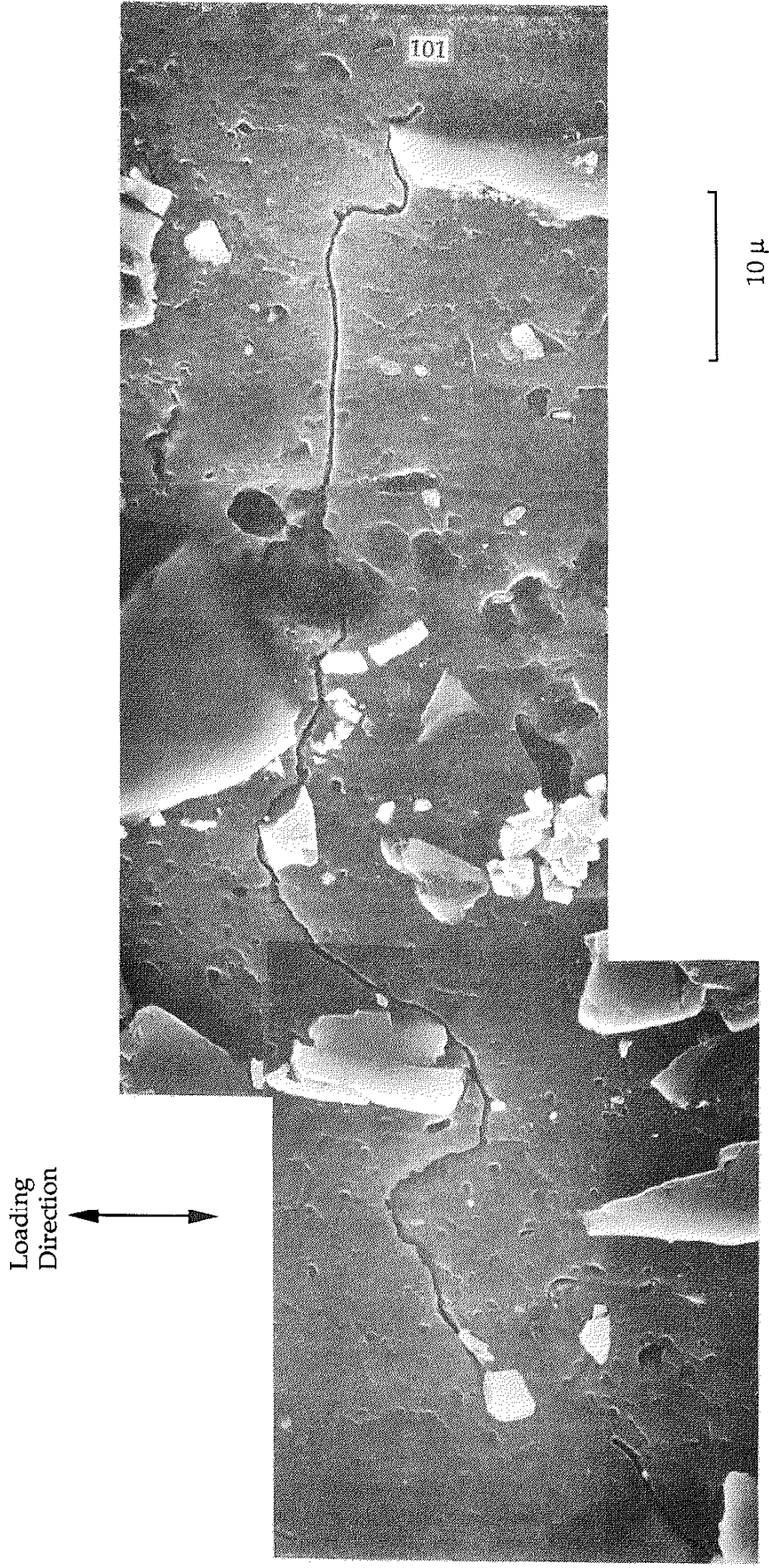


Figure 4.23: Transgranular and intergranular (mixed) crack growth, reinforced material, isothermal fatigue, 200 °C, $\dot{\epsilon} = 3.0 \times 10^{-3}$ 1/sec

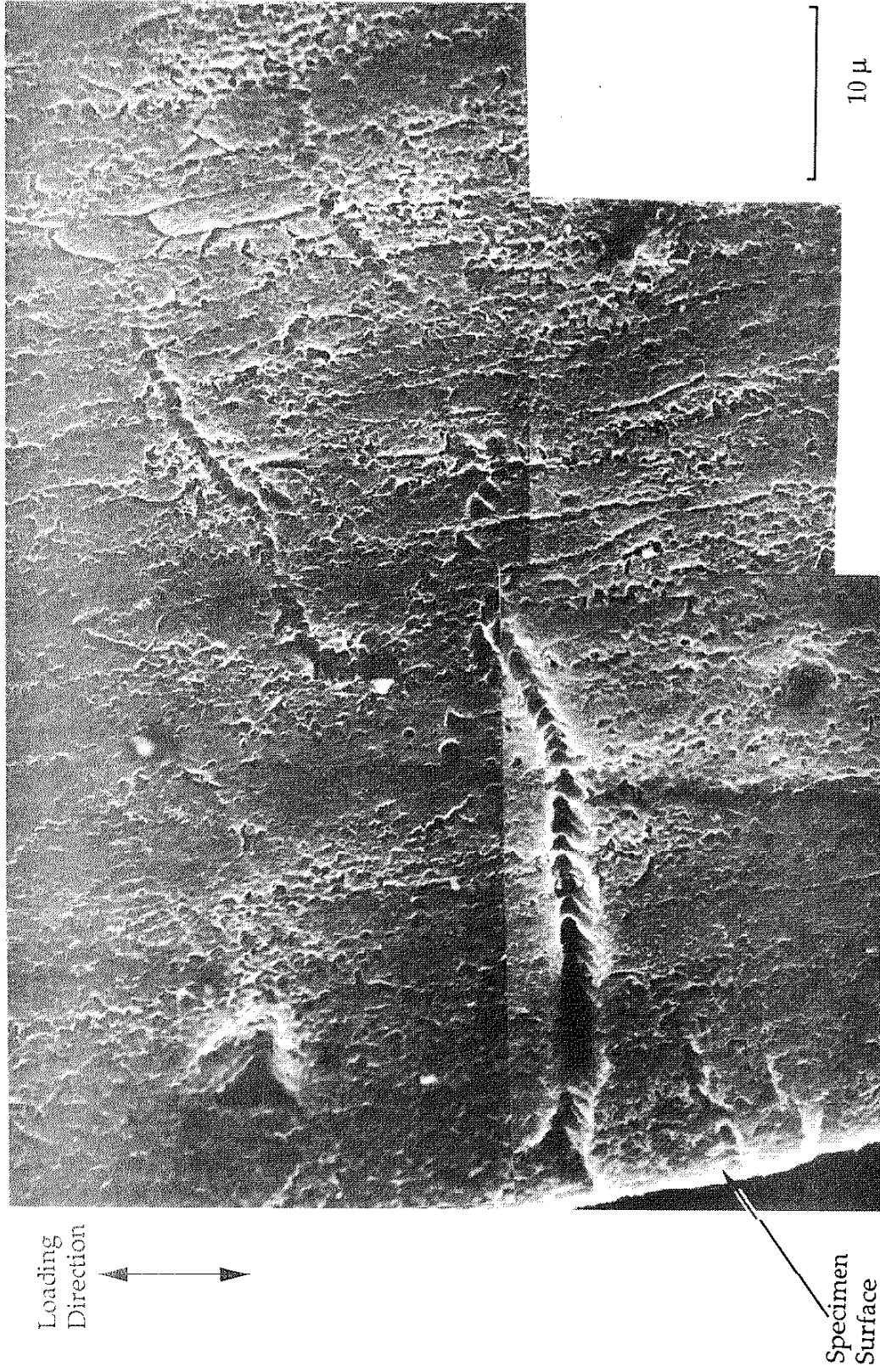


Figure 4.24: Transgranular crack growth in the unreinforced material, TMF OP 100-200 °C

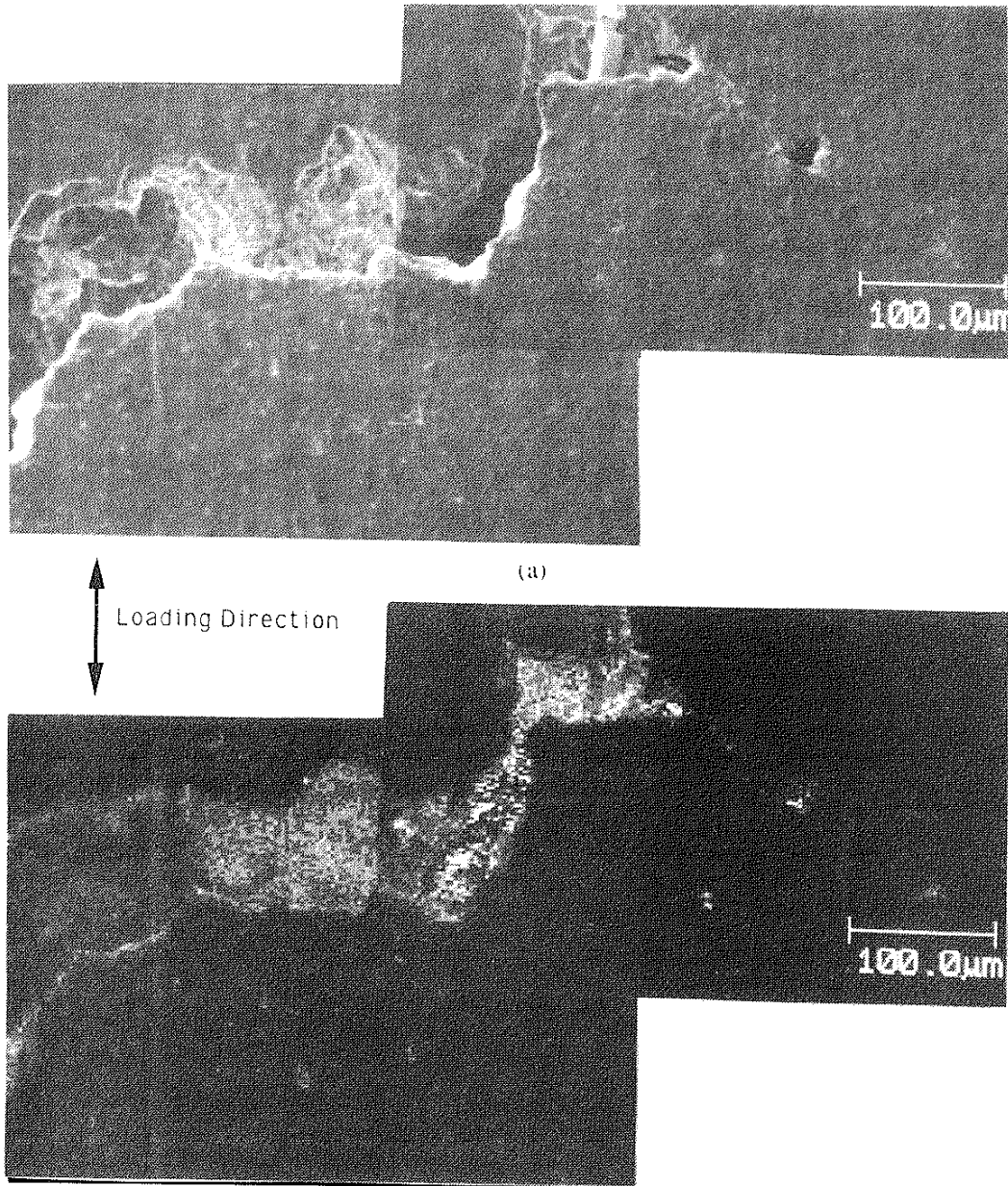


Figure 4.25: Auger electron spectroscopy analysis of crack tip, TMF OP 100-300 °C,
a) SEM photograph, b) Oxygen dot map

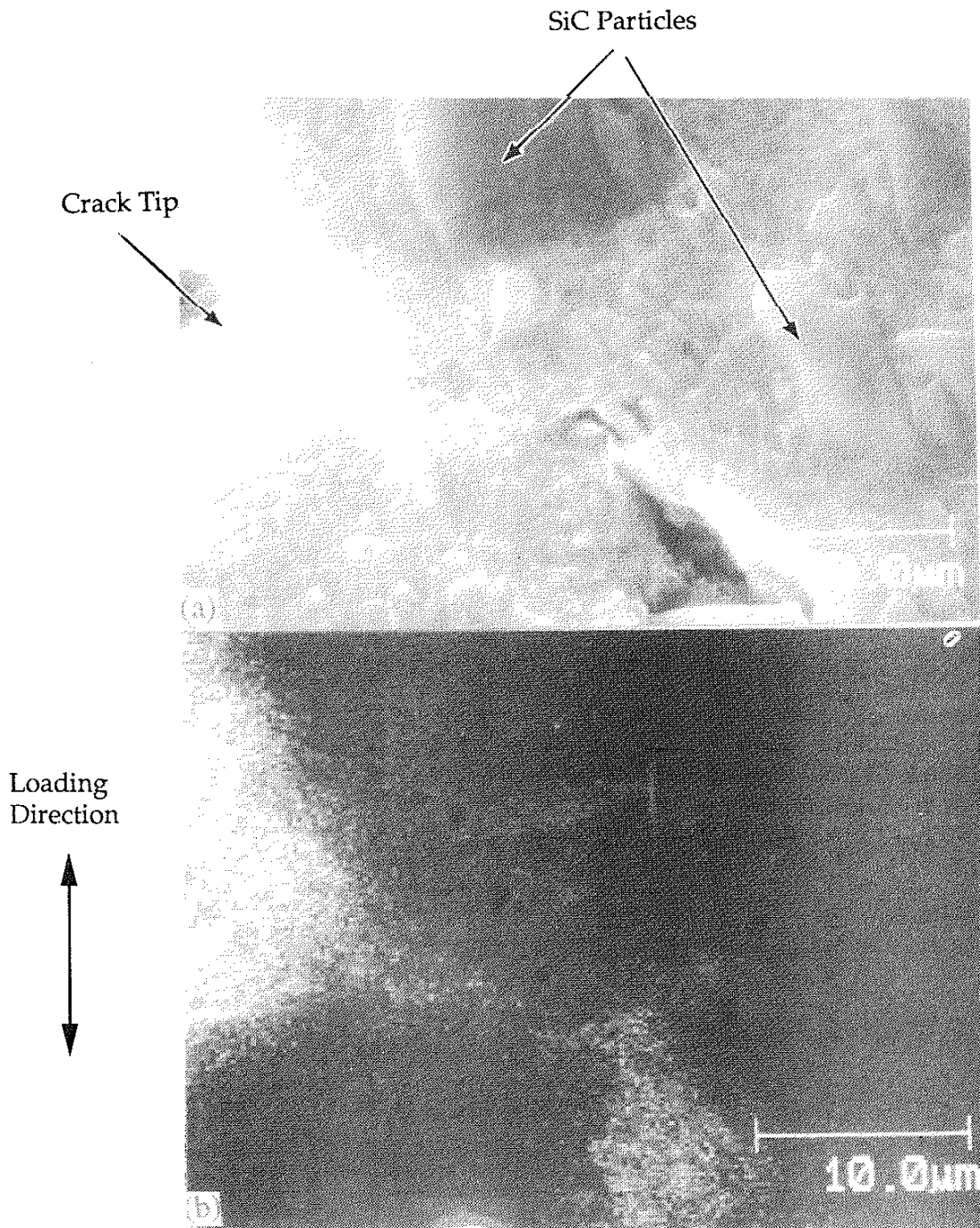


Figure 4.26: Auger electron spectroscopy analysis of crack tip, TMF OP 100-300 °C,
a) SEM photograph, b) Oxygen dot map

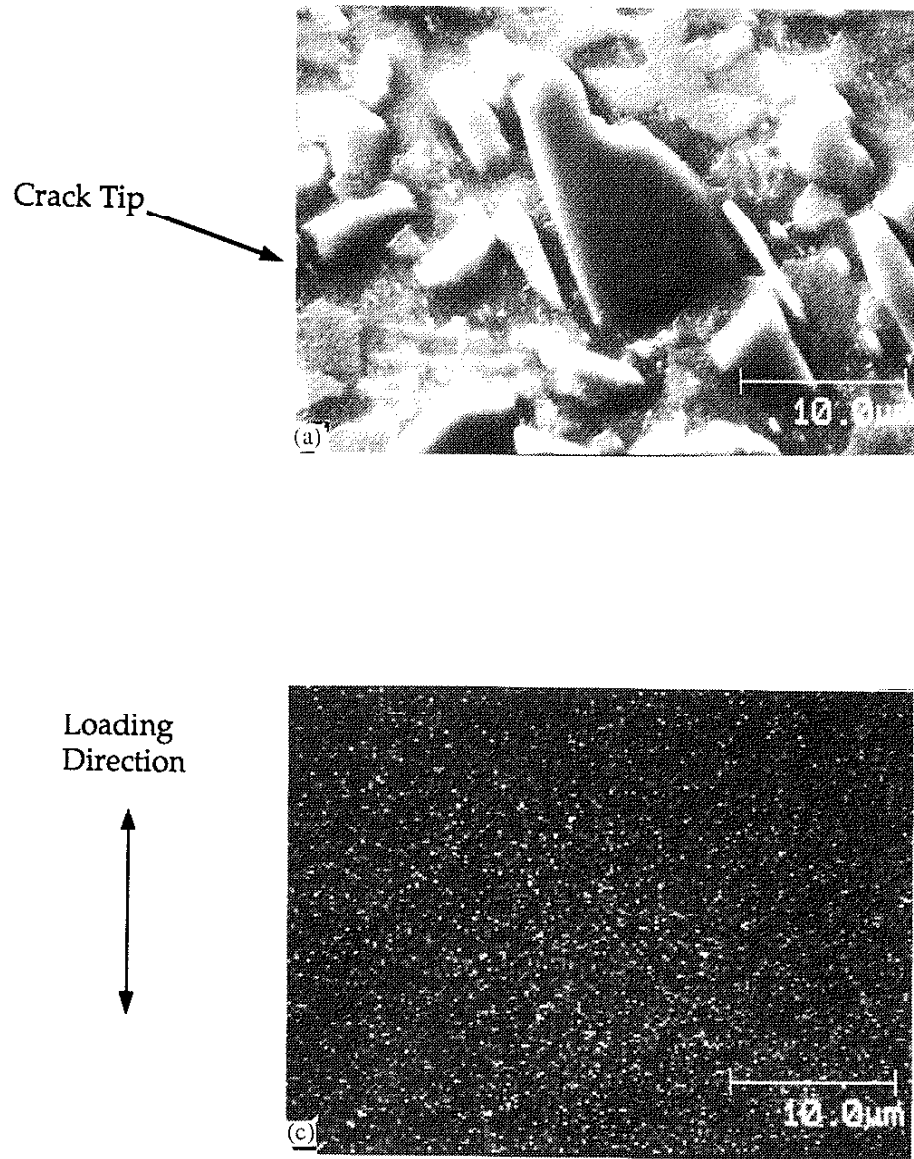


Figure 4.27: Auger electron spectroscopy analysis of crack tip, TMF IP 100-300 °C,
a) SEM photograph, b) Oxygen dot map

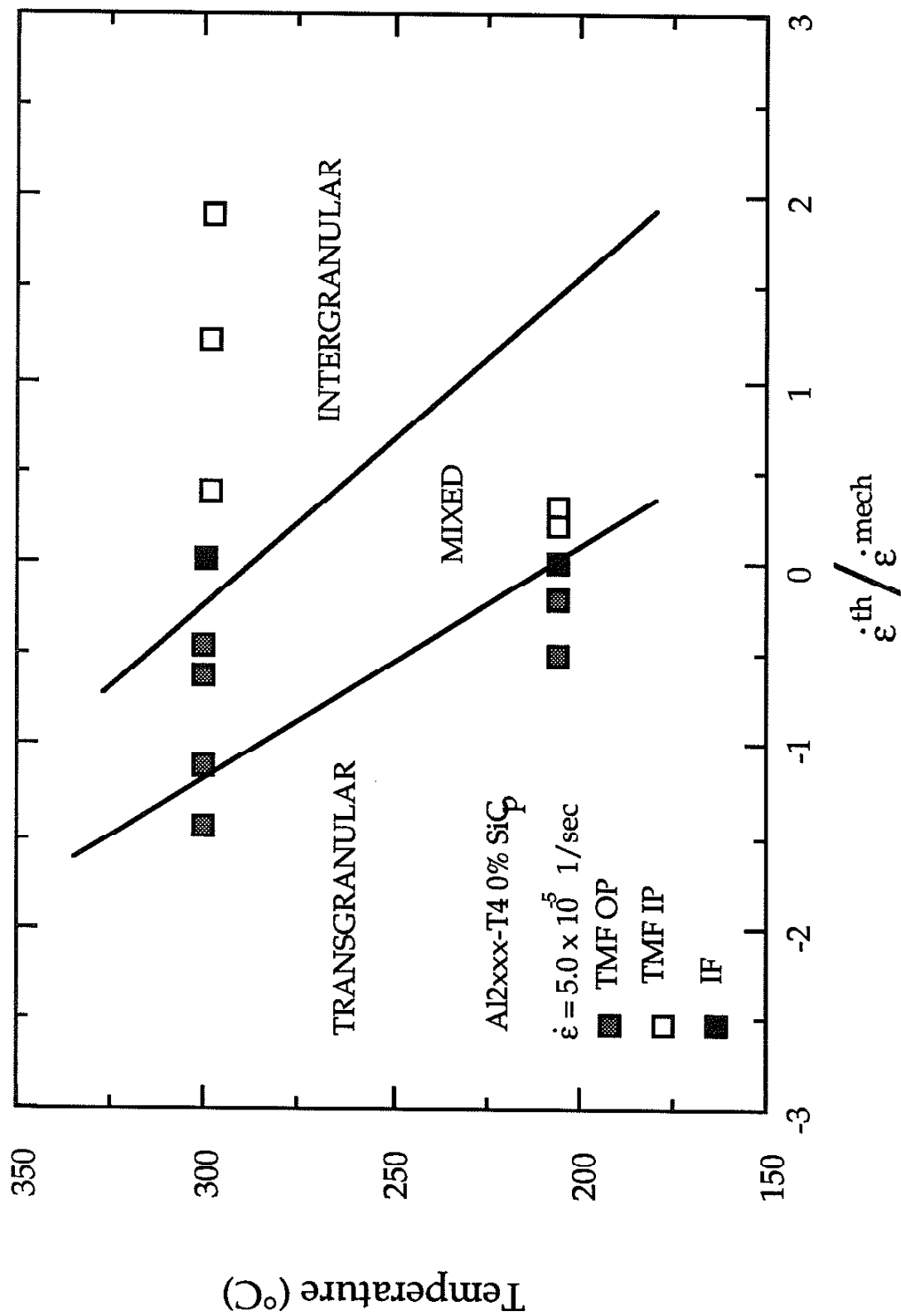


Figure 4.28: Crack growth map at $\dot{\epsilon} = 5.0 \times 10^{-5} \text{ 1/sec}$, unreinforced material

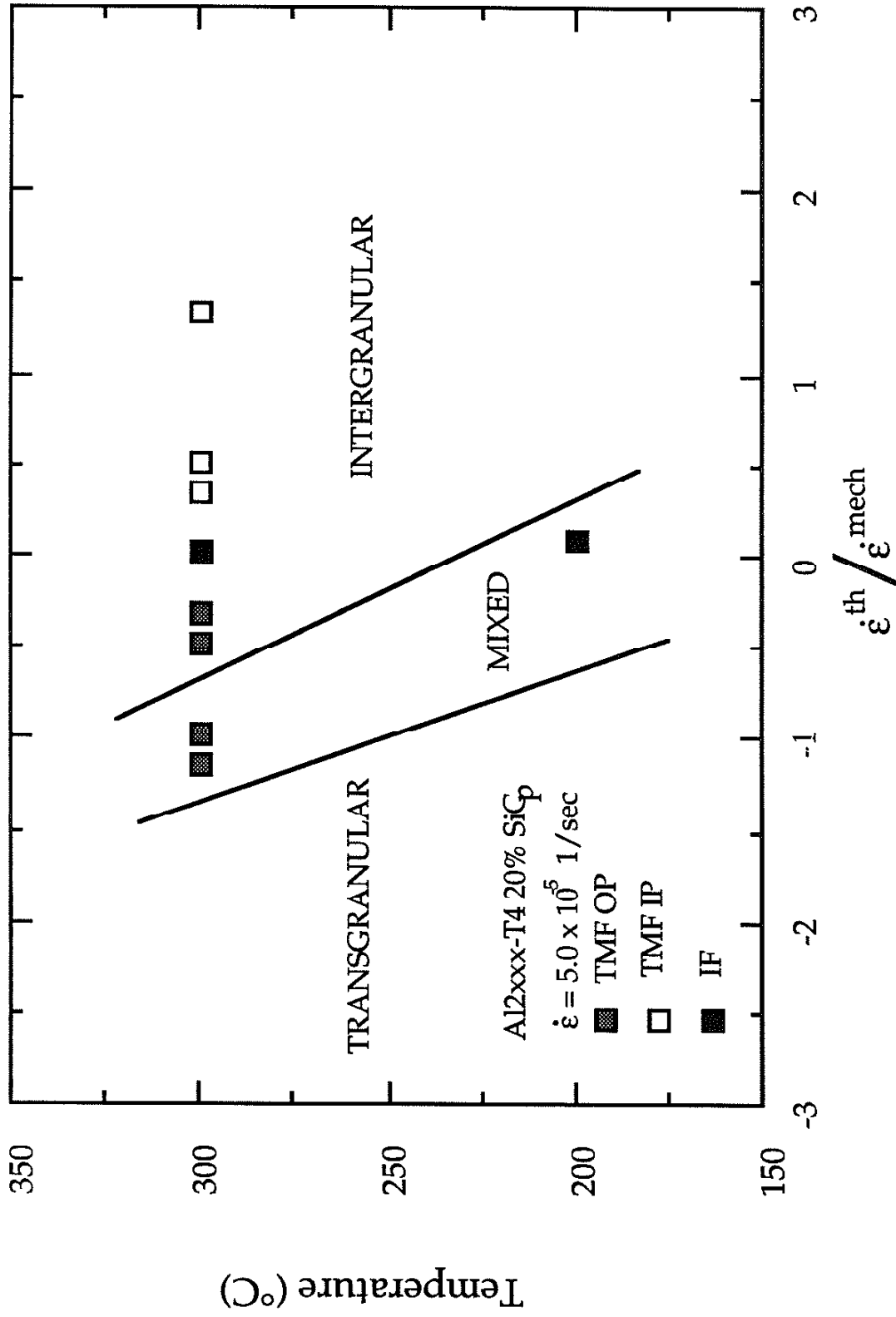


Figure 4.29: Crack growth map at $\dot{\epsilon} = 5.0 \times 10^5 \text{ 1/sec}$, reinforced material

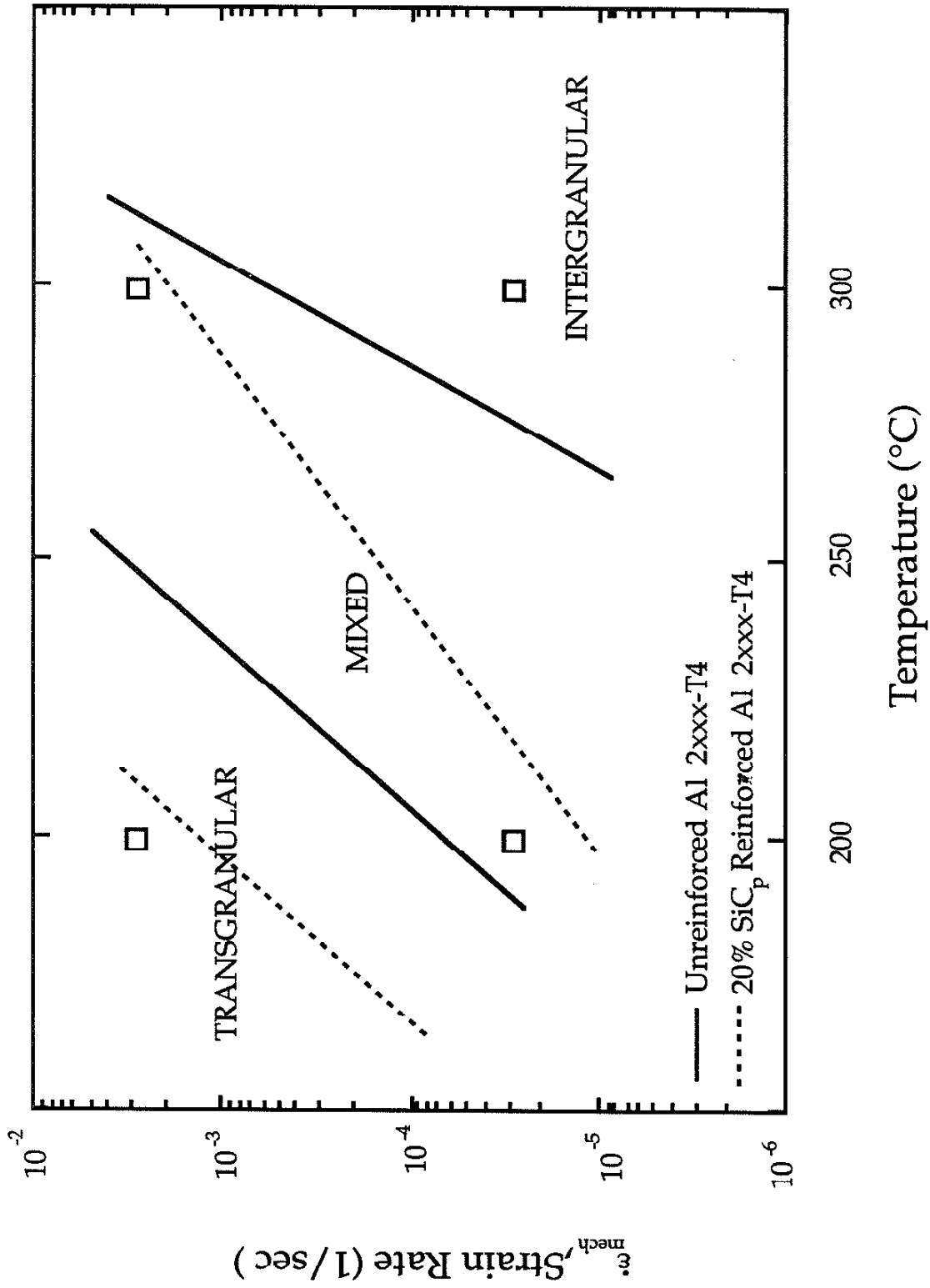


Figure 4.30: Crack growth map of reinforced and unreinforced materials

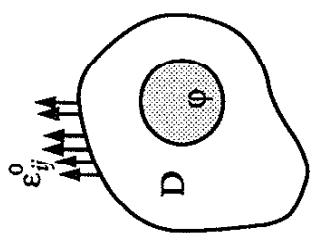
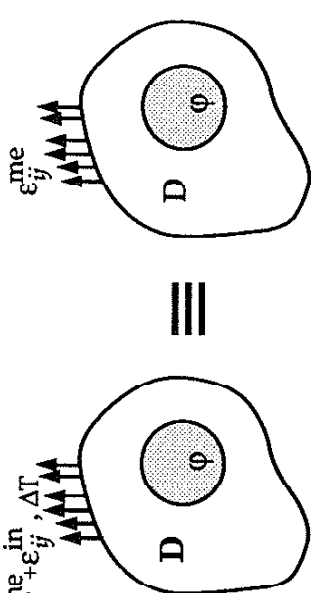
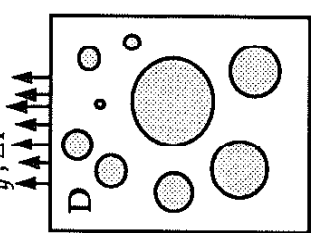
a) Eshelby's Equivalent Inclusion Model	b) Single Inclusion in Infinite Elastic-Plastic Matrix Under Thermomechanical Loading	c) Eshelby's Modified Equivalent Inclusion Model
		
<p>MATRIX</p>	<p>MATRIX</p>	<p>MATRIX</p>
<p>REINFORCEMENT</p>	<p>REINFORCEMENT</p>	<p>REINFORCEMENT</p>
<p>Net Strain $\epsilon_{ij}^m = \epsilon_{ij}^0$</p>	<p>Net Strain $\epsilon_{ij}^{me} + \epsilon_{ij}^{in} + \theta_{ij}^m \Delta T$</p>	<p>Net Strain $\epsilon_{ij}^{ce} + \epsilon_{ij}^m$</p>
<p>Eigen strain $\epsilon_{ij}^{pm} = 0$</p>	<p>Eigen strain $\epsilon_{ij}^{in} + \theta_{ij}^m \Delta T$</p>	<p>Eigen strain 0</p>
<p>Stress $\sigma_{ij}^m = C_{ijkl}^m \epsilon_{kl}^0$</p>	<p>Stress $C_{ijkl}^m \epsilon_{kl}^{me}$</p>	<p>Stress $C_{ijkl}^m (\epsilon_{kl}^{ce} + \epsilon_{kl}^m)$</p>
<p>Net Strain $\epsilon_{ij}^r = \epsilon_{ij}^0 + \epsilon_{ij}^{cn}$</p>	<p>Net Strain $\epsilon_{ij}^{me} + \epsilon_{ij}^{in} + \theta_{ij}^m \Delta T$</p>	<p>Net Strain $\epsilon_{ij}^{ce} + \epsilon_{ij}^r$</p>
<p>Eigen strain $\epsilon_{ij}^{pr} = 0$</p>	<p>Eigen strain $\theta_{ij}^m \Delta T$</p>	<p>Eigen strain $(\theta_{ij}^r - \theta_{ij}^m) \Delta T - \epsilon_{ij}^{in}$</p>
<p>Stress $\sigma_{ij}^r = C_{ijkl}^r (\epsilon_{kl}^0 + \epsilon_{kl}^{cn})$</p>	<p>Stress $C_{ijkl}^r (\epsilon_{kl}^{me} + \epsilon_{kl}^{in} + \theta_{kl}^m \Delta T - \epsilon_{kl}^{pr})$</p>	<p>Stress $C_{ijkl}^r (\epsilon_{kl}^{ce} + \epsilon_{kl}^r)$</p>
<p>Transf. strain $\epsilon_{ij}^{**} = \epsilon_{ij}^*$</p>	<p>Transf. strain $\epsilon_{ij}^* + \theta_{ij}^r \Delta T$</p>	<p>Transf. strain $\epsilon_{ij}^* - \epsilon_{ij}^{in} - (\theta_{ij}^m - \theta_{ij}^r) \Delta T$</p>

Figure 5.1: Schematic illustration of Eshelby's model modified to handle thermal and mechanical mismatch under thermo-mechanical deformations. a) Eshelby's equivalent inclusion model, b) Thermomechanical loading of a single inclusion in infinite elastic-plastic matrix, c) Eshelby's equivalent inclusion model modified for finite volume fraction of reinforcement

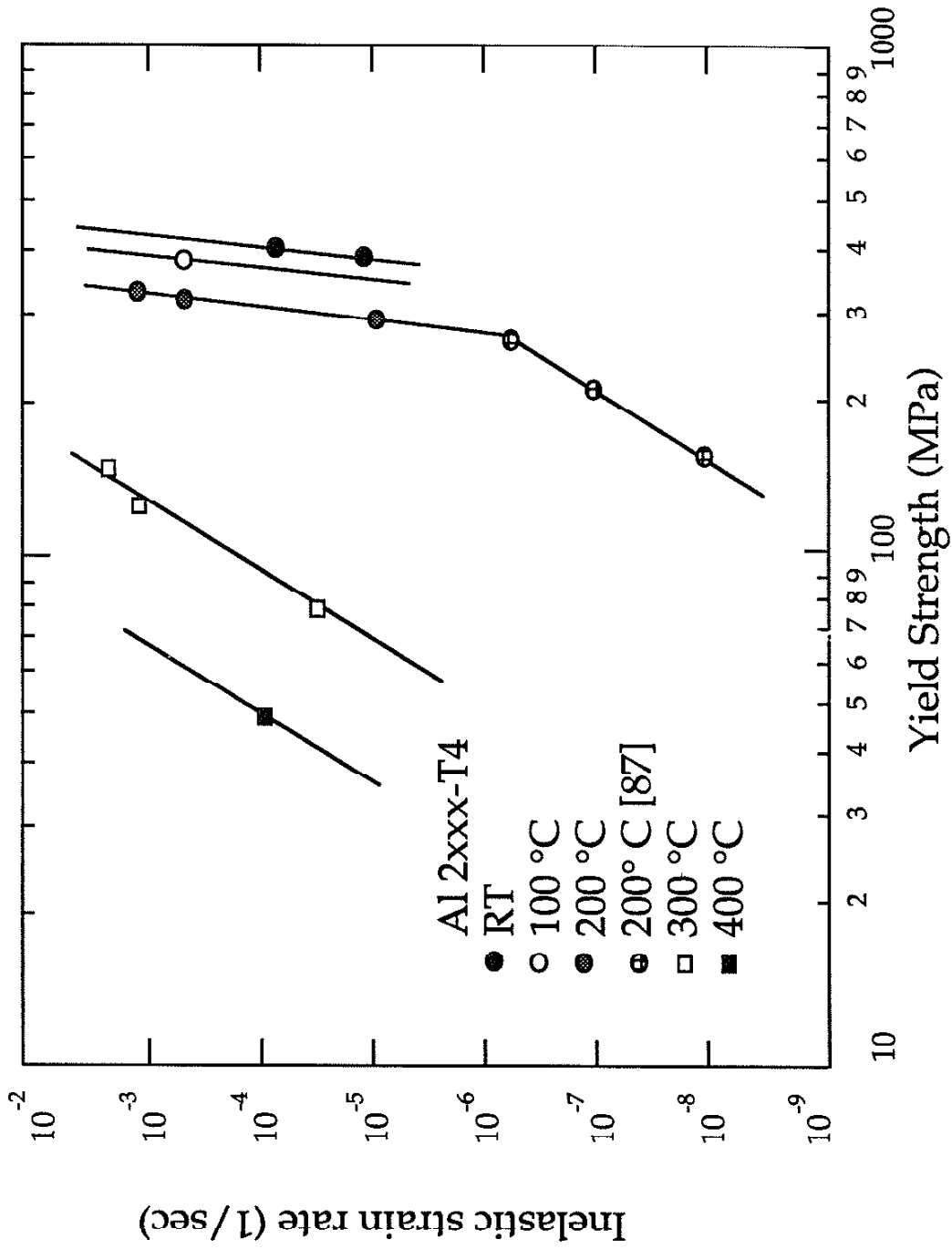


Figure 5.2: Inelastic strain rate versus yield strength for Al2xxx-T4

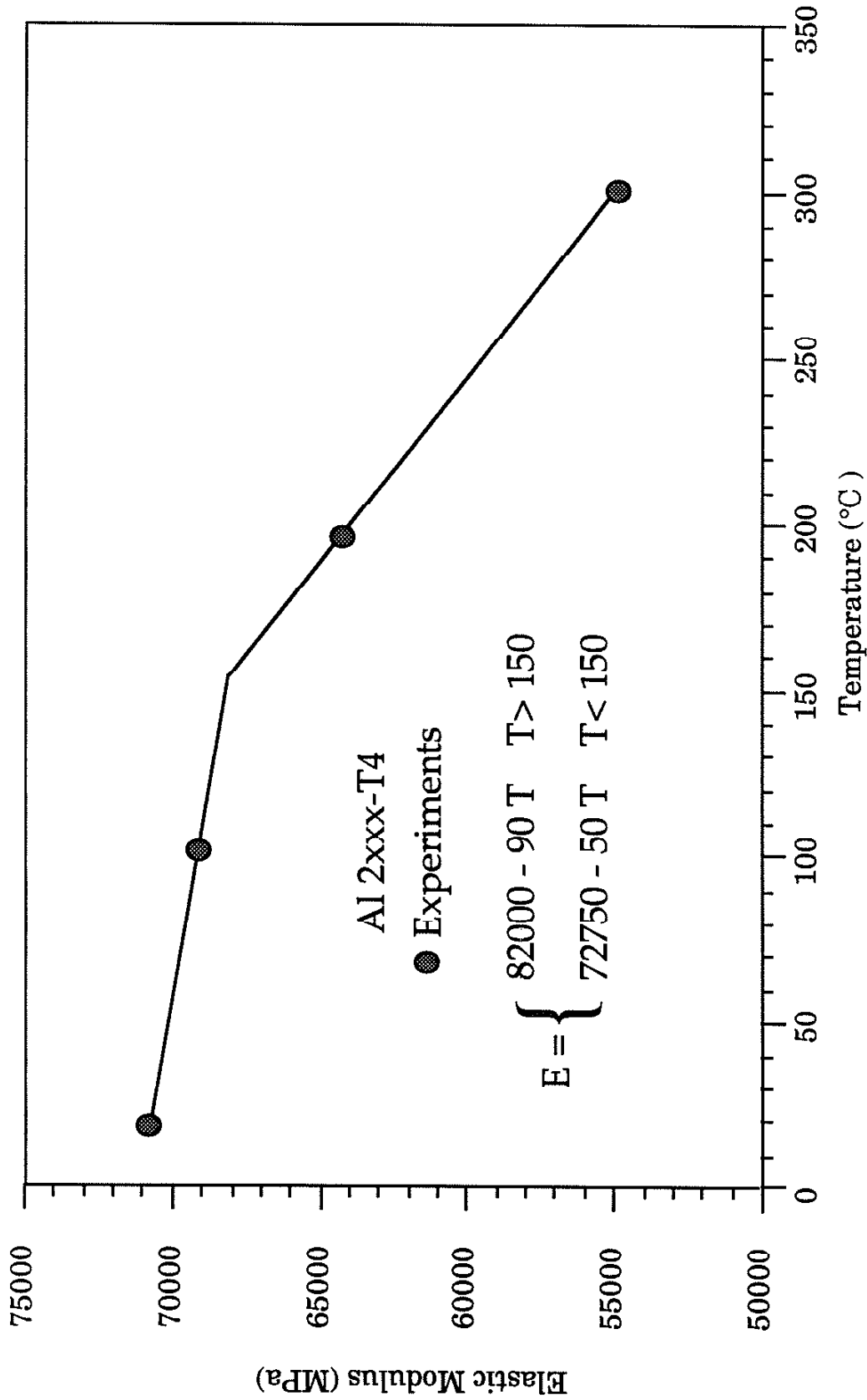


Figure 5.3: Change in elastic modulus with temperature for Al 2xxx-T4

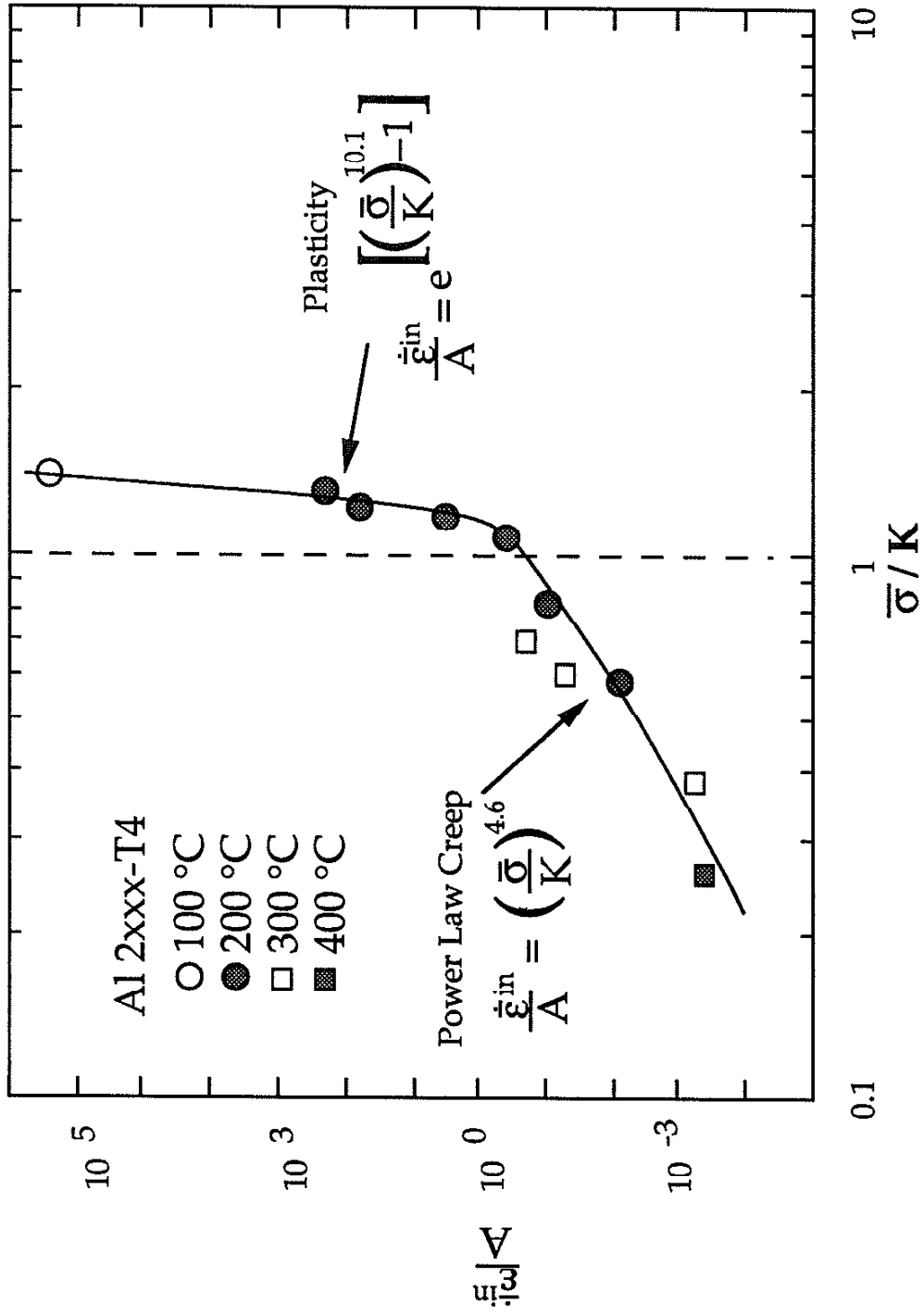


Figure 5.4: Flow Rule for Al2xxx-T4

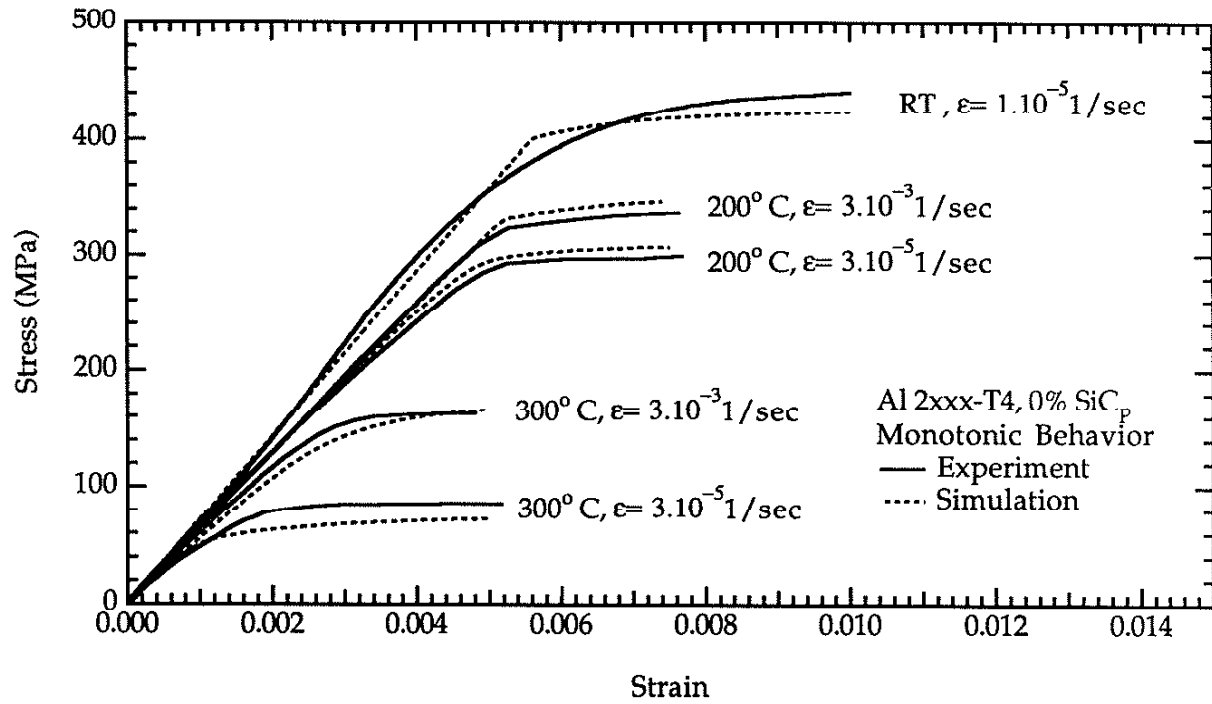


Figure 5.5: Monotonic stress-strain behavior of Al 2xxx-T4, experiments and simulations

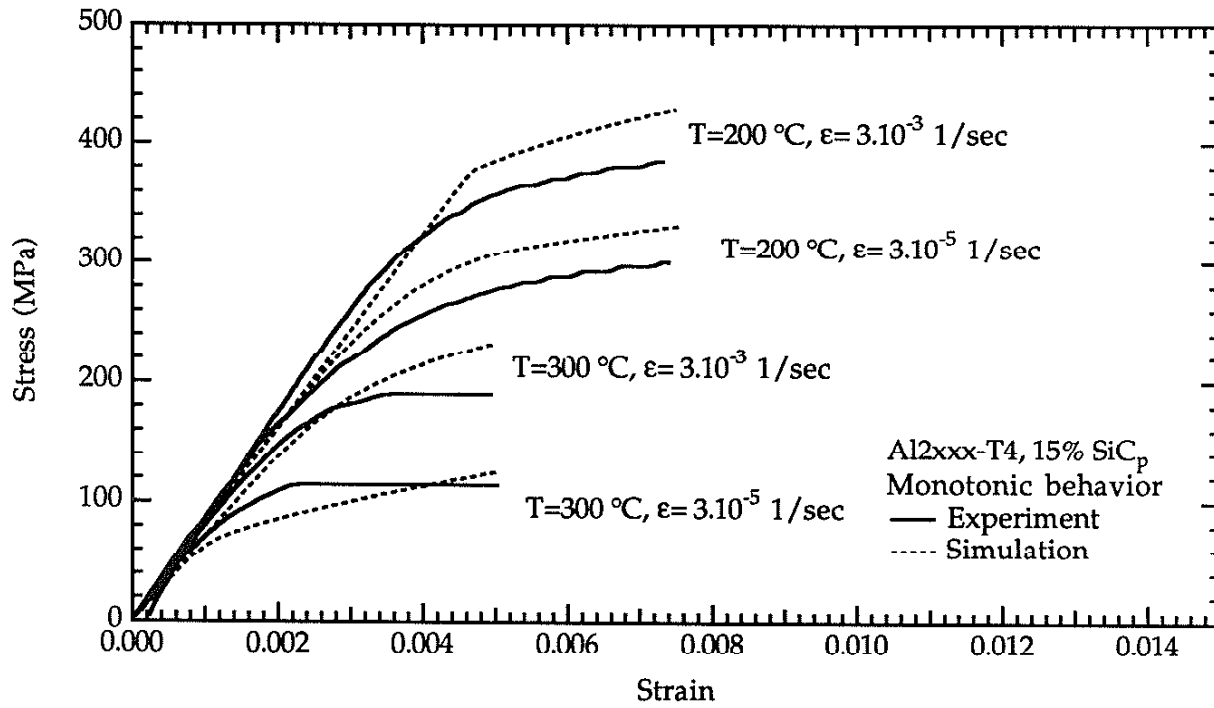


Figure 5.6: Monotonic stress-strain behavior of Al_{2xxx}-T4 15% SiC_p experiments and simulations

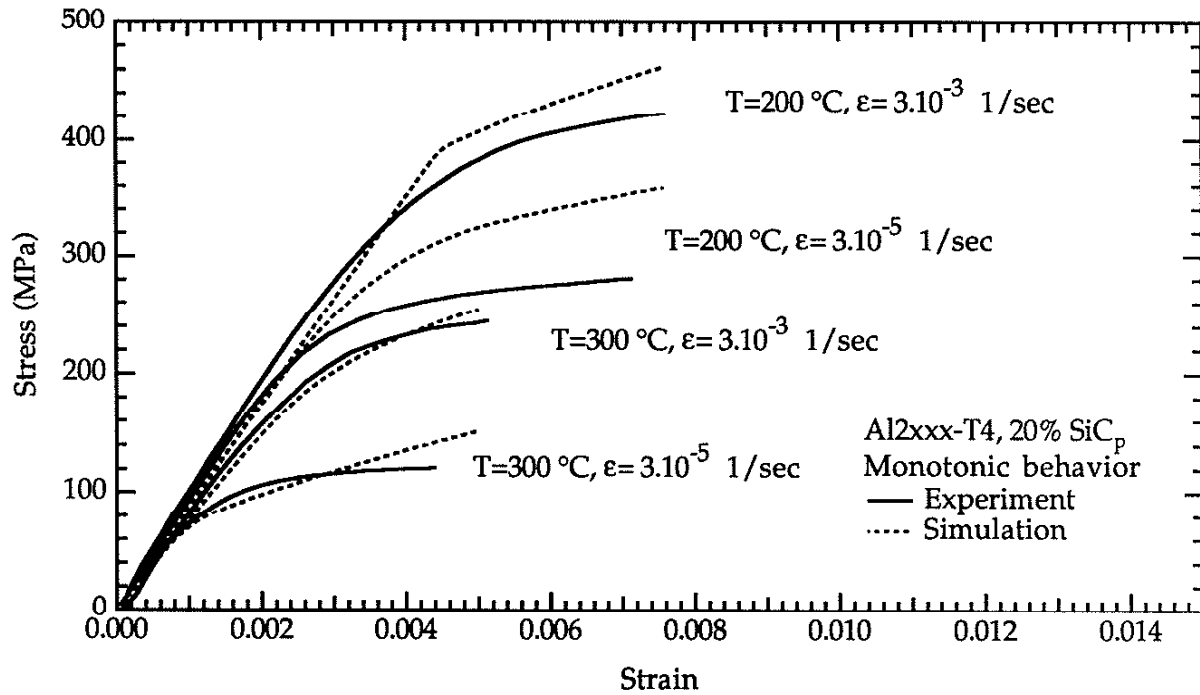


Figure 5.7: Monotonic stress-strain behavior of Al_{2xxx}-T4 20% SiC_p experiments and simulations

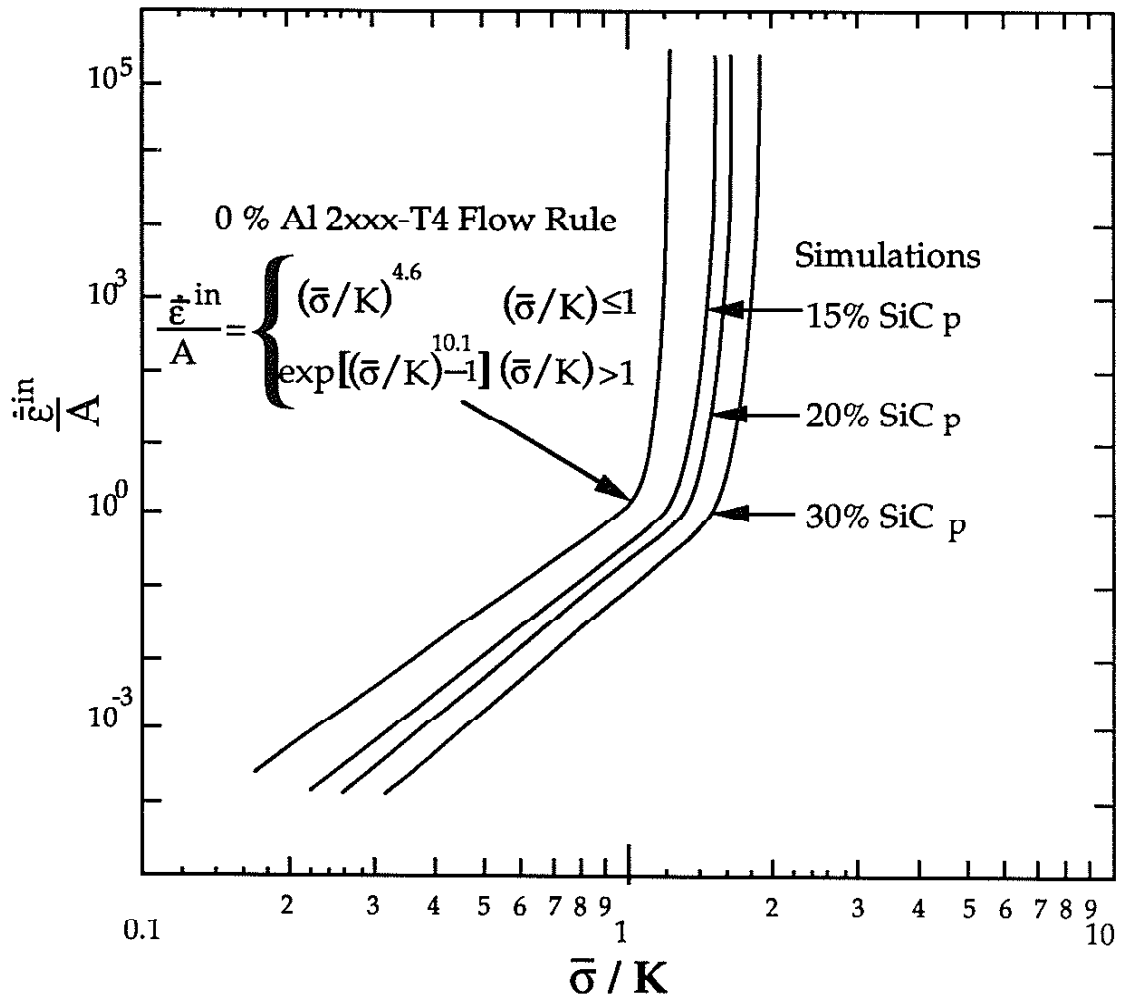


Figure 5.8: Flow rule relating inelastic strain rate to effective stress for Al 2xxx-T4 and simulations for 15%, 20% and 30% SiC reinforcement

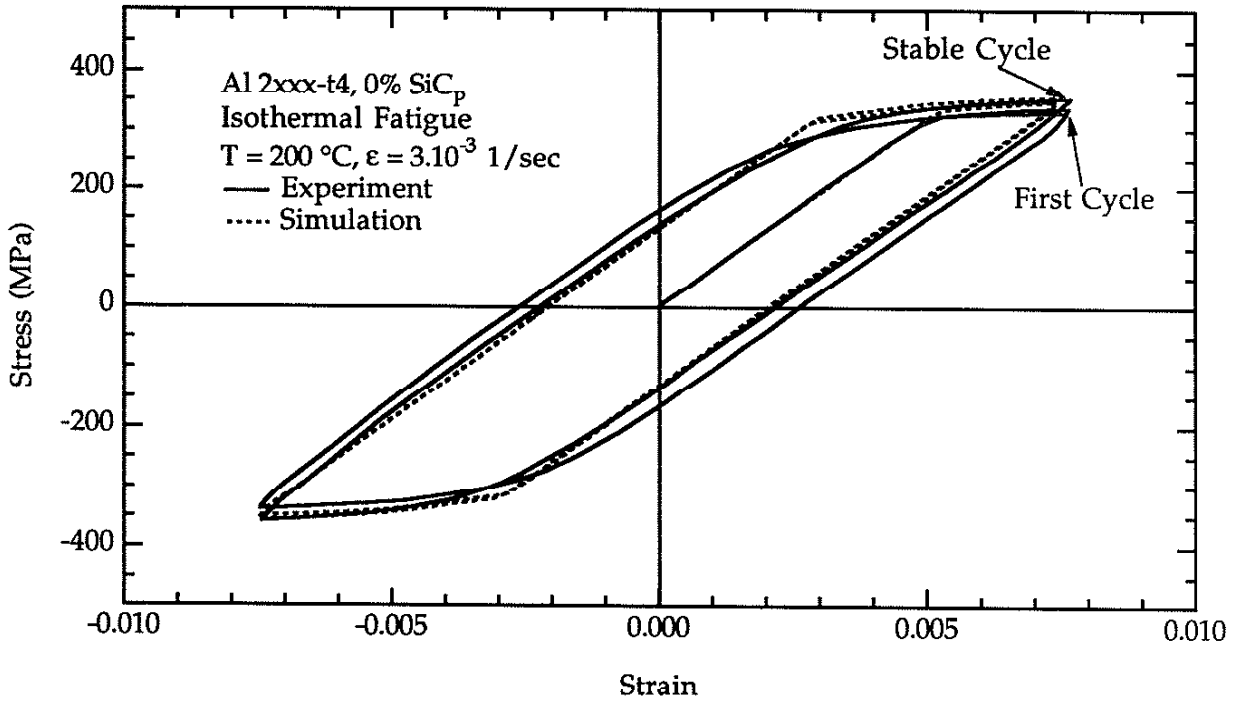


Figure 5.9: Isothermal cyclic stress-strain behavior of Al 2xxx-T4 experiment and simulation T = 200 °C, $\epsilon = 3.10^{-3}$ 1/sec

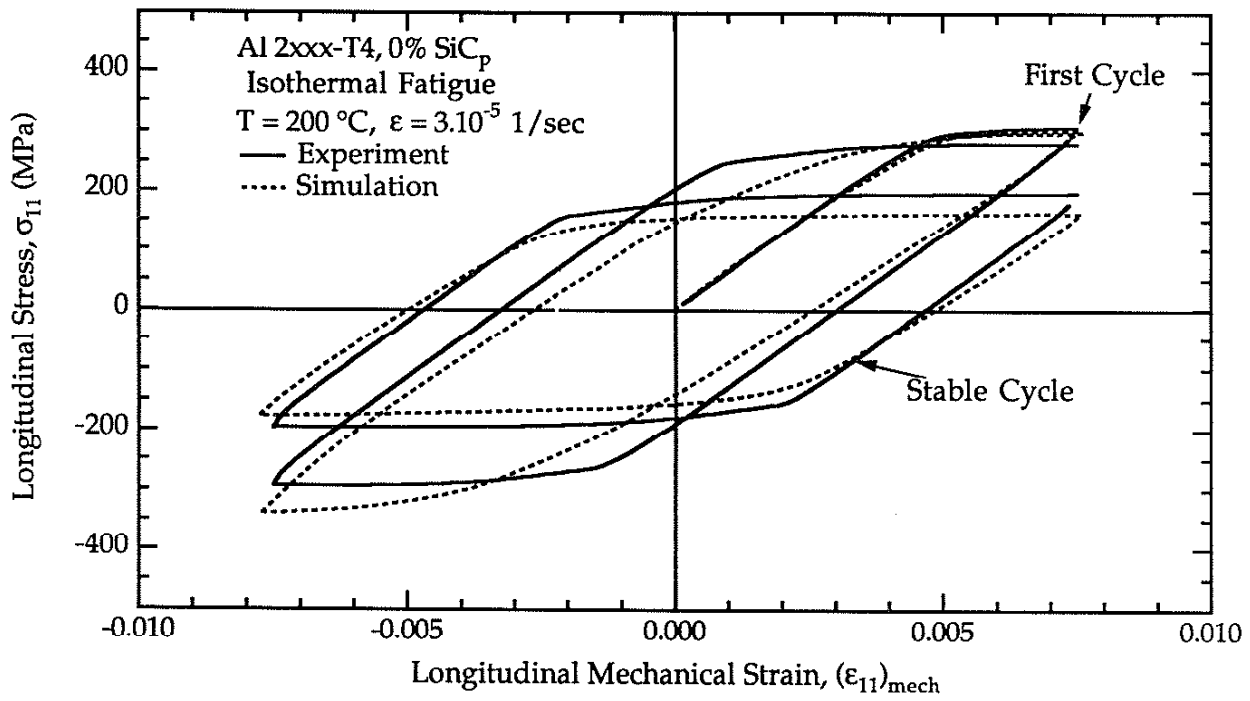


Figure 5.10: Isothermal cyclic stress-strain behavior of Al 2xxx-T4 experiment and simulation, $T = 200$ °C, $\dot{\epsilon} = 3.10^{-5}$ 1/sec

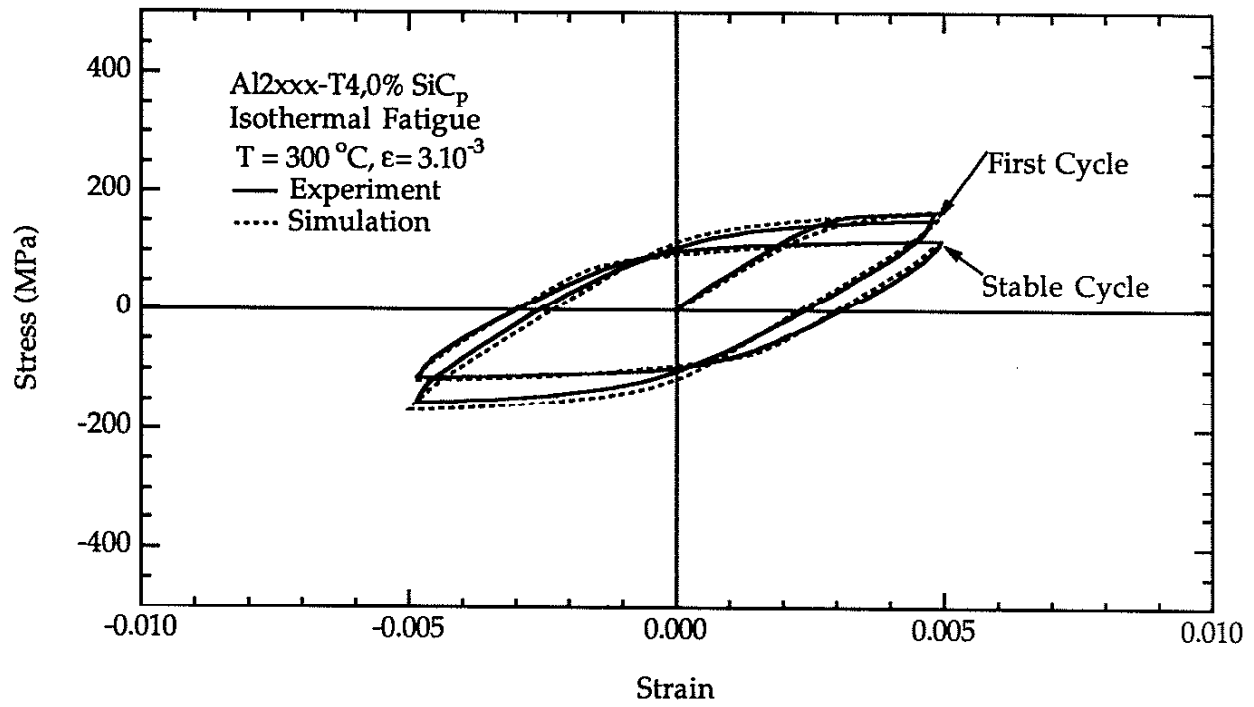


Figure 5.11: Isothermal cyclic stress-strain behavior of Al_{2xxx}-T4 experiment and simulation, T = 300°C, $\epsilon = 3.10^{-3}$

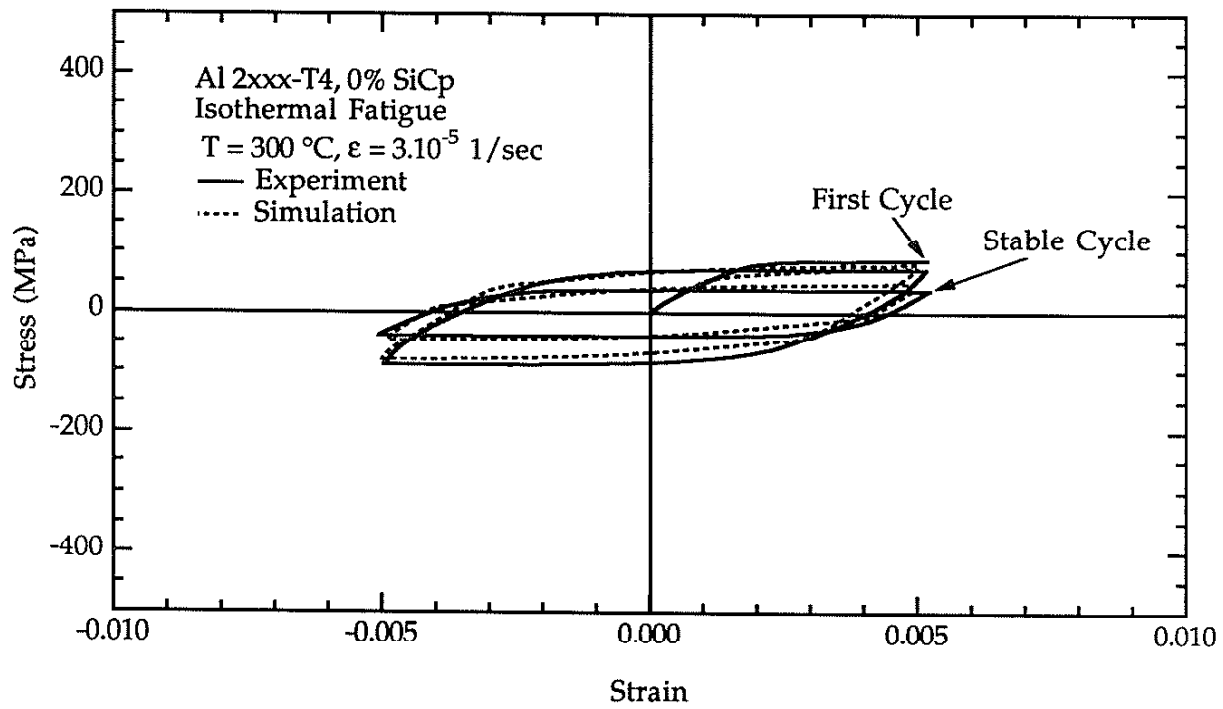


Figure 5.12: Isothermal cyclic stress-strain behavior of Al 2xxx-T4 experiment and simulation, $T = 300\text{ }^{\circ}\text{C}$, $\epsilon = 3.10^{-5}\text{ 1/sec}$

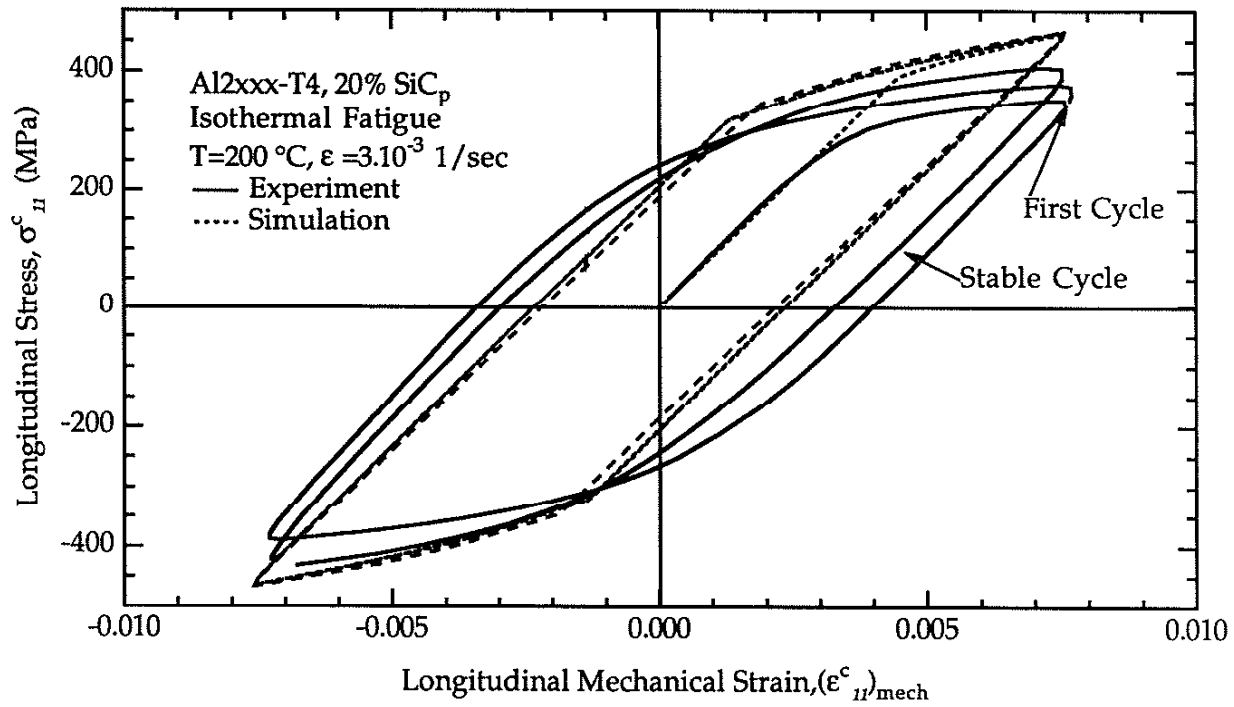


Figure 5.13: Isothermal cyclic stress-strain behavior of Al2xxx-T4 20%SiC_p, experiment and simulation, longitudinal stress-strain behavior, T=200 °C, $\epsilon = 3.10^{-3}$ 1/sec

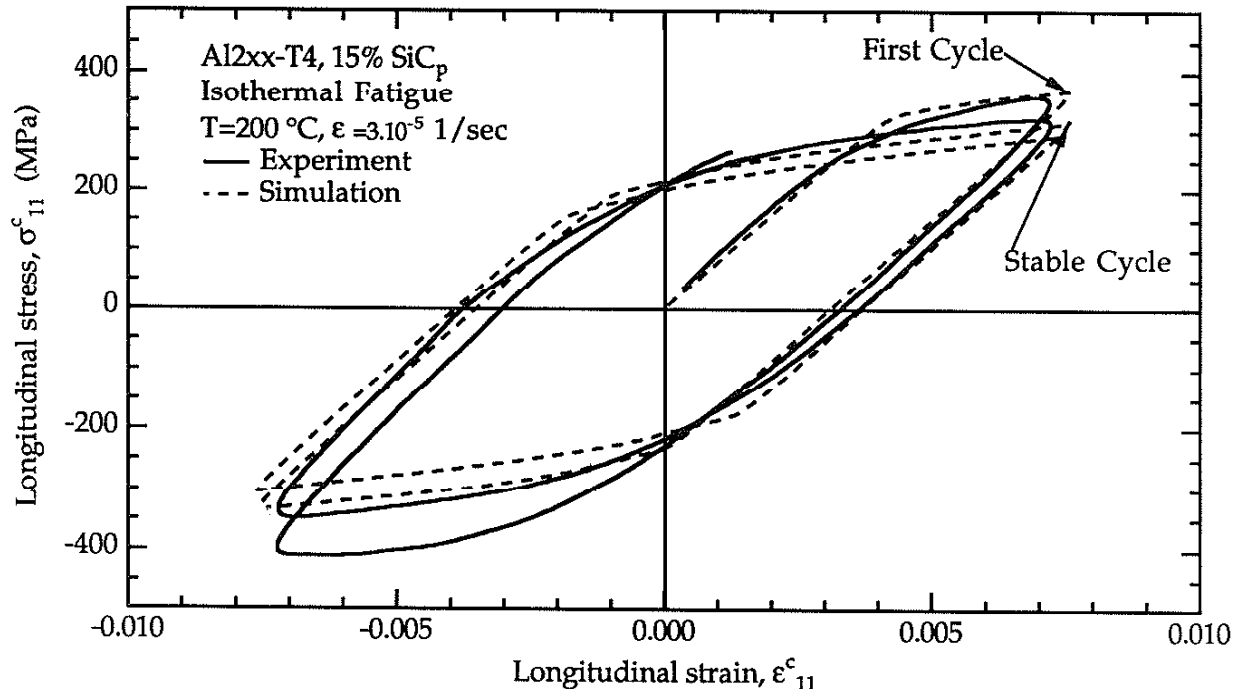


Figure 5.14: Isothermal cyclic stress-strain behavior of Al 2xxx-T4 15% SiC_p, experiment and simulation, longitudinal stress-strain behavior, T=200 °C, $\dot{\epsilon} = 3 \cdot 10^{-5}$ 1/sec

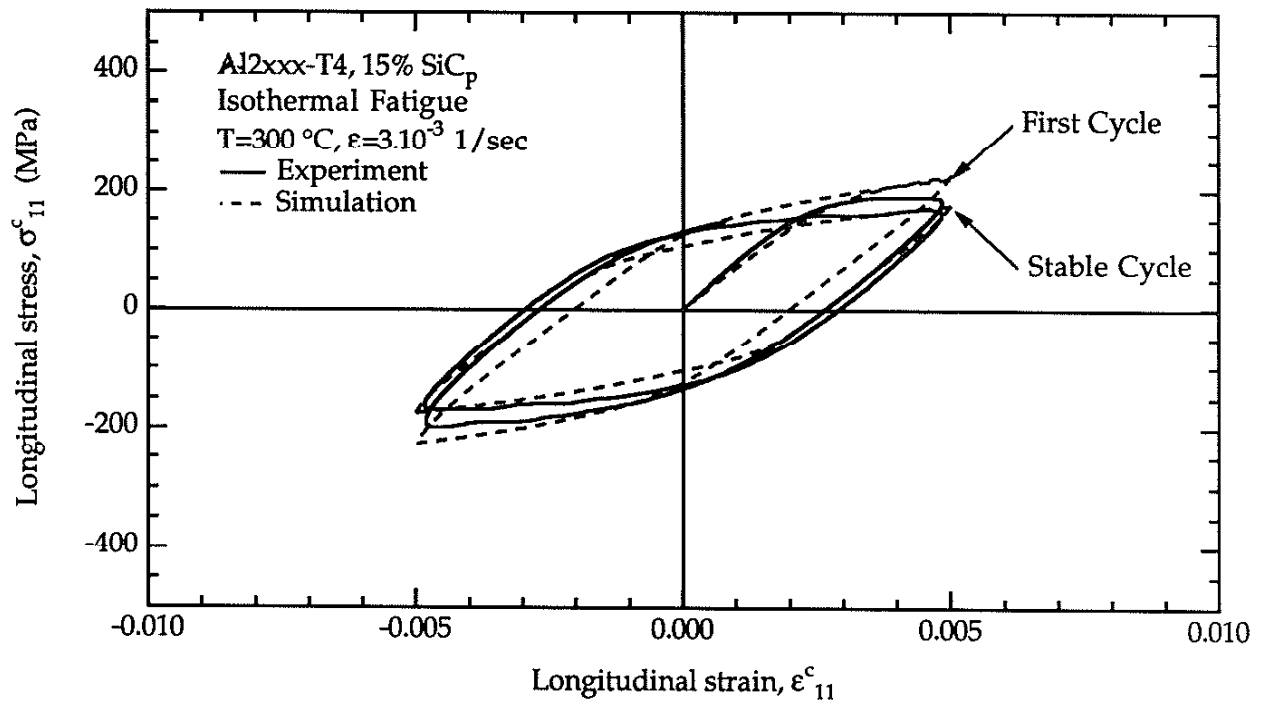


Figure 5.15: Isothermal cyclic stress-strain behavior of Al 2xxx-T4 15% SiC_p, experiment and simulation, longitudinal stress-strain behavior, T=300 °C, $\dot{\epsilon}=3.10^{-3}$ 1/sec

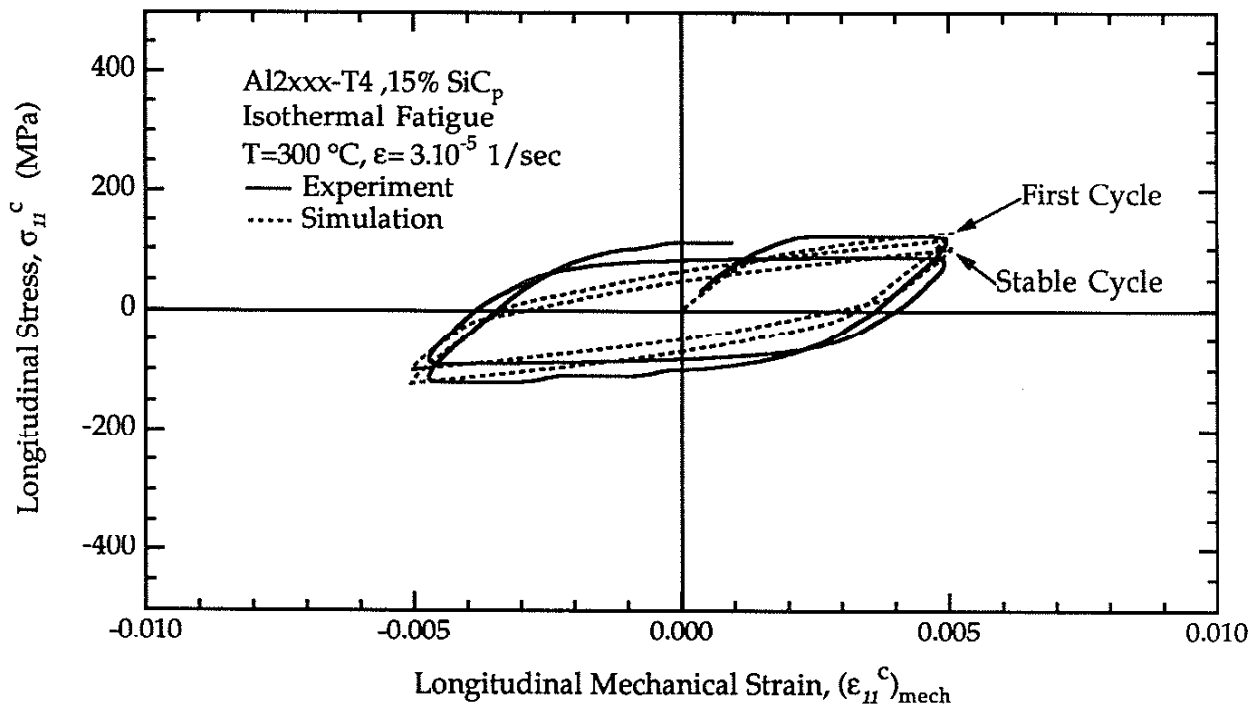


Figure 5.16: Isothermal cyclic stress-strain behavior of Al2xxx-T4 15%SiC_p, experiment and simulation, longitudinal stress-strain behavior, T=300 °C, $\epsilon=3.10^{-5}$ 1/sec

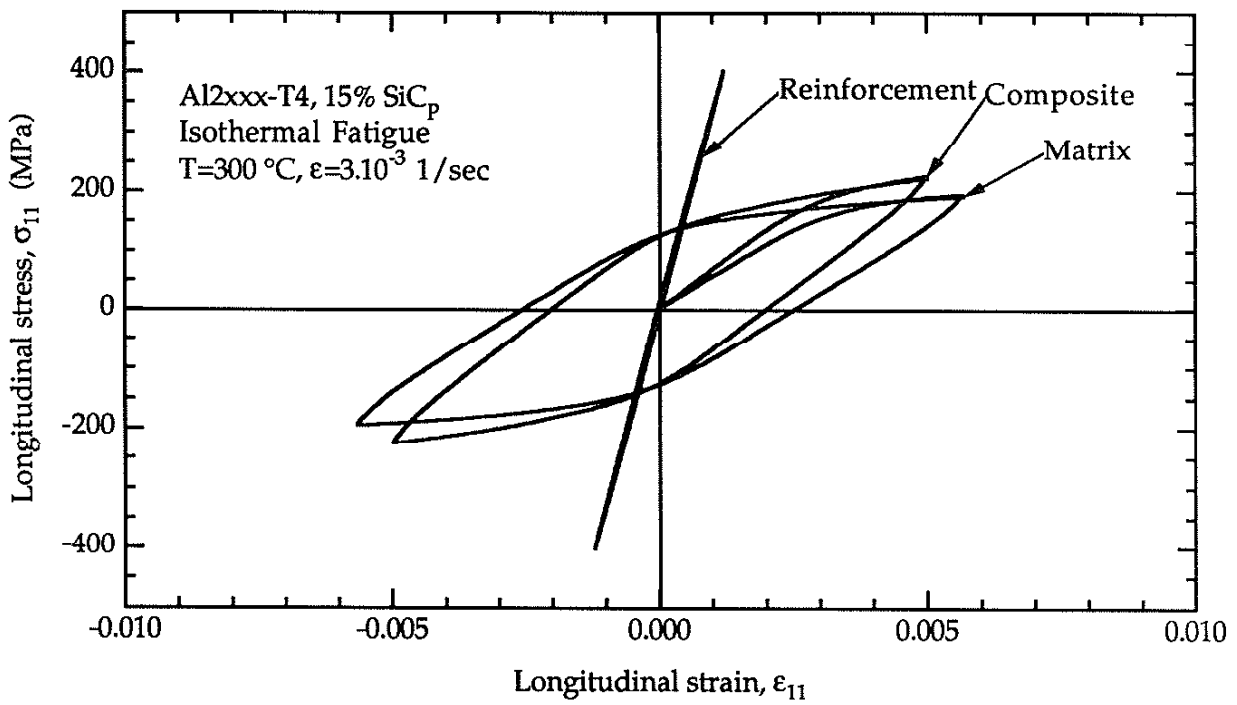


Figure 5.17: Isothermal cyclic stress-strain behavior of Al 2xxx-T4 15% SiC_p, longitudinal stress-strain behavior simulations of matrix, reinforcement, and composite

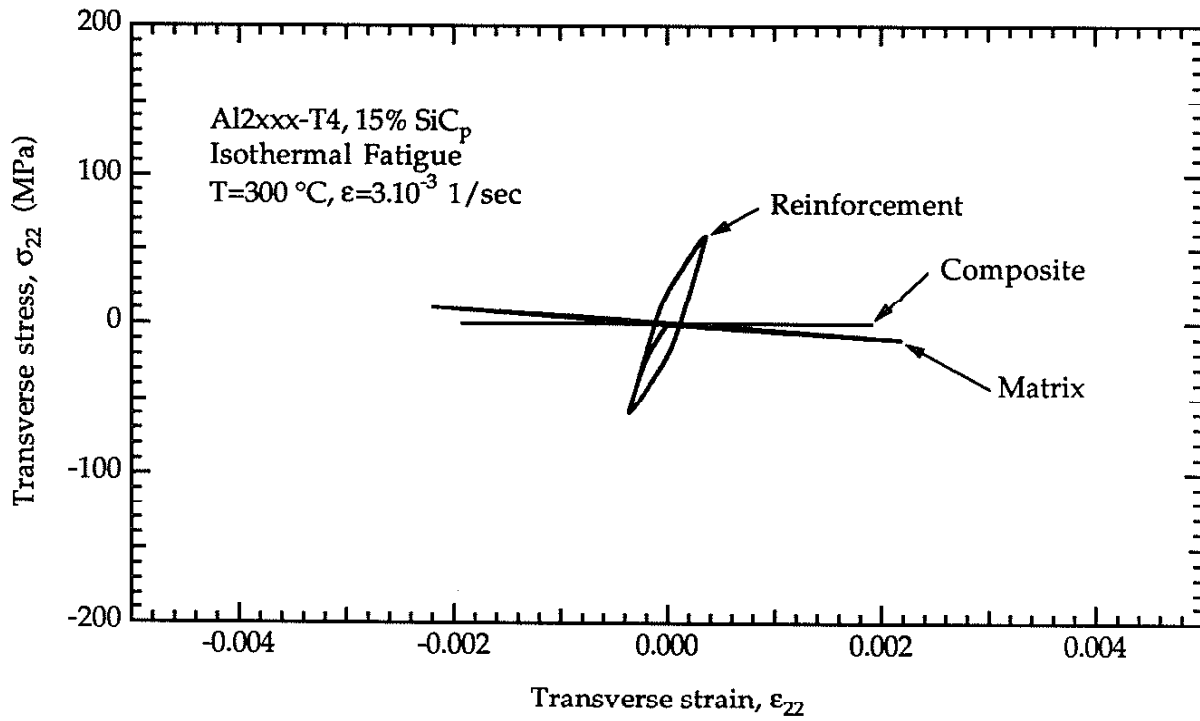


Figure 5.18: Isothermal cyclic stress-strain behavior of Al 2xxx-T4 15% SiC_p transverse stress-strain behavior simulations of matrix, reinforcement, and composite

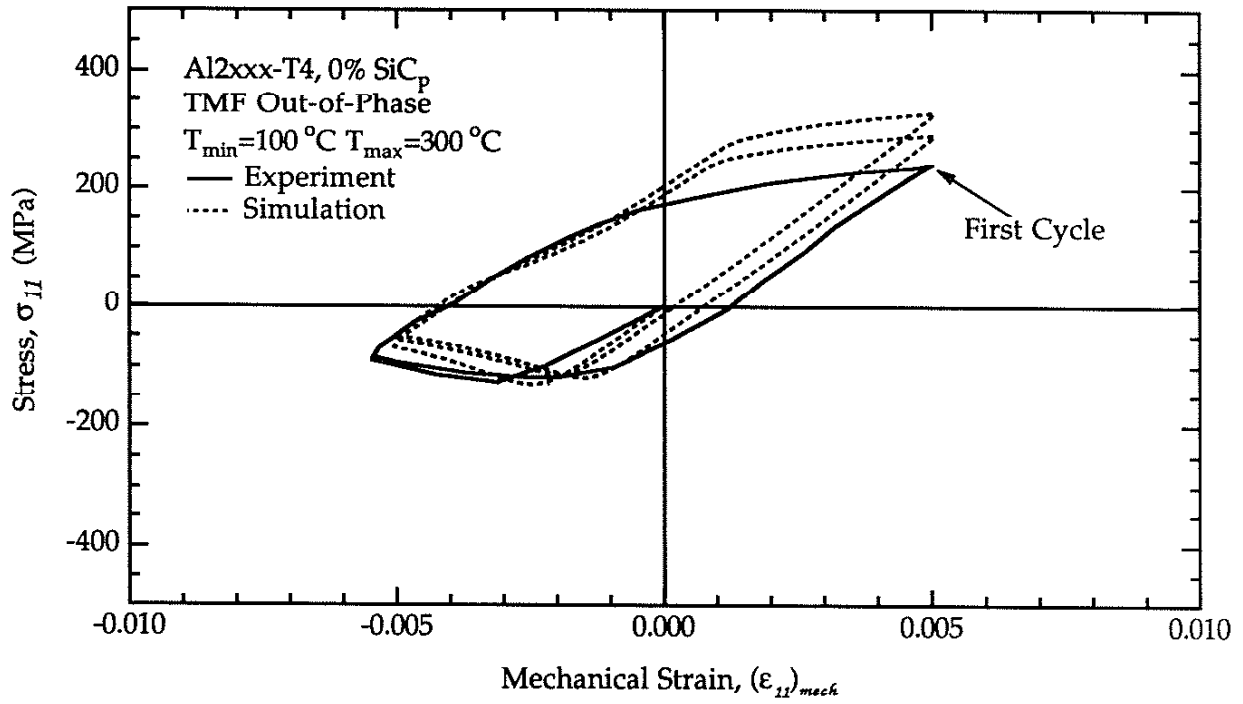


Figure 5.19: TMF OP 100-300 °C cyclic stress-strain behavior of Al₂xxx-T4, experiment and simulation

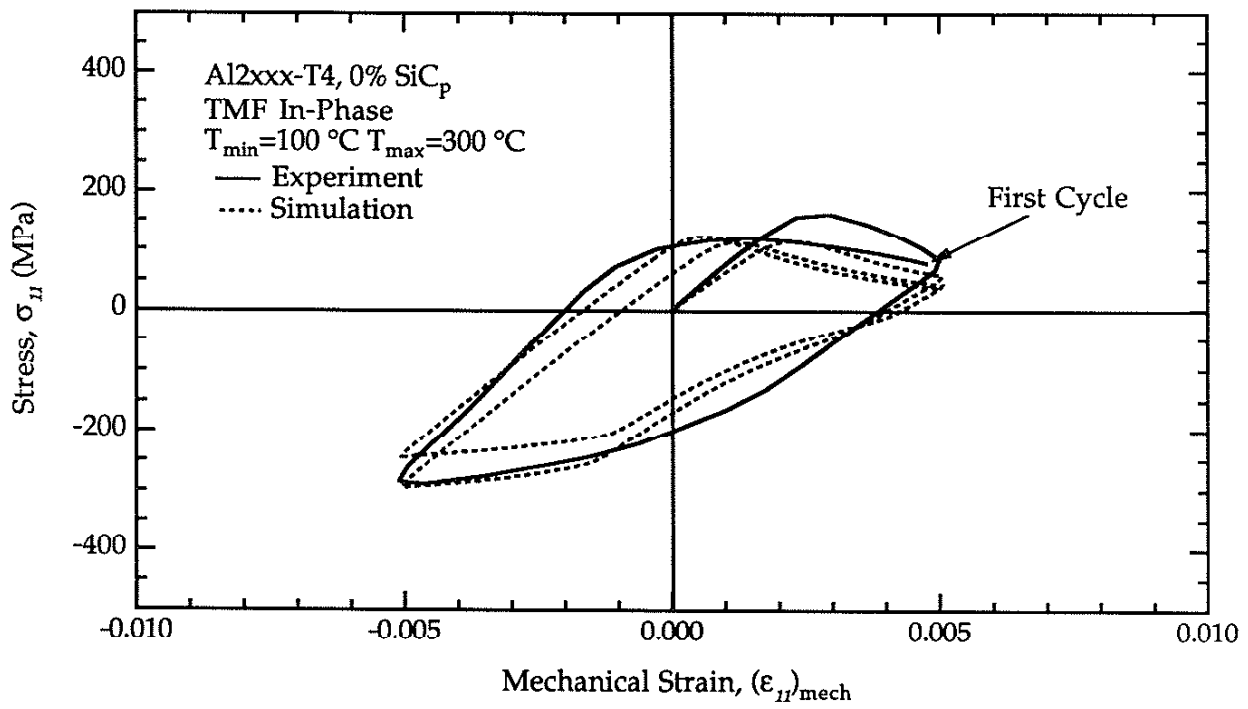


Figure 5.20: TMF IP 100-300 °C cyclic stress-strain behavior of Al₂xxx-T4, experiment and simulation

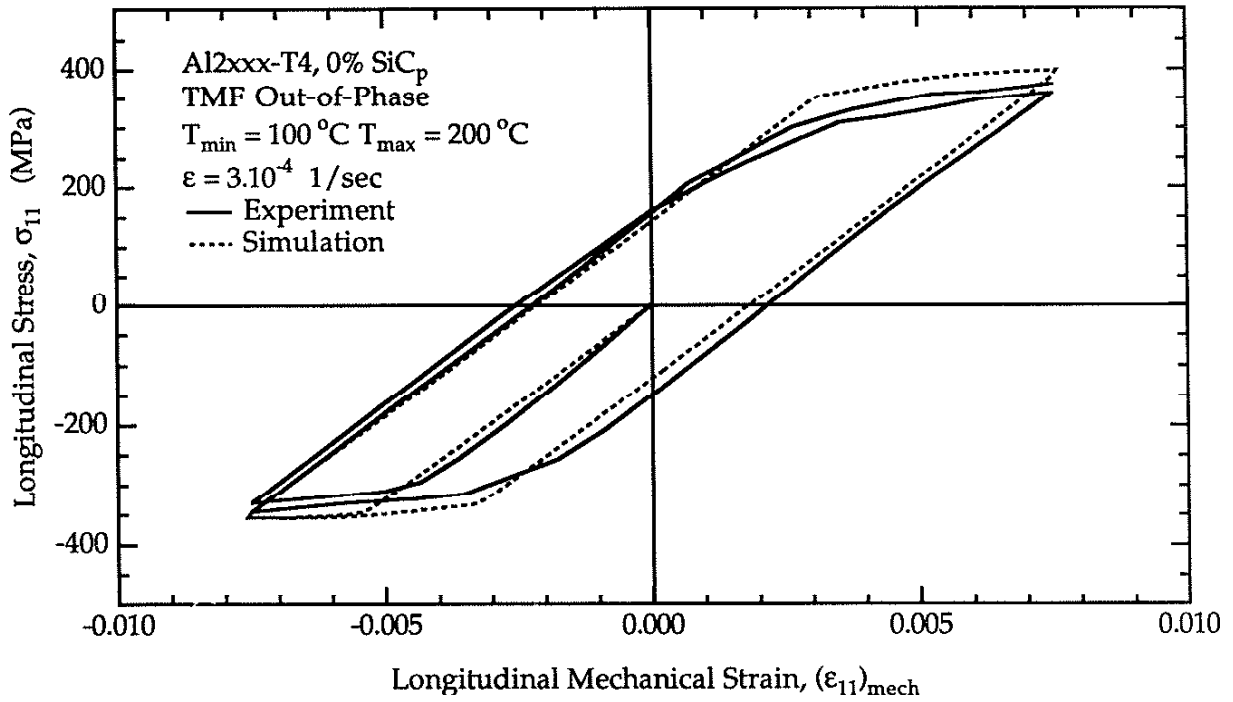


Figure 5.21: TMF OP 100-200 °C cyclic stress-strain behavior of Al2xxx-T4, experiment and simulation

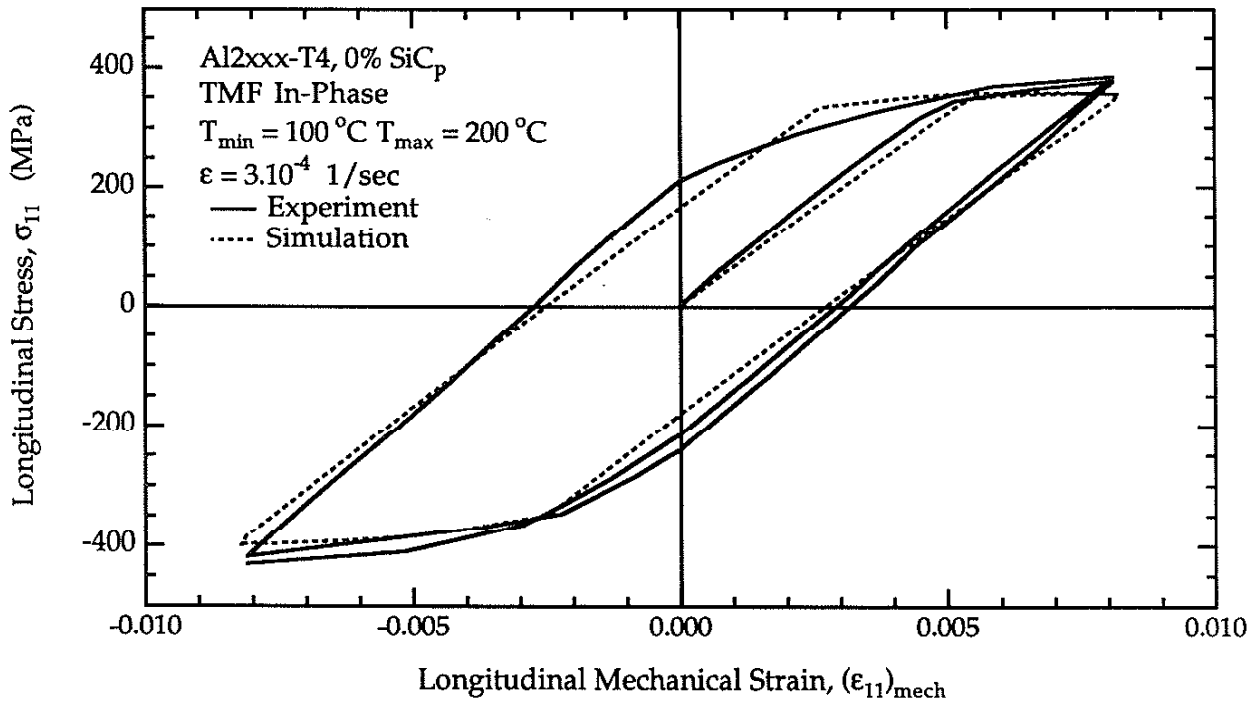


Figure 5.22: TMF IP 100-200 °C cyclic stress-strain behavior of Al 2xxx-T4, experiment and simulation

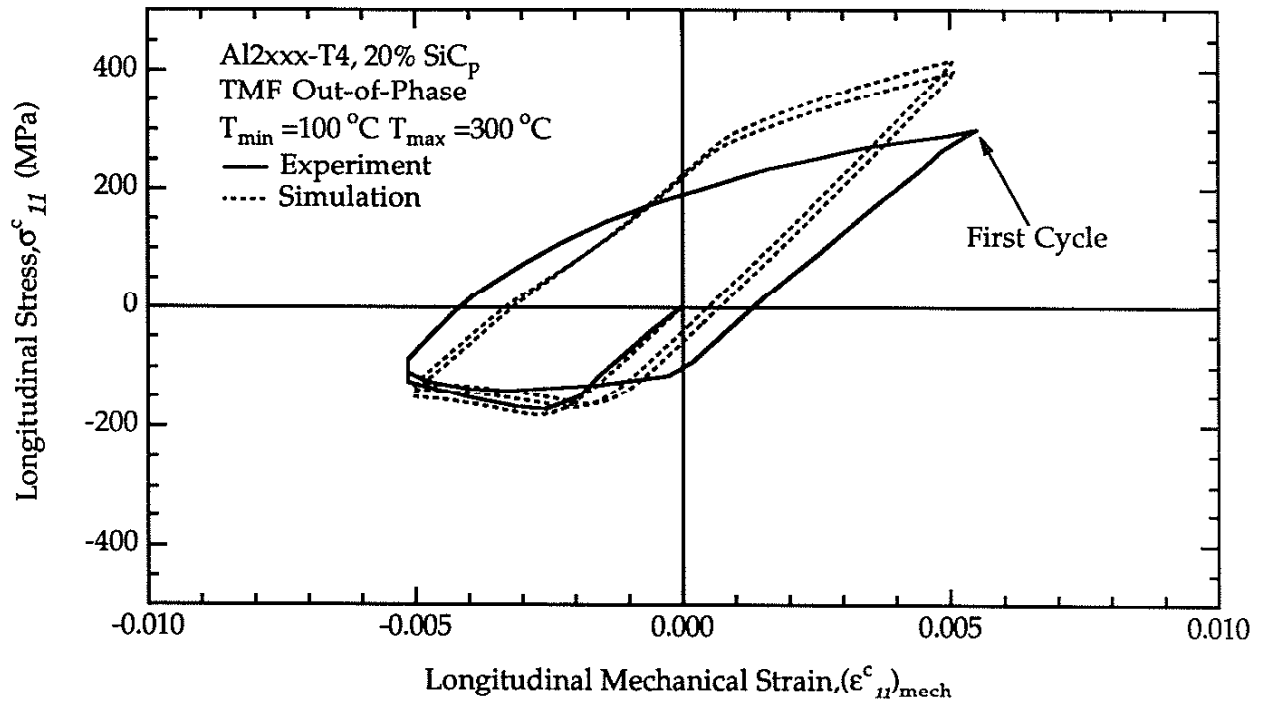


Figure 5.23: TMF OP 100-300 °C cyclic stress-strain behavior of Al₂xxx-T4 20%SiC_p, experiment and simulation

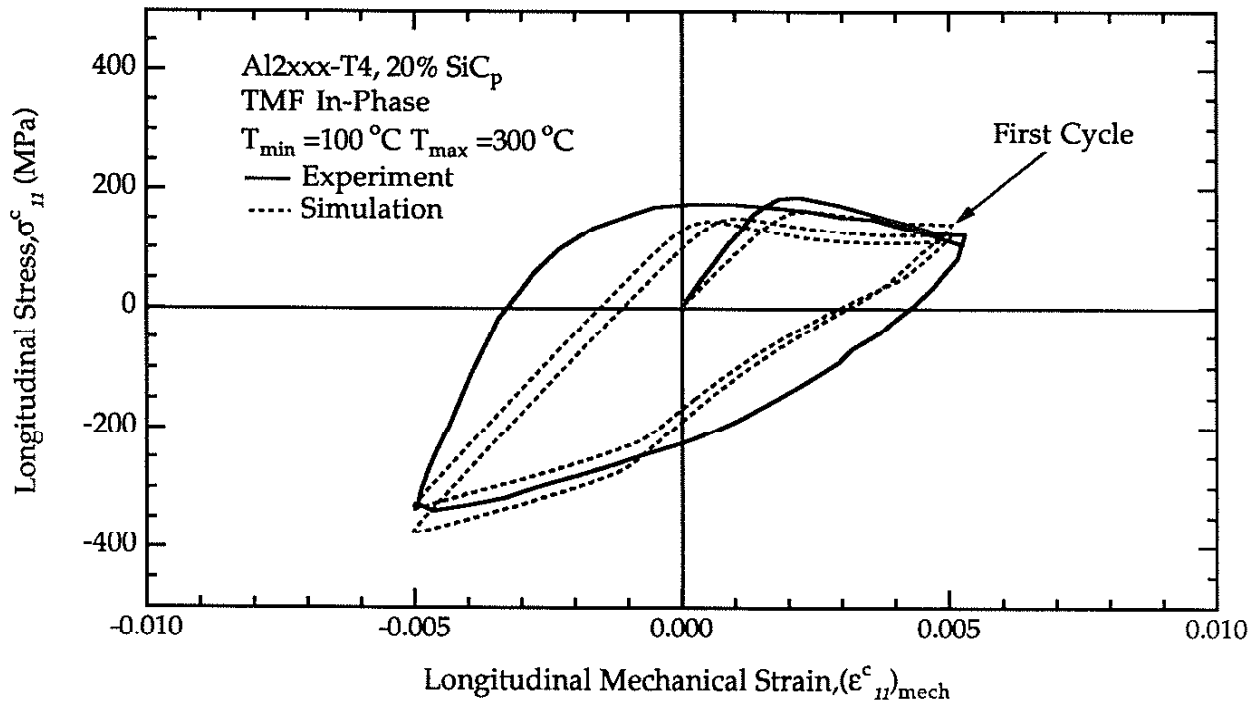


Figure 5.24: TMF IP 100-300 °C cyclic stress-strain behavior of Al₂xxx-T4 20%SiC_p, experiment and simulation

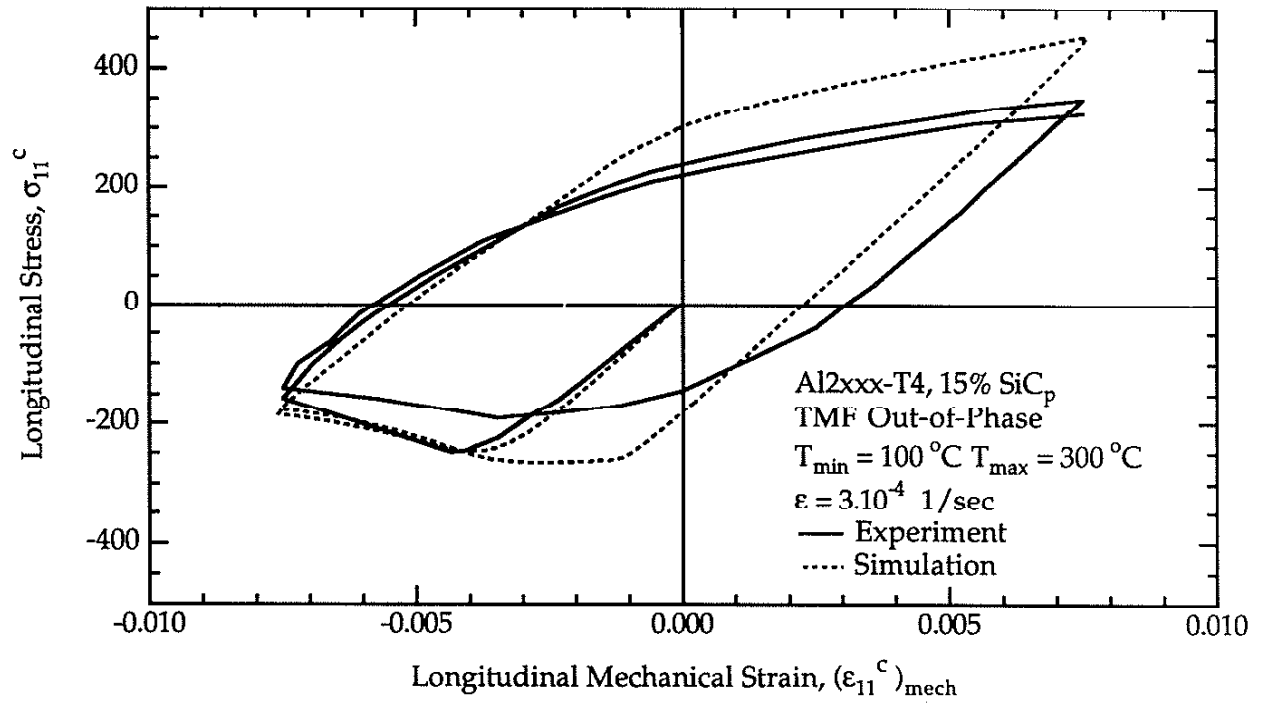


Figure 5.25: TMF OP 100-300 °C cyclic stress-strain behavior of Al₂xxx-T4 15% SiC_p experiment and simulation

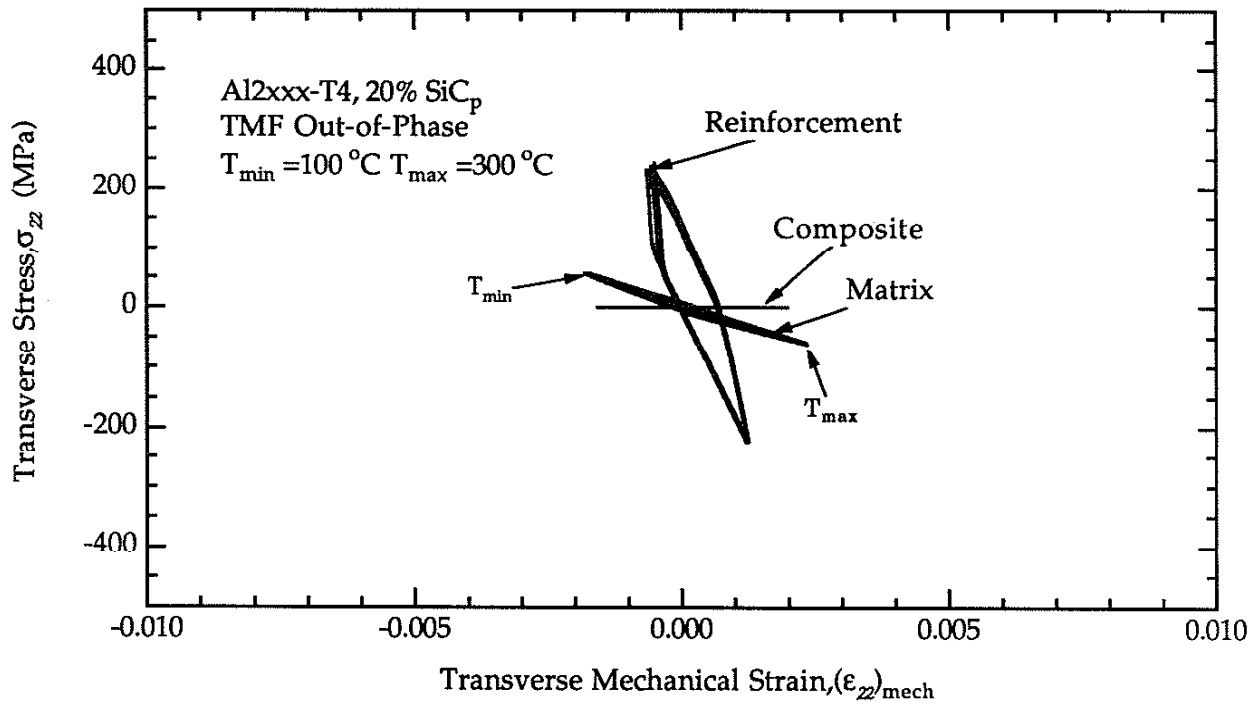


Figure 5.26: TMF OP stress-strain behavior of Al 2xxx-T4 20%SiC_p, transverse stress-strain behavior simulations of matrix, reinforcement, and composite

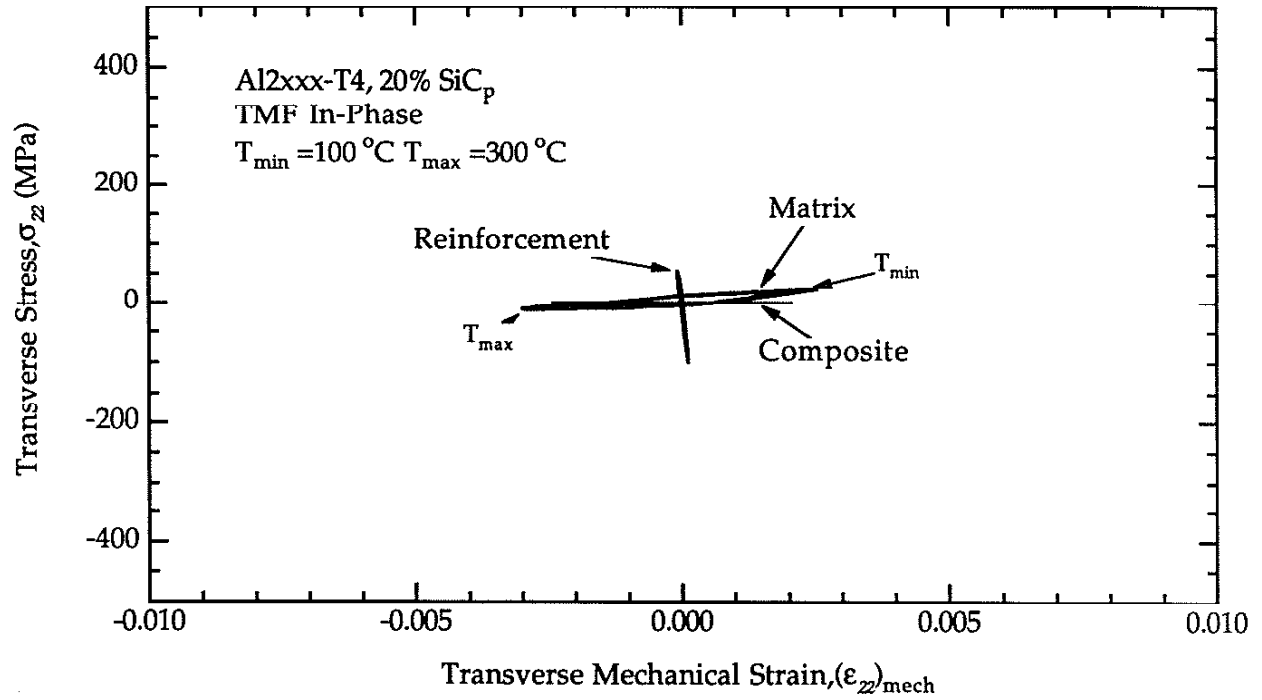


Figure 5.27: TMF IP 100-300 °C stress-strain behavior of Al₂xxx-T4 20%SiC_p, transverse stress-strain behavior simulations of matrix, reinforcement, and composite

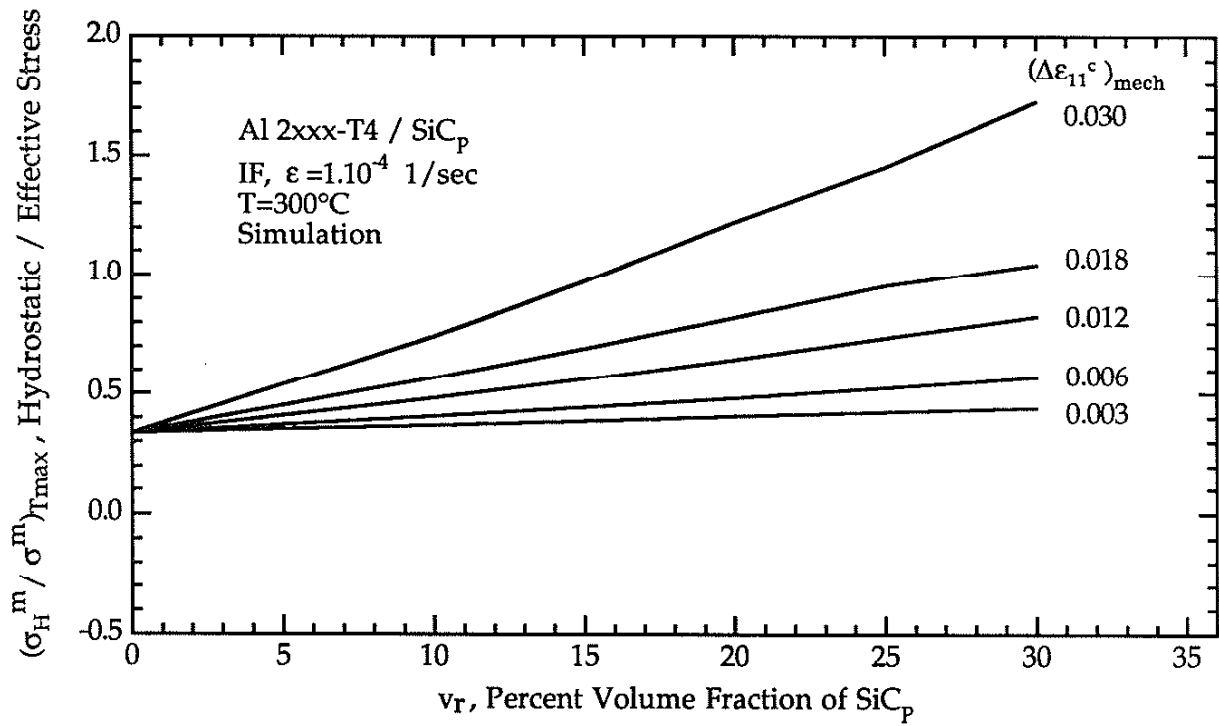


Figure 5.28: Ratio of hydrostatic stress to effective stress in the matrix versus volume fraction of reinforcement, isothermal fatigue simulations, T=300°C

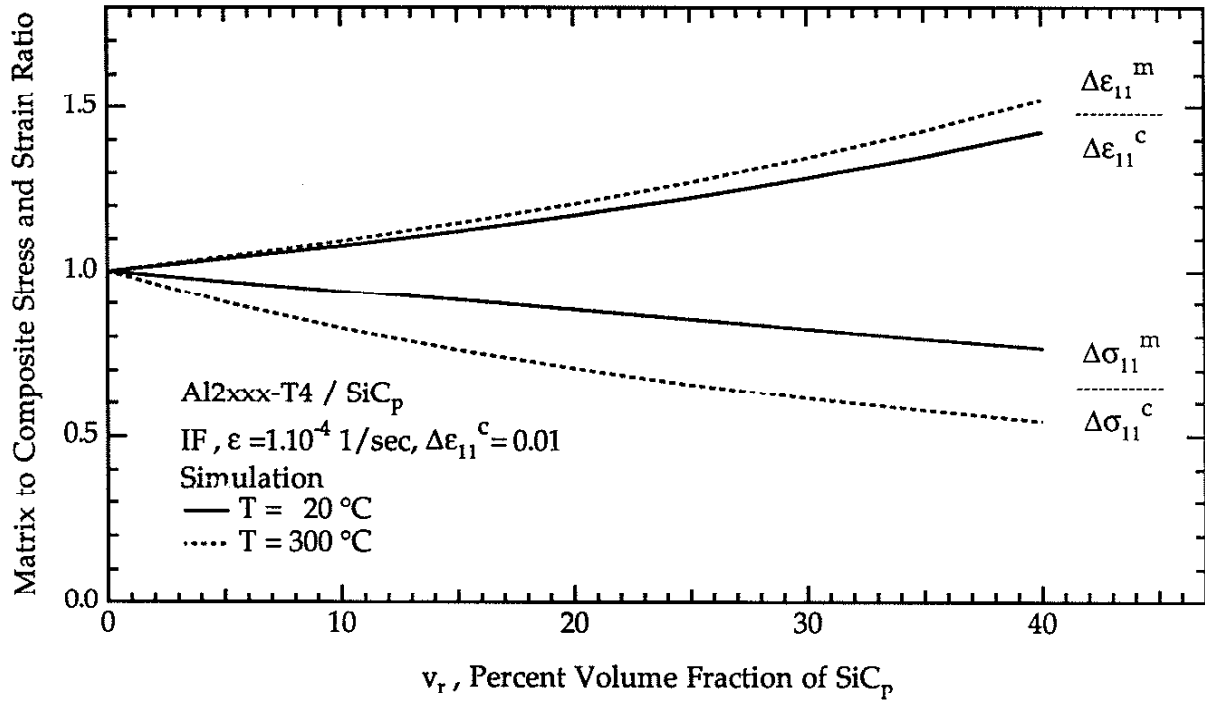


Figure 5.29: Ratio of matrix strain (stress) to composite strain (stress) isothermal fatigue simulations T=20 °C, T=300 °C

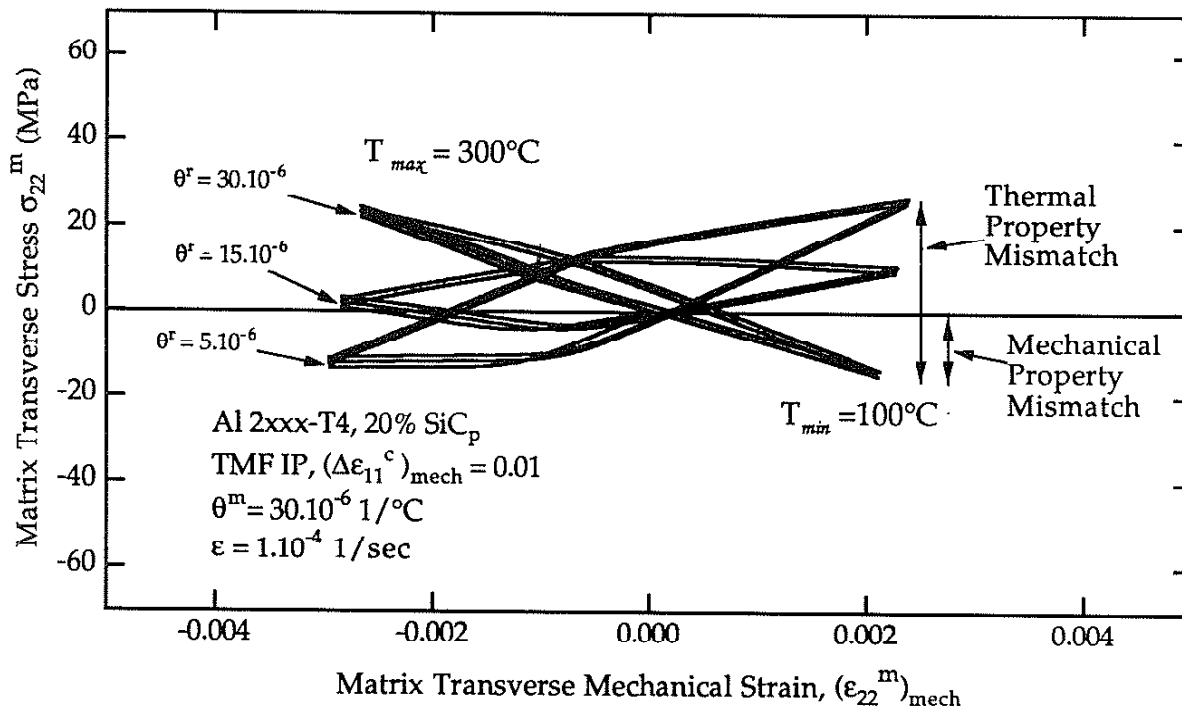


Figure 5.30: TMF IP, simulation of transverse stress-strain behavior in the matrix for different thermal expansion coefficient mismatch of matrix and reinforcement

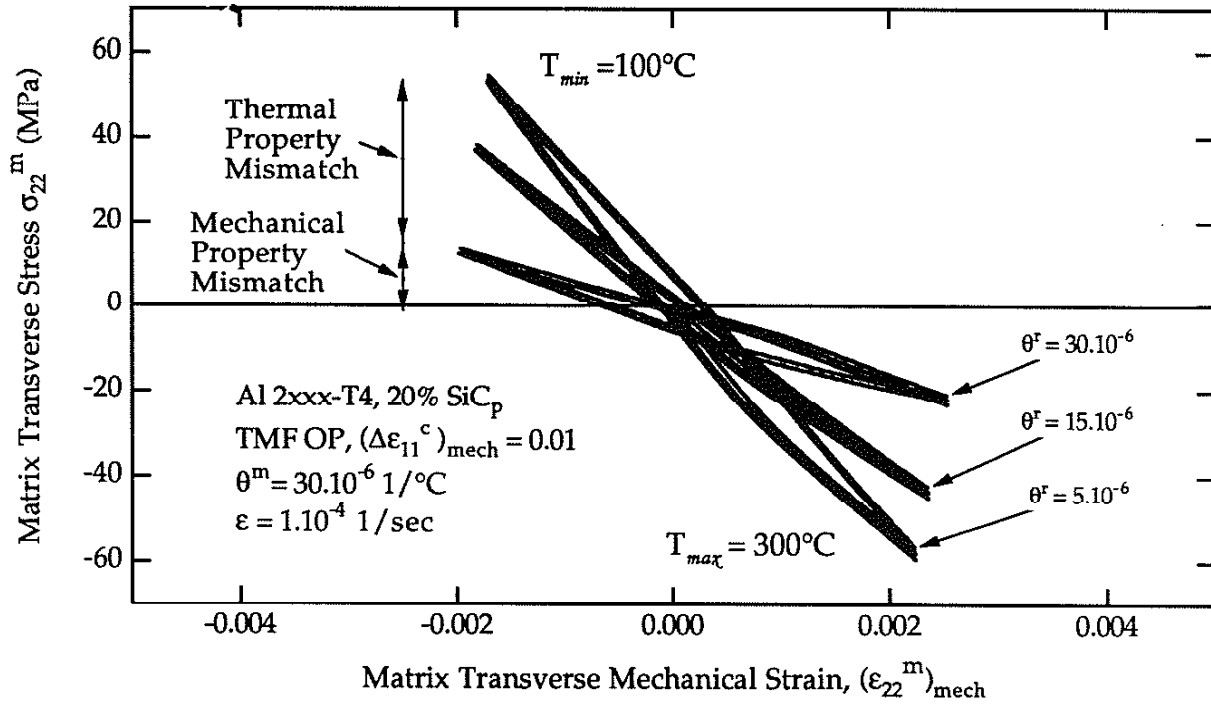


Figure 5.31: TMF OP, simulation of transverse stress-strain behavior in the matrix for different thermal expansion coefficient mismatch of matrix and reinforcement

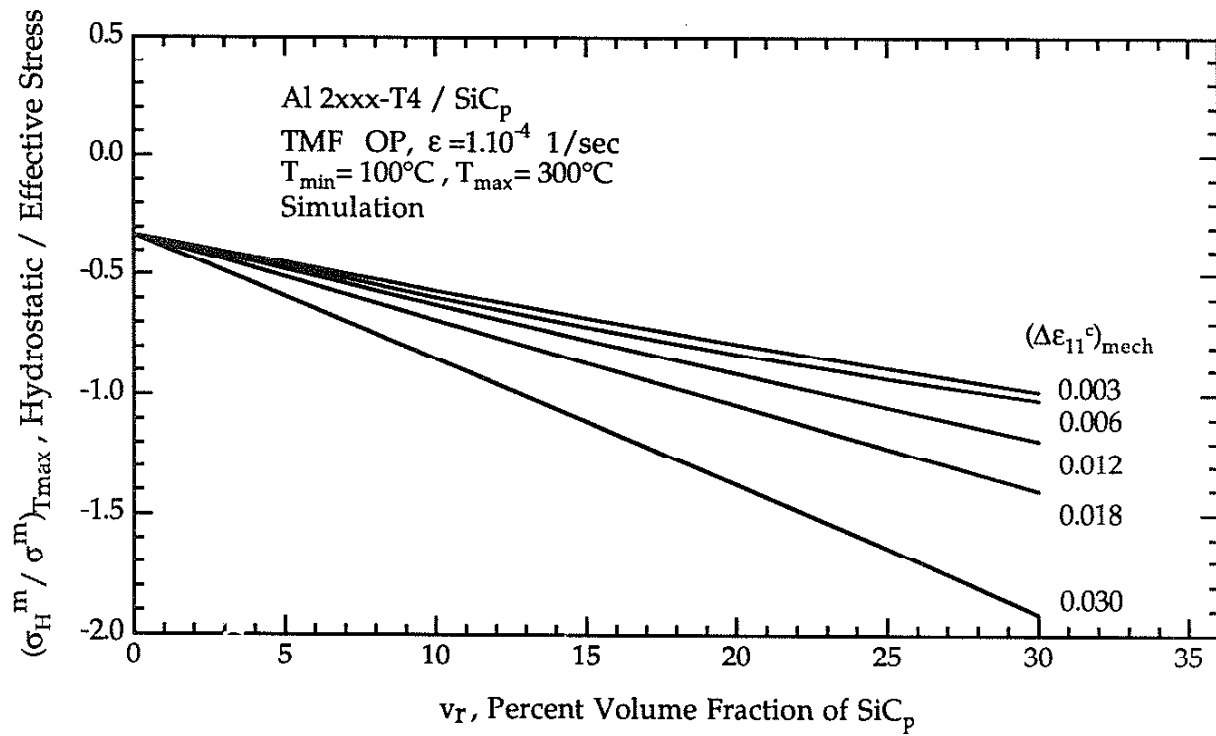


Figure 5.32: Ratio of hydrostatic stress to effective stress in the matrix versus volume fraction of reinforcement at 300°C end of a TMF OP cycle, simulation

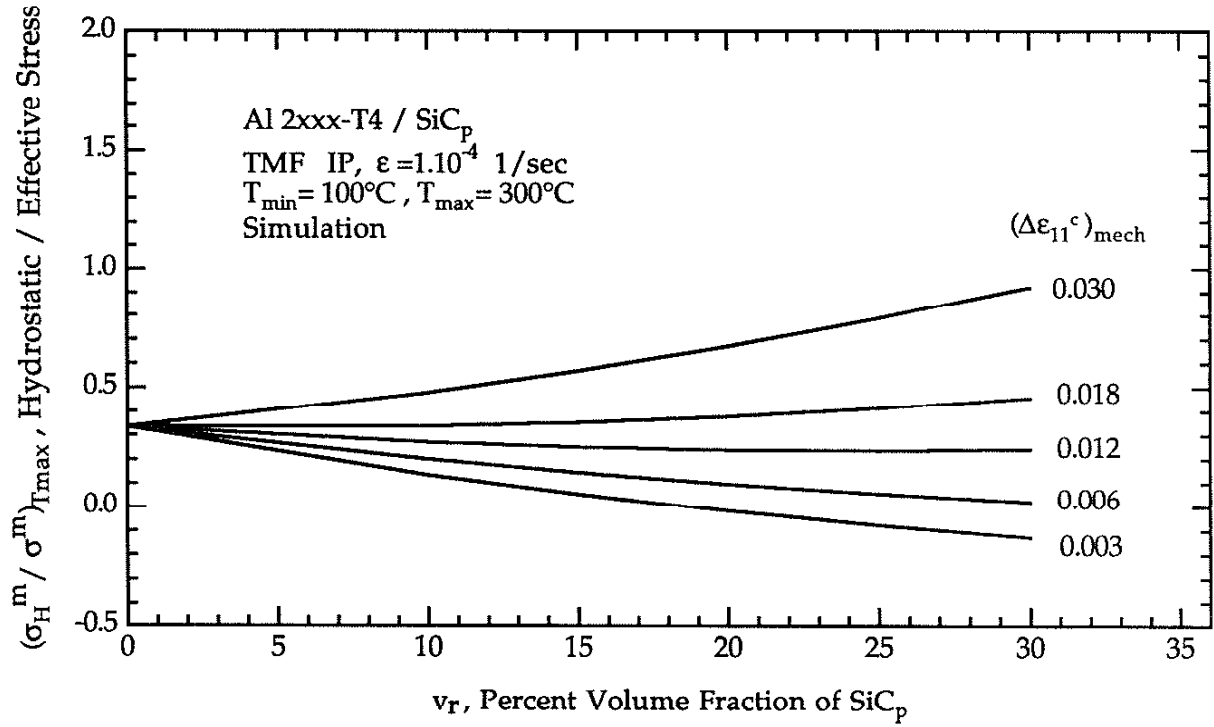


Figure 5.33: Ratio of hydrostatic stress to effective stress in the matrix versus volume fraction of reinforcement at 300°C end of a TMF IP cycle, simulation

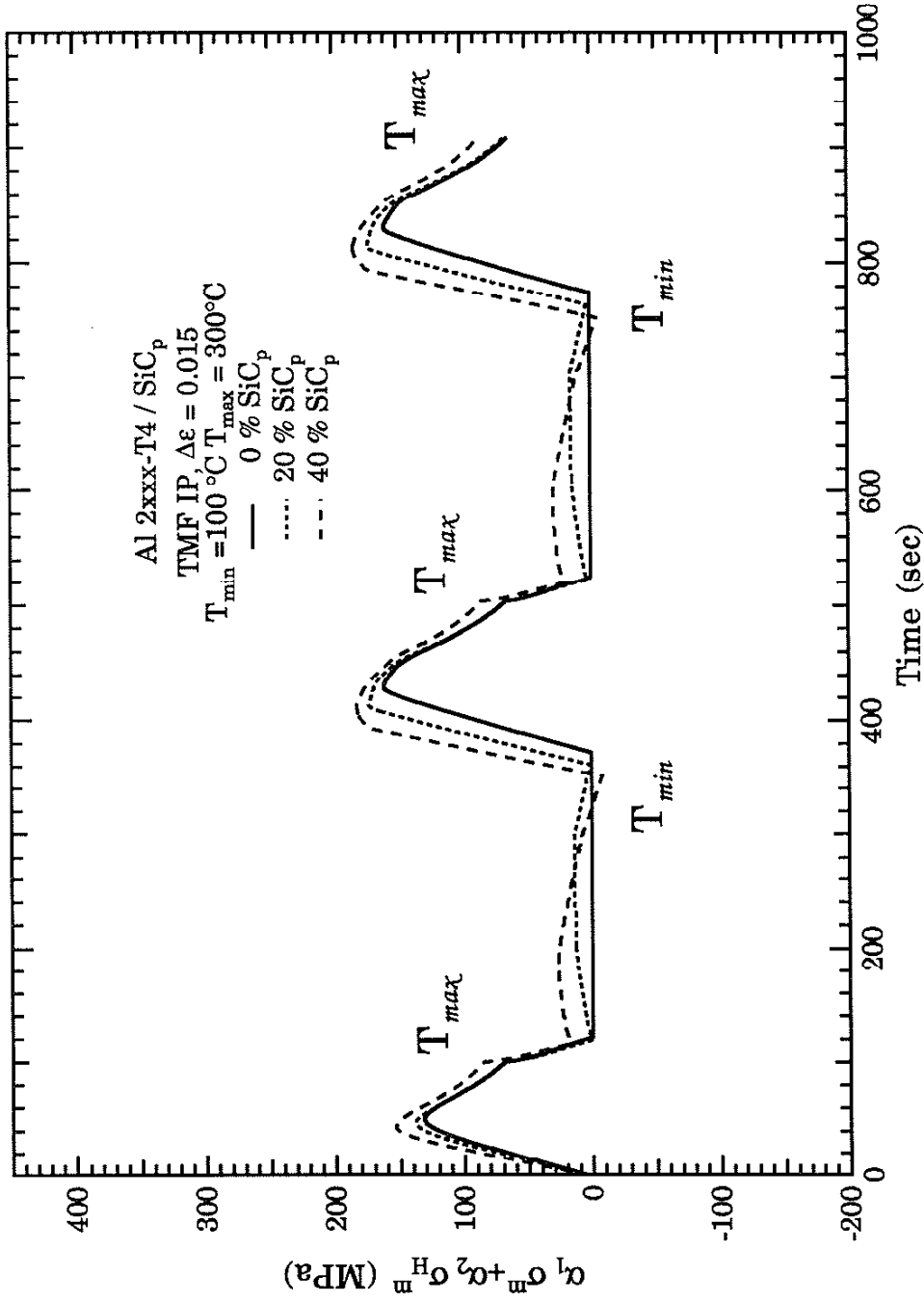


Figure 6.1: The variation $\alpha_1 \sigma_m + \alpha_2 \sigma_H^m$ of during a TMF IP loading cycle

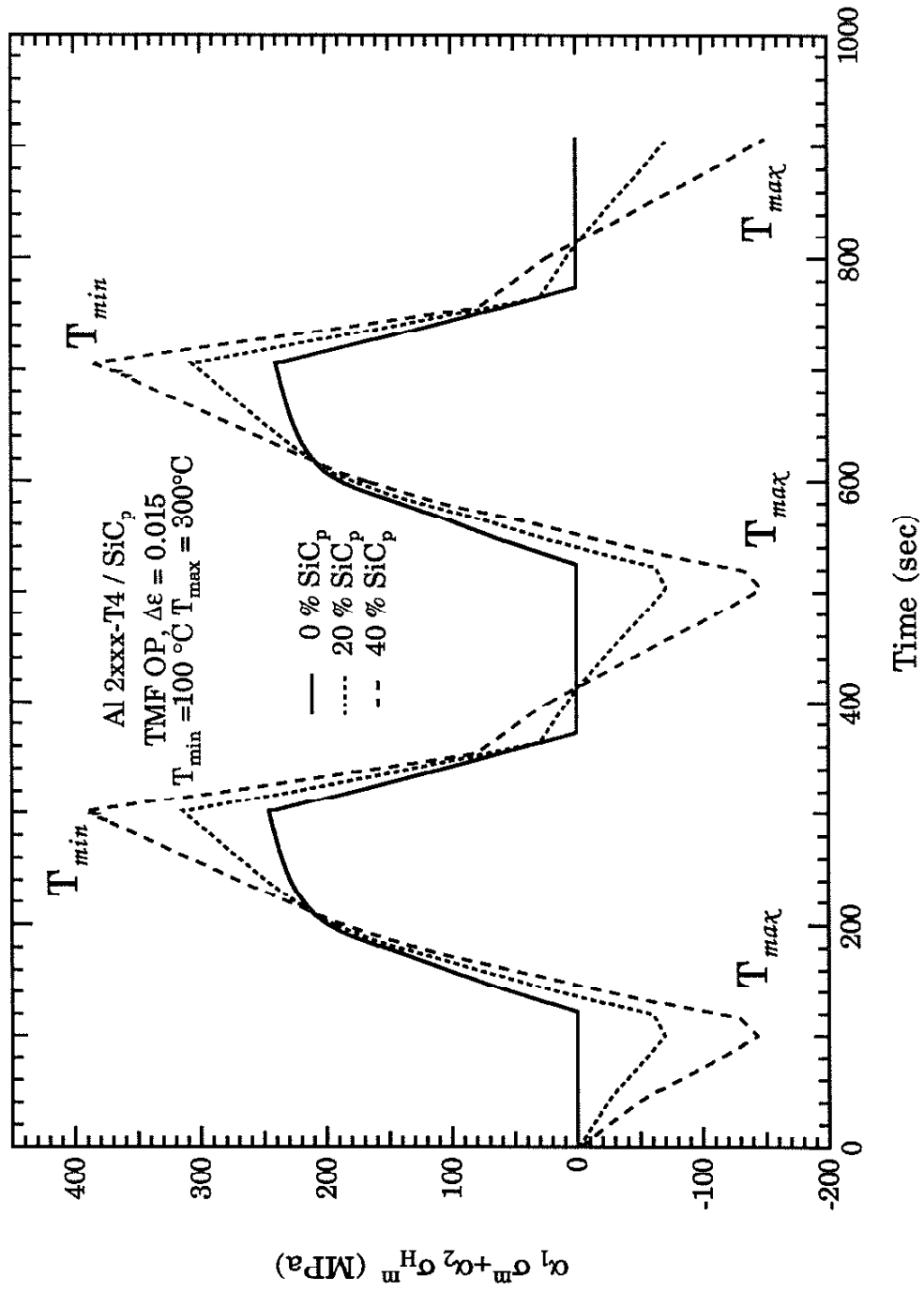


Figure 6.2: The variation of $\alpha_1 \sigma_1^m + \alpha_2 \sigma_2^m$ during a TMF OP loading cycle

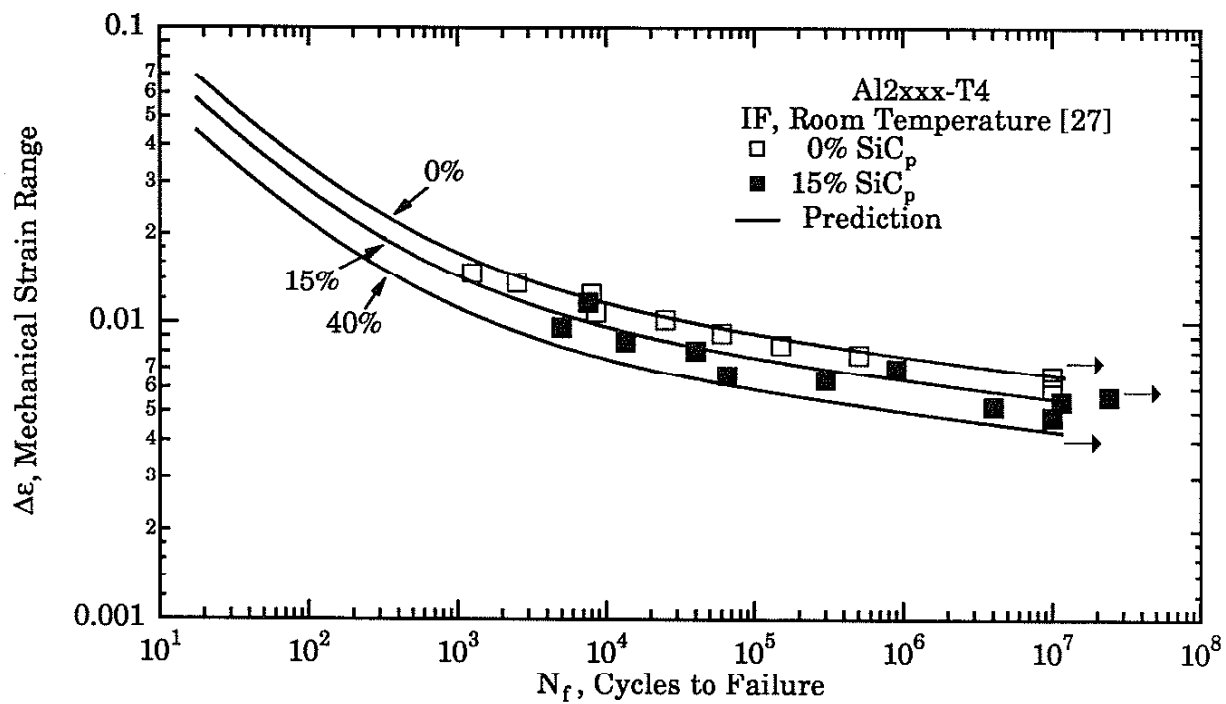


Figure 6.3: Room temperature strain-life behavior and predictions

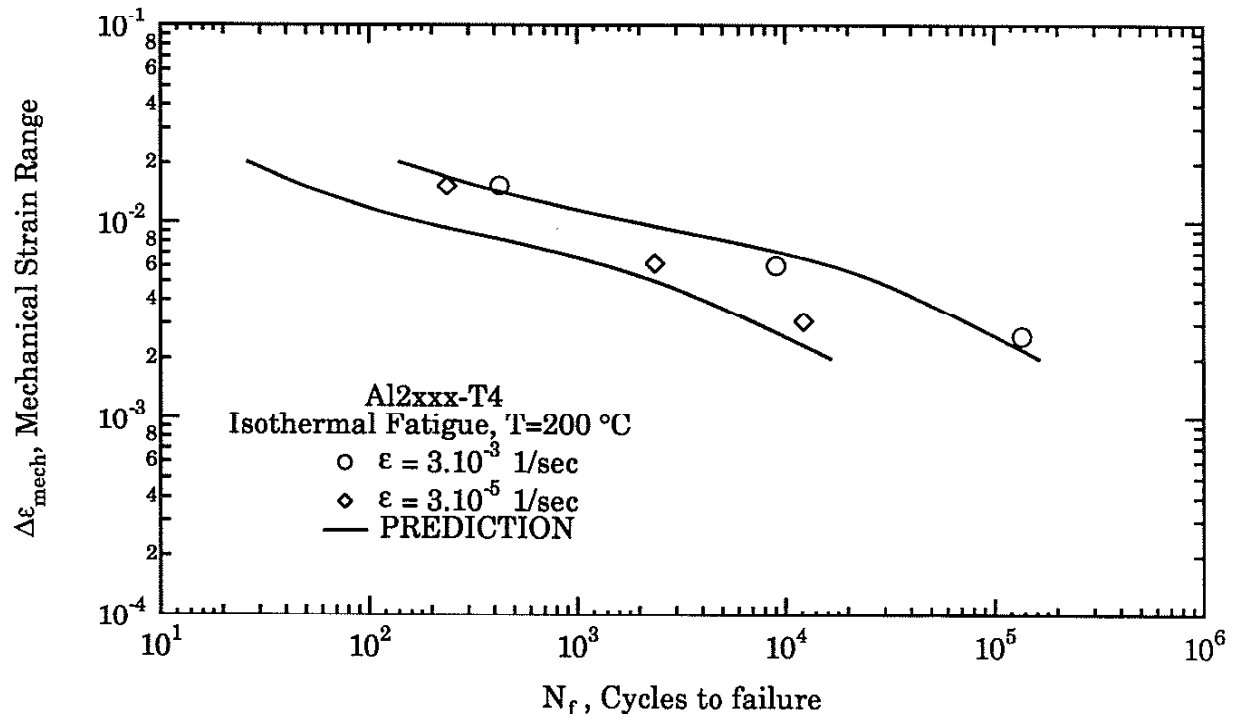


Figure 6.4: Isothermal strain-life prediction, unreinforced Al2xxx-T4, T=200°C
 $\epsilon=3.10^{-3}$ 1/sec, 3.10^{-5} 1/sec

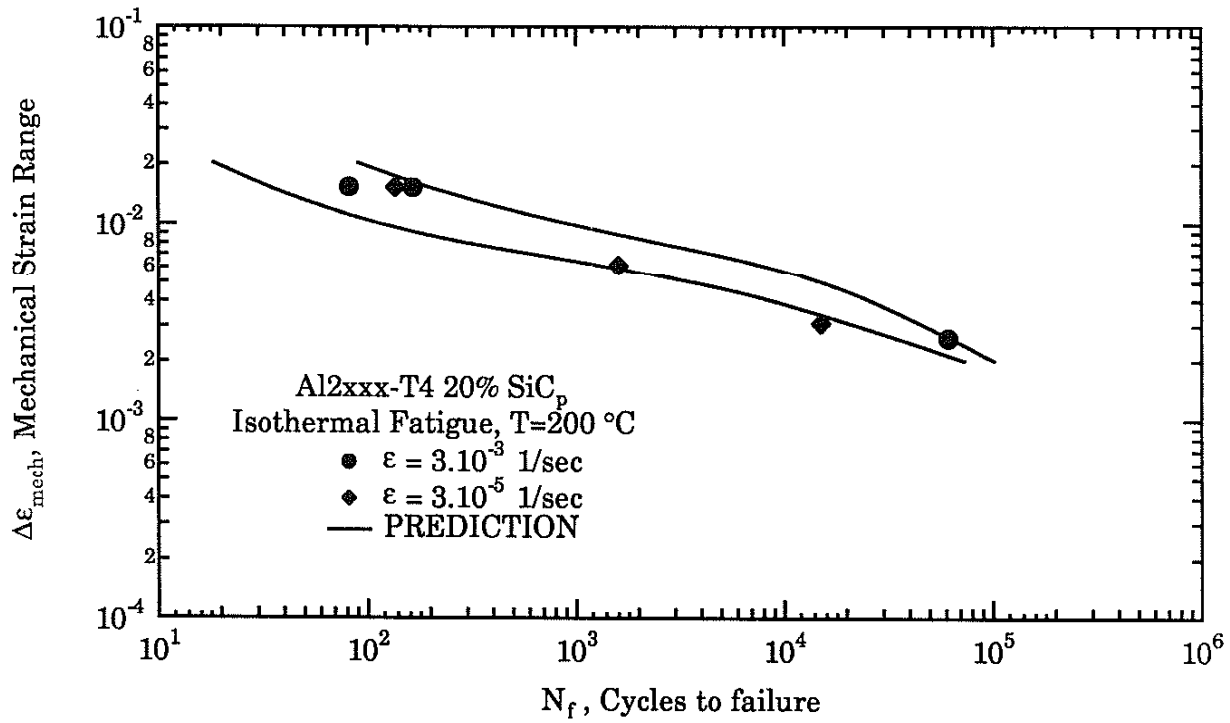


Figure 6.5: Isothermal strain-life prediction, 20% reinforced Al₂xxx-T4, T=200°C
 $\epsilon=3.10^{-3}$ 1/sec, 3.10^{-5} 1/sec

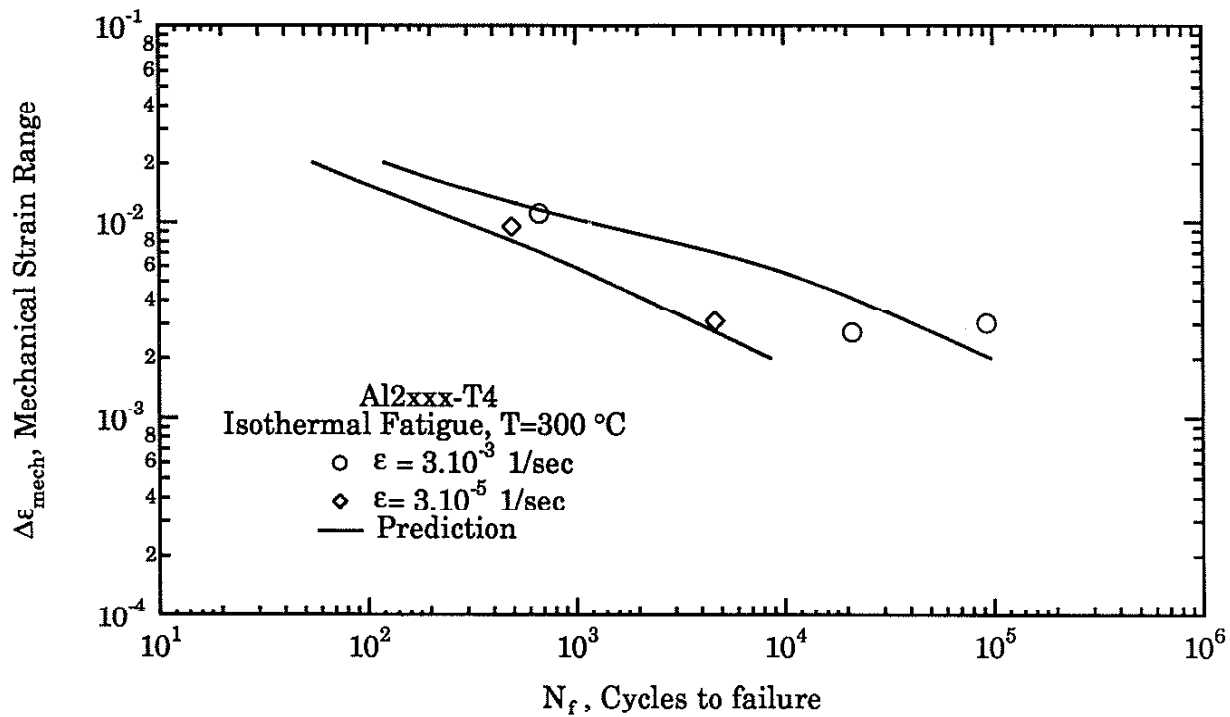


Figure 6.6: Isothermal strain-life prediction, unreinforced Al2xxx-T4, T=300°C
 $\epsilon=3.10^{-3}$ 1/sec, 3.10^{-5} 1/sec

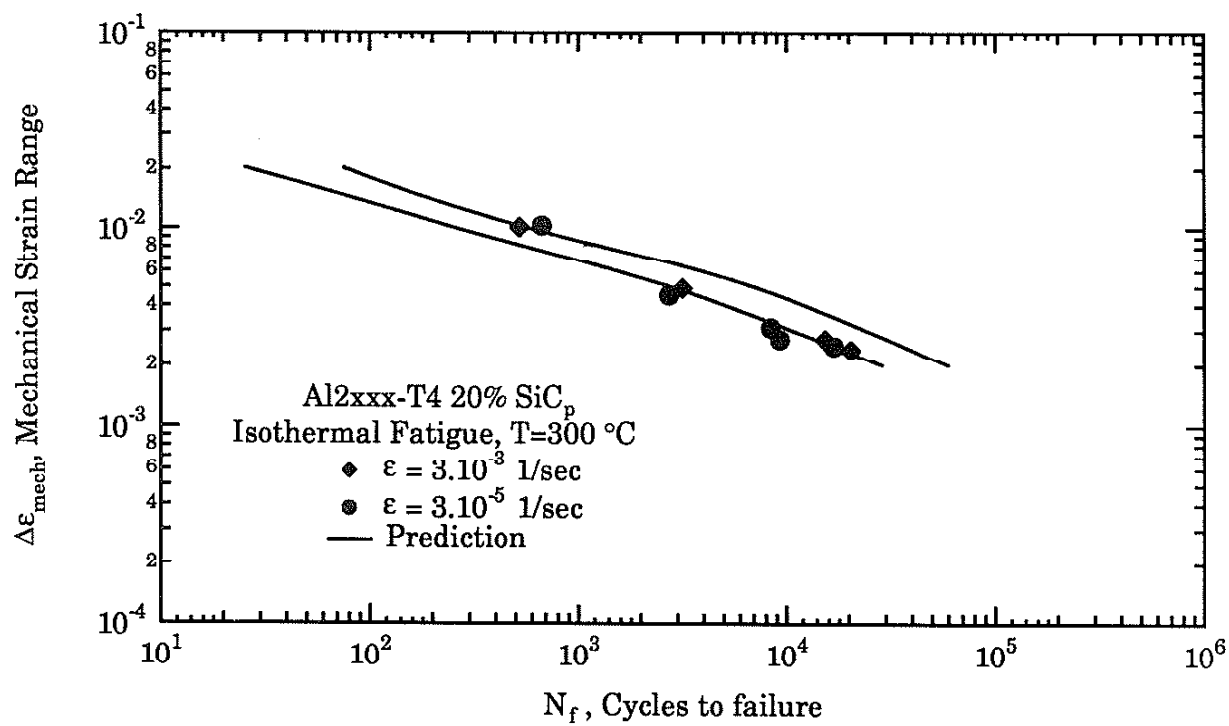


Figure 6.7: Isothermal strain-life prediction, 20% reinforced Al₂xxx-T4, T=300°C
 $\epsilon=3.10^{-3}$ 1/sec, 3.10^{-5} 1/sec

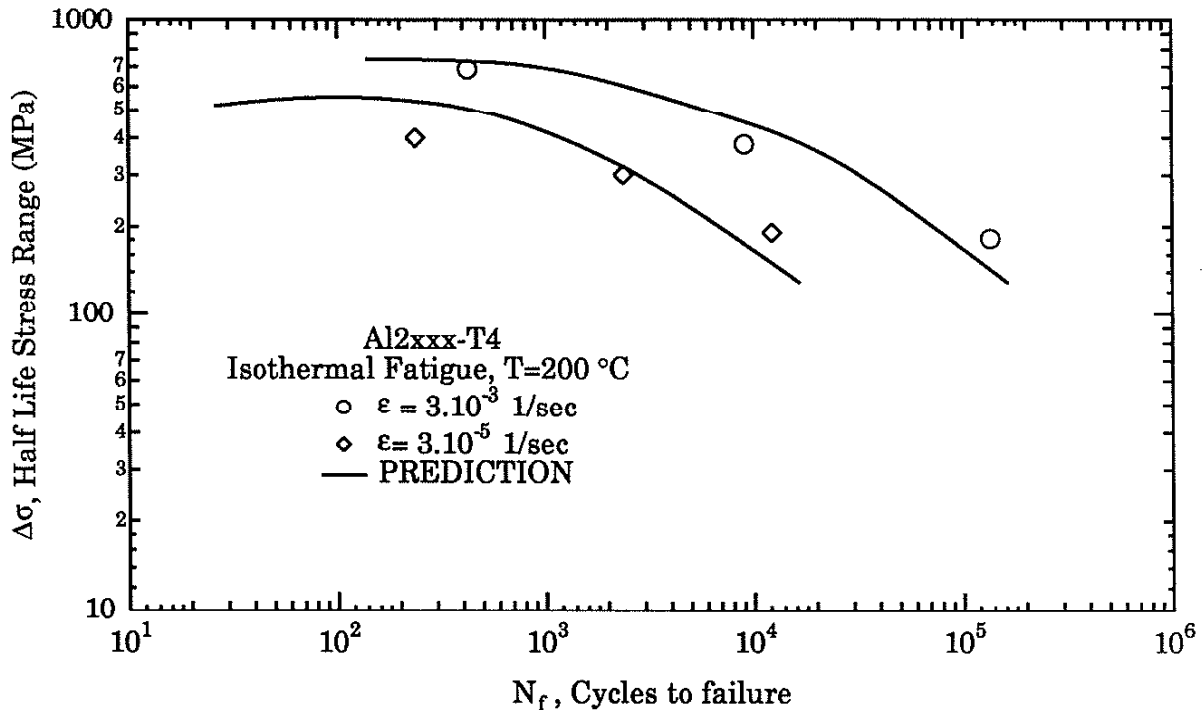


Figure 6.8: Isothermal stress-life prediction, unreinforced Al2xxx-T4, T=200°C
 $\epsilon=3.10^{-3}$ 1/sec, 3.10^{-5} 1/sec

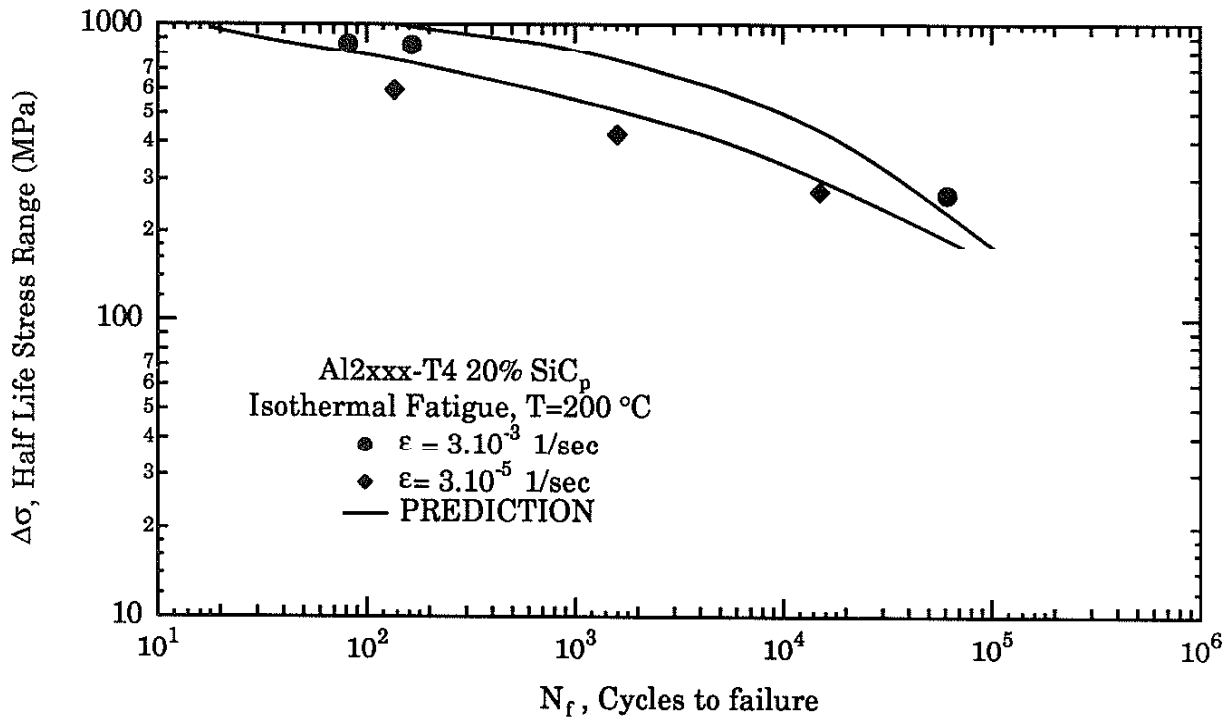


Figure 6.9: Isothermal stress-life prediction, 20% reinforced Al₂xxx-T4, T=200°C
 $\epsilon=3.10^{-3}$ 1/sec, 3.10^{-5} 1/sec

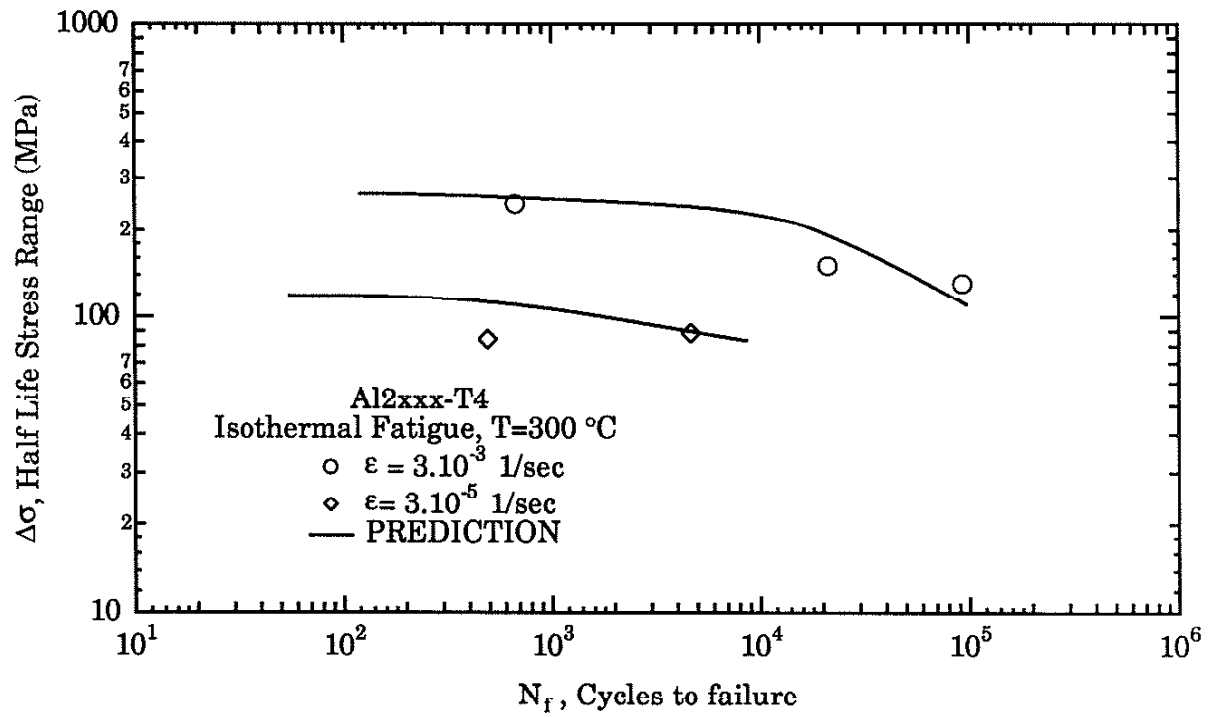


Figure 6.10: Isothermal stress-life prediction, unreinforced Al2xxx-T4, T=300°C
 $\epsilon=3.10^{-3}$ 1/sec, 3.10^{-5} 1/sec

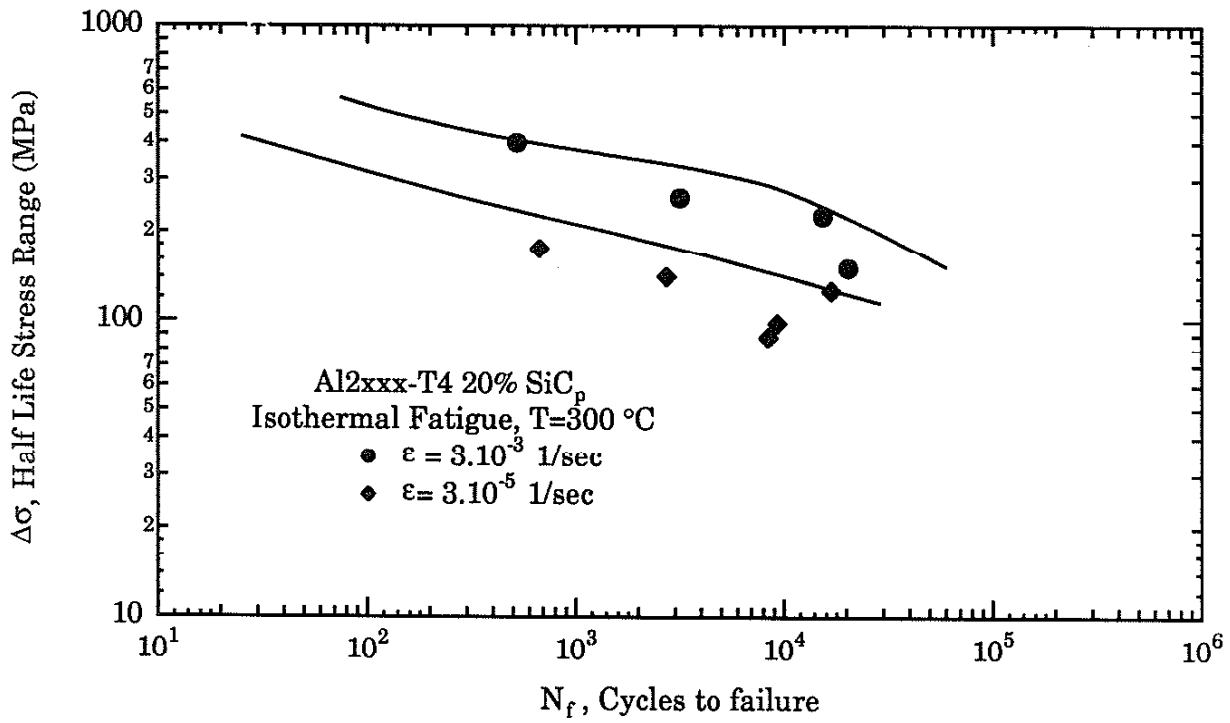


Figure 6.11: Isothermal stress-life prediction, 20% reinforced Al_{2xxx}-T4, T=300°C
 $\epsilon=3.10^{-3}$ 1/sec, 3.10^{-5} 1/sec

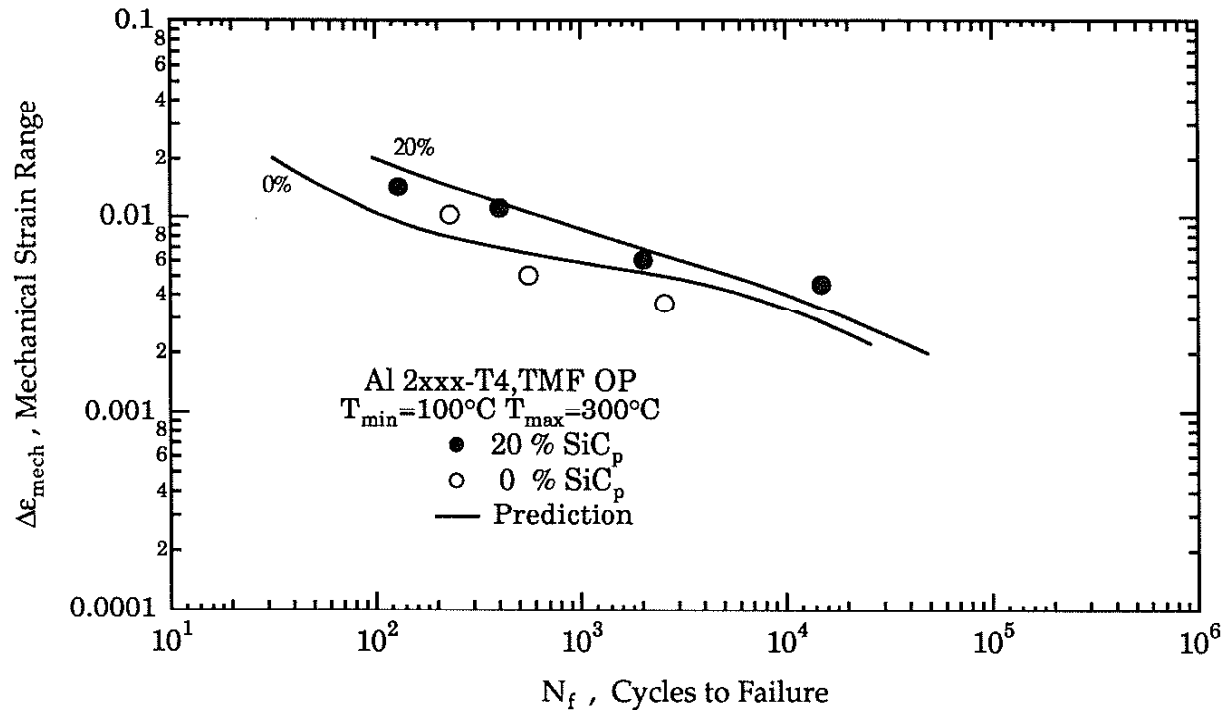


Figure 6.12: TMF OP life predictions 0%, 20% reinforced Al2xxx-T4

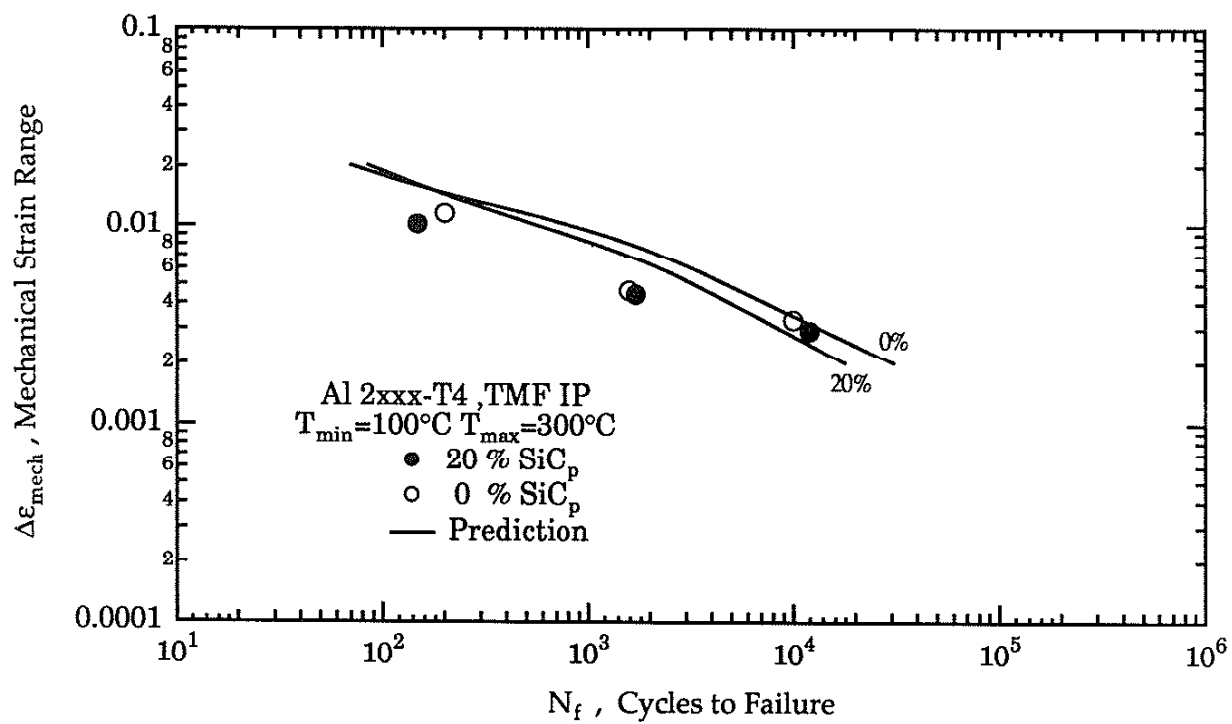


Figure 6.13: TMF IP life predictions 0%, 20% reinforced Al2xxx-T4

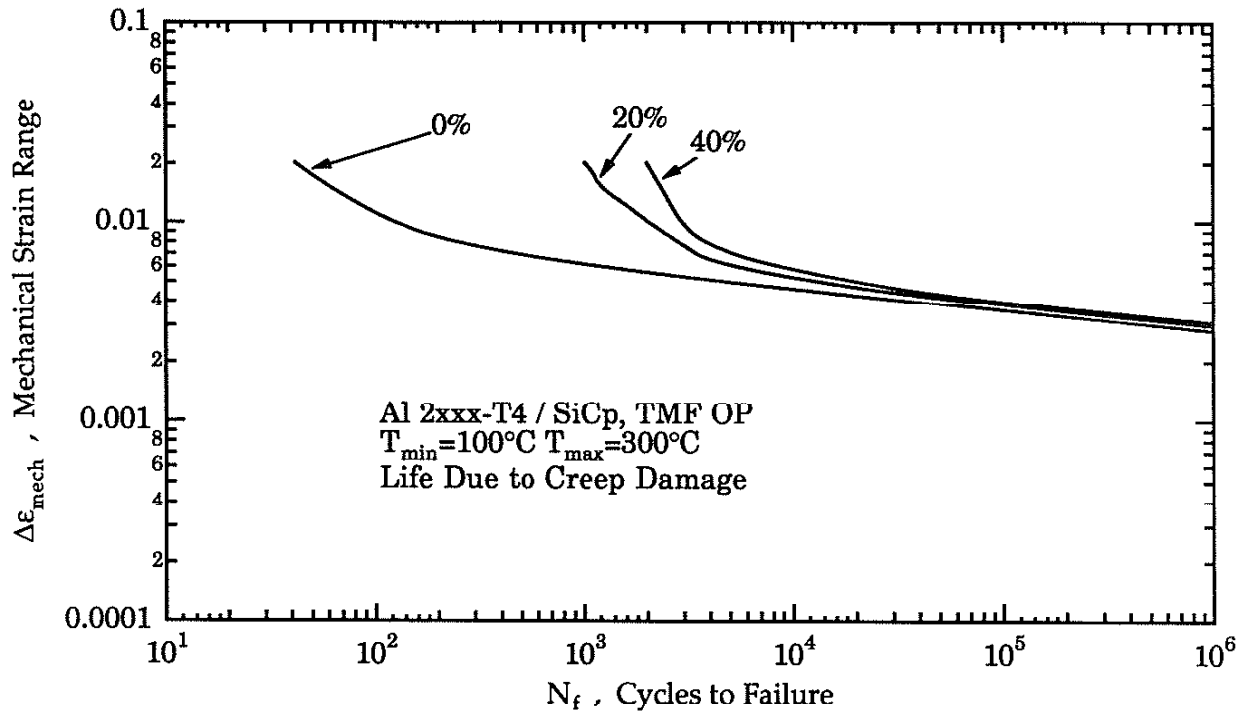


Figure 6.14: TMF OP life predictions 0%, 20%, 40% SiC_p reinforced Al2xxx-T4,
 $\epsilon = 3.10^{-5}$ 1/sec, creep damage only

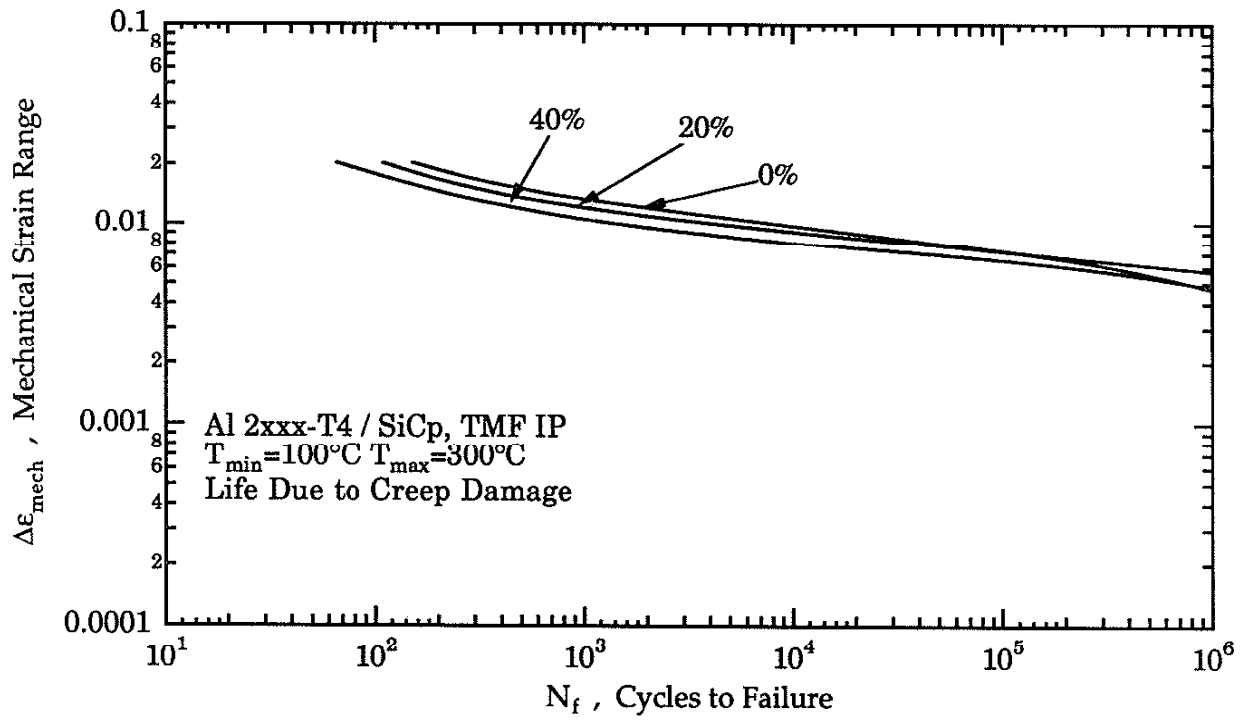


Figure 6.15: TMF IP life predictions 0%, 20%, 40% SiC_p reinforced Al2xxx-T4,
 $\dot{\epsilon} = 3.10^{-5}$ 1/sec, creep damage only

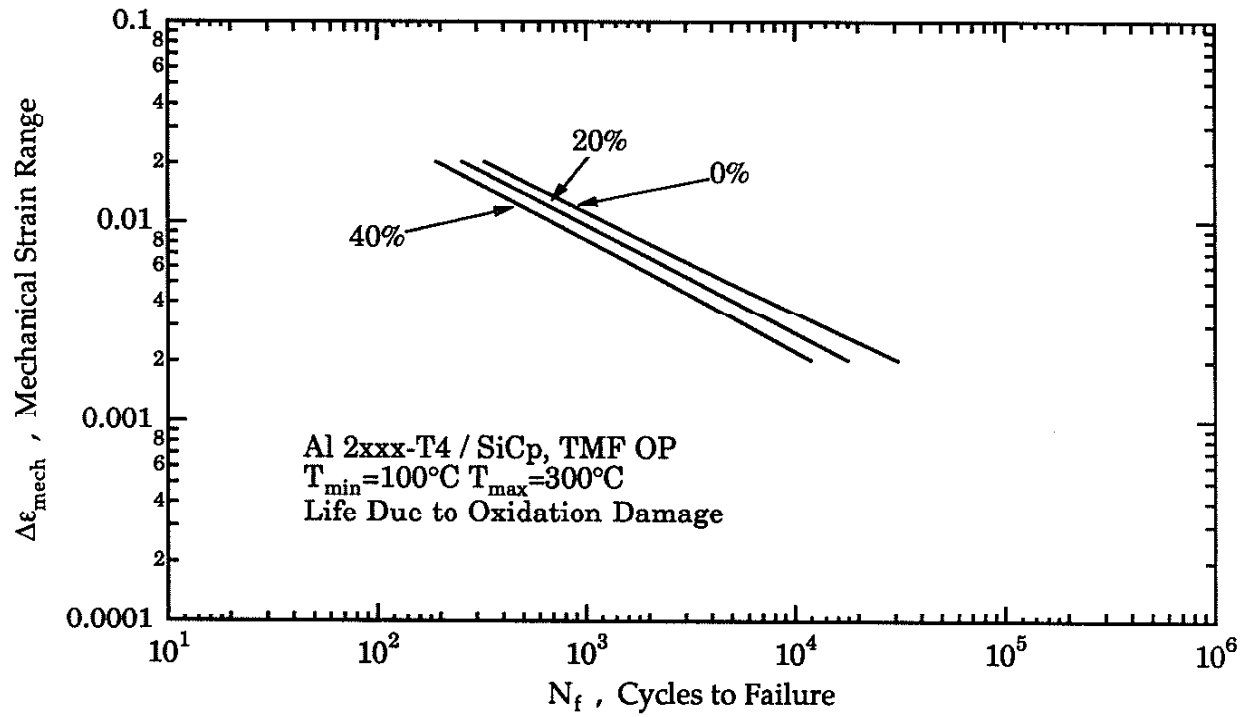


Figure 6.16: TMF OP life predictions 0%, 20%, 40% SiC_p reinforced Al2xxx-T4, $\epsilon = 3.10^{-5}$ 1/sec, oxidation damage only

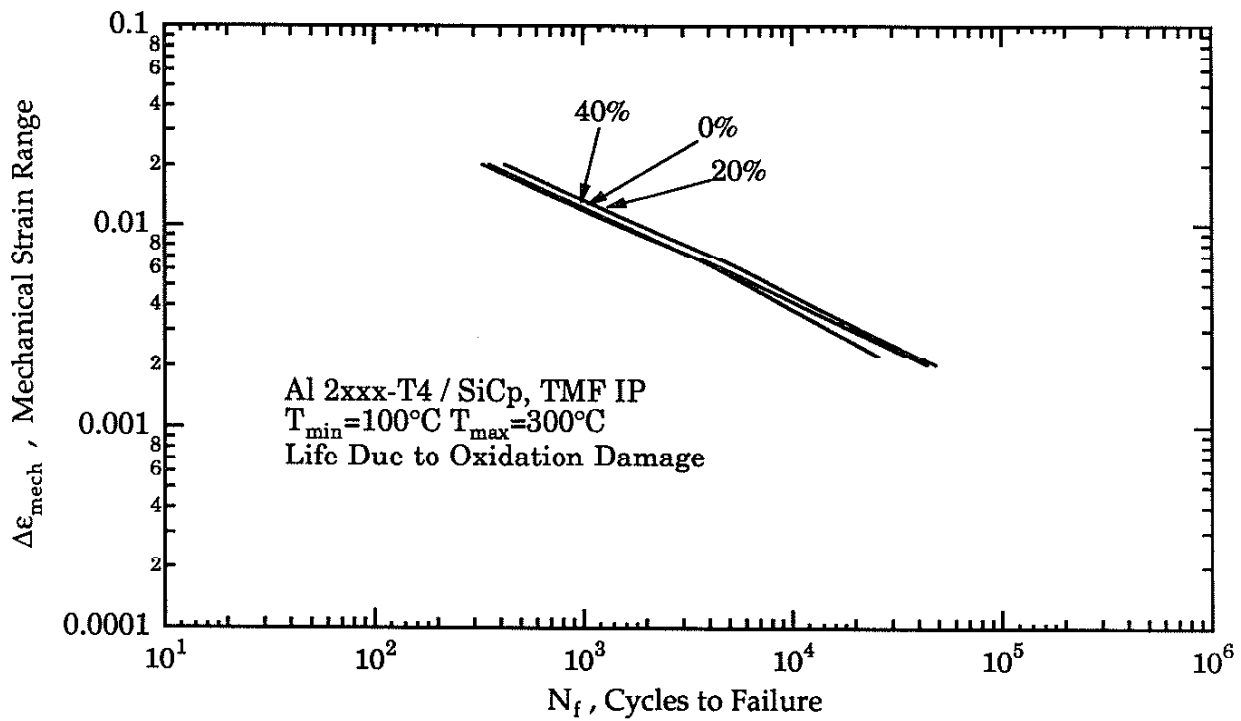


Figure 6.17: TMF IP life predictions 0%, 20%, 40% SiC_p reinforced Al2xxx-T4
 $\epsilon = 3 \cdot 10^{-5}$ 1/sec, oxidation damage only

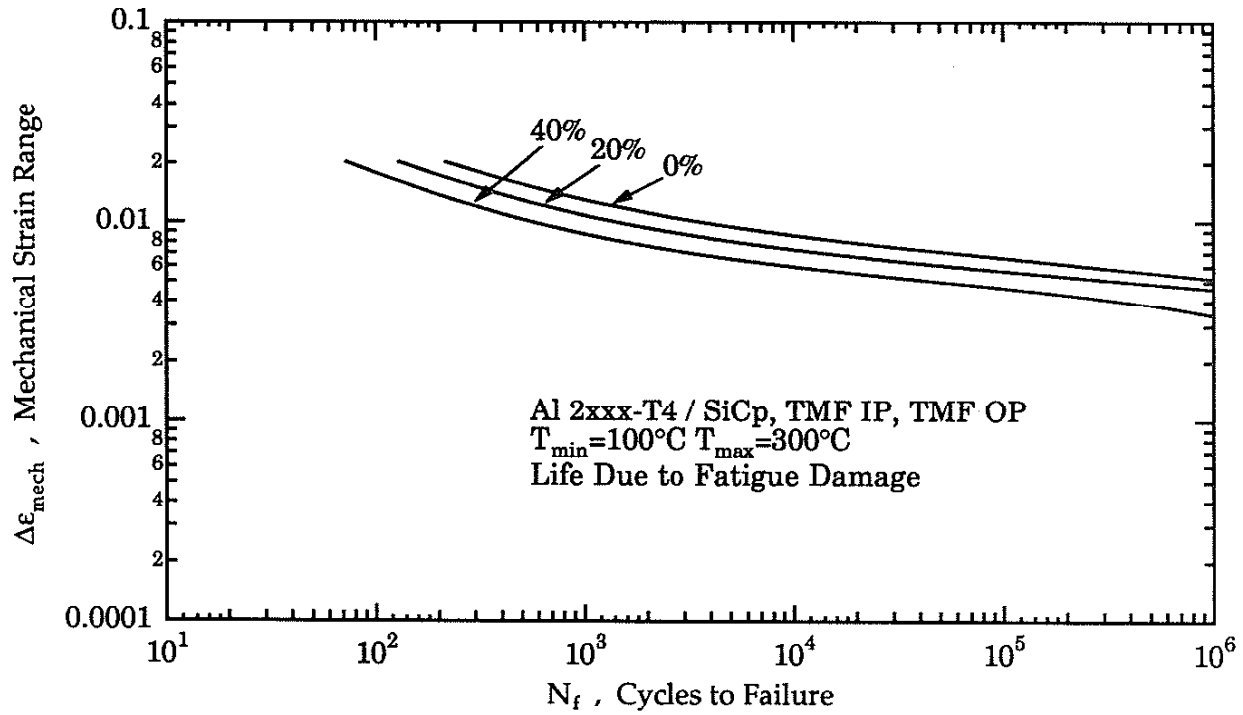


Figure 6.18: TMF IP and TMF OP life predictions 0%, 20%, 40% SiC_p reinforced Al2xxx-T4
 $\epsilon = 3 \cdot 10^{-5}$ 1/sec, fatigue damage only

REFERENCES

1. Neu, R.W., Sehitoglu, H., "Thermomechanical Fatigue, Oxidation and Creep; Part I Damage Mechanisms", Metallurgical Transactions, Vol. 20A, pp.1755-1783, 1989
2. Neu, R.W., Sehitoglu, H., "Thermomechanical Fatigue, Oxidation and Creep; Part II A Life Prediction Model", Metallurgical Transactions, Vol. 20A, pp. 1769-1783, 1989
3. Boismier, D.A., Sehitoglu, H., "Thermomechanical Fatigue of Mar-M247: Part 1- Experiments", ASME J. Eng Mats Techn., Vol. 112, pp. 68-79, 1990
4. Boismier, D.A., Sehitoglu, H., "Thermomechanical Fatigue of Mar-M247: Part 2- Life prediction", ASME J. Eng Mats Techn., Vol. 112, pp. 80-89, 1990
5. Nair, S. V., Tien, J. K., and Bates, R. C., "SiC Reinforced Aluminum Metal Matrix Composites", International Metals Reviews, Vol. 30, No. 6, pp. 275-290, 1985
6. Philips, W.L., "Elevated Temperature Properties of SiC Whisker Reinforced Aluminum", Proc. of Int. Conf. on Composite Materials, ed. B. Noton, Metal. Soc. of AIME, pp. 567-576, 1978
7. Boland, P. L., Digiovanni, P. R., and Franceschi, L. "Short Term High Temperature Properties of Reinforced Metal Matrix Composites", ASTM STP 964, pp. 346-375, 1988
8. Bhat, S., Laird, C., "Cyclic Stress-Strain Response and Damage Mechanisms at High Temperature", ASTM STP 675, pp. 592-623, 1979
9. Bhat, S., Laird, C., "High Temperature Cyclic Deformation of Precipitation Hardened Alloy-Part I Partially Coherent Precipitates", Acta Metallurgica, Vol. 27, pp. 1861-1871, 1979
10. Bhat, S., Laird, C., "High Temperature Cyclic-Deformation of Precipitation Hardened Alloy-Part II Fully Coherent Precipitates", Acta Metallurgica, Vol. 27, pp. 1873-1883, 1979

11. Baik, S., Raj, R., "Mechanisms of Creep Fatigue Interaction", *Metallurgical Transactions*, Vol. 13A, pp. 1215-1221, 1982
12. Smith, H. H., Michel, D. J., and Reed, J. R., "Fatigue Crack Propagation in Rapidly Solidified Aluminum Alloys at 25°C and 300°C", *Metallurgical Transactions*, Vol. 20A, pp. 2425-2430, 1989
13. Srivatsan, T.S. "Mechanisms of Damage in High-Temperature, Low-Cycle Fatigue of an Aluminum Alloy", *Int. Journal of Fatigue*, pp. 91-99, 1988
14. Hordon, M. J., "Fatigue Behavior of Aluminum in Vacuum", *Acta Metallurgica*, Vol. 14, pp. 1173-1178, 1966
15. Meyn, D. A., "The Nature of Fatigue Crack Propagation in Air and in Vacuum for 2024 Aluminum", *Transactions of ASM*, Vol.61, pp. 52-61, 1968
16. Bowles, C. Q., Schijve, J., "Crack Tip Geometry for Fatigue Cracks Grown in Air and in Vacuum", *ASTM STP 811*, pp. 400-426, 1983
17. Beck, A. F., Heine, M. A., Caule, E. J., and Pryor, M. J., "The Kinetics of the Oxidation of Al in Oxygen at High Temperature", *Corrosion Science*, Vol. 7, pp. 1-22, 1967
18. VanBeek, H.D., Mitteneiger, E.J., "Amorphous and Crystalline Oxides on Aluminum", *Thin Solid Films*, Vol. 122, pp. 131-151, 1984
19. Shinohara, K., Seo, T., and Kyogoku, H., "Transmission Electron Microscopy Studies on the Oxidation of Aluminum", *Z. Metallkde*, Vol. 73, pp. 774-780, 1982
20. Logsdon, W.A., Liaw, P.K., "Tensile, Fracture Toughness and Fatigue Crack Growth Rate Properties of Silicon Carbide Whisker and Particulate Reinforced Aluminum Metal Matrix Composites", *Eng. Fracture Mechanics*, Vol. 24, No. 5, pp. 737-751, 1986
21. Crowe, C.R., Gray, R.A, and Hasson, D.F, "Microstructure Controlled Fracture Toughness of SiC/Al Metal Matrix Composites", *Proc. 5th*

- Int. Conf. on Composite Materials, W.C. Harrigan, Jr, J. Strife, and A.K. Chingra, eds., TMS, Warrandale, PA, pp. 843-866, 1985
22. Davidson, D.L., "The Effect of Particulate SiC on Fatigue Crack Growth in a Cast-Extruded Aluminum Alloy Composite", *Metallurgical Transactions*, Vol. 22A, pp. 97-112, 1991
 23. Shang, J. K., Yu, W., and Ritchie, R. O., "Role of Silicon Carbide Particles in Fatigue Crack Growth in SiC Particulate Reinforced Aluminum Alloy Composites", *Material Science and Engineering*, Vol. A102, pp. 181-192, 1988
 24. Flom, Y., Arsenault, R.J., "Interfacial Bond Strength in an Aluminum Alloy 6061-SiC Composite", *Materials Science and Engineering*, Vol. 77, pp. 191-197, 1986
 25. Nieh, T.G., Rainen, R.A., and Chellman, D.J., " Microstructure and Fracture in SiC Whisker Reinforced 2124 Aluminum Composite", *Proc. 5th Int. Conf. on Composite Materials*, W.C. Harrigan, Jr, J. Strife, and A.K. Chingra, eds., TMS, Warrandale, PA, pp. 825-841, 1985
 26. Williams, D.R., Fine, M.E, " Quantitative Determination of Fatigue Microcrack Growth in SiC Whisker Reinforced 2124 Al Alloy Composites", *Proc. 5th Int. Conf. on Composite Materials*, W.C. Harrigan, Jr, J. Strife, and A.K. Chingra, eds., TMS, Warrandale, PA, pp. 639-670, 1985
 27. Bonnen, J. J., Allison, J. E., and Jones, J. W., "Fatigue Behavior of a 2xxx Series Aluminum Alloy Reinforced with 15% SiCp", *Metallurgical Transactions*, Vol. 22A, 1991
 28. Davidson, D. L., " Fracture Characteristics of Al- 4%Mg Mechanically Alloyed with SiC", *Metallurgical Transactions*, Vol. 18A, pp. 2115-2128, 1987
 29. Yau, S.S., Mayer, G., "Fatigue of Metal Matrix Composite Materials", *Material Science and Engineering*, Vol. 82, pp. 45-57, 1986

30. Christman, T. and Suresh, S., "Effects of SiC Reinforcement and Aging Treatment on Fatigue Crack Growth in an Al-SiC Composite", *Mater. Sci. Eng.*, Vol. A102, pp. 211-216, 1988
31. Arsenault, R.J., Pande, C.S., "Interfaces in Metal Matrix Composites", *Scripta Metallurgica*, Vol. 18, pp. 1131-1134, 1984
32. Cao, L., Geng, L., Yao, C.K., and Lei, T.C., "Interface in Silicon Carbide Whisker Reinforced Aluminum Composites", *Scripta Metallurgica*, Vol. 23, pp. 227-230, 1989
33. Divecha, A.P., Fishman, S.G., and Karmarkar, S.D., "Silicon Carbide Reinforced Aluminum- A Formable Composite", *Journal of Metals*, pp. 12-17, 1981
34. Lloyd, D.J., "Aspects of Fracture in Particulate Reinforced Metal Matrix Composites", *Acta Metallurgica*, Vol. 39, No. 1, pp. 59-71, 1991
35. You, C.P., Thompson, A.W., and Bernstein, I.M., "Proposed Failure Mechanism in Discontinuously Reinforced Aluminum", *Scripta Metallurgica*, Vol. 21, pp. 181-85, 1987
36. Lewandoski, J.J., Liu, C, and Hunt, W.H., Jr., "Effects of Matrix Microstructure and Particle Distribution on Fracture of an Aluminum Metal Matrix Composite", *Mater. Sci. Eng.*, Vol. A107, pp. 241-255, 1989
37. Hu, M.S., "Some Effects of Particle Size on the Flow Behavior of Al-SiCp Composites", *Scripta Metallurgica*, Vol. 25, pp. 695-700, 1991
38. Manoharan, M., Lewandoski, J.J., " Crack Initiation and Growth Toughness of an Aluminum Metal Matrix Composite", *Acta Metallurgica*, Vol. 38, No. 3, pp. 489-496, 1990
39. Yang, J., Cady, C, Hu, M.S., Zok, F., Mehrebian, R., and Evans, A.G., "Effects of Damage on the Flow Strength and Ductility of a Ductile Al Alloy Reinforced With SiC Particulates", *Acta Metallurgica*, Vol. 38, No. 12, pp. 2613-2619, 1990

40. Flom, Y., Arsenault, R.J., "Deformation of SiC/Al Composites", *Journal of Metals*, pp. 31-34, 1986
41. Mott, G., Liaw, P.K., "Correlation of Mechanical and Ultrasonic Properties of Al-SiC Metal-Matrix Composite", Vol. 19A, pp. 2233-2246, 1988
42. Crowe, C.R., Hasson, D.F., *Int. Conf. on the Strength of Metals and Alloys VI*, R.C. Gifkins, ed., Pergamon Press, New York NY, pp. 859-865, 1982
43. Harris, S.J., "Cast Metal Matrix Composites", *Mater. Sci. and Technol.*, Vol. 4, pp. 231-239, 1988
44. Hurd, N.J., "Fatigue Performance of Alumina Reinforced Metal Matrix Composites", *Mater. Sci. and Technol.*, Vol. 4, pp. 513-517, 1988
45. Webster, D., "Effect of Lithium on the Mechanical Properties and Microstructure of SiC Whisker Reinforced Aluminum Alloys", *Metallurgical Transactions*, Vol. 13A, pp. 1511-1519, 1982
46. Nieh, T. G., "Creep Rupture of a Silicon Carbide Reinforced Aluminum Composite", *Metallurgical Transactions*, Vol. 15A, pp. 139-146, 1984
47. Pickard, S.M., Derby, B., "The Deformation of Particle Reinforced Metal Matrix Composites During Temperature Cycling", *Acta Metallurgica*, Vol. 38, No 12, pp. 2537-2552, 1990
48. Nardone, V.C., Strife, J.R., "Analysis of Creep Behavior of Silicon Carbide Whisker Reinforced 2124 Al(T4)", *Metallurgical Transactions*, Vol. 18A, pp. 109-114, 1987
49. Mishra, R.S., Mukherjee, A.K., "On Superplasticity in Silicon Carbide Reinforced Aluminum Composites", *Scripta Metallurgica*, Vol. 25, pp. 271-275, 1991

50. Morimoto, T., Yamaoka, T., Lilholt, H., and Taya, M., "Second Stage Creep of SiC Whisker/6061 Aluminum Composite at 573K", *J. Eng. Mater. Technol.*, Vol. 110, pp. 70-76, 1988
51. Nardone, V.C., Prewo, K.M., "On the Strength of Discontinuous Silicon Carbide Reinforced Aluminum Composites", *Scripta Metallurgica*, Vol. 20, pp. 43-48, 1986
52. Kamat, S.V., Rollett, A.D., and Hirth, J.P., "Plastic Deformation in Al Alloy Matrix Alumina Particulate Composites", *Scripta Metallurgica*, Vol. 25, pp. 27-32, 1991
53. Aikin, R.M., Jr, Cristodolou, L., "The Role of Equiaxed Particles on the Yield Stress of Composites", *Scripta Metallurgica*, Vol. 25, pp. 9-14, 1991
54. Evans, A.G., Hutchinson, J.W., and McMeeking, R.M., "Stress-strain behavior of Metal Matrix Composites with Discontinuous Reinforcements", *Scripta Metallurgica*, Vol. 25, pp. 3-8, 1991
55. Papazian, J. M., Adler, P. N., "Tensile Properties of Short Fiber Reinforced SiC-Al Composites; Part 1. Effects of Matrix Precipitates", *Metallurgical Transactions*, Vol. 21A, pp. 401-410, 1990
56. Miller, W.S, Humphreys, F.J., "Strengthening Mechanisms in Particulate Metal Matrix Composites", *Scripta Metallurgica*, Vol. 25, pp. 33-38, 1991
57. Arsenault, R.J., Wang, L., and Feng, C.R., "Strengthening of Composites Due to Microstructural Changes in the Matrix", *Acta Metallurgica*, Vol. 39, No 1, pp. 47-57, 1991
58. Arsenault, R.J., Fisher, R.M., "Microstructure of Fiber and Particulate SiC in 6061 Al Composites", *Scripta Metallurgica*, Vol. 17, pp. 67-71, 1983

59. Arsenault, R.J., "The Strengthening of Aluminum Alloy 6061 by Fiber and Platelet Silicon Carbide", *Material Science and Engineering*, Vol. 64, pp. 171-181, 1984
60. Taya, M., Mori, T., "Dislocations Punched-out Around a Short Fiber in a Short Fiber Metal Matrix Composite Subjected to Uniform Temperature Change", *Acta Metallurgica*, Vol. 35, pp. 155-162, 1987
61. Taya, M., Lulay, K.E., and Lloyd, D.J., "Strengthening of a Particulate Metal Matrix Composite by Quenching", *Acta Metallurgica*, Vol. 39, pp. 73-87, 1991
62. McHugh, P.E., Varias, A.G., Asaro, R.J., and Shih, C.F., "Computational Modeling of Microstructures", *Future Generation of Computer Systems*, Vol. 5, pp. 295-318, 1989
63. Christman, T., Suresh, S., "Microstructural Development in an Aluminum Alloy-SiC Whisker Composite", *Acta Metallurgica*, Vol. 36, No. 7, pp. 1691-1704, 1988
64. Hershey, A. V., "The Elasticity of an Isotropic Aggregate of Anisotropic Cubic Crystals", *Journal of Applied Mechanics*, Vol. 21, pp. 236-240, 1954
65. Hershey, A. V., "The Plasticity of An Isotropic Aggregate of Anisotropic Face-Centered Cubic Crystals", *Journal of Applied Mechanics*, Vol. 21, pp. 241-249, 1954
66. Kroner, E., "On the Plastic Deformation of Polycrystals", *Acta Metallurgica*, Vol. 9, pp. 155-161, 1961
67. Budiansky, B. and Wu, T.T., "Theoretical Prediction of Plastic Strains of Polycrystals", *Proceedings of 4th U.S. National Congress of Applied Mechanics*, ASME, New York, pp. 1175-1185
68. Hill, R., "Continuum Mechanics of Elastoplastic Polycrystals", *J. of Mechanics and Physics of Solids*, Vol. 13, pp. 89-101, 1965
69. Hill, R., "A Self-Consistent Mechanics of Composite Materials", *J. of Mechanics and Physics of Solids*, Vol. 13, pp. 213-222, 1965

70. Eshelby, J.D., "The Determination of the Elastic Field of an Ellipsoidal Inclusion and Related Problems", Proc. Royal Society, Vol. A241, pp. 376-396, 1957
71. Eshelby, J.D. "Chapter 3 :Elastic Inclusions and Inhomogeneities", Progress in Solid Mechanics, Vol.3, pp. 87-140, 1961
72. Hutchinson, J.W., "Plastic Stress-strain relations of F.C.C Polycrystalline metals Hardening According to Taylor's Rule", J. of Mechanics and Physics of Solids, Vol. 12, pp. 11-24, 1964
73. Hutchinson, J.W., "Plastic Deformation B.C.C. Polycrystals", J. of Mechanics and Physics of Solids, Vol. 12, pp. 15-33, 1964
74. Laws, N., McLaughlin, R., "Self-consistent Estimates for the Viscoelastic Creep Compliances of Composite Materials", Proc R. Soc. (London), Vol. A359, 251-273, 1978
75. Brown, G. M., "A Self Consistent Polycrystalline Model for Creep Under Combined Stress State", J. of Mechanics and Physics of Solids, Vol. 18, pp. 367-381, 1970
76. Hutchinson, J.W., "Bounds and Self-Consistent Estimates for Creep of Polycrystalline Materials", Proc R. Soc. (London), Vol. A348, pp. 101-127, 1976
77. Russell, W. B., " On the Effective Moduli of Composite Materials: Effect of Fiber Length and Geometry at Dilute Concentrations", Z. Agnew. Math. Physics, Vol. 24, pp. 581, 1973
78. Tanaka, K., Mori, T., "The Hardening of Crystals by Non-Deforming Particles and Fibres", Acta Metallurgica, Vol. 18, pp. 931-941, 1970
79. Tanaka, K., Wakashima, K., and Mori, T., "Plastic Deformation Anisotropy and Work-Hardening of Composite Materials", J. of Mechanics and Physics of Solids, Vol.21, pp. 207-214, 1973
80. Mori, T., Tanaka, K., "Average Stress in Matrix and Average Elastic Energy of Materials With Misfitting Inclusions", Acta Metallurgica, Vol. 21, pp. 571-574, 1973

81. Wakashima, K., Otsuka, M., and Umekawa, S., "Thermal Expansions of Heterogeneous Solids Containing Aligned Ellipsoidal Inclusions", *Journal of Composite Materials*, Vol. 8, pp. 391-404, 1974
82. Arsenault, R. J., Taya, M., "Thermal Residual Stress in Metal Matrix Composites", *Acta Metallurgica*, Vol. 35, pp. 651-659, 1987
83. Tandon, G.P., Weng, G.J., "A Theory of Particle-Reinforced Plasticity", *Journal of Applied Mechanics*, Vol. 55, pp. 126-135, 1988
84. Mura, T., "Micromechanics of Defects in Solids", Martinus Nijhoff Publishers, 1989
85. Slavik, D., H. Sehitoglu, "A Constitutive Model for High Temperature Loading Part I: Experimentally Based Form of the Equations", *Thermal Stress, Material Deformation, and Thermomechanical Fatigue*, ASME, PVP-123, pp. 65-73, 1987
86. Slavik, D., and H. Sehitoglu, "A Constitutive Model for High Temperature Loading Part II: Comparisons of Simulations with Experiments" *Thermal Stress, Material Deformation, and Thermomechanical Fatigue*, ASME, PVP-123, pp. 75-82, 1987
87. Ding, J. L., Lee, S. R., "Controlled Strain Rate Tests at Very Low Strain Rates of 2618 Aluminum at 200°C", *Nonlinear Constitutive Relations for High Temperature Applications*, NASA Conference Publication 10010, pp. 225-238, 1986
88. Levy, A. and Papazian, J. M., "Tensile Properties of Short Fiber-Reinforced SiC/Al Composites: Part II Finite Element Analysis", *Metallurgical Transactions*, Vol. 21A, pp. 411-420, 1990
89. Duva, J.M., "A Self-Consistent Analysis of the Stiffening Effect of Rigid Inclusions on a Power-Law Material", *ASME J.Eng. Materials and Technology*, Vol. 106, pp. 317-321, 1984
90. Bao, G., Hutchinson, J. W., and McMeeking, R. M., "Particle Reinforcement of Ductile Matrices Against Plastic Flow and Creep", U. Calif. Santa Barbara Report, May 1990

91. Christman, T., Needleman, A., and Suresh, S., "An Experimental and Numerical Study of Deformation in Metal Matrix Composites", *Acta Metallurgica*, Vol. 37, No. 11, pp. 3029-3050, 1989
92. Majumdar, S. and Maiya, P. S., "A Mechanistic Model for Time-Dependent Fatigue," *ASME, ASME J. Engineering Materials and Technology*, Vol. 102, pp. 159-167, 1980
93. Manson, S. S., Halford, G. R., and Hirschberg, M. H., "Creep Fatigue Analysis by Strain Range Partitioning", *NASA TMX-67838*, 1971
94. Coffin, L.F., Jr., "Fatigue at High Temperature", *Fatigue at Elevated Temperatures*, ASTM STP 520, pp. 5-34, 1973.
95. Challenger, K.D., Miller, A.K., and Landgon, R.L., "Elevated Temperature Fatigue with Hold Time in a Low Alloy Steel: A Predictive Correlation", *J. Materials for Energy Systems*, Vol. 3, pp. 51-61, 1981
96. Antolovich, S. D., R. Baur, and S. Liu, "A Mechanistically Based Model for High Temperature LCF of Ni Base Superalloys," *Superalloys 1980*, pp. 605-613, 1980
97. Saxena, A., Bassani, J.L., "Time-Dependent Fatigue Crack Growth Behavior at Elevated Temperature," *Fracture: Int. of Microstructure, Mechanisms and Mechanics*, Ed. by Joseph M. Wells and John D. Landes, TMS-AIME, pp. 357-383, 1984
98. Reuchet, J., L. Remy, "Fatigue Oxidation Interaction in a Superalloy - Application to Life Prediction in High Temperature Low Cycle Fatigue," *Metallurgical Transactions*, Vol. 14A, pp. 141-149, 1983
99. Halford, G. R., Manson, S. S., "Life Predictions of Thermal-Mechanical Fatigue Using Strain Range Partitioning," *ASTM STP 612*, pp. 239-254, 1976
100. ASME Boiler and Pressure Vessel Code, Case N-47-23, Class 1 Components in Elevated Temperature Service, Section III, Division 1, 1986.

101. Lemaitre, J. and Plumtree, A., "Application of Damage Concepts to Predict Creep-Fatigue Failures," ASME J. Engineering Materials and Technology, Vol. 101, pp. 284-292, 1979
102. Liu, H. W., and Y. Oshida, "Grain Boundary Oxidation and Fatigue Crack Growth at Elevated Temperatures," Theo. and Appl. Fract. Mech., Vol. 6, pp. 85-94, 1986
103. Jaske, C. E., "Creep-Fatigue Crack Growth in Type 316 Stainless Steel," ASME International Conference on Advances in Life Prediction Methods, pp. 93-103, 1983
104. Majumdar, S., "Thermomechanical Fatigue of Type 304 Stainless Steel", Thermal Stress, Material Deformation, and Thermomechanical Fatigue, ed., by H. Sehitoglu and S. Y. Zamrik, ASME, PVP-Vol. 123, pp. 31-36, 1987
105. Morrow, J., "Internal Friction, Damping and Cyclic Plasticity", ASTM STP 378, pp. 45-87, 1965
106. Hart, R.K., Maurin, J. K., "The Nucleation and Growth of Oxide Islands on Aluminum", Surface Science, Vol. 20, pp. 285-303, 1970
107. Gulbransen, E.A., Wysong, W.S. J., Phys. Colloid. Chem., Vol. 51, pp. 1087, 1947.
108. Baik, S., Raj, R., "Wedge Type Creep Damage in Low Cycle Fatigue," Metallurgical Transactions, Vol. 13A, pp. 1207-1214, 1982
109. Raj, R., Ashby, M. F., "Intergranular Fracture at Elevated Temperatures", Acta Metallurgica, Vol. 23, pp. 653, 1975
110. Hayhurst, D. R., "Creep Rupture under Multi-axial States of Stress", J. Mech. Phys. Solids, Vol. 20, pp. 381-390, 1972
111. Hayhurst, D. R., "On the Role of Creep Continuum Damage in Structural Mechanics", Chap. 3, Engineering Approaches to High Temperature Design, Vol. 2 in the Series, Recent Advances in Creep and Fracture of Engineering Materials and Structures, Ed. by B. Wilshire and D. R. J. Owen, 1983

112. Trampczynski, W.A., Hayhurst, D.R., Leckie, F.A., "Creep Rupture of Copper and Aluminum under Non-Proportional Loading", *J. Mech. Phys. Solids*, Vol. 29, No.5-6, pp. 353-374, 1981